UNIVERSITAT DE BARCELONA

Multidisciplinary characterization of diapiric basins integrating field examples, numerical and analogue modelling: Central High Atlas Basin (Morocco)

Mar Moragas Rodriguez

Consejo Superior de Investigaciones Científicas (CSIC)
Institut de Ciències de la Terra Jaume Almera (ICTJA)
Departament de Estructura i Dinámica de la Terra

Universitat de Barcelona (UB)
Departament de Mineralogia, Petrologia i Geologia Aplicada

Programa de doctorat de Ciències de la Terra

Multidisciplinary characterization of diapiric basins integrating field examples, numerical and analogue modelling: Central High Atlas Basin (Morocco)

Memoria presentada per Mar Moragas Rodriguez al Departament de Mineralogia, Petrologia i Geologia Aplicada de la Universitat de Barcelona per a optar al grau Doctor en Geologia sota la dirección dels doctors Jaume Vergés i Masip i Elisabet Playà Pous

Mar Moragas Rodriguez

Barcelona, 2017

Directors:

Dr. Jaume Vergés i Masip **Dra. Elisabet Playà Pous**

The research reported in this thesis is a contribution of the
Group of Dynamics of the Lithosphere (GDL)
Department of Structure and Dynamic of the Earh
Institute of Earth Sciences Jaume Almera (ICTJA–CSIC)

PRESENTATION

This dissertation constitutes the work that I have done for the degree of PhD at the Mineralogy, Petrology and Applied Geology Department of the University of Barcelona (UB). It is prepared in the format recommended by university. This work, conducted in the Institute of the Earth Sciences Jaume Almera (ICTJA–CSIC), was elaborated in the framework of a collaborative project between the Group of Dynamics of the Lithosphere (GDL) at the Institute of Earth Sciences Jaume Almera of the CSIC in Barcelona, Spain and the Statoil Research Centre of Bergen in Norway. The focused of this project was the study of diapiric basin dynamics in the Central High Atlas of Morocco. Several fieldworks were done during the period of 2011–2017 in order to collect sedimentological and structural data and samples, resulting geological maps, cross-sections and reports prepared by Group of Dynamic of the Lithosphere. Some of the results were published in international journals as it is detailed below:

Saura, E., Vergés, J., Martín-Martín, J.D., Messager, G., Moragas, M., Razin, P., Grélaud, C., Joussiaume, R., Malaval, M., Homke, S., 2014. Syn-to post-rift diapirism and minibasins of the Central High Atlas (Morocco): the changing face of a mountain belt. Journal of the Geological Society 171, 97-105.

Martín-Martín, J.D., Vergés, J., Saura, E., Moragas, M., Messager, G., Baqués, V., Razin, P., Grélaud, C., Malaval, M., Joussiaume, R., Casciello, E., Cruz-Orosa, I., Hunt, D.W., 2016. Diapiric growth within an Early Jurassic rift basin: the Tazoult salt wall (Central High Atlas, Morocco). Tectonics 35, 1-31.

Moragas, M., Vergés, J., Saura, E., Martín-Martín, J.-D., Messager, G., Merino-Tomé, Ó., Suárez-Ruiz, I., Razin, P., Grélaud, C., Malaval, M., Joussiaume, R., Hunt, D.W., 2016. Jurassic rifting to post-rift subsidence analysis in the Central High Atlas and its relation to salt diapirism. Basin Research, 1-27.

Vergés, J., Moragas, M., Martín-Martín, J.D., Saura, E., Razin, P., Grélaud, C., Malaval, M., Joussiaume, R., Messager, G., Sharp, I., Hunt, D.W., 2017. Salt tectonics in the Atlas mountains of Morocco, in: Soto, J.I., Tari, G., Flinch, J. (Eds.), Permo-Triassic Salt Provinces of Europe, North Africa and the Atlantic Margins: Tectonics and hydrocarbon potential Elsevier.

Moragas, M., Vergés, J., Nalpas, T., Saura, E., Martín-Martín, J.-D., Messager, G., Hunt, D.W., Submitted. The impact of syn- and post-extension prograding sedimentation on the development of salt-related rift basins and their inversion: Clues from analogue modelling.

Saura, E., Martín-Martín, J.D., Vergés, J., Moragas, M., Casciello, E., Baqués, V., Razin, P., Grélaud, C., Messager, G., Hunt, D., In prep. Shoulder to shoulder architecture of a diapiric rift basin at the onset of continental break-up: The Central High Atlas Jurassic diapiric province.

ACKNOWLEDGMENTS / AGRAÏMENTS

The development of this research allowed me to work on topics that I never dealt with before, such as large scale geological processes, diapiric basin dynamics, subsidence and geohistory analysis, thermal modelling and analogue modelling. That was possible due to the fact that this thesis was elaborated in the framework of a collaboration between the Group of Dynamics of the Lithosphere and the Statoil Research Centre of Bergen in Norway, which allowed me to study not only the Central High Atlas of Morocco but also other regions (Iberian Range, Cantabrian basin, Pyrenees and Onshore Angola) as well as to collaborate with a wide variety of experts (structural geologist, sedimentologist, petrologists, among others). For all the aforementioned, some acknowledgments are required.

Un agraïment als meus directors de tesis. Primer de tot a en Jaume Vergés haig d'agrair-li l'esforç i el temps que ha dedicat a discutir tots els aspectes de la recerca que aquí es presenta. A la Dra. Elisabet Playà, agrair-li el seu constant recolzament i el seu guiatge des del moment en que vàrem començar a treballar plegades.

Thanks to Statoil for allowing me to publish part of this research. A special thanks to those involved in the Moroccan project since its beginning, Grégoire Messager and David Hunt, for the interesting discussions about local and regional processes and for their support. This acknowledgement requires to be extended to other Statoil people whom I was lucky to work with during the past last six years (Giulio Casini, Ian Sharp, Michael Zeller, Fabio Lapponi...). All our discussions allowed me to go a little further in this research.

Merci à l'équipe de Bordeaux; Philippe Razin, Carine Grélaud, Manon Malaval and Rémi Joussiaume, pour les discussions très intéressantes sur la sédimentologie et la géologie marocaine.

Mes sincères remerciements à Dr. Thierry Nalpas pour sa guidance au cours des travaux de modélisation analogique et discussion ultérieure des résultats. Donc, aussi, un grand merci à J.J. Kermarrec et Pascal Rolland pour son aider dans le laboratoire de Géosciences-Rennes, Université de Rennes 1.

Muchas gracias a Oscar Merino-Tomé de la Universidad de Oviedo por permitir la utilización de datos de Djebel Bou Dahar, así como agradecer las interesantes discusiones sobre la evolución Jurásico temprana de la zona.

Un gràcies infinit als membres del GDL (Group of Dynamics of the Lithosphere). A n'Eduard Saura i a en Juan Diego Martín-Martín (Juandi). Podria fer un llistat interminable d'agraïments només per a vosaltres, però com a mínim, no puc més que agrair-vos les hores de treball i de discussió sobre la geologia estructural i l'evolució de les estructures diapíriques. A Emilio Casciello, gracias por las conversaciones de cinco minutos que se transforman en discusiones de una hora sobre geología regional. Finalment un gran gràcies a la Vinyet Baqués que, tot i que no ha pogut presenciar el tram final del desenvolupament de aquesta tesis, hi ha estat molt present des de l'altre banda del Atlàntic. Aquests agraïments s'estenen, per suposat, a la resta de membres del GDL i del Institut de Ciències de la Terra Jaume Almera per compartir amb mi aquests anys de recerca: Ylenia Almar, Giulio Casini, Elisenda Costa, Yohann Poprawski, Daniel Vazquez i Israel Cruz. Un especial gràcies a Manel Fernandez i Ignacio Marzán per la seva ajuda a l'hora d'entendre les bases pel desenvolupament dels models tèrmics.

Un reconocimiento especial para los compañer@s que han compartido tantos momentos en el instituto: Alba, Juan, Alberto, Giovanni, Jan, Mireia, Juve, Cris, Max, Steph, Ángel, Pilar, Paula, Raquel, y l@s chic@s de la primera y segunda planta, Robert, Elena, Guio y Chusa. Espero no olvidar a nadie, pero es que seis años dan para mucho. Una menció especial per en Marc Español; gràcies per les lluites constants amb les actualitzacions de GENEX i FlowFlow, saps que sense tu aquesta tesis no s'hagués pogut acabar. I finalmente, Lavinia, gracias por tu incondicional apoyo en los últimos 6 años, las risas, los cafés, los grandes momentos dentro y fuera del instituto. Sé que he ganado una gran amistad.

Un agraïment a tota la gent de l'antic departament GPPG de la Facultat de Geologia (UB): Guillem, Ramon, Carmen, Sergi, David, Eduard, Ander, Emili, Anna Travé, Gemma Alias, Ramon Salas, ... I una menció especial per la Irene, amb qui he compartit més d'un viatge amb gran dosis de riures (Oviedo, Mainz, Scotland, ...). També un gran gràcies a l'Eloi Carola (xic no sé on posar-te ☺) per els seus xiulets de recolzament que m'han motivat a seguir avançant. Agrair al grup d'Evaporites haver tingut la sort de treballar amb ells i aprendre'n tant com he pogut; moltes gràcies Fede Ortí, Laura Rosell, Lluís Gibert i Montserrat Inglés.

Gràcies a tots aquells companys geòlegs que han estat recolzant-me: Mireia (dels Aiguamolls ☺), Andreu, Patrix, Nuria, Sheila, Monica, Cris, Ana, Kartu, Edu, Eli, Alba, Diana. I gràcies a aquells no geòlegs: Miri, Albert, Miguel, Marta, Enric, Lay, Laia, Anna, Isa ...

Finalment, aquest treball no hagués estat possible sense el recolzament incondicional de la meva família. Gràcies Mare i Oriol, i tiets Hermen i Tonyi, per estar en tot moment al peu del canó, al meu costat. Ho hem fet!

SUMMARY

The complexity of the interplay between tectonics and sedimentation increases when salt tectonics is involved because of the ductility of salt and its ability to flow. Discrimination between extensional tectonics and salt-related processes is problematic; especially where salt-related rift basins were inverted as occurred in the Central High Atlas in Morocco.

The aim of the present work was to analyse and understand the dynamics of the Central High Atlas diapiric basin during the Early Jurassic rift and subsequent post–rift periods using a multidisciplinary workflow integrating fieldwork, analogue models and subsidence and thermal numerical modelling. Two regions were examined to assess the effects of salt tectonics in the evolution of the basin; the Djebel Bou Dahar platform-basin system represented the fault domain of the rift basin where diapiric activity was not described and the Tazoult–Amezraï area and Imilchil diapiric province corresponding to the unstable domain of the basin characterised by the presence of diapiric salt ridges and minibasins.

Results from analogue models highlighted the intrinsic interrelation between extension, diapirism and sedimentation that characterised the diapiric domain of the Central High Atlas. Longitudinal and transverse sedimentary progradations and their timing had a strong impact in the migration of ductile layers, in the growth of diapirs and in their lateral structural variations; triggering well-developed passive diapirs in the proximal domains and incipient reactive diapirs or poorly developed roller-like and passive diapirs in the distal domains of the sediment source. Analogue models including post–diapiric compression fairly reproduced the observed structure in the studied areas. Modelling with 6% and 10% of shortening, slightly lower than the Atlas one, produced the progressive close-up of the two flanks of salt walls and their final welding as well as the steepening of their outward flanks, with dips increasing from 8^{o}-17^{o} prior to compression to 30^{o}-50^{o} after compression.

Subsidence curves varied depending on the analysed localities of the rift basin. Djebel Bou Dahar showed long-term and low-rate tectonic and total subsidence (0.06 and 0.08 mm yr^{-1}, respectively). The roughly parallel evolution of both total and tectonic subsidence curves indicates the main extensional tectonic influence on subsidence pattern, as corroborated by the syndepositional activity of the outcropping Sinemurian-Pliensbachian normal faults. In the unstable domain, Amezraï minibasin centre showed tectonic and total subsidence rates between 0.06-0.32 and 0.19-0.98 mm yr^{-1}, rates one order of magnitude higher than in the Djebel Bou Dahar. These subsidence rates were up to two-fold their equivalent rates in the

Tazoult salt wall (0.01-0.27 and 0.09-0.74 mm yr^{-1}). In the Imilchil diapiric province lateral shifts of the main subsiding depocenters were recorded during Toarcian to Callovian times (tectonic and total subsidence rates up to 0.23 and 0.90 mm yr^{-1}). The subsidence of the unstable domain was caused by the combination of normal fault extension and salt withdrawal from beneath the minibasins during rifting, being the salt-related subsidence predominant during the post–rift and masking the expected subsidence pattern for a rift to post–rift transition.

For the first time, 27 new vitrinite reflectance data were used to build the thermal evolution and associated geohistory of the Central High Atlas. Thermal models, with heat flows of 105 mW/m^2 (from 189 to 140 Ma) followed by 60 mW/m^2 and 70 mW/m^2 (from 189 to 182.7 Ma) followed by 60 mW/m^2, pointed to a post–Middle Jurassic evolution characterised by long-term and low-rate subsidence and an overburden between 1200-2400 m on the Tazoult–Amezraï area.

The comparison of subsidence curves from this study with Saharan Atlas and Tunisian Atlas showed that peak of subsidence in these salt-related domains became younger to the east.

RESUM EN CATALÀ

La interacció entre tectònica i sedimentació augmenta en complexitat quan la tectònica salina hi està involucrada degut a la ductilitat de la salt i la seva capacitat per fluir. Així doncs, la discriminació entre processos associats a tectònica extensiva i a tectònica salina és problemàtica; especialment quan les conques diapíriques extensives han estat invertides com és el cas del Alt Atles Central (Marroc).

L'objectiu principal d'aquesta tesis és analitzar i entendre els processos que interaccionaren a la conca diapírica de l'Alt Atles Central durant el rift Juràssic i el subseqüent període post–rift, utilitzant una metodologia multidisciplinària que integra treball de camp, models analògics i models numèrics (corbes de subsidència i models tèrmics). S'han estudiat dos dominis de la conca extensiva per avaluar els efectes de la tectònica salina en la seva evolució; el sistema de plataforma a conca de Djebel Bou Dahar representa el domini on no s'hi ha descrit activitat diapírica ("Fault domain"), i les àrees de Tazoult–Amezraï i Imilchil corresponen al domini inestable de la conca caracteritzat per la presencia de estructures diapíriques i miniconques associades.

Els models analògics mostren la intrínseca relació entre extensió, diapirisme i sedimentació que caracteritza el domini diapiric de la conca. Les progradacions longitudinals i transversals i el moment en quan s'inicien tenen un gran impacte en la migració dels nivells dúctils, en el mode de creixement diapiric i en variacions laterals de les seves geometries; donant lloc a diapirs passius ben desenvolupats en les zones proximals de la conca envers diapirs reactius incipients, i tipus passiu i "roller-like" poc desenvolupats en les zones distals. Els models anàlegs que inclouen una fase post–diapírica compressiva reprodueixen geometries similars a les observades a la zona d'estudi. Els models amb 6 i 10% d'escurçament, lleugerament més baixos que els de l'Atles, donen lloc a una reducció progressiva de l'amplada de les estructures diapíriques fins al seu tancament complet, així com a un increment dels cabussaments dels flancs exteriors, de 8^{o}-17^{o} abans de la compressió fins a 30^{o}-50^{o} després de la compressió.

Les corbes de subsidència varien segons el domini de la conca analitzat. a Djebel Bou Dahar es donà un període llarg de baixes taxes de subsidència tectònica i total (0.06 i 0.08 mma^{-1}, respectivament) durant el Juràssic Inferior. L'evolució paral·lela de les dues corbes indica una influencia principalment tectònica on els patrons de subsidència, que es corrobora per l'activitat sin-deposicional de falles durant el Sinemurià i Pliensbachià. En el domini inestable, el centre de la Amezraï minibasin es registraren unes taxes de subsidència tectònica i total

entre 0.17-0.32 mma^{-1} i 0.38-0.98 mma^{-1}, taxes un ordre de magnitud majors que a Djebel Bou Dahar. Aquestes taxes són fins a dues vegades les taxes equivalents en el flanc del diapir de Tazoult (0.01-0.27 mma^{-1} i 0.09-0.74 mma^{-1}). A la zona d'Imilchil, s'hi registraren migracions dels depocentres subsidents des del Toarcià fins al Callovià (taxes de subsidència tectònica i total fins a 0.23 i 0.90 mma^{-1}). La subsidència del domini inestable estigué causada per una combinació de subsidència associada a activitat de falles normals i subsidència associada a migració de salt durant la fase extensiva del Juràssic inferior, sent la subsidència associada a migració salina la predominant durant la fase post–extensiva, emmascarant el patró de subsidència esperat en un estadi de transició rift a post–rift.

Per primera vegada, es presenta l'evolució tèrmica i la geohistòria associada de la part central del Alt Atles Central. Els models tèrmics emprats per a la construcció de la geohistòria completa de la conca, avaluats utilitzant 27 noves dades de reflectància de vitrinites de la zona d'estudi, apunten a una evolució post– Juràssic Mitjà caracteritzada per un període llarg amb baixes taxes de subsidència que hauria enterrat la zona de Tazoult–Amezraï entre 1200-2400 m, en comptes de una complexa historia que inclouria diversos esdeveniments de exhumació com s'han registrats en altres zones del Atles Marroquí.

INDEX

CHAPTER 1. INTRODUCTION 1

CHAPTER 2. THE GEOLOGY OF THE CENTRAL HIGH ATLAS (MOROCCO) 7

2.1. THE CENTRAL HIGH ATLAS 9

2.2.1. Structural framework 9

2.2.2. Post–Variscan geodynamic evolution of the Central High Atlas 11

2.2. STUDIED AREAS 18

2.2.1. Djebel Bou Dahar 18

2.2.2. Tazoult–Amezraï area 20

2.2.3. Imilchil diapiric province 25

CHAPTER 3. DATABASE 29

3.1. INTRODUCTION 29

3.2. DJEBEL BOU DAHAR 29

3.3. TAZOULT–AMEZRAÏ AREA 32

3.4. IMILCHIL DIAPIRIC PROVINCE 36

CHAPTER 4. METHODS 41

4.1. ANALOGUE MODELLING 41

4.2. GEOHISTORY MODELLING 44

4.2.1. Subsidence analysis 44

4.2.2. Thermal modelling 46

CHAPTER 5. ANALOGUE MODELLING FROM EXTENSION TO INVERSION OF A RIFT DIAPIRIC BASIN 49

5.1. MODEL A1; SYN-RIFT PHASE WITH NO SEDIMENTATION 49

5.2. MODELS B1, B2, B3 AND B4; SYN- AND POST–RIFT PHASES WITH VARIABLE SEDIMENTATION 51

5.3. MODELS C1 AND C2; SYN- AND POST–RIFT PHASES WITH HOMOGENEOUS SEDIMENTATION AND SUBSEQUENT COMPRESSION (6% AND 10% SHORTENING) 60

CHAPTER 6. SUBSIDENCE ANALYSIS AND THERMAL MODELLING: GEOHISTORY OF THE CENTRAL HIGH ATLAS (MOROCCO) 67

6.1. SUBSIDENCE ANALYSIS 67

6.1.1. Djebel Bou Dahar 67

6.1.2. Tazoult–Amezraï area 70

6.1.3. Imilchil diapiric province 73

6.1.4. Composite subsidence curve from the unstable domain 81

6.2. THERMAL MODELLING 84

6.2.1. Thermal models considering Late Jurassic and Early Cretaceous continuous sedimentation 85

6.2.2. Thermal models considering Late Jurassic–Early Cretaceous exhumation in the Central High Atlas basin 91

6.2.3. Evaluation of thermal models 95

6.2.4. Geohistory model of the Tazoult–Amezraï area 98

CHAPTER 7. DISCUSSION 103

7.1. ANALOGUE MODELLING RESULTS APPLIED TO THE CENTRAL HIGH ATLAS SALT-RELATED STRUCTURES 103

7.2. RIFT TO POST–RIFT SUBSIDENCE EVOLUTION IN THE CENTRAL HIGH ATLAS 107

7.2.1. Early and Middle Jurassic subsidence evolution 107

7.2.2. Post–Middle Jurassic evolution 110

7.3. ALONG STRIKE SUBSIDENCE VARIATIONS OF THE ATLAS FROM MOROCCO TO TUNISIA 112

CHAPTER 8. CONCLUCIONS 117

CHAPTER 9. REFERENCES 121

CHAPTER 10. ANNEXES 137

LIST OF FIGURES

CHAPTER 1: INTRODUCTION

Fig. 1.1. Sketch map showing the Atlas system extending from Morocco to Tunisia. Red, blue and black box show study areas of this study, and stars indicate the location of published subsidence studies 2

Fig. 1.2. Workflow showing the structure of this study, the methods used and main obtained results. 3

CHAPTER 2: THE GEOLOGY OF THE CENTRAL HIGH ATLAS (MOROCCO)

Fig. 2.1. General map of the Atlas range showing location and age of diapiric structures or diapiric and chart showing the timing of the Atlas rift phases according to different published works. 8

Fig. 2.2. Central High Atlas geological map and regional cross-section. 10

Fig. 2.3. Structural map of the Central High Atlas showing the distribution of diapiric ridges and minibasins 11

Fig. 2.4. Late Norian paleogographic map of the Atlas system from the Atlantic coast of Morocco to the Mediterranean coast of Tunisia 12

Fig. 2.5. Paleogeographic maps of the Central High Atlas basin during Early and Middle Jurassic, including the location of diapiric structures. Maps correspond to: a) Hettangian–Early Sinemurian; b) Late Sinemurian; c) Pliensbachian; d) Toarcian; e) Aalenian–Bajocian and f) Bathonian–Callovian. 15

Fig. 2.6. Geological map, restored cross-section, stratigraphic log and pictures from the non-diapiric Djebel Bou Dahar platform –basin system 19

Fig. 2.7. Geological map of the diapiric Tazoult–Amezraï area. 21

Fig. 2.8. Cross-section, field pictures and stratigraphic log from the diapiric Tazoult–Amezraï area. 22

Fig. 2.9. Geological map and cross-sections from the Imilchil diapiric province. 26

Fig. 2.10. Stratigraphic log and field picture from the Imilchil diapiric province. *28*

CHAPTER 3: DATABASE

Fig. 3.1. Dataset from Djebel Bou Dahar platform-basin system 31

Fig. 3.2. Simplified geological map of the Tazoult Amezraï area showing the distribution of the available cross-sections and stratigraphic logs based on collected field data. 32

Fig. 3.3. Dataset from the diapiric Tazoult–Amezraï area. 34

Fig. 3.4. Collected vitrinite samples dataset: location, pictures and reflectance values 35

Fig. 3.5. Dataset from Imilchil diapiric province 37

Fig. 3.6. Original and filtered thickness maps from Imilchil diapiric province. 88

CHAPTER 4: METHODS

Fig. 4.1. Photographs of the materials and sketch of experimental modelling device used in analogue modelling 42

Fig. 4.2. Diagram showing the tectonic stages, sedimentation pattern and degree of compression applied to analogue models 43

Fig. 4.3. Compilation of initial porosity and density values extracted from GENEX used in 1D subsidence analysis 45

Fig. 4.4. Workflow showing the routine used in the thermal modelling process 47

CHAPTER 5: ANALOGUE MODELLING FROM EXTENSION TO INVERSION OF A RIFT DIAPIRIC BASIN

Fig. 5.1. Overhead views and sections from Model A1 model characterised by an extension phase (total extension=2 cm) with no sedimentation. 50

Fig. 5.2. Overhead views and sections from Model B1 that is characterised by an extensional phase (total extension=2 cm) and a post–extensional phase (3 h) with homogeneous sedimentation 52

Fig. 5.3. Overhead views and sections from Model B2 that is characterised by an extensional phase (total extension=2 cm) with homogeneous sedimentation and a post–extensional stage (3 h) with longitudinal prograding sedimentation. 54

Fig. 5.4. Overhead views and sections from Model B3 that is characterised by an extensional phase (total extension=2 cm) with homogeneous sedimentation and a post–extensional stage (3 h) with transverse prograding sedimentations. 55

Fig. 5.5. a) Overhead views and sections from Model B4 that is characterised by an extensional phase (total extension=2 cm) and a post–extensional phase (3 h) with longitudinal prograding sedimentation. b) Plot showing the sediment and silicone thickness and along the model as revealed by sections obtained from the model 57

Fig. 5.6. Overhead views and sections showing models C1 and C2. These models are constituted by an extensional phase (total extension=2 cm), a post–extensional phase with homogeneous sedimentation, and a final compression phase with a total amount of shortening of 3 cm (6%) in Model C1 and 5 cm (10%) in Model C2. 62

Fig. 5.7. Comparison between traces of pre-extension layers in purely extensional models and in models including 6% and 10% of compression. 63

Fig. 5.8. Comparison between cross-sections from models including compression with the new proposed cross-section of the Tazoult–Amezraï area 65

CHAPTER 6: SUBSIDENCE ANALYSIS AND THERMAL MODELLING: GEOHISTORY OF THE CENTRAL HIGH ATLAS (MOROCCO)

Fig. 6.1. Plots of total and tectonic subsidence curves from Djebel Bou Dahar 68

Fig. 6.2. Comparison between subsidence curves from Djebel Bou Dahar and subsidence curves from Rich area published by Lachkar et al. (2009) 70

Fig. 6.3. Plots of total and tectonic subsidence curves from Tazoult diapir and Amezraï minibasin. 72

Fig. 6.4. Plots of total and tectonic subsidence curves from Imilchil diapiric province 74

Fig. 6.5. Plots showing subsidence trends from Imilchil diapiric province 77

Fig. 6.6. Total subsidence and total subsidence rate maps from Imilchil diapiric province 78

Fig. 6.7. Composite subsidence curves from the unstable domain of the Central High Atlas built using Djebel Bou Dahar, Amezraï minibasin and Ikkou minibasin east curves 82

Fig. 6.8. a) and b) Maps showing the location of synclines filled by post–Bathonian deposits and location of published thermochronological studies. c) Diagram showing detailed geological events defined for each proposed thermal model 85

Fig. 6.9. Thermal model plots based on the present-day Amezraï minibasin stratigraphic section with no additional burial. 87

Fig. 6.10. Thermal model plots based on the present-day Amezraï minibasin stratigraphic section with no additional burial showing the required values of heat flow to obtain the best fit between vitrinite reflectance from samples and the calculated vitrinite reflectance profiles 88

Fig. 6.11. Thermal model plots based on the present-day Amezraï minibasin stratigraphic section including required additional burial from Late Jurassic to Cenozoic to obtain the best fit between vitrinite reflectance from samples and the calculated vitrinite reflectance profiles 90

Fig. 6.12. Published curves from thermochronological models in the Moroccan Atlas 92

Fig. 6.13. Thermal model plots based on the present-day Amezraï stratigraphic section including two events of sedimentation and uplift/exhumation: Late Jurassic-Early Cretaceous and Cenozoic in age 94

Fig. 6.14. Root Mean Square Error (RMSE) calculation used to evaluate thermal models 97

Fig. 6.15. Geohistory plots of the Amezraï minibasin section showing the temperature evolution and the vitrinite reflectance isolines distribution corresponding to thermal models with a continuous sedimentation episode from Late Jurassic up to Cenozoic basin inversion. 100

Fig. 6.16. Geohistory plots of the Amezraï minibasin section showing the temperature evolution and the vitrinite reflectance isolines distribution corresponding to thermal models including two events of uplift/exhumation: Late Jurassic-Early Cretaceous and Cenozoic in age. 101

CHAPTER 7: DISCUSSION

Fig. 7.1. Step by step evolution of the Tazoult diapir from the onset of diapirism to the fossilization of the diapiric structures coupled with images of equivalent stages obtained from analogue modelling 105

Fig. 7.2. Comparison of total subsidence curves from the studied areas with subsidence curves from other localities in the Moroccan Atlas 108

Fig. 7.3. Comparison of subsidence curves and tectonic stages from Tazoult–Amezraï area with subsidence curves from West High Atlas, Algeria and Tunisia 114

CHAPTER 10: ANNEXES

Fig. 10.1. 3D surfaces corresponding to the 5 sedimentary units described in the Imilchil diapiric province and thickness measures 137

Fig. 10.2. Quantified parameters used for the frequency distribution analysis for each sedimentary unit in the Imilchil Diapiric Province 139

Fig. 10.3. Layering configuration, overhead view and cross-sections of the testing analogue model with no diapiric structures formed 140

Fig. 10.4. Thermal model plots based on the present-day Tazoult diapir stratigraphic section. where the thermal parameters and amount of burial from Amezraï minibasin models were applied 142

CHAPTER 1

INTRODUCTION

1. INTRODUCTION

The interaction between extensional tectonics and salt diapirism was commonly studied based on field and seismic examples, analogue and numerical models. Since the 1970s, numerous studies examined the subsidence in extensional rift and rift-drift settings (Steckler and Watts, 1978; Jarvis, 1984; Doglioni et al., 1998; Gupta et al., 1998). More recently, subsidence studies were focused on the interplay between active extension and salt diapirism and the impact of this interaction on the subsidence patterns and stratigraphic record of salt-related rift basins (Richardson et al., 2005; Kane et al., 2010; Mannie et al., 2014; Jackson and Lewis, 2015; Warsitzka et al., 2017).

In terms of understanding salt tectonics, the advent of high quality marine seismic data revolutionised our understanding of rift and post–rift subsidence patterns and processes on continental margins. We have also come to better understand how extensive salt deposition can significantly modify the subsidence and tectonics on Mesozoic continental margins, such as the North and South Atlantic (Stapel et al., 1996; Alves et al., 2003; Zühlke et al., 2004; Dupré et al., 2007; Contreras et al., 2010; Pereira and Alves, 2011; Mohriak and Leroy, 2012). Working onshore, without good quality seismic data, distinction between tectonic rifting processes and salt-related subsidence patterns can however be more problematic; especially in mountain belts where Mesozoic rift basins and passive margins were inverted; i.e. Alps, Pyrenees, Carpathians, Betic-Rif or Atlas, where this study is focused on (Ríos, 1948; Moseley et al., 1981; McClay et al., 2004; Graham et al., 2012; Saura et al., 2014).

The Atlas Mountains are located in the northwestern margin of the continental African plate and extends for 2000 km in a roughly west-east direction from the Atlantic coast of Morocco to the Mediterranean coast of Algeria and Tunisia (Fig. 1.1). The High Atlas (Morocco) forms a SW-NE trending intracontinental chain developed over the African continental crust, which was only slightly thinned during its pre-orogenic evolution (Mattauer et al., 1977; Rodgers, 1987; Ziegler et al., 1995; Frizon de Lamotte et al., 2008). The thinning of the African crust triggered the formation of Triassic-Jurassic rift basins, which were inverted during the Cenozoic convergence between Africa and Europe.

The area is characterized by extended outcropping of lower to middle Jurassic deposits locally disrupted by SW-NE narrow ridges cored by Triassic clays and magmatic rocks (Laville and Harmand, 1982; Laville, 1988; Frizon de Lamotte et al., 2008). Traditionally, this

configuration was linked to the formation of complex strike-slip and transtensive basins during the Jurassic rifting (Laville and Harmand, 1982; Amilibia et al., 2005), although diapirism in the Central High Atlas was long acknowledged based on local structures described as diapirs i.e. Toumliline diapir, Tazoult ridge or Tassent ridge (Bouchouata, 1994; Bouchouata et al., 1995; Teixell et al., 2003; Ayarza et al., 2005; Michard et al., 2011). However, based on integrated structural and stratigraphic work, Saura et al. (2014) interpreted the Central High Atlas (Morocco) as an extensive diapiric province punctuated by ENE-WSW structural highs representing diapiric walls with the intervening synclines being minibasins that were active during Early and Middle Jurassic, being coetaneous to the Early Jurassic rifting phase occurred in the area (Ellouz et al., 2003; Lachkar et al., 2009; Moragas et al., 2016).

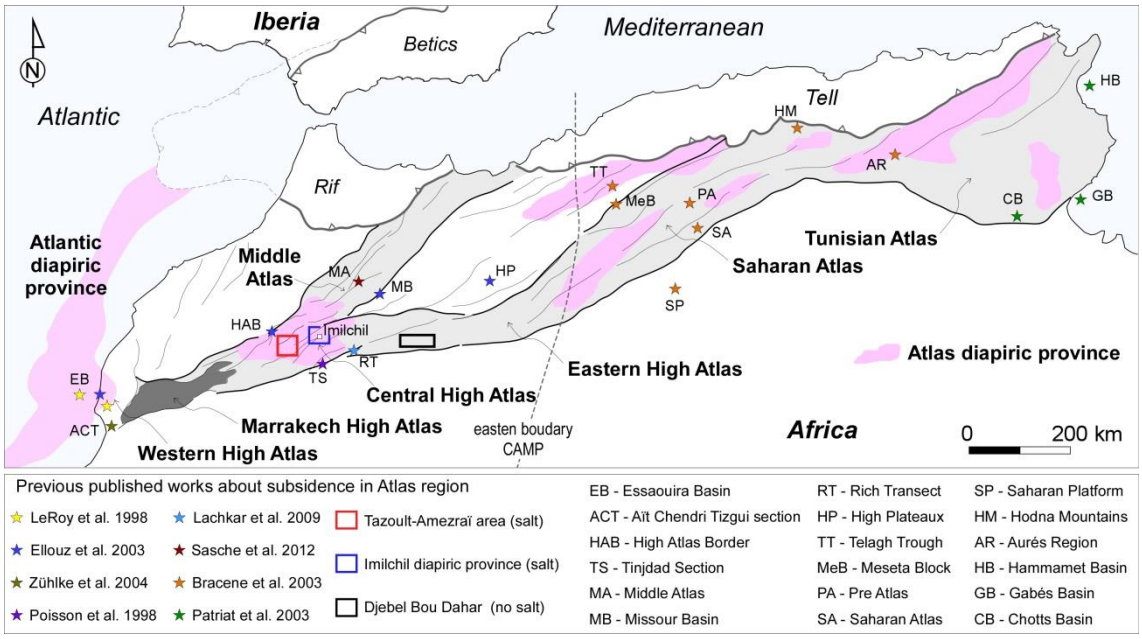

Fig. 1.1. Sketch map showing the Atlas system extending from Morocco to Tunisia (modified from Moragas et al., 2016). Red, blue and black box show study areas of this study, and stars indicate the location of published subsidence studies.

Subsidence analysis of the Atlas Jurassic rift basin was extensively reported in the literature (Fig. 1.1). However, only a few studies correspond to the Central High Atlas in Morocco (Poisson *et al.*, 1998; Ellouz *et al.*, 2003; Lachkar *et al.*, 2009) and these were mostly localised along the margins of the Atlas Fold Belt abutting stable areas. As such, these studies did not take into consideration the influence of the extensive salt diapirism that was focused towards the centre of the rift basin.

Concerning the post–Middle Jurassic subsidence evolution of the area, there is no a complete agreement about what occured in the central part of the Central High Atlas due to

the general scarcity of post–Middle Jurassic sedimentary record. Thus, according to subsidence analysis from the basin margins and thermochronological studies emplaced all around the Moroccan Atlas there are two contrasting proposed scenarios for this part of the geological history: i) long-term low-rate subsidence episode from Middle Jurassic up to the inversion of the basin during the Alpine orogeny (Ellouz et al., 2003; Barbero et al., 2007; Haddoumi et al., 2010) and ii) complex evolution including two exhumation events in the Late Jurassic-Early Cretaceous and in the Cenozoic respectively (Ghorbal et al., 2008; Saddiqi et al., 2009; Domènech et al., 2016).

The objective of the present thesis is the better understanding of the diapiric basin dynamics of the Central High Atlas during Jurassic rifting and subsequent post–rift stage. To reach this objective, a multidisciplinary workflow (Fig. 1.2) based on field data was followed in order to integrate and combine the results from different modelling methods. These methods were used to deal with three specific objectives derived from the main objective of this research.

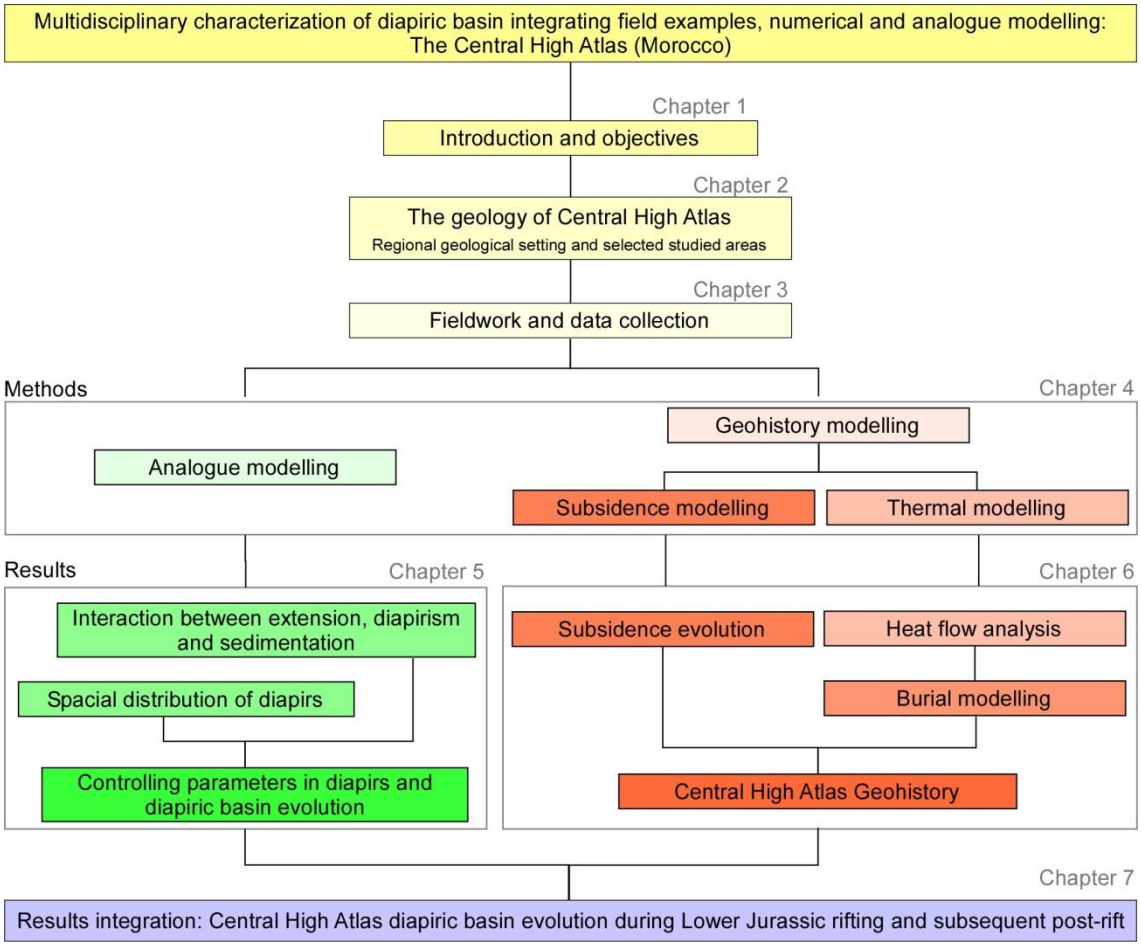

Fig. 1.2. Workflow showing the structure of this study, the methods used and main obtained results.

1) To analyse the evolution model of the diapiric structures developed during the Lower and Middle Jurassic in the Central High Atlas (Morocco) integrating field work and analogue modelling results.

This objective was faced considering the extensive previous published works about the relationship between extension and diapir formation using analogue models. Continuous regional and the forced folding of post–salt strata may trigger reactive diapirism by means of upwards migration of salt between overburden blocks. If the overburden is thin enough (active diapirism) or if there is a sedimentation input (passive diapirism), reactive diapirs can evolved to more mature structures (Vendeville and Jackson, 1992; Jackson et al., 1994). In cases where the salt layer lies over a faulted basement, the extension above and below salt can be partially coupled depending on the thickness of the salt layer (Vendeville and Jackson, 1992; Nalpas and Brun, 1993; Vendeville et al., 1995; Dooley et al., 2003; Dooley et al., 2005), and therefore the basement geometry influences the extensional structures developed in post–salt layers. However, in most previous models the sedimentation during extension and coeval diapiric evolution phases was homogeneous and they do not deal with differential sedimentation e.g progradation of a sedimentary wedge.

Together with the study of extensional regimes, modelling studies were used to examine the impact of the progradation of a sedimentary system above a ductile layer. The progradation of a sedimentary wedge promotes the mobilization of a ductile substrate and causes a variety of geometries in the system, with the formation of half-grabens and growth of diapirs in the proximal part and the production of active fold-and-thrust belts in the distal part of the prograding system, where well-developed diapirs were also observed (Koyi, 1996; McClay et al., 1998; McClay et al., 2003; Vendeville, 2005). Previous published models also showed that the geometry and distribution of diapirs increase in complexity with: i) the progradation of sedimentary lobe, where the radial shape of the prograding system generates a complex network of polygonal or circular depocenters separated by salt ridges (Gaullier and Vendeville, 2005), ii) the basement topography beneath the ductile layer and the consequent thickness variation of the mobile silicone (Ge et al., 1997; Dooley et al., 2017) and iii) the confluence of two sedimentary wedges (Guerra and Underhill, 2012). The outstanding results obtained in all these models, however, were not applied in modelling a tectonically active regime such as an extensional system.

In the present study, new analogue models were carried out, integrating extension and diapir growth with different sedimentation patterns (Fig. 1.2). The development of these

models improved the insights about how sedimentation, tectonics and salt diapirism interact during extension and post–extension events in a diapiric basin. In addition, compression was applied to some of the models in order to analyse the deformation pattern of inverted diapiric basins. The final geometries from these models were compared with natural examples from the Central High Atlas, and allowed reaching a better understanding of the interaction among extension, diapirism and sedimentation to be reached and applied to the subsidence analysis.

2) To evaluate the role of salt tectonics within the Central High Atlas of Morocco subsidence evolution, contrasting different areas in order to determine the contribution of both tectonic- and salt-tectonic driven subsidence patterns.

To address this objective, subsidence curves from different localities were analysed and compared. The selected areas are representative of diverse palaeogeographic and tectonic settings, i.e. from the periphery of the Early Jurassic rift basin and the rift axis (Fig. 1.1). In the rifted basin margin, a system of normal faults and tilted blocks developed and controlled the formation of carbonate platform and the transition to more basinal settings. In this context the Djebel Bou Dahar area was selected considering that it is a superbly exposed, well-known and well-constrained example of an Early Jurassic carbonate platform developed on top of a basement high controlled and bounded by normal faults (Kenter and Campbell, 1991; Verwer et al., 2009a; Merino-Tomé et al., 2012). In contrast to the periphery of the Central High Atlas basin, the central part of the Early Jurassic rifting basin was characterized by the growth of diapiric structures, considered to be contemporaneous with the activity of normal faults at depth (Grélaud et al., 2014; Saura et al., 2014; Joussiaume, 2016; Malaval, 2016; Martín-Martín et al., 2016; Vergés et al., 2017). The Tazoult–Amezraï area and Imilchil Diapiric Province present excellent case studies of diapir structures due to the combination of good exposure and very good lateral continuity of key units flanking the diapiric cores.

3) To assess the two contrasting post–Middle Jurassic geohistories in the central part of the basin using thermal models and vitrinite reflectance data.

New vitrinite reflectance data permitted thermal modelling of the Tazoult–Amezraï area located in the central part of the basin. Vitrinite reflectance data were used to evaluate thermal models for the two aforementioned contrasting geohistories proposed for the Central High Atlas: i) post–Middle Jurassic evolution with long-term low-rate subsidence episode

associated to a continuous sedimentation episode during Late Jurassic-Early Cretaceous up to the inversion during the Alpine orogeny and ii) post–Middle Jurassic evolution including two exhumation events in the Late Jurassic-Early Cretaceous and in the Cenozoic respectively. The complete geohistory of the central part of the diapiric basin was obtained combining the results from these thermal models and the results from the subsidence analysis. Together, the subsidence results from the centre and periphery of the Central High Atlas Rift basin were compared to previous studies both in the same region and with other diapiric regions extending from the Atlantic margin in Morocco to Algeria and Tunisia. This comparison helped to better understand of the role of salt tectonics in subsidence evolution along and across the Atlas rift basin (Fig. 1.1).

CHAPTER 2

THE GEOLOGY OF THE CENTRAL HIGH ATLAS (MOROCCO)

2. THE GEOLOGY OF THE CENTRAL HIGH ATLAS (MOROCCO)

The Atlas system is divided into two major domains, separated by the West Moroccan Arch, with different geodynamic stories: the Atlantic and the Tethyan provinces (Frizon de Lamotte et al., 2008; Frizon de Lamotte et al., 2009; Domènech et al., 2015).

The Atlantic domain includes the Western High Atlas and the Atlantic margin of Morocco (Fig. 2.1). This area was affected by a rifting phase from late Permian up to the lowermost part of the Early Jurassic and evolved as a part of the Atlantic passive margin affected by halokinesis during the post–rift stage since the Lower Cretaceous times (Hafid et al., 2008; Redfern et al., 2010; Tari and Jabour, 2013). From Upper Cretaceous on into the present, this Atlantic domain was subjected, like the rest of the Atlas belt, to a compression due to convergence between Africa and Europe. This compression resulted in reverse faulting, inversion of selected Triassic to Jurassic syn-rift structures (Hafid et al., 2006) or, as in the Essaouira basin, in a general reduction of sedimentation rate and a Late Cretaceous sedimentary hiatus linked to a regional event and the onset of orogenic processes (Neumaier et al., 2015). Diapirism is extensively present in the Atlantic domain of the Atlas system, mainly in the Atlantic margin of Morocco (Fig. 2.1). There, the salt diapirism inception was dated from the Middle Jurassic and diapiric activity still being active up to the present day (Tari et al., 2003; Hafid et al., 2006; Hafid et al., 2008; Tari and Jabour, 2013).

Contrarily, the Tethyan domain is constituted by the Middle and High Atlas (Central and Eastern) in Morocco, the Saharan Atlas in Algeria and the Tunisian Atlas in the easternmost part of the system (Fig. 2.1). The geodynamic evolution of the Central High Atlas will be detailed in the following section; however, it is required to highlight the connection of a part of the Moroccan Atlas to the Tethyan domain. The rift phase onset occurred in Lower Permian south east of Tunisia (Guiraud, 1998) but the main phase took place during at least Middle and Upper Triassic times and spanned through time differently depending on the regarding sector of the Atlas Tethyan domain as it is described in Frizon de Lamotte et al. (2009) and reference therein (Fig. 2.1). Once the rifting phase ends, the post–rift phase extended up to the inversion of the systems from the Late Cretaceous onwards.

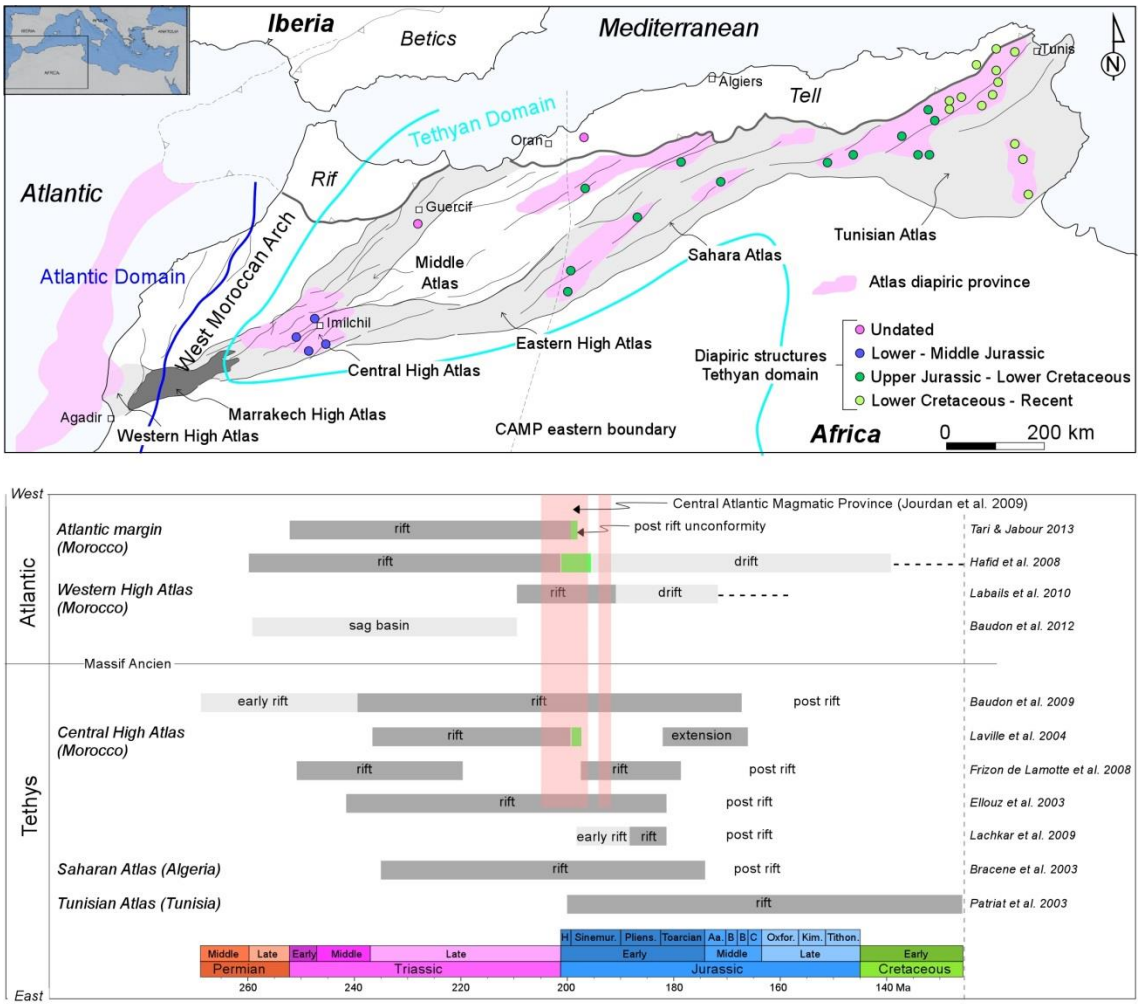

Fig. 2.1. General map of the Atlas range showing location and age of diapiric structures or diapiric domains (see details in the text). The lower chart shows the timing of the Atlas rift phase according to different published works. Time scale according to Gradstein et al. (2012). the boundary of the location of the West Moroccan Arch boundaries, modified from Frizon de Lamotte et al. (2009) and according to Domènech et al. (2015)

Diapir activity was also described in different locations throughout the Tethyan domain and at different ages. Overall, the diapir activity in the Moroccan Atlas was dated as Early to Middle Jurassic (Bouchouata et al., 1995; Ettaki et al., 2007; Michard et al., 2011; Saura et al., 2014; Martín-Martín et al., 2016; Moragas et al., 2016; Teixell et al., 2017; Vergés et al., 2017). Late Jurassic to Early Cretaceous diapirism was recognized in the Saharan Atlas (Algeria) (Perthuisot and Rouvier, 1992; Vially et al., 1994; Bracène, 2002). In this part of the Tethyan Atlas domain, salt diapirism was clearly recordered in some carbonate units with lateral facies changes linked to the diapir growh (Herkat, 1982; Nouiouat, 1994; Bracène et al., 2003). It was in Tunisian Atlas where diapirism was recorded at younger ages (Fig. 2.1), ranging from the end of the

Lower Cretaceous to recent times (Perthuisot, 1981; Snoke et al., 1988; Zouaghi et al., 2013; Masrouhi et al., 2014).

2.1. THE CENTRAL HIGH ATLAS

2.1.1. STRUCTURAL FRAMEWORK

The Central High Atlas is currently a doubly-verging chain, resulted from the inversion during the Alpine orogeny of the Triassic-Jurassic rift basin (Laville et al., 1977; Mattauer et al., 1977; Beauchamp et al., 1999; Frizon de Lamotte et al., 2000; Piqué et al., 2000; Teixell et al., 2003; Arboleya et al., 2004). In the central part of the range, the most extended outcropping materials are the Lower to Middle Jurassic sedimentary successions deposited during the rift and post–rift phases occurred in the Central High Atlas domain. These deposits form broad synclines or tabular plateaux separated by narrow anticlines or thrust faults. The cores of the anticlines, or ridges, are composed by Triassic evaporite-bearing shales and sandstones, often intruded by Middle to Upper Jurassic gabbros (Hailwood and Mitchell, 1971; Laville and Harmand, 1982; Jossen and Couvreur, 1990; Frizon de Lamotte et al., 2008). Contrarily, Upper Jurassic, Cretaceous and Cenozoic deposits are very limited exposed, only observable in some synclines located in the north and the south border of the chain (Fig. 2.2).

The trend of the ridges as well as main individual structures (faults and folds) is mainly NE-SW, slightly oblique to the general trend of the range. Michard et al. (2011) summarised the different processes that classically were ascribed to the formation of these ridges. Some authors invoked to Jurassic compressional folding associated with reverse faults (Studer and Du Dresnay, 1980) or to Jurassic transpression along NE-trending sinistral strike-slip faults associated with en-échelon opening (Laville and Piqué, 1992). However, there are not evidences of a regional Jurassic compressive event (Frizon de Lamotte et al., 2000; Gomez et al., 2000; Frizon de Lamotte et al., 2008). The presence of Jurassic intrusions in the core of the ridges caused that their emplacement was considered as the origin of their formation (Schaer and Persoz, 1976; Laville and Harmand, 1982). Finally, other authors linked their formation to the uplifting of the borders of tilted blocks created by synsedimentary extensional faulting (Jenny et al., 1981; Poisson et al., 1998). Only few studies in local structures pointed to a diapiric origin for these ridges; i.e Tazoult ridge (Bouchouata, 1994; Bouchouata et al., 1995), Ikerzi ridge (Ettaki et al., 2007) and Tassent ridge (Michard et al., 2011).

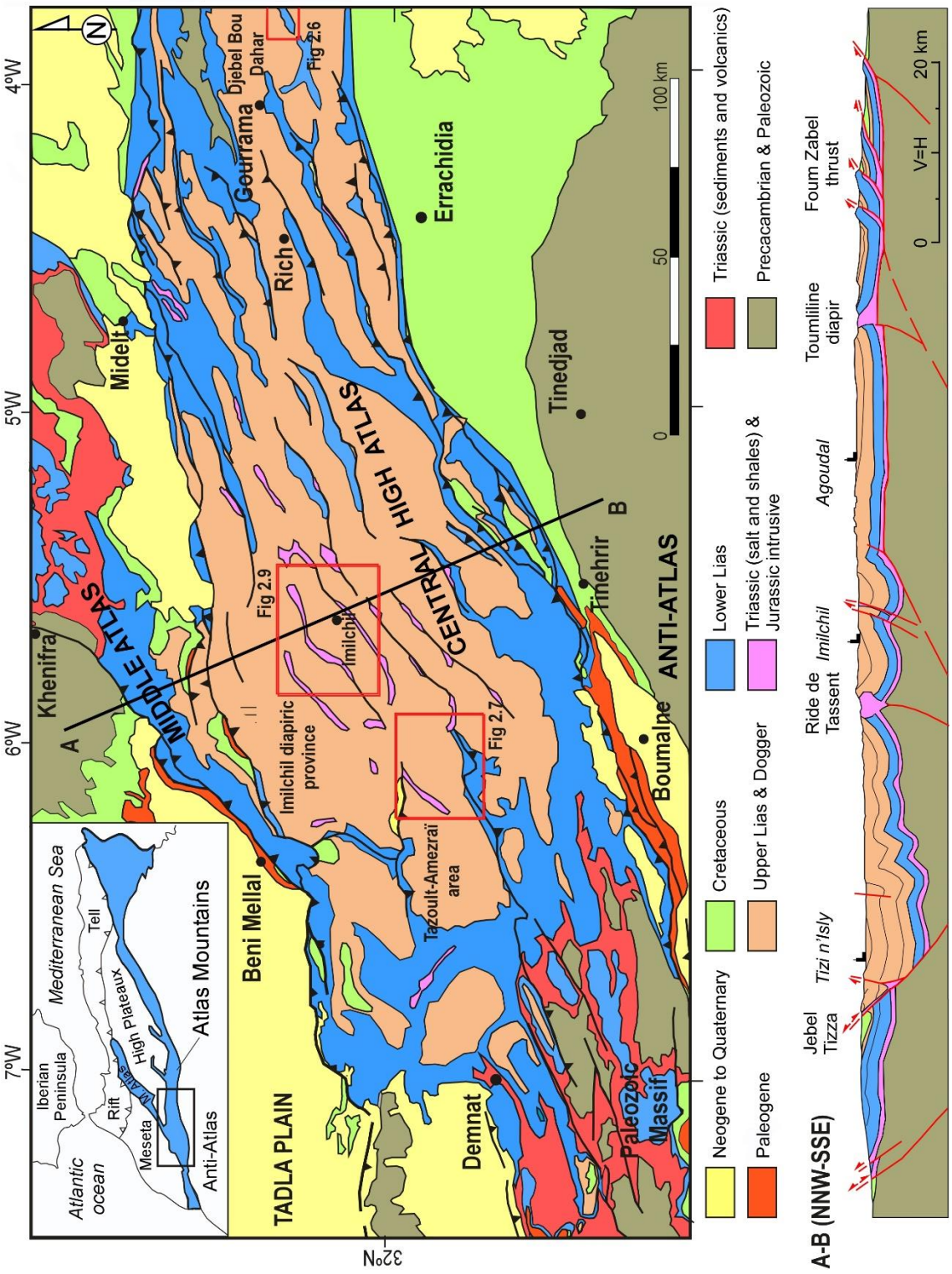

Fig. 2.2. Central High Atlas geological map and regional cross-section modified from Teixell et al. (2003) and GDL (2011). Boxes show the location of the studied areas.

Considered the interpretation of local diapiric structures in the Central High Atlas, a new interpretation of the entire Central High Atlas appeared where diapirism was extensively present during at least Mesozoic times. Rowan and Vendeville (2007), based on satellite images, geological maps and previous published works, suggested that the entire Central High Atlas could be a diapiric basin with squeezed diapirs separating elliptical depocenters. Saura et al. (2014), based on detailed structural and sedimentological studies, demonstrated that the area was a complex diapiric basin and they presented clear examples of diapiric structures. These authors enumerated at least 10 diapiric ridges and 11 associated minibasins filled by thick Lower and Middle Jurassic sedimentary successions (Fig. 2.3).

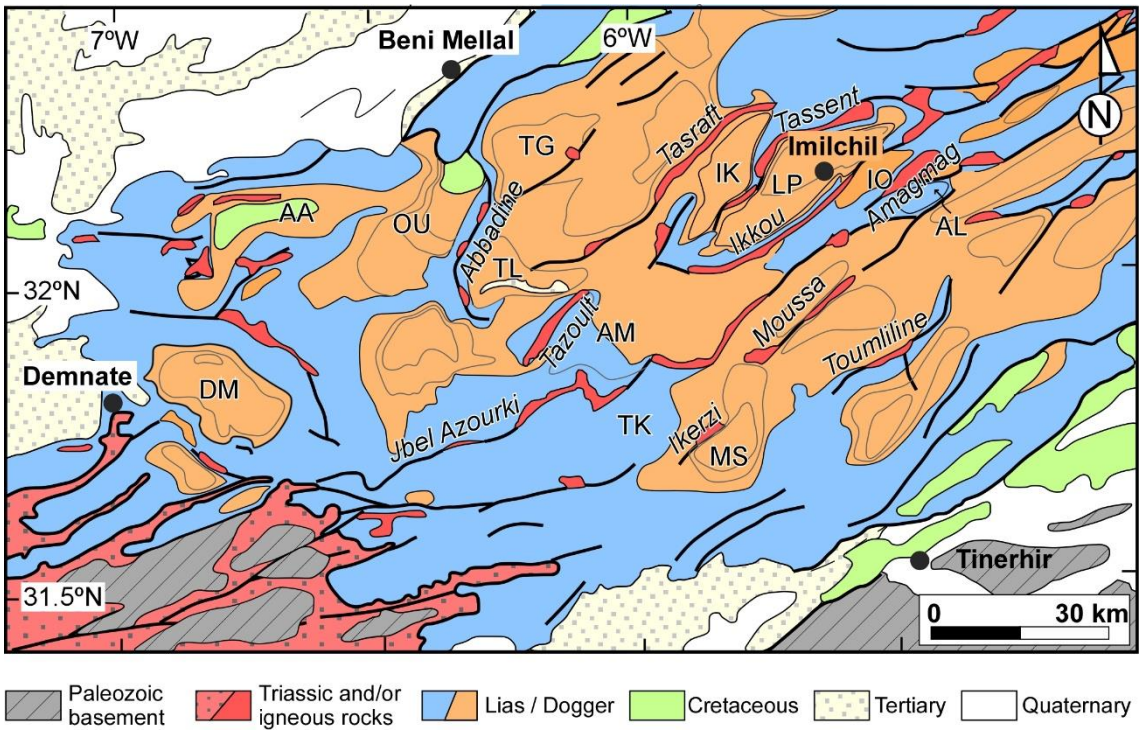

Fig. 2.3. Structural map of the Central High Atlas modified after Saura et al. (2014). Diapiric ridges and minibasins are labelled. Minibasins: AA – Aït Attab; AL – Almghou; AM – Amezraï; DM – Demnate; IK – Ikassene; IO – Ikkou; LP– Lake Plateau; MS – Msemrir; OU – Ouaouizaght; TG – Taguelft; TL – Tilouguite; TK-Takrakart.

2.1.2. POST–VARISCAN GEODYNAMIC EVOLUTION OF THE CENTRAL HIGH ATLAS

After the Variscan orogeny, successive extensional episodes occurred in Morocco in an overall rifting context. In the Central High Atlas, two rifting phases were defined. In order to differentiate both they are called rifting phase 1 (Permian to Triassic) and rifting phase 2 (Early Jurassic) respectively.

In the Central High Atlas, the rift phase 1 spanned from Late Permian to Late Triassic, but with a significantly more intense activity during the Middle-Late Triassic (Laville et al., 2004; Frizon de Lamotte et al., 2009). The structures resulting during this extensional event only crop out in Marrakech High Atlas, in the boundary between the westernmost part of the Central High Atlas and the West Moroccan Arch (Fig. 2.1). Based on a detailed structural analysis of around 200 km of the Tizi n'Test fault zone, Domènech et al. (2015) determined a highly fragmented fault zone, where the faults controlling the opening of Triassic basin were arranged as a wide deformation band. Both symmetric and asymmetric grabens would compose the extensional basin including a palaeohigh that separated the Atlantic and Tethyan domains. These grabens were bounded by high angle normal faults with a dominant dip slip movement and reveal clear thickness variations within the half graben fills that are up to 2 km thick (Baudon et al., 2009; Domènech, 2015; Domènech et al., 2015).

The deposition occurred in the arid climatic setting of the Late Triassic was characterized by continental red bed deposits, Fig. 2.4, and the local development of thick evaporitic successions accumulated in fault-controlled depocentres from the Atlantic Moroccan margin in the west to Algeria and Tunisia in the east (Oujidi et al., 2000; Le Roy and Piqué, 2001; Courel et al., 2003; Laville et al., 2004; Turner and Sherif, 2007; Frizon de Lamotte et al., 2008; Gouiza et al., 2010). Based on current distribution of diapiric structures, in the Late Triassic-Early Jurassic evaporite deposition is thought to have occurred in the basin centre, perhaps controlled by topography inherited from the rift.

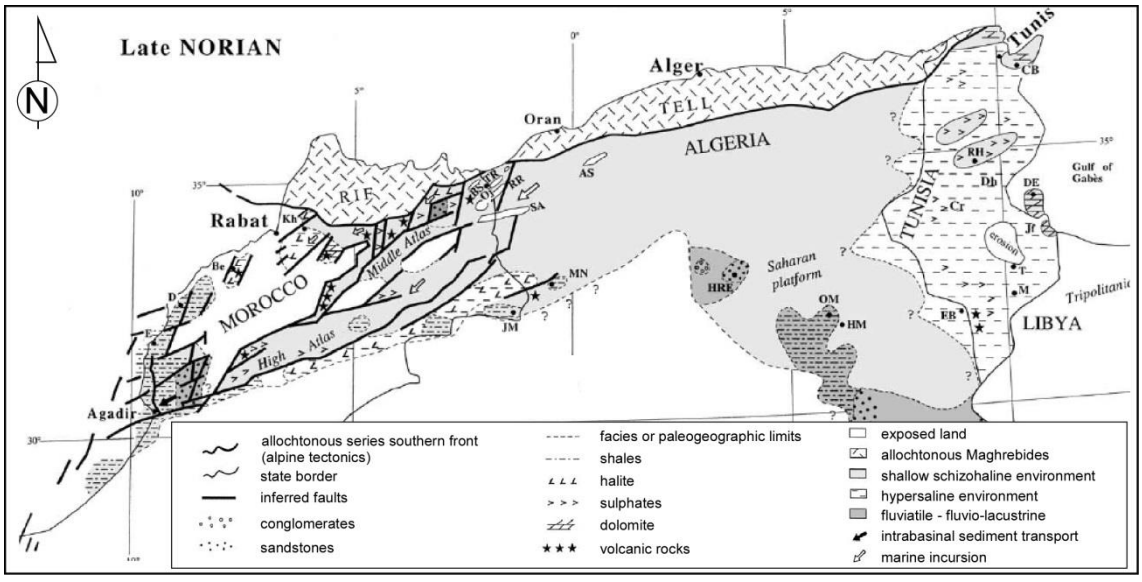

Fig. 2.4. Late Norian palaeogographic map of the Atlas system from the Atlantic coast of Morocco to the Mediterranean coast of Tunisia, modified from Courel et al. (2003). This map show the distribution of the depositional environments occurred in the latest stage of the first rifting event (rift phase 1).

After the deposition of the Triassic terrigenous-evaporitic succession, during the earliest Jurassic, a marine transgression coming from the east (Piqué et al., 2002) caused changes in the depositional setting, transforming the entire Central High Atlas basin into a very shallow marine basin with the spread deposition of Hettangian to lower Sinemurian peritidal carbonates (Fig. 2.5).

The second rift phase (phase 2) is thought to be the post–Hettangian reactivation of the Late Permian – Late Triassic western Tethyan rift; itself considered to represent the eastern propagation of the central Pangea breakup (Frizon de Lamotte et al., 2008; Frizon de Lamotte et al., 2009). Review of the literature indicates that the precise timing of the Early Jurassic rift and post–rift phases is contestable (Fig. 2.1). Some authors indicated Sinemurian and Pliensbachian ages for this phase 2, followed by a post–rift stage characterised by low subsidence rates linked to thermal subsidence (but may include some subsidence peaks), (i.e. Ellouz et al., 2003; Frizon de Lamotte et al., 2009; Lachkar et al., 2009). In contrast, Brede et al. (1992), Laville (2002) and Laville et al. (2004) proposed that the phase 2 terminated in the earliest Jurassic and was followed by a post–rift stage during the middle and late Early Jurassic, with only local and low activity of extensional pre-existing faults. According to these authors, from Toarcian to Bajocian-Bathonian (?), the region was under a transtensional regime with development of deep troughs and coeval volcanic intrusions. The differences in proposed time for the rifting stage (from Early to Middle Jurassic) are associated to the almost lack of normal faulting cutting post–Lower Jurassic strata. Along with the lack of observed normal faulting affecting post–Lower Jurassic units, the significant diapiric activity described in the Central High Atlas (Bouchouata et al., 1995; Ettaki et al., 2007; Michard et al., 2011; Saura et al., 2014; Martín-Martín et al., 2016) also difficult the establishment of the rifting phases occurred in the basin.

Thus, in tectonostratigraphic terms three distinct domains were recognised in the Central High Atlas basin within the Jurassic rift phase (Phase 2) (Fig. 2.5); A) a stable domain bounding the basin, B) a fault block domain, that appears to lack salt tectonics and C) an unstable domain with elongated ridges cored shales and evaporites that are interpreted as Jurassic aged diapiric structures (i.e. Saura *et al*. 2014). According to Saura et al. (2014), the diapiric activity in the Central High Atlas covers a time range from Pliensbachian up to Callovian times and is thus partially coeval to major rifting phases during the Jurassic. This unstable domain had a complex palaeogeography and subsidence history reflecting the localised influence of diapirism. In this overall setting, shallow water lower Jurassic carbonate platforms nucleated

both along the basin margin, and along localised tectonic/salt-related highs. Deeper basinal areas and troughs/minibasins were filled with deep-water limestones and marls (Fig. 2.5). Major tectonic reorganisation of the Central High Atlas occurred during the Late Bathonian, when carbonate platforms were progressively overlaid by deltaic and continental sediments during the late Bathonian as it is show in the correlation panel of Fig. 2.5.

During Late Jurassic and Early Cretaceous, an important magmatic activity occurred in the Central High Atlas. This was recorded by the emplacement of igneous bodies dated up to 140 Ma in the cores of diapiric ridges and the local deposition of lava flows dated up to 110 Ma (Frizon de Lamotte et al., 2008; Charrière et al., 2011; Michard et al., 2011). For this time range, two different geological histories were proposed in the Central High Atlas. Firstly, during this time a roughly continuous subsidence occurred in the basin allowing the deposition of thin/condensed continental deposits as it is recorded in the scattered synclines with Upper Jurassic-Lower Cretaceous red beds outcropping along the norther border of the basin, where dating of the deposits were carried out using palaeontological studies (Haddoumi et al., 2002; Ellouz et al., 2003; Barbero et al., 2007; Haddoumi et al., 2010). Contrarily, Frizon de Lamotte et al. (2009) proposed a widening and uplift of the West Moroccan arch (see location in Fig. 2.1) linked to a thermal doming that would affected partially the Central High Atlas basin. This uplift was recorded in Paleozoic samples from the Moroccan Meseta and the Anti-Atlas system as was has detailed in thermochronological studies (Ghorbal et al., 2008; Saddiqi et al., 2009; Ruiz et al., 2011).

In contrast, the upper Cretaceous strata show relatively uniform thickness distribution along the High Atlas recording a more uniform subsidence distribution during post–rift conditions (Gouiza et al., 2010). The post–rift stage lasted up to the onset of the inversion of the Atlas range that possibly started during the Late Cretaceous (Frizon de Lamotte et al., 2009; Frizon de Lamotte et al., 2011; Babault et al., 2013; Domènech, 2015; Neumaier et al., 2015), with further minor vertical movements occurring up to the Middle Eocene. Contrarily, a more complete Middle Eocene to Oligo-Miocene sedimentary record can be observed in the Central High Atlas (Tesón and Teixell, 2008). Here, a large Middle and Late Miocene clastic influx in the Ouarzazate basin was directly related to shortening (Tesón et al., 2010), that continued until very recent times. The aforementioned exhumation history, in particular occurred during the younger episode, was considered to reflect both crustal shortening and deep mantle processes (e.g., Teixell et al., 2005; Missenard et al., 2006; Fullea et al., 2010).

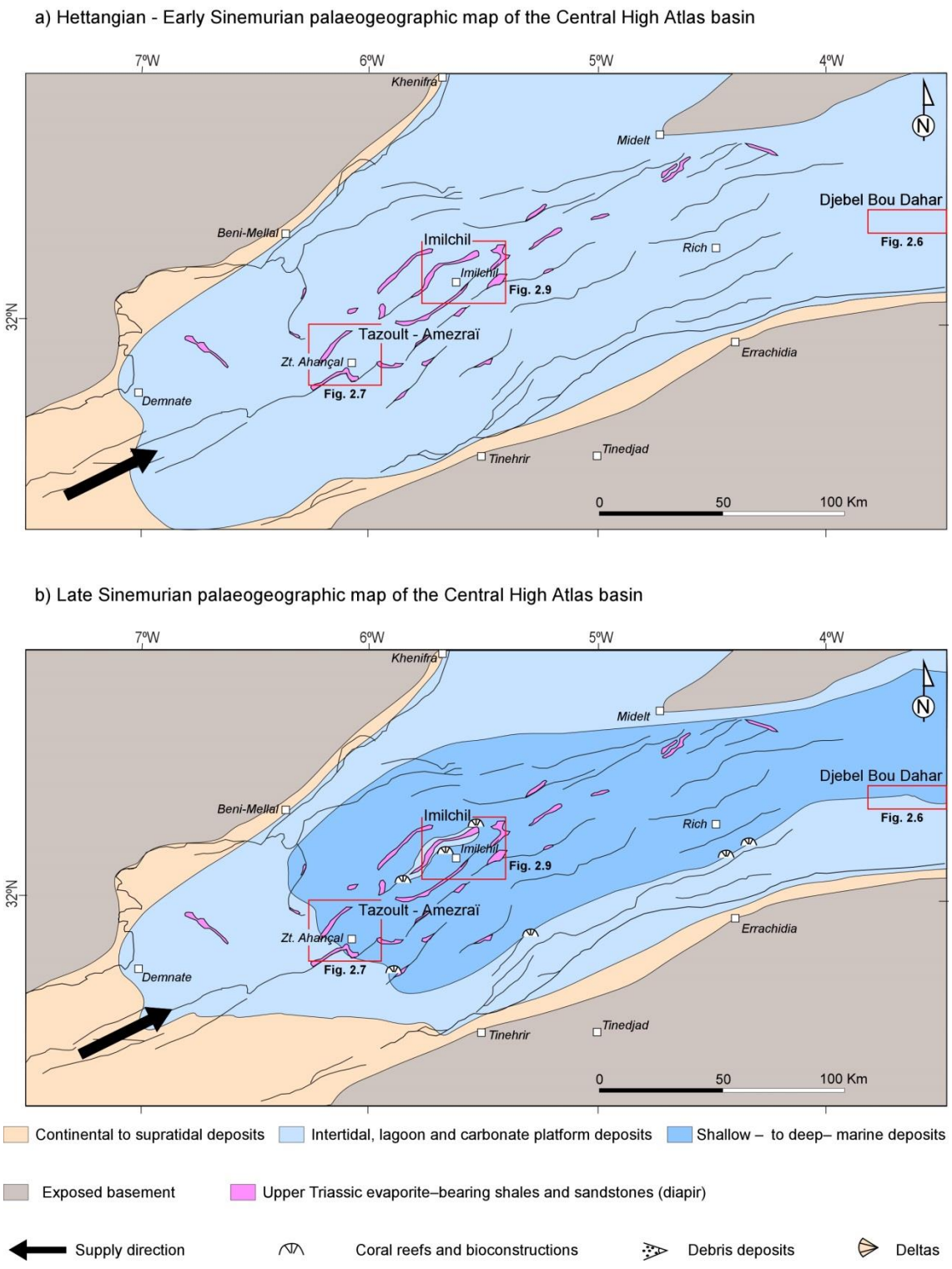

Fig. 2.5. (Continued in following pages). Palaeogeographic maps of the Central High Atlas basin during Early and Middle Jurassic, including the location of diapiric structures (coloured in pink) based on Saura et al. (2014) and reference therein. Red boxes show the location of the studied areas. Maps correspond to: a) Hettangian – Early Sinemurian; b) Late Sinemurian; c) Pliensbachian; d) Toarcian; e) Aalenian – Bajocian and f) Bathonian Callovian which include the location of the correlated stratigraphic logs (red dots). Maps are compiled from Septfontaine (1988), Poisson et al. (1998), Piqué et al. (2000), Souhel et al. (2000), Milhi et al. (2002) and Pierre et al. (2010).

c) Pliensbachian palaeogeographic map of the Central High Atlas basin

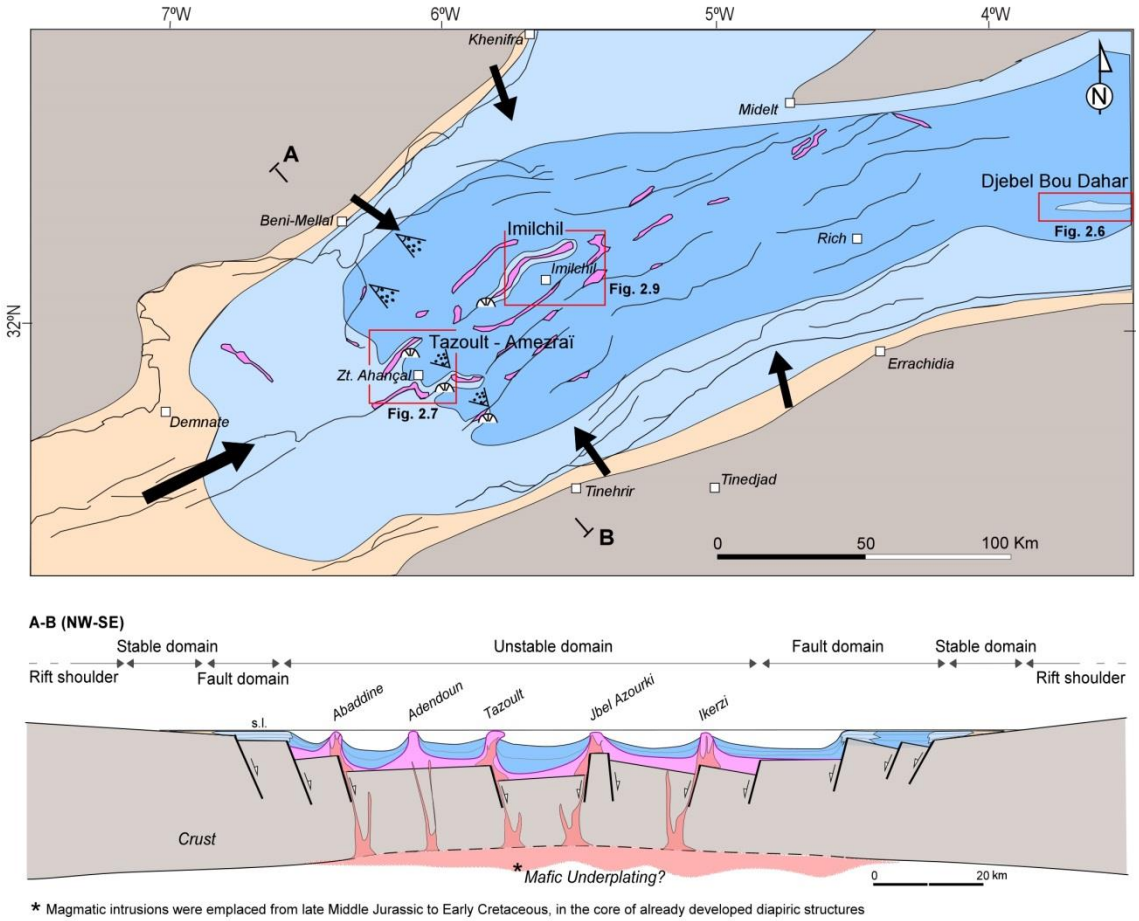

* Magmatic intrusions were emplaced from late Middle Jurassic to Early Cretaceous, in the core of already developed diapiric structures

d) Toarcian palaeogeographic map of the Central High Atlas basin

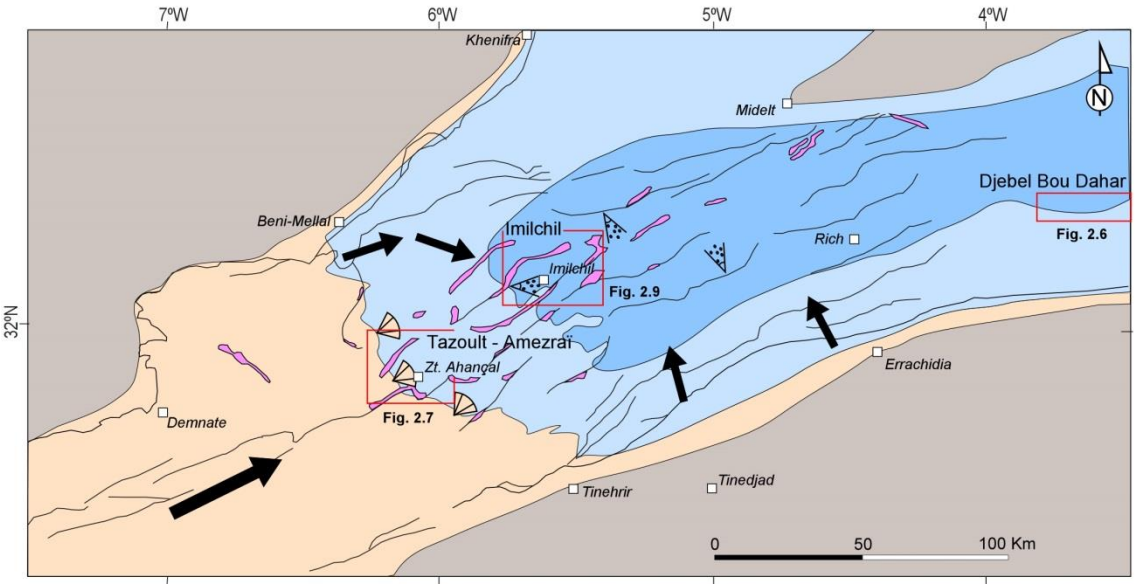

Fig. 2.5. Continued

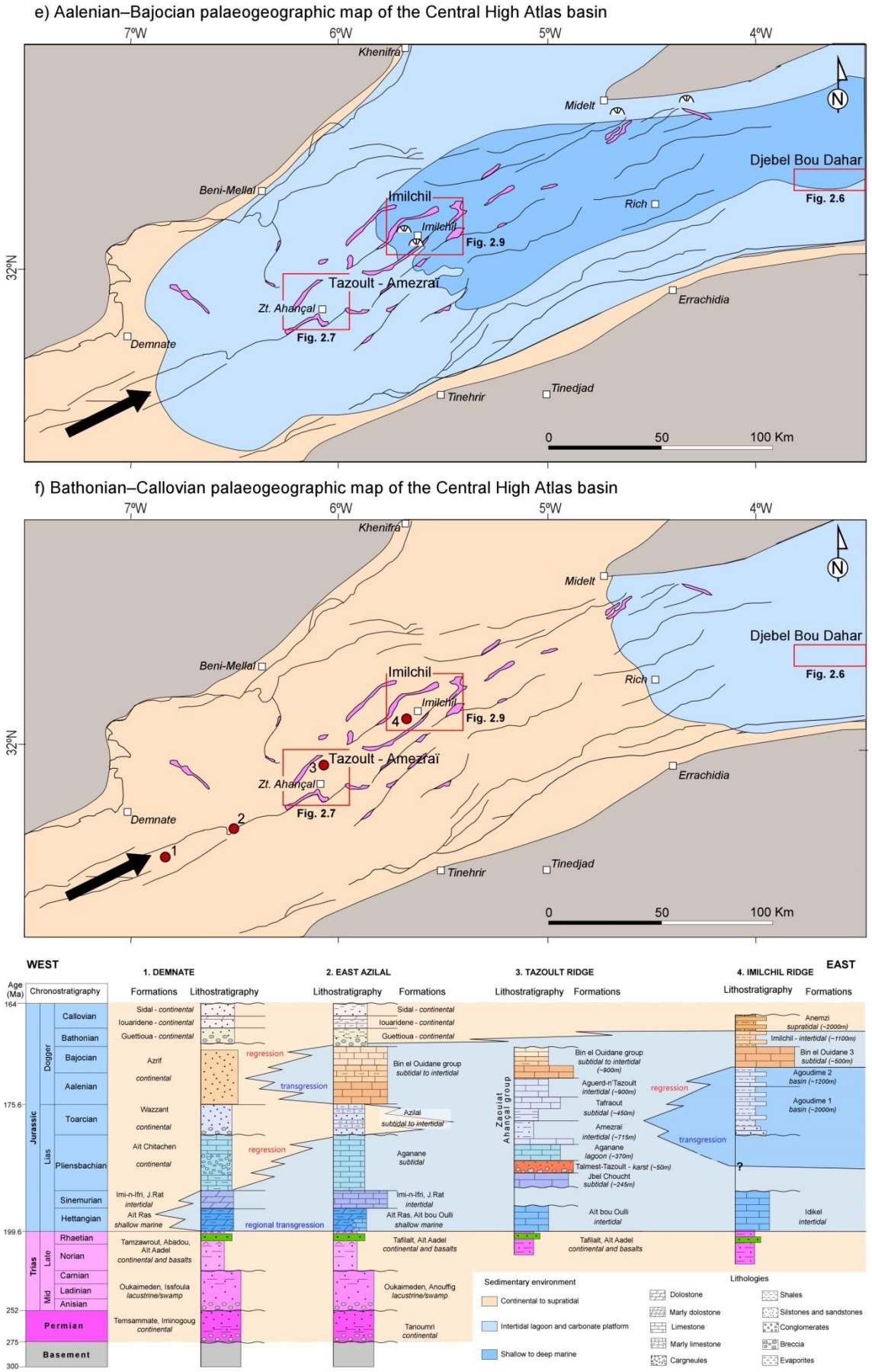

Fig. 2.5. Continued

2.2. STUDIED AREAS

The present research is based on data coming from three areas of the Central High Atlas. These areas represent i) the Fault domain of the Jurassic rift basin (Djebel Bou Dahar in Fig. 2.5c) and ii) the unstable domain characterised by the development of diapiric structures (Tazoult–Amezraï area and Imilchil in Fig. 2.5c).

2.2.1. DJEBEL BOU DAHAR

The Djebel Bou Dahar carbonate platform is located in the southern margin of the Early Jurassic rift basin, around 275 km eastward from the Tazoult area, in the so-called fault domain (Fig. 2.5c). The Djebel Bou Dahar- platform is flanked by two east-west trending synclines with thick successions, that represent Early and Middle Jurassic depocenters (i.e. the Djebel Oukhasas syncline in the north and the Beni Bassia syncline in the South) (Du Dresnay, 1976). In contrast to the widespread development of salt diapirs in the Central High Atlas basin, salt diapir activity was absent in the Djebel Bou Dahar tectonic block. Here extensional tectonics controlled platform-basin evolution during Sinemurian to early Bajocian (Merino-Tomé et al., 2012).

The Djebel Bou Dahar platform, is a relatively narrow elongated platform developed on a fault block, and locally lies directly on metamorphic basement (Fig. 2.6a). The carbonate nucleated during the Early Jurassic (Hettangian?—Early Sinemurian; Fig. 2.5a), the time that marine transgression was recorded in the Central High Atlas rift basin. The platform started as a broad, shallow-water carbonate system and evolved, from middle Sinemurian to the end of the Pliensbachian, into a high-relief isolated platform developed around the footwall uplift of a rotating fault-block (Merino-Tomé et al., 2012). Excellent exposure, limited tectonic deformation and preservation of many aspects of the platform-to-basin morphology and stratal patterns (Fig. 2.6b) allow the reconstruction of several continuous platform-to-basin profiles to be done at key different stages of the platform evolution (Kenter and Campbell, 1991; Verwer et al., 2009a; Merino-Tomé et al., 2012).

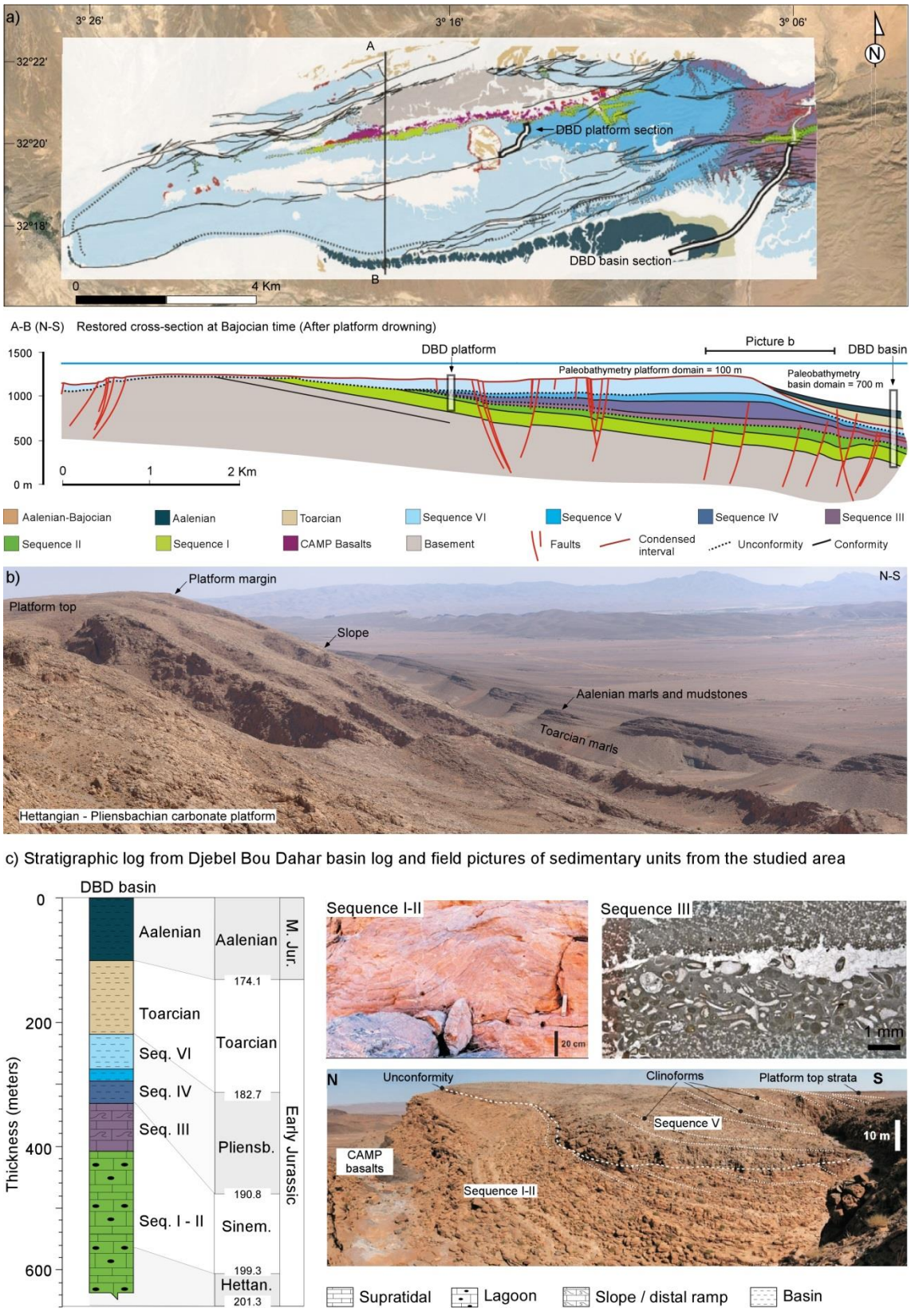

Fig. 2.6.a) Geological map and restored cross-section (A'-A) from Djebel Bou Dahar platform modified after Merino-Tomé et al. (2012). The location of the studied stratigraphic sections, which will be detailed in Chapter 3, is indicated in both images. b) Field picture of the Djebel Bou Dahar area showing the geometry of the carbonate platform in the slope domain. c) Stratigraphic log from the basin domain accompanied by field and microscope images from Merino-Tomé et al. (2012).

The Hettangian to Pliensbachian sedimentary record of the Djebel Bou Dahar carbonate platform and basin is divided in six sequences (Fig. 2.6) which were summarised according to detailed description by Merino-Tomé et al. (2012). Sequence I and II are characterized by a homogeneous facies distribution interpreted as a low angle carbonate ramp (Verwer et al., 2009a; Merino-Tomé et al., 2012). Both sequences consist of tabular and parallel bedded alternations of subtidal, intertidal and supratidal limestones and dolostones. Sequence III was developed as a low-relief platform with a maximum deposits thickness of 100 m that thins toward the central part of the platform domain (see restored cross–section in Fig. 2.6). This sequence is composed mainly by coated-grain skeletal packstone to grainstone. Sequence IV shows wedge-shape geometry with different platform top and slope facies belts. In the slope basinal domain maximum thickness is around 200 m whereas in the central area this sequence did not accumulate and it is record the exposure and karstification of the Sequences I and II. Sequence V and VI corresponds to the latest stage of the development of the high relief carbonate platform, with a clear facies changes from the platform top domain (including lagoon and upper slope facies) towards the basin (mainly composed by marls and locally siltstones) (Kenter and Campbell, 1991; Verwer et al., 2009b). The platform drowned in the Toarcian, and its slopes were onlapped by Toarcian, Aalenian and lower Bajocian shales, limestone–marl alternations and dark lime mudstones, representing deep-water pelagic and hemipelagic sediments. These were accumulated in palaeo-water depths exceeding the storm wave base and the base of the photic zone.

2.2.2. TAZOULT – AMEZRAÏ AREA

The Tazoult–Amezraï area is located in the central part of the Central High Atlas, which is defined as the unstable domain of the rift basin (Fig. 2.5). The Amezraï minibasin is an open syncline bounded to the north by the Tazoult diapiric ridge and to the south by the Jbel Azourki-Tafraout salt wall (Fig. 2.7). Detailed structural reconstruction indicates that both the Tazoult and the Jbel Azourki-Tafraout diapiric structures were controlled at depth by normal faults (Saura et al., 2014; Martín-Martín et al., 2016; Vergés et al., 2017). In this study area, it was possible to differentiate between Jurassic diapiric deformation and later Alpine deformation due to the presence of Middle Jurassic age units, which fossilize the diapiric structures.

The Tazoult and Azourki-Tafraout, as well as other salt structures from the Central High Atlas detailed in Saura et al. (2014), show multiple examples of halokinetic geometries recording the diapir growth including bed thinning, wedging, onlaps and truncations that comprise composite stacks of halokinetic wedges and hook sequences (*sensu* Giles and Lawton, 2002). Additionally, in the Central High Atlas the influence of diapir growth on the carbonate deposition was recorded by the rapid lateral facies associated with the local shallow bathymetries developed over the diapirs, as well as in the rotation, karstification and erosion of the carbonate platforms in proximity to the diapirs (Baqués et al., 2015; Joussiaume, 2016; Malaval, 2016; Martín-Martín et al., 2016).

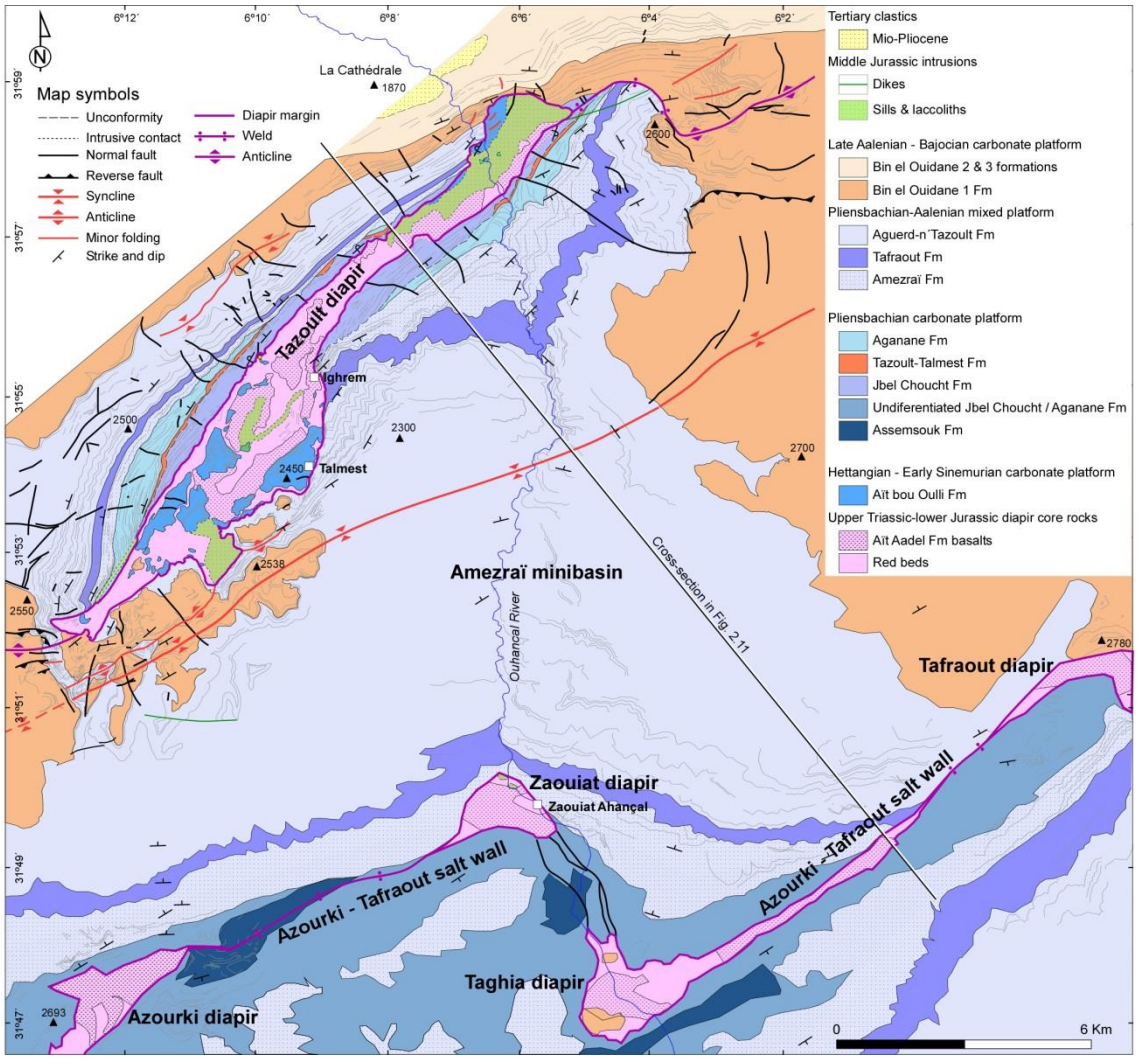

Fig. 2.7. Geological map of the Tazoult–Amezraï area modified from Martín-Martín et al. (2016) and Malaval (2016).

The Tazoult Ridge is a NE-SW-trending elongated four-way closure salt wall of a 20 km long and 0.6 to 3 km wide. The core is made of Late Triassic red beds and CAMP basalts and includes blocks (slivers) of Hettangian-Lower Sinemurian carbonates and Middle Jurassic gabbro intrusions (Fig. 2.7). The salt wall core is bounded in both flanks by sub-vertical Pliensbachian thick platform carbonates that grades to late Pliensbachian-Aalenian siliciclastic-carbonate mixed deposits upsection and away from the flanks (Fig. 2.8). The Early Jurassic halokinetic depositional sequences are partially fossilized along the flanks and closures of the ridge by shallow marine late Aalenian-Bajocian platform carbonates that form a relatively uniform unit across the area (Fig. 2.7 and 2.8). The extensive and well-preserved halokinetic strata on the flanks of the Tazoult Ridge document the timing of diapir activity, that ranges from Pliensbachian to Bajocian, lasting at least 15-20 My (Bouchouata, 1994; Bouchouata et al., 1995; Saura et al., 2014; Martín-Martín et al., 2016). The normal fault affecting the basement beneath the evaporite-bearing unit (Fig. 2.8) is interpreted by Saura et al. (2014) and Martín-Martín et al. (2016) according to non-direct field evidences.

The Azourki-Tafraout salt wall is an ENE-WSW complex long structure composed by several open and welded segments (Fig. 2.7). Although there is no direct evidence of basement faults, the Azourki-Tafraout is notably segmented along strike and closely mimic patterns associated the segmented normal faults at depth (Saura et al., 2014). The four open segments, from west to east Azourki, Zaouiat, Taghia and Tafraout diapirs, are composed by Triassic red shales and basalt and only locally Middle Jurassic intrusions (Fig. 2.7). Early Jurassic carbonate units and mixed siliciclastic-carbonate deposits are flanking the structure, dipping away from the ridge with opposite polarity on both sides of the structure. As in the Tazoult ridge, the uppermost part of the Aalenian-Bajocian carbonate platforms fossilized the structure.

Fig. 2.8. (Next page) Cross-section across the Amezraï area (see location in Fig. 2.7) with the location of two stratigraphic logs detailed in Chapter 3 Database. a) and b) are satellite image and field picture respectively of halokinetic geometries observed in the Tazoult diapir flanks; c) and d) interpreted field pictures of mixed siliciclastic-carbonate succession stacked as hook and wedge sequences linked to the growth of the Tafraout diapir. e) Stratigraphic log from centre of Amezraï minibasin accompanied by field pictures from the different sedimentary units. Jbel Choucht picture show the occurrence of abundant lithiotis (long skeletals) and gastropods (arrowed). The Aganane Fm. picture corresponds to oncolytic rudstone facies from lagoon deposition. Aguerd-n'Tazoult reddish sandstones deposited in supratidal environment. Bin el Ouidane 1 Fm. consists on oolitic grainstone deposited in shallow marine platforms. Data have been published in GDL (2011), GDL (2012), Saura et al. (2014) and Martín-Martín et al. (2016).

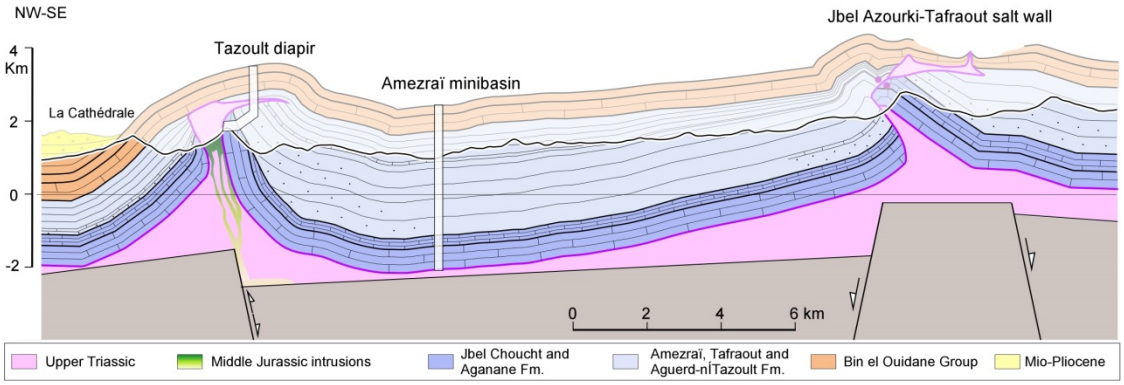

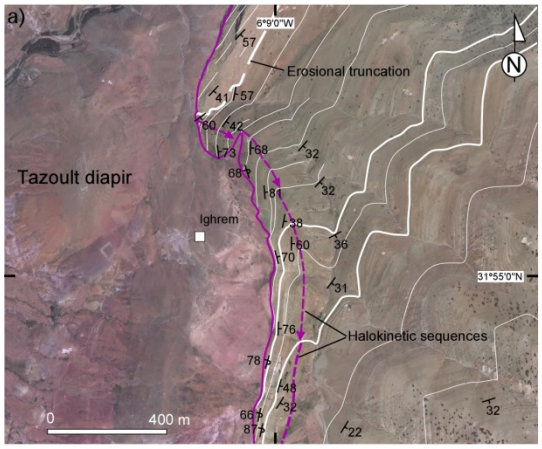

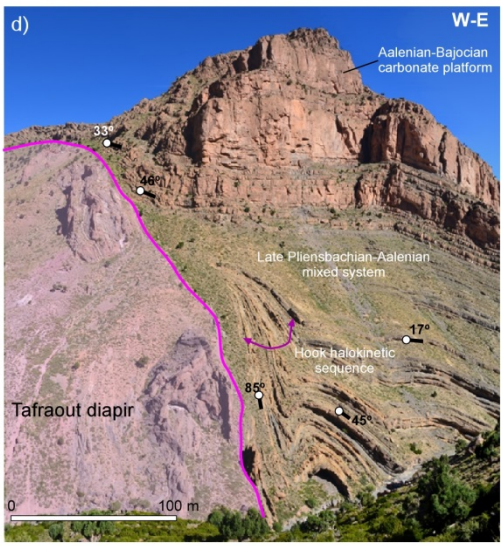

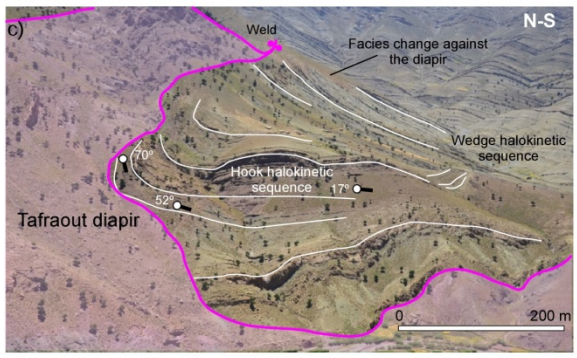

e) Stratigraphic log from Amezraï minibasin and field pictures of sedimentary units in Tazoult-Amezraï area

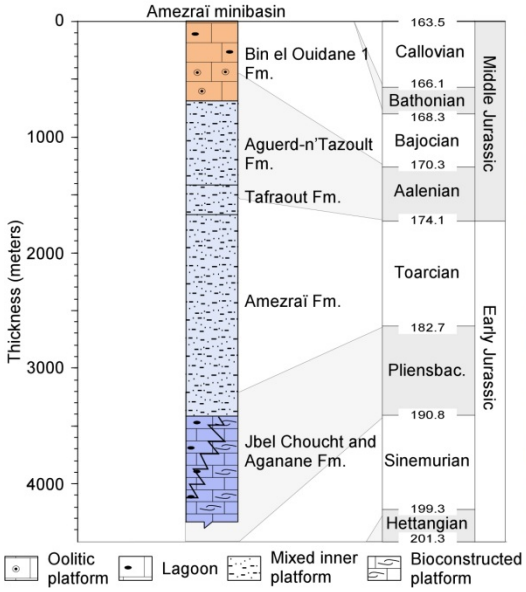

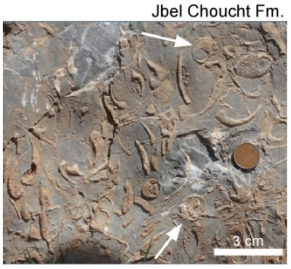

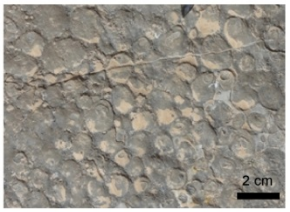

The Amezraï minibasin was filled with shallow marine deposits that range from Pliensbachian to Bajocian ages. The lowermost part of the sedimentary succession comprises Pliensbachian shallow marine platform carbonates (Jbel Choucht and Aganane formations). The Jbel Choucht Fm. (Fig. 2.8) consists of well-bedded limestones characterised by the occurrence of abundant bioconstructions dominated by large bivalves (lithiotis type) together with corals and gastropods (Jossen and Couvreur, 1990; Martín-Martín et al., 2016). The Jbel Choucht formation change laterally and vertically to the Aganane Fm. composed by oncolitic wackestones to rudstones (Fig. 2.8), mudstones, marls and limestones with algal lamination, deposited in a lagoon depositional environment (Bouchouata et al., 1995; Joussiaume, 2016; Malaval, 2016). Between both formations, a breccia unit (Tazoult-Talmest Fm.) crops out in both flanks of the Tazoult ridge (Fig. 2.7), recording a karstification and exposure stage in the area (Baqués et al., 2015; Martín-Martín et al., 2016).

The Pliensbachian carbonate platform system was overlaid by the mixed siliciclastic-carbonate deposits of the Zaouiat Ahançal Group (from base to top: Amezraï, Tafraout and Aguerd-n'Tazoult formations) (Jossen and Couvreur, 1990; Bouchouata, 1994; Bouchouata et al., 1995; Martín-Martín et al., 2016). The Zaouiat Ahançal Group is a more than 1500 m thick shallow marine mixed siliciclastic-carbonate platform dated as Late Pliensbachian to Aalenian. The Amezraï Fm. consists of metre-thick beds of red to green clays and marls, ripple-bedded sandstones and siltstones deposited in an intertidal to supratidal environment (Jossen and Couvreur, 1990; Souhel et al., 2000). The Tafraout Fm. consists of marly limestones, green marls and sandstones with corals deposited in an intertidal to subtidal environment (Jossen and Couvreur, 1990; Joussiaume, 2016; Malaval, 2016) and finally the Aguerd-n'Tazoult Fm. consists of yellow to red limestones, marls and red sandstones (Fig. 2.8), micritic limestones with algal lamination, oolitic grainstones and dolostones deposited in a intertidal to supratidal environment (Jossen and Couvreur, 1990).

Finally, The Zaouiat Ahançal Group was overlapped by Aalenian to Bajocian shallow marine limestones of the Bin el Ouidane 1 Fm. which consists of oolitic grainstones interpreted as a shallow platform deposits (Fig. 2.8). These deposits are relatively layer-cake, and appear to fossilize diapiric activity on the Tazoult ridge and Jbel Azourki-Tafraout salt wall (Fig. 2.7 and 2.8).

2.2.3. IMILCHIL DIAPIRIC PROVINCE

The Imilchil diapiric province is also located in the unstable domain of the Jurassic rift basin (Fig. 2.5). The area was previously described as a tabular area characterized by regular open folding linked to the inversion of the basin (Poisson et al., 1998; Teixell et al., 2003), although other authors point that the anticlines were caused by the emplacement of magmatic intrusions during Middle Jurassic times (Laville and Harmand, 1982; Laville, 1988; Laville and Piqué, 1992). However, recently this interpretation was revised and changed and four diapiric structures bounding three elongated minibasins (Fig. 2.9) were described in detail by Michard et al. (2011), GDL (2011), Saura et al. (2014) and Joussiaume (2016). The four diapiric structures, Tasraft, Tassent, Ikkou and Amagmag ridges (Fig. 2.9), are NE-SW trending elongated structures up to 30 km long and 3 km wide. These structures are cored by Triassic shales and evaporites with magmatic intrusive bodies and slivers of Hettangian carbonate rocks (Fig. 2.9). The salt wall cores are bounded by Toarcian to Callovian deposits arranged in halokinetic sequences all along the ridges (Fig. 2.10). The northern flank of the Tassent ridges is bounded by overturned and sedimentary-fanned strata of Toarcian to Aalenian deep marine deposits (Fig. 2.10a and b). The southern flank is characterized by the presence of fanning, onlaps and truncation affecting the entire Middle Jurassic succession. The younger Middle Jurassic units (Bathonian-Callovian in age) seal the Ikkou ridge recording the end of the structure growing.

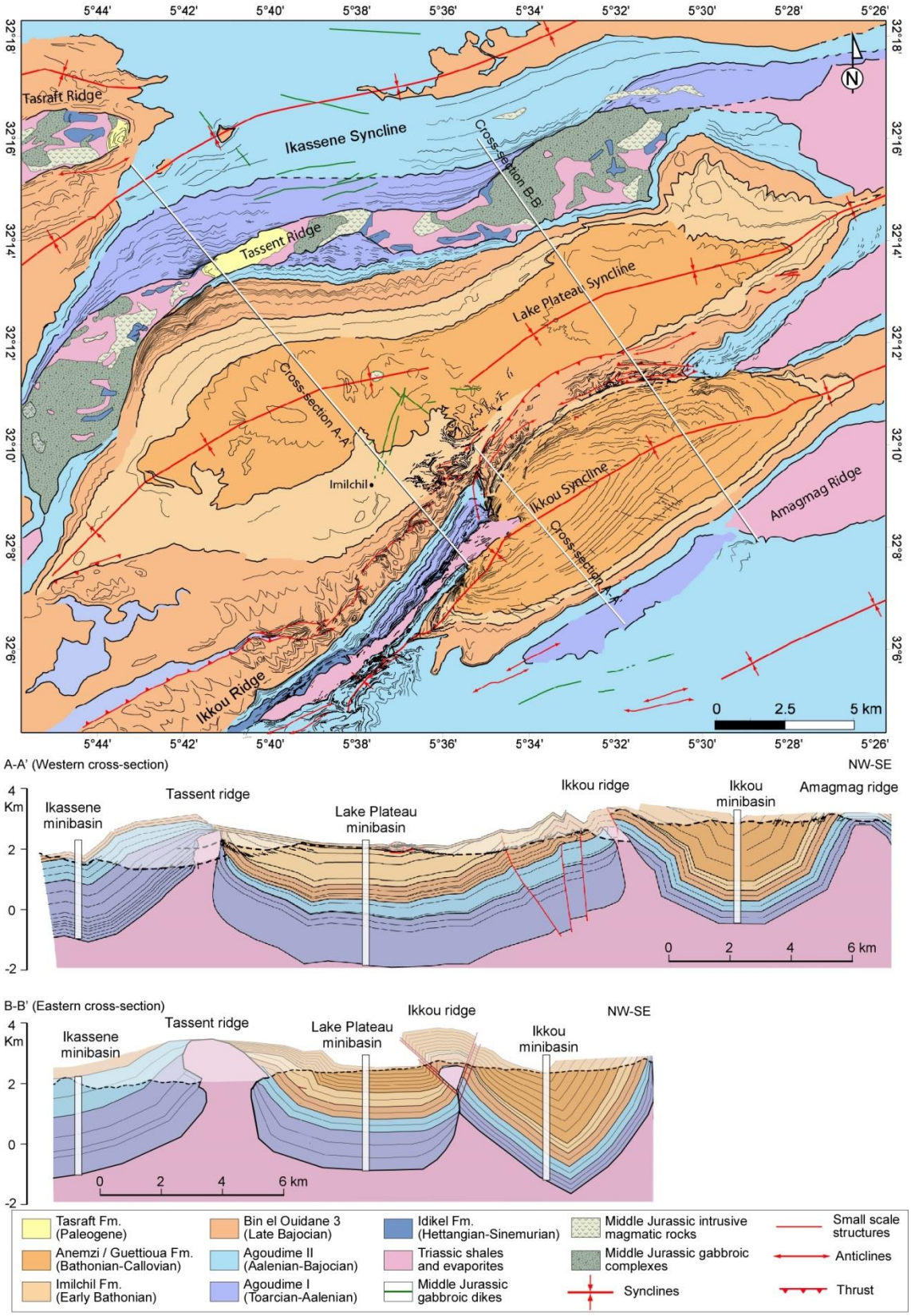

Fig. 2.9. Geological map of the Imilchil area modified from Fatah et al. (1990) and Fadile (2003) according to fieldwork and remote sensing mapping by GDL (2011). Western and eastern cross-sections across the Imilchil diapiric province including the location of stratigraphic logs used in the present study. Cross-sections have been modified from GDL (2012).

The three minibasins located in the Imilchil diapiric province, from north to south Ikassene, Lake Plateau and Ikkou minibasins (Fig. 2.9), were filled by Toarcian to Callovian deposits that recorded the upward transition from deep marine to continental depositional environments.

The oldest formations outcropping in the area are the Agoudime I and Agoudime II Fm. (Fig. 2.10) which are deep marine deposits constituted by thin laminated grey marls and mudstones with up to 25 cm thick beds of grainstone with reworked bioclasts (gastropods and bivalves). Using ammonite specimens, the age of the Agoudime I Fm. was established from Toarcian to Aalenian, whereas the Agoudime II Fm. ranges from Aalenian to the earliest Bajocian. According to Fadile (2003), the ammonite fauna from the Agoudime II Fm. range from Concavum-Discites to Sauzei-Humphriesianum biozones.

Bin el Ouidane 3 Fm. (Bajocian) is made of massif dark micritic limestones, massive oncolytic and bioclastic wackestones to packstone associated with oolitic grainstone banks, corresponding to the distal barrier facies of a shallow platform (Malaval et al., 2014; Joussiaume, 2016). Base and top of the Bin el Ouidane 3 Fm. is marked by the presence of metric bioconstructions, mainly built by corals, with several shapes and distributions that range from isolated patches to lined reefs (Fig. 2.10).

Imilchil Fm. (Bathonian) was interpreted as inner platform sediments deposited in an intertidal depositional environment with the influence of terrigenous input (Fadile, 2003; Joussiaume, 2016). This formation is an alternation of marls and limestones with an increasing upward trend of the siliciclastic content marked by the presence of siltstones and fine to medium coarse sandstones beds with cross lamination. This formation also contains laminated marls and limestones including calcarenites, dark mudstones and grainstones levels with braquiopods and gastropods as well as typical intertidal evidences such as mudcracks and teepee structures (Joussiaume, 2016).

The younger formation is the Anemzi/Guettioua Fm., Bathonian to Callovian in age (Fadile, 2003; Charrière et al., 2011; Ibouh et al., 2014; Joussiaume, 2016). This red coloured continental sedimentary unit is rich in red shales, siltstones and sandstone beds ranging from fine to coarse grain size with current ripples and other sedimentary structures (Fig. 2.10).

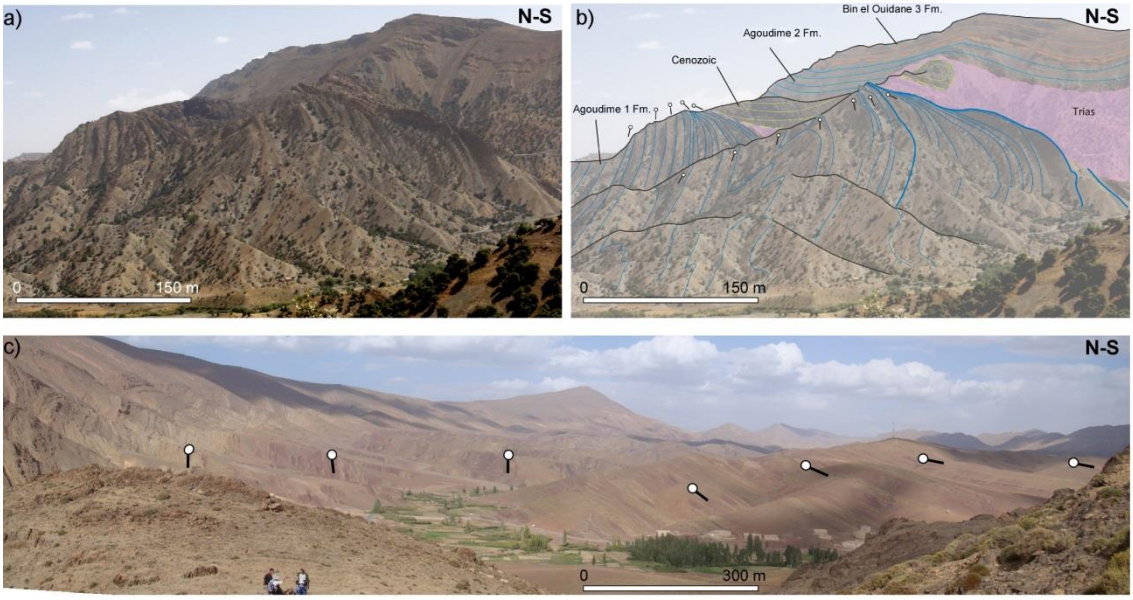

d) Stratigraphic log and field pictures of sedimentary units from Imilchil diapiric province

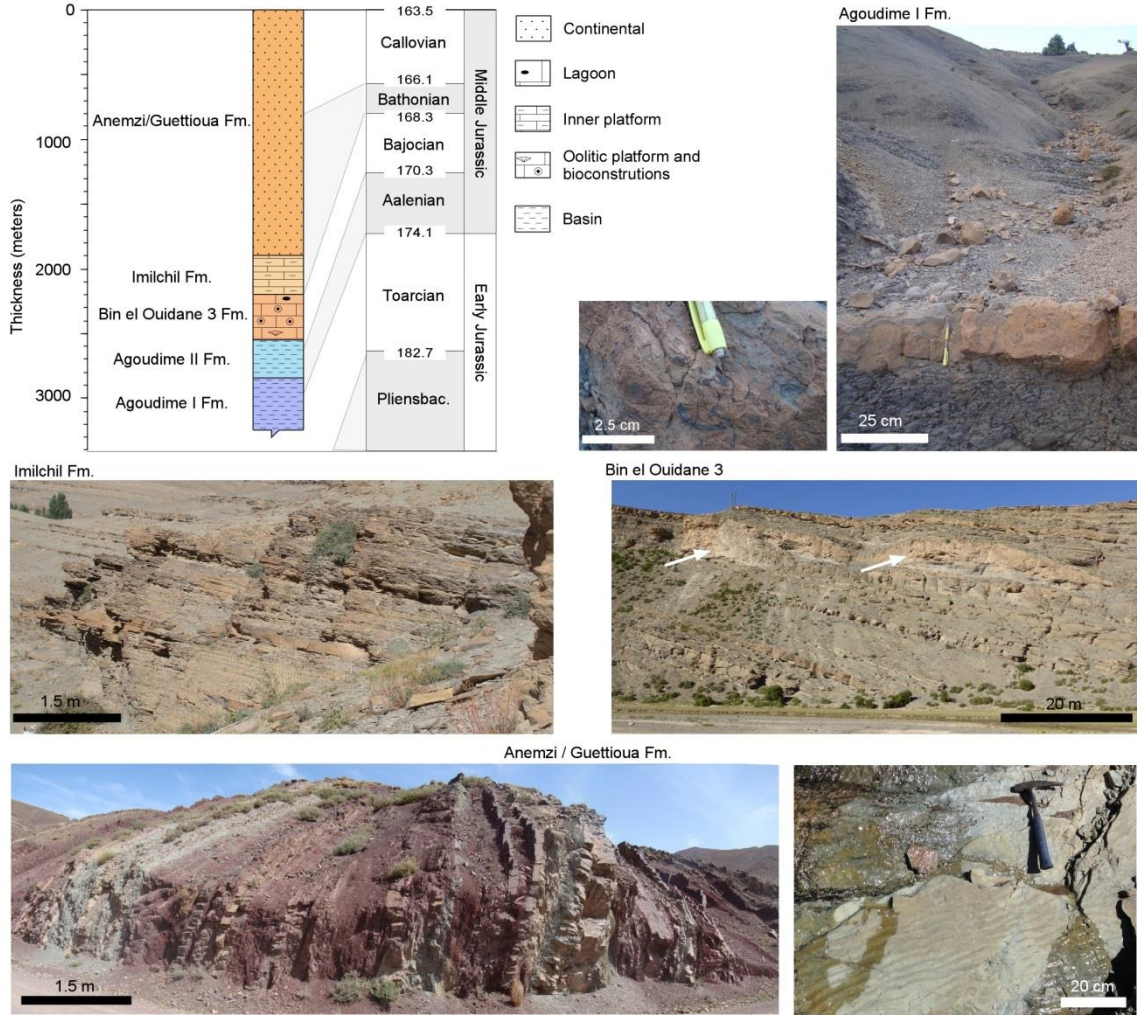

Fig. 2.10. a) and b) Original and interpreted photograph of the "Vélodrome" outcrop in the north flank of the Tassent ridge, where Agoudime I Fm. is overturned, thinned and arranged in halokinetic sequences. c) Ikkou minibasin photograph showing dip changes of the Bathonian-Callovian red beds. d) Stratigraphic log and field pictures from different sedimentary units outcropping in the Imilchil diapiric province.

CHAPTER 3

DATABASE

3. DATABASE

3.1. INTRODUCTION

Data used for the study of the subsidence evolution of the Djebel Bou Dahar area, corresponding to the Fault domain of the Central High Atlas Jurassic rift basin (Fig. 2.5), were provided by Dr. Oscar Merino Tomé from the University of Oviedo. Data came from several fieldworks campaigns carried out in the Djebel Bou Dahar platform within the framework of the project "*A GIS-based digital outcrop model integrating depositional anatomy and lithofacies of a continuously exposed Lower Jurassic carbonate platform: Djebel Bou Dahar (High Atlas, Morocco)*" (Funded by Shell and Chevron), a collaborative project developed from 2004 to 2007.

Data from diapiric areas that characterise the unstable domain of the Jurassic rift basin, Tazoult–Amezraï area and Imilchil diapiric province, were collected during five fieldwork campaigns from 2011 to 2015 by the Group of Dynamic of the Lithosphere (GDL) of the Institute of Earth Science Jaume Almera (CSIC). These fieldwork seasons were focused on the collection of dip data, cartography, cross-section building, identification of the main boundaries of sedimentary units and collection of vitrinite samples and diagenetic studies sampling. Some of the campaigns involved the carbonate sedimentologist from the EGID Institute, Bordeaux Montaigne University (France) and the carbonate research group from Statoil research centre in Bergen. The large amount of collected data was used for different purposes in the different research groups, and part of it was used for the completion of the present thesis. This is detailed in the present chapter.

3.2. DJEBEL BOU DAHAR

From the Djebel Bou Dahar area, stratigraphic information was compiled from two sedimentary logs, representing the top of the carbonate platform and the basinal domain respectively. The platform and coeval basinal deposits were divided into six sequences (Sequence I-VI; Merino-Tomé et al., 2012) and detailed sedimentological studies carried out in the area allow determining for each sequence the ages, thicknesses, lithology percentages, sedimentary environments and palaeobathymetry estimations (Fig. 3.1).

In the Djebel Bou Dahar platform section, an erosional event was defined between 195.3 and 187.3 Ma (Fig. 3.1). The amount of erosion is the difference between the present-day thicknesses of sequences I and II in the basin and platform sections, assuming that they were deposited as constant thickness units from basin to platform (see details of platform evolution in Merino-Tomé et al., 2012).

As introduced earlier, the well-preserved carbonate platform-top to basin profiles of the Djebel Bou Dahar platform (Fig. 3.1) reveal stratal geometries, that underwent relatively little deformation and permit the reconstruction of primary carbonate platform-basin relief (platform slope height from basin floor areas) throughout its evolution (Verwer et al., 2009a; Verwer et al., 2009b; Merino-Tomé et al., 2012; Della Porta et al., 2014). The paleobathymetry estimation for sequences III to VI was based on facies analysis integrated with restored platform and slope geometries, although decompaction was not considered (Fig. 3.1). Less constrained palaeobathymetric estimations correspond to the Toarcian and Aalenian, when the platform was drowned in response to the Toarcian oceanic anoxic event (OAE). Condensed pelagic deposits and hard grounds typify the platform top sedimentation during Toarcian and Early Aalenian times, while pelagic sedimentation occurred in the nearby basinal areas, indicating that water depths exceeded the depths of the lower boundary of the photic zone and the base of storm waves. In the absence of good palaeontological or sedimentological criteria, the values of 100 m water depth for the platform top, and 715 m for the nearby basin section have to be considered as minimum values during the Toarcian and Aalenian periods (Fig. 3.1).

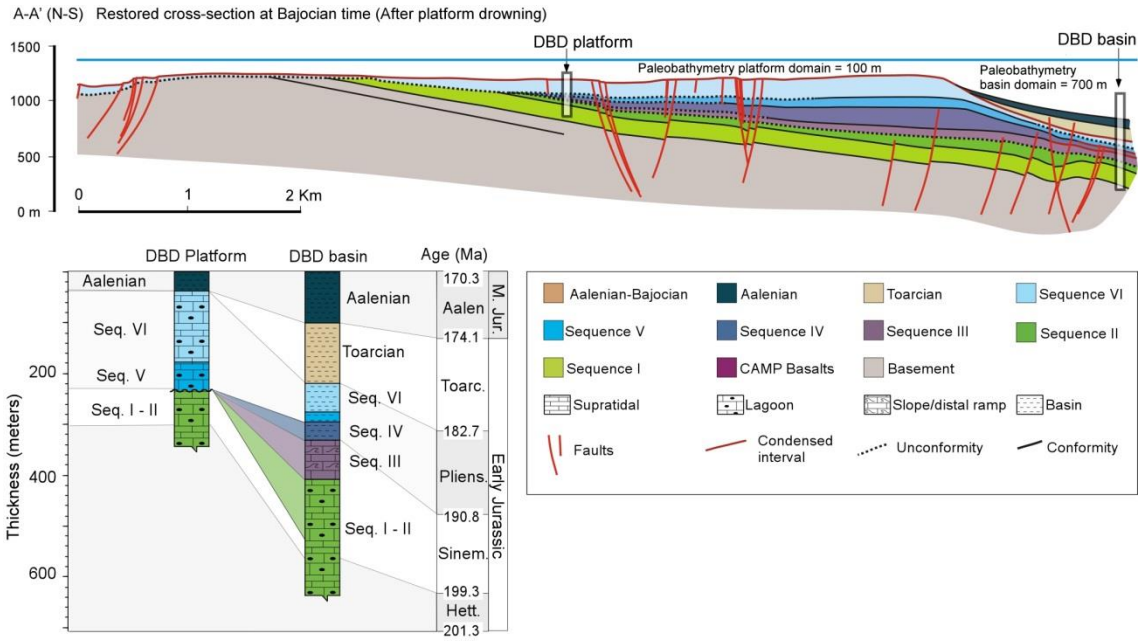

Djebel Bou Dahar	Age Base (Ma)	Age Top (Ma)	Thicknesses (m)	Lithology						Sedimentary Environment	Bathymetry (m)
				Sand	Silt	Shale	Limestone	Marls	Dolostone		
Basin section											
Aalenian	172.2	170	100	----	----	----	90	10	----	?	520
Toarcian	182.2	172.2	119	----	----	43	7	50	----	Basin	610
Drowning	183.2	182.2	0	----	----	----	----	----	----	Drowning	715
Sequence VI	186	183.2	57	----	----	----	58	42	----	Basin	500
Sequence V	187.3	186	18.5	----	----	----	65	35	----	Basin	430
Sequence IV	190.8	187.3	37.3	----	----	----	79	21	----	Basin	210
Sequence III	195.3	190.8	76.2	----	----	----	99	1	----	Distal ramp	0
Sequence I and II	200.5	195.3	226.7	----	----	1	65	2	32	Lagoon to intertidal	0
Platform section											
Aalenian	172.2	170	35	----	----	----	90	10	----	?	100
Toarcian	182.2	172.2	0.5	----	----	43	7	50	----	Condense level	100
Drowning	183.2	182.2	0	----	----	----	----	----	----	Drowning	100
Sequence VI*	186	183.2	134.7	----	----	----	39	----	----	Supratidal to lagoon	0
Sequence V*	187.3	186	55.3	----	----	----	90	----	----	Supratidal to lagoon	0
Erosion	195.3	187.3	-111	----	----	----	----	----	----	Supratidal	<0
Sequence I and II*	200.5	195.3	226.6	----	----	1	64	1	32	Supratidal to lagoon	0

* remnant % corresponds to early cemented lithologies

Fig. 3.1. Restored cross–section (A'-A) from Djebel Bou Dahar platform modified after Merino-Tomé et al. (2012) showing the location of the studied stratigraphic sections and their correlation. Table of stratigraphic units defined in the Djebel Bou Dahar area with their corresponding base and top ages (Merino-Tomé et al., 2012), thicknesses, lithology percentages and bathymetry estimations.

3.3. TAZOULT–AMEZRAÏ AREA

Detailed RS-mapping and structural analysis of the Tazoult–Amezraï area permitted the construction of several cross-sections across the Tazoult ridge and the Azourki-Tafraout salt wall (Fig. 3.2) and one regional cross-section crossing the entire studied area (GDL, 2011, 2012; Martín-Martín et al., 2016). Based on the regional cross-section it was possible to obtained thickness values for the different sedimentary units cropping out in the area (Fig. 3.3).

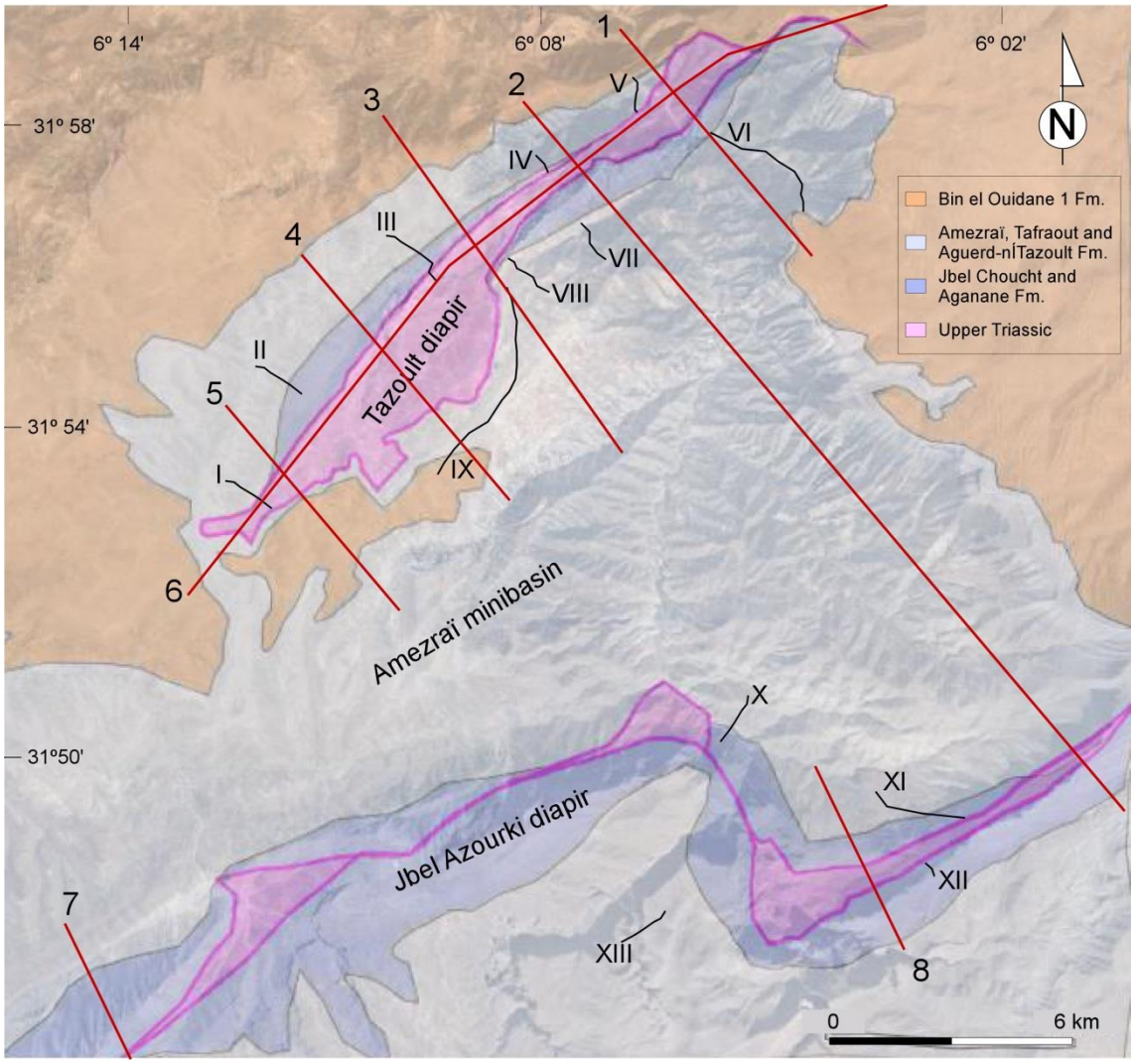

Fig. 3.2. Simplified geological map of the Tazoult Amezraï area showing the distribution of the resulting sections and stratigraphic logs based on collected field data. Red lines labelled in Arabic numbers show the position of the cross-section compiled in GDL (2011), GDL (2012), Saura et al. (2014) and Martín-Martín et al. (2016). Black lines labelled in roman numbers indicates the location of detailed stratigraphic logs by Joussiaume et al. (2014) and Malaval (2016).

However, the thicknesses of lower Jurassic sedimentary units in the central part of the Amezraï minibasin are poorly constrained because of the lack of subsurface data. The cross-

section through the studied area displayed a conservative thickness of the lower Jurassic sedimentary units and, therefore, an underestimation of thicknesses was expected in the central part of the Amezraï minibasin (Amezraï minibasin log, Fig. 3.3). Additionally, no Hettangian-Sinemurian strata are exposed in the area, although they are present as inclusions within the diapir and the Sinemurian Bou Imoura Fm. is exposed 20 km to the north, where it reaches a thickness of c.1000 m (Grélaud et al., 2014). Given the above considerations, sedimentary units older than Jbel Choucht Fm. were not considered in this area (Fig. 3.3). Erosional events have not been quantified in the Tazoult–Amezraï area; but a non-depositional event is defined between 175 and 171.1 Ma in the Tazoult diapir log (Hiatus in Fig. 3.3). In the Amezraï minibasin log the sedimentary record is continuous from the Early to the Middle Jurassic in the Amezraï section.

The ages of the different sedimentary units were established according to the published data in the studied area (Jossen and Couvreur, 1990; Bouchouata, 1994; Bouchouata et al., 1995). The estimation of the lithology percentage and the interpretation of sedimentary palaeoenvironment and related palaeobathymetry values were based on field observations and detailed sedimentological studies (Fig. 3.2) (GDL, 2011, 2012; Saura et al., 2014; Joussiaume, 2016; Malaval, 2016; Martín-Martín et al., 2016; Vergés et al., 2017). In the Tazoult–Amezraï area, all of the exposed formations were deposited in shallow marine environments (here, considered within palaeo-water depths from 0 to 30 m) (Fig. 3.3). Due to the lag of subsurface data, all sedimentary units were considered as homogeneous in terms of lithologies and paleobathymetry estimations throughout the entire area. It should be noted that the values of palaeobathymetry from shallow marine depositional environments show an error which is much smaller than the values set in deep water environments (Dupré et al., 2007; Lachkar et al., 2009; Xie and Heller, 2009), thus the errors linked to palaeobathymetry estimation can be considered as minimal.

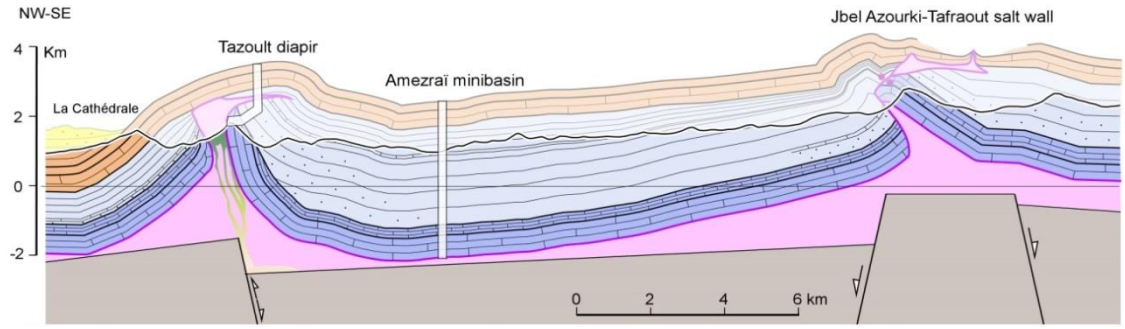

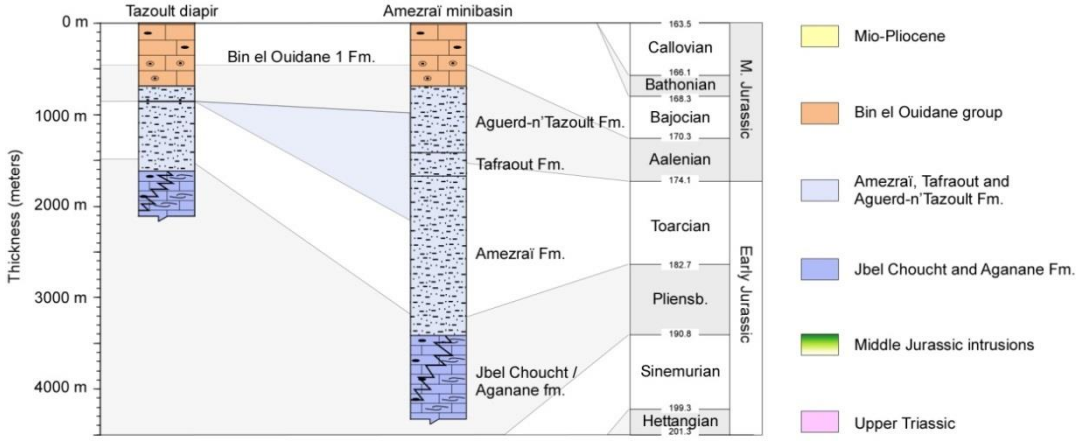

Tazoult - Amezraï	Age Base (Ma)	Age Top (Ma)	Thicknesses (m)	Lithology						Sedimentary Environment	Bathymetry (m)
				Sand	Silt	Shale	Limestone	Marls	Dolostone		
Tazoult diapir section											
Bin el Ouidane 1	170.7	170	690	----	5	5	75	15	----	Shallow platform	30
Aguerd-n'Tazoult	171.1	170.7	176	----	5	----	65	30	----	Supratidal to intertidal	10
Hiatus	175	171.1	0	----	----	----	----	----	----	----------	----
Amezraï	185	175	775	15	15	25	25	20	----	Supratidal to intertidal	10
Jbel Choucht / Aganane	189	185	470	----	----	5	70	25	----	Shallow platform & Lagoon	30
Bou Imoura	195.3	189	----	----	----	----	80	20	----	Shallow platform	30
Aït Bou Oulli	201.3	195.3	----	----	----	10	20	----	70	Supratidal to intertida	0
Amezraï minibasin section											
Bin el Ouidane 1	170.7	170	693.8	----	5	5	75	15	----	Shallow platform	30
Aguerd-n'Tazoult	172.2	170.7	713.2	----	5	----	65	30	----	Supratidal to intertidal	10
Tafraout	174.5	172.2	256.8	10	10	----	40	40	----	Intertidal to subtidal	20
Amezraï	185	174.5	1748.9	15	15	25	25	20	----	Supratidal to intertidal	10
Jbel Choucht / Aganane	189	185	906.9	----	----	5	70	25	----	Shallow platform & Lagoon	30
Bou Imoura	195.3	189	----	----	----	----	80	20	----	Shallow platform	30
Aït Bou Oulli	201.3	195.3	----	----	----	10	20	----	70	Supratidal to intertida	0

Fig. 3.3. Cross-section across the Tazoult–Amezraï area (cross-section 2 from Fig. 3.2) showing the location of the studied stratigraphic logs and their correlation. The thinning on the diapir flanks is well constrained and observed at outcrop, whereas thicknesses of units in the core of the minibasin are not well constrained and are likely conservative. Table show the data corresponding to the stratigraphic units from the area with their corresponding base and top ages (Jossen and Couvreur, 1990; Bouchouata, 1994; Bouchouata et al., 1995), thicknesses, lithology percentages and bathymetry estimations.

Twenty-seven vitrinite samples were collected throughout the Tazoult–Amezraï area (Fig. 3.4), with the most continuous sampling along the Aguerd-n'Tazoult Formation. The vitrinite reflectance values roughly range from 0.81 to 1.98%, in agreement with their stratigraphic position. Nevertheless, samples collected adjacent to those diapiric structures that were intruded by Middle-Late Jurassic igneous bodies (i.e. < 200 m) showed anomalously high values of vitrinite reflectance up to 3.05%. Vitrinite reflectance was analysed in the Instituto Nacional del Carbón (INCAR-CSIC) in Oviedo, Spain. Several observation points of reflectance were considered for each sample and mean value of reflectance (%) and associated standard deviation was obtained.

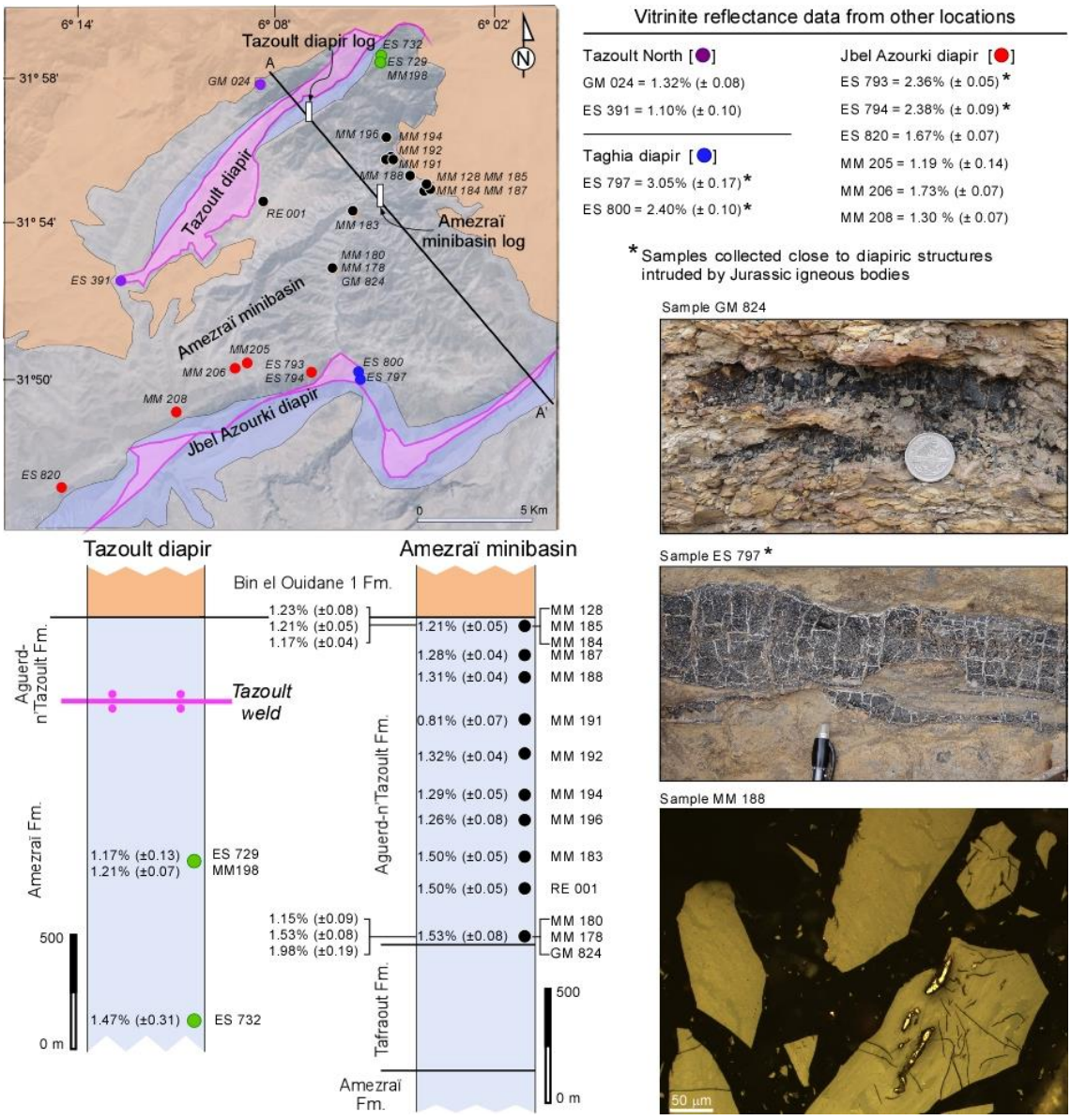

Fig. 3.4. Location of collected vitrinite samples (colour dots in Tazoult–Amezraï area map and stratigraphic logs) coupled with reflectance values (%) and associated standard deviation. Photographs of vitrinite hand samples and microscope (provided by INCAR) included.

3.4. IMILCHIL DIAPIRIC PROVINCE

Detailed RS-mapping and structural analysis of the Imilchil diapiric province allow two regional cross-sections (western and eastern) to be constructed across the entire area (Fig. 2.9 and Fig. 2.10). Using these cross-sections, it was possible to obtain thickness values for the different sedimentary units in six sedimentary logs (Fig. 3.5). However, the thicknesses of different sedimentary units in the central part of the three minibasins (Ikassene, Lake Plateau and Ikkou) are poorly constrained because of the lack of subsurface data. The cross-section through the studied area displays a conservative thickness of the lower and middle Jurassic sedimentary units and, therefore, an underestimation of thicknesses was expected in all the sedimentary logs (Fig. 2.10 and Fig. 3.5).

Sediments older than Toarcian are not exposed in the area, although the Sinemurian and Pliensbachian are extensively exposed throughout the Central High Atlas (Warme, 1988; Souhel et al., 2000; Wilmsen and Neuweiler, 2008). Given the above considerations, sedimentary units older than Agoudime I Fm. were not considered in this area (Fig. 3.5). The ages of the different sedimentary units have been established according to geological map from Imilchil (Fadile, 2003) and the estimation of the lithology percentage and the interpretation of sedimentary palaeoenvironment (Fig. 3.5) were based on field observations (GDL, 2011, 2012; Saura et al., 2014) and detailed sedimentological studies (Malaval et al., 2014; Joussiaume, 2016).

Palaeobathymetry estimations in this area were established using the sedimentary environment interpretation. In the Imilchil diapiric province, the older sedimentary units are composed by deep marine deposits, and they were associated to a 150 m of palaeobathymetry. This value must be considered as a minimum palaeobathymetry in deep marine environments for the interpretation of the subsidence analysis results as it was pointed by Lachkar et al. (2009). The younger deposits (from Bin el Ouidane 3 to Anemzi/Guettioua Fm.) were deposited in shallow marine to continental environments (here, considered within palaeo-water depths from 30 to 0 m) (Fig. 3.5). All sedimentary units were considered as homogeneous in terms of lithologies and paleobathymetry estimations throughout the entire area.

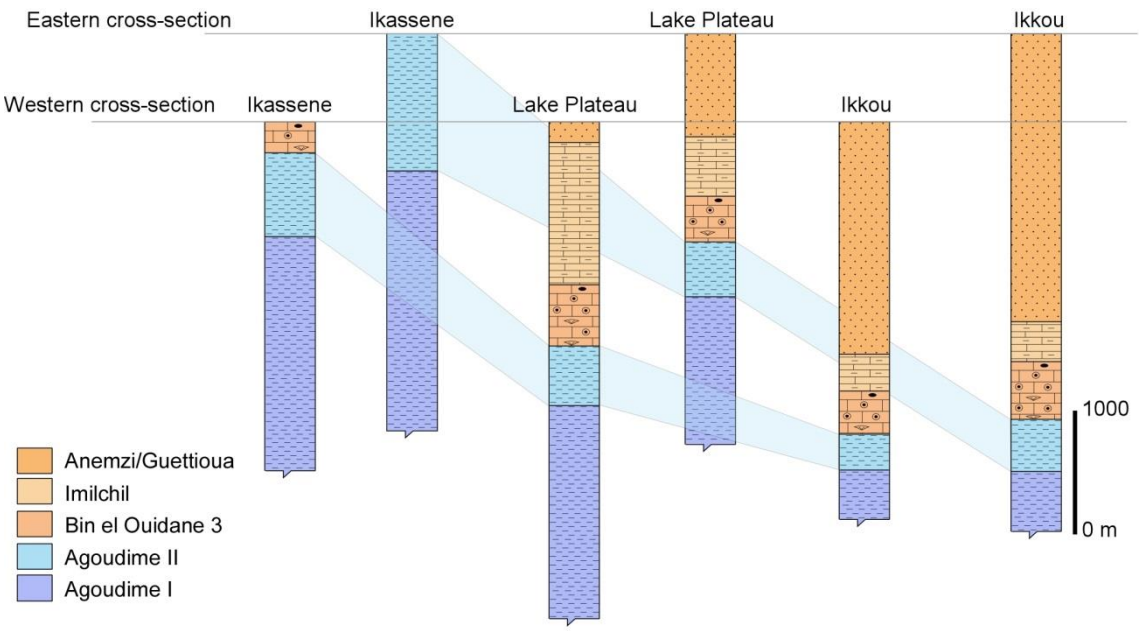

Imilchil diapiric province	Age Base (Ma)	Age Top (Ma)	Thicknesses (m)		Lithology						Sedimentary Environment	Bathymetry (m)
			W log	E log	Sand	Silt	Shale	Limestone	Marls	Dolostone		
Ikassene												
Anemzi/Guettioua	167.7	163	0	0	30	30	30	5	5	----	Supratidal	0
Imilchil	168.5	167.7	0	0	10	10	----	20	60	----	Supratidal to intertidal	20
Bin el Ouidane 3	170.2	168.5	240	0	----	----	----	85	15	----	Shallow platform	30
Agoudime II	172.5	170.2	709	1227	----	----	----	40	60	----	Basin	150
Agoudime I	183	172.5	1898	2000	----	----	10	20	----	70	Basin	150
Lake Plateau												
Anemzi/Guettioua	167.7	163	165	848	30	30	30	5	5	----	Supratidal	0
Imilchil	168.5	167.7	1152	468	10	10	----	20	60	----	Supratidal to intertidal	20
Bin el Ouidane 3	170.2	168.5	506	392	----	----	----	85	15	----	Shallow platform	30
Agoudime II	172.5	170.2	481	418	----	----	----	40	60	----	Basin	150
Agoudime I	183	172.5	1734	1253	----	----	10	20	----	70	Basin	150
Ikkou												
Anemzi/Guettioua	167.7	163	1886	2330	30	30	30	5	5	----	Supratidal	0
Imilchil	168.5	167.7	303	367	10	10	----	20	60	----	Supratidal to intertidal	20
Bin el Ouidane 3	170.2	168.5	341	455	----	----	----	85	15	----	Shallow platform	30
Agoudime II	172.5	170.2	329	430	----	----	----	40	60	----	Basin	150
Agoudime I	183	172.5	405	493	----	----	10	20	----	70	Basin	150

Fig. 3.5. Correlation panel of the six stratigraphic logs obtained from western and eastern cross-section from Imilchil diapiric province (see location in Fig. 2.10). The thinning on the diapir flanks is well constrained and observed at outcrop, whereas thicknesses of units in the core of the minibasin are not well constrained and are likely conservative. Table show the data corresponding to the stratigraphic units from the area with their corresponding base and top ages (Fadile, 2003), thicknesses, lithology percentages and bathymetry estimation.

Based on presented cross–sections (Fig. 2.9), RS-Mapping and collected dip data (GDL, 2011, 2012), 3D surfaces of the base of the outcropping sedimentary units in the Imilchil diapiric province were available to be used in the present research. Using Move software (Midland Valley), GDL provided a large amount of thickness data (up to 6000 thickness values) measured orthogonal to the surfaces (Annexes; subsection 9.1). Using Temis Flow software (BeicipFranlab), discrete thickness measures were used to build thickness maps for each sedimentary unit applying linear interpolation (Fig. 3.6); however, some anomalous thickness values were detected. These anomalies were mainly located in the vicinities of the diapiric structures, where the overturned layers from the 3D model caused the overestimation of thicknesses. In order to filter the extreme values considered as thickness anomalies, a statistical analysis of frequencies distribution was applied (see details in Annexes; Subchapter 10.1). The rejected values were those with a frequency range equal or lower than 2%. Applying this frequency threshold, a new set of filtered maps was obtained with a minimized effect of thickness overestimation but with a minimum alteration of the main thickness variation trends in the area (Fig. 3.6). The filtered thickness maps were used for the construction of preliminary total subsidence maps in the Imilchil diapiric province (see Chapter 6.1 Subsidence analysis). The calculation of total subsidence requires bathymetry data and lithology composition. They were considered homogeneous and equal to those used in the 1D model throughout the entire area. However, recent detailed sedimentology studies of the area presented by Joussiaume (2016) described facies variation link to bathymetric changes due to the diapir activity. Thus, heterogeneities in lithology distribution and palaeobathymetry variations need to be considered in future models.

*Fig. 3.6. (Next page) Thickness maps of 36.2*26.5 km (x and y, respectively), with a regular grid spacing of 100 m, for each sedimentary unit outcropping in the Imilchil diapiric province: Agoudime I Fm., Agoudime II Fm., Bin el Ouidane 3 Fm., Imilchil Fm. and Anemzi/Guettioua Fm. Left side maps corresponds to the original thickness maps and right side maps corresponds to the filtered ones (see text for details), colour scale is different for each sedimentary unit. The pink dotted areas correspond to the present day diapiric ridges; Tassent ridge (north) and Ikkou ridge (south), where the thickness is assumed as 0 m for the entire modelled time range. Black boxes mark the area covered by the 3D model from which the thickness values have been obtained.*

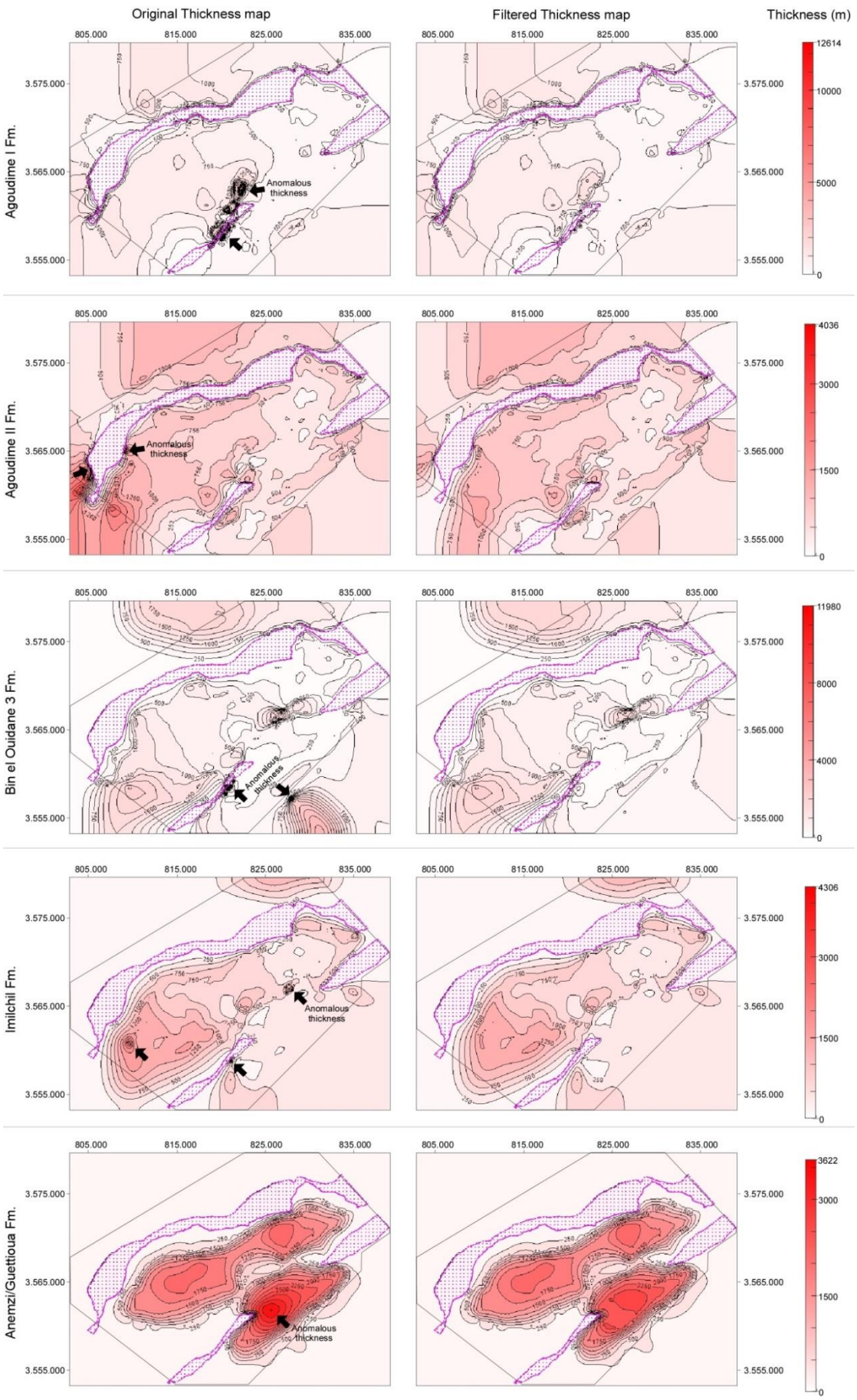
Original Thickness map
Filtered Thickness map
Thickness (m)
Agoudime I Fm.
Agoudime II Fm.
Bin el Ouidane 3 Fm.
Imilchil Fm.
Anemzi/Guettioua Fm.
Anomalous thickness
805.000
815.000
825.000
835.000
3.575.000
3.565.000
3.555.000
12614
10000
5000
0
4036
3000
1500
11980
8000
4000
4306
3622

CHAPTER 4

METHODS

4. METHODS

4.1. ANALOGUE MODELLING

The analogue models presented in this thesis were developed in the Experimental Tectonics Laboratory of Géosciences Rennes (Université de Rennes 1, France). Classical techniques were applied for brittle/ductile analogue modelling experiments. These techniques include velocity discontinuity (VD) (e.g., Malavieille, 1984; Balé, 1986; Ballard et al., 1987; Allemand et al., 1989), the use of silicone and sand (Faugère and Brun, 1984), and diverse scaling issues (Davy and Cobbold, 1991; Weijermars et al., 1993). In experiments to simulate the brittle behaviour of sedimentary rocks with Mohr-Coulomb properties, dry Fontainebleau quartz sand (manufactured by SIBELCO France) was used, with a mean grain size of approximately 250 μm, an internal friction angle of 30-35° (Krantz, 1991) and a density (ρ) of approximately 1500 kg/m^3. Sand layers of different colours were used to emphasise the structures; however, the colour of the sand does not modify its behaviour (Fig. 4.1a and b). Silicone putty was used to simulate the behaviour of ductile layers (Fig. 4.1c) such as evaporite, under compacted shale or overpressured shales (e.g., Cohen and McClay, 1996; Wu and McClay, 2011). The mean viscosity of the putty is ~3x10^4 Pa s at 20 °C and its mean density is ~1000 kg/m^3 (Silicone putty SGM 36, manufactured by Rhône-Poulenc, France).

The modelling device used in this study constitutes three rigid blocks and represents a simple geometry of the basin basement with a central graben bounded by two synthetic faults dipping at 60° (Fig. 4.1). The footwall blocks were fixed to the mobile walls, whereas the central hangingwall block was not fixed, allowing it to subside during extension. A constant velocity of 0.5 cm/h was applied to each mobile wall by a screw jack, during both extension and compression, implying a total deformation velocity of 1 cm/h. The model was filled with a ductile silicone layer representing evaporite-bearing or salt units deposited during rift and post–rift events (Fig. 4.1c). The ductile layer was covered by a thin pre-extension brittle layer of 1 cm of sand representing a sedimentary succession deposited during a short post–rift phase, prior to renewed extension (representing the Hettangian carbonates in the study area).

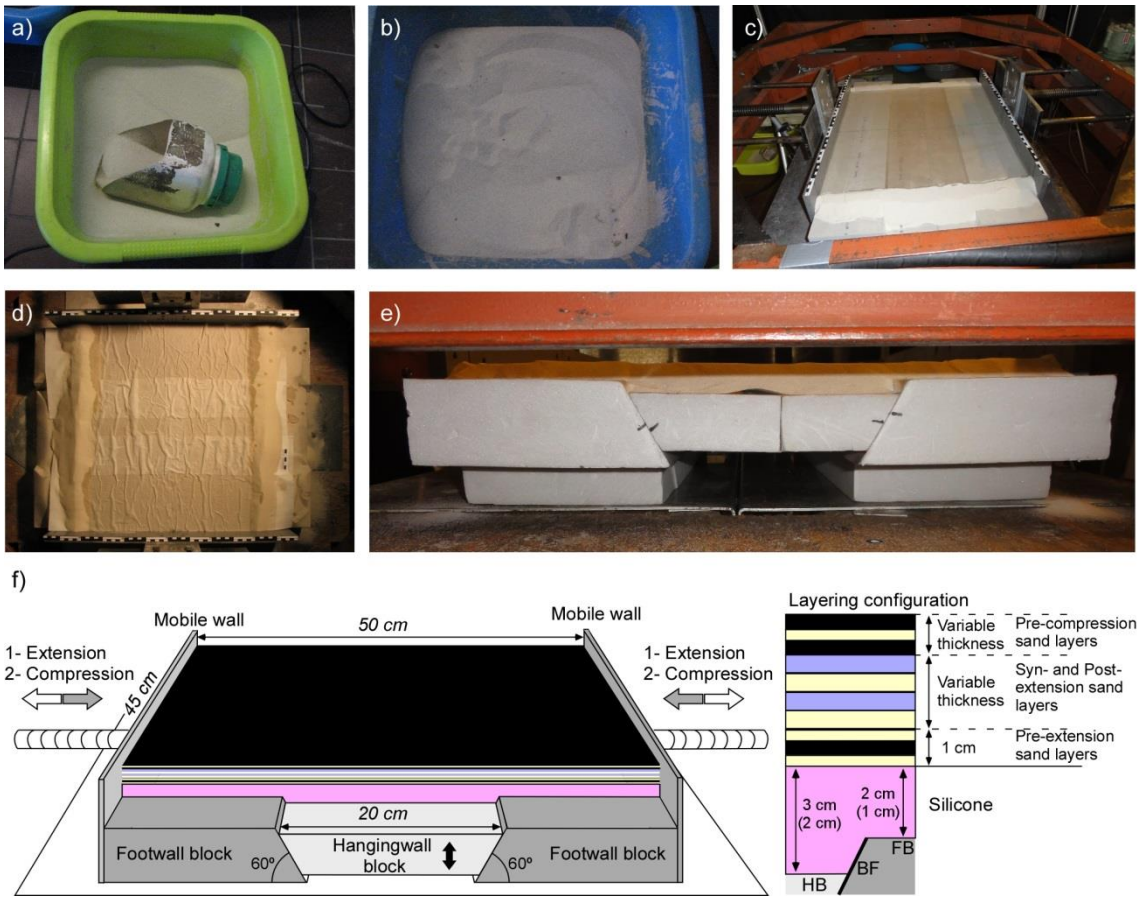

Fig. 4.1. Photographs of material used in the analogue modelling and sketch of modelling device. a) and b) different coloured sand behaviour of sedimentary rocks; c) Overview of the experimental device including silicone putty; d) top view of humidification step after model ending; e) detailed image of the rigid blocks used to simulate the basement geometry and f) experimental modelling device setup composed by a single central graben bounded by two fault planes dipping 60º. In the right-hand side, column showing the configuration of the different layers composing the model (HB: Hangingwall block, FB: Footwall block, BF: Basement fault). Silicone thickness values between parentheses correspond to the thickness used in the Model A1.

A test model with a thin silicone layer, 1.5 cm in the hangingwall and 1 cm in the footwalls, was run, but it did not produce diapiric structures (see details in Annexes, Subchapter 10.2). Thus, in all the models, the thickness of the silicone was increased to between 2 and 3 cm in the hangingwall and to between 1 and 2 cm in the footwalls to generate diapirs (Fig. 4.1). The 2–3-cm model thicknesses would correspond to about 1600–2400 m in nature.

The evolution of a diapiric basin was analysed by running three sets of models (Fig. 4.2) representing the three main tectonic stages of the Central High Atlas: extension (rifting), tectonic quiescence (post–rift) and compression (inversion). The influence of different amounts of sedimentation within the geometry of the diapirs was determined by applying variable sedimentation rates during the extension and post–extension phases (Fig. 4.2). Model

A represents the evolution of the system during extension (2 h with a total extension of 2 cm) without the influence of coeval syn-rift sedimentation. Model set B (four models) represents the evolution of the system during extension (2 h with a total extension of 2 cm), with the sedimentation rate being equal to the subsidence rate, followed by a post–extension phase (3 h) with a sedimentation rate equal to or lower than the rate of diapir growth. Model set C (two models) represents the complete evolution of the basin, which includes extension and post–extension periods, both with homogeneous sedimentation, followed by compression with shortening, perpendicular to the rifting tectonic trends, amounting to 3 cm and 5 cm (6 % and 10 %, respectively) (Fig. 4.2).

The results of the modelling were recorded by taking photographs of the surface of each experiment every 6 minutes, corresponding to 0.1 cm of deformation during the extension and compression phase. To induce sand cohesion before slicing, a thick layer of white sand was sprinkled on top of the model before its humidification at the end of each experiment (Fig. 4.1d). Cross–sections were cut through the central part of the models, and thus parallel to the extension and shortening directions (perpendicular to the basement faults).

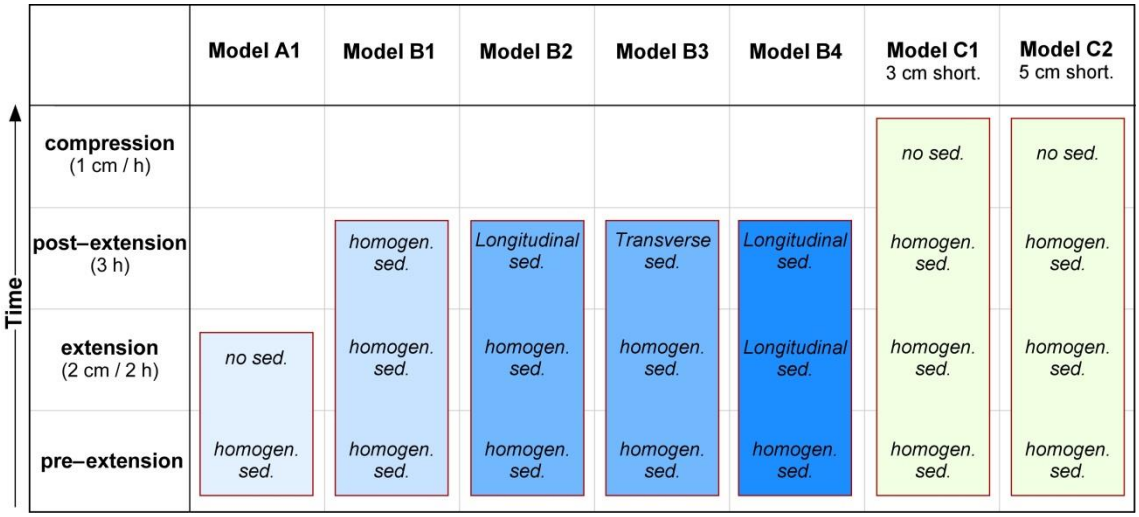

Fig. 4.2. Diagram showing the modelled tectonic phases through time (extension, post–extension and compression), the applied sedimentation pattern (none, homogeneous or progradation) and degree of compression involved in each model.

4.2. GEOHISTORY MODELLING

4.2.1. SUBSIDENCE ANALYSIS

1D subsidence analysis were performed using GENEX® 4.0.3 (Beicip Franlab-IFP) in two sections of the Djebel Bou Dahar platform, two sections of the Tazoult–Amezraï area and six sections from Imilchil diapiric province. The analysis were carried out using formation ages, formation thicknesses, lithology percentages, sedimentary environments and palaeobathymetry estimations detailed in the Chapter 3 (Fig. 3.1, Fig. 3.3 and Fig. 3.5). The output data from this modelling method was the tectonic and total subsidence evolution including quantification (rates) of the geological events occurred in the basin.

The software calculated total and tectonic subsidence through time by backstripping sediments and water load assuming local isostatical compensation; i.e. the Airy model (Steckler and Watts, 1978; Sclater and Christie, 1980; Bond and Kominz, 1984). The total subsidence (Z) at the bottom of the sedimentary cover is the sum of the tectonic subsidence (Z_t) and the deflection due to the sediment load (D). To calculate the tectonic subsidence (Z_t) against the total subsidence (Z), the software computed deflection (D) applying the equation of Watts and Steckler (1981):

$$D = S\frac{d_s - d_w}{d_m - d_w} + P_w - Sl\frac{d_w}{d_m - d_w}$$

In this equation, *S* corresponds to sedimentary column thickness, *ds* is the average density of the sedimentary column calculated using lithology quantification (Fig. 4.3), d_m is the molten mantle density (3.3 g/cm^3), d_w is the density of water (1.0 g/cm^3), P_w is the palaeobathymetry estimation and *Sl* corresponds to the eustatic sea level. However, GENEX® does not apply corrections that consider eustatic variations, and thus the results were interpreted taking this assumption into account.

Decompaction of each unit was computed by the software using the equation of porosity vs depth, first presented by Athy (1930), where $\phi(z) = \phi_0 * e^{-cz}$. ϕ is porosity, ϕ_0 is the initial porosity, *c* is the compaction factor and *z* the burial depth. Because there was not direct or indirect data coming from cores or diagraphies, decompaction was based on specific porosity/depth curves that GENEX® established for each sedimentary unit according to the lithology percentage composing them (Fig. 4.3). The most outstanding porosity/depth trend

was displayed by the Toarcian unit of the Djebel Bou Dahar (see details in Fig. 3.1), that it is rapidly compacted due to the high content in shales and marls (around 93%). Also remarkable was the initial porosity of the Sequence VI in the platform log of Djebel Bou Dahar, which has a very low initial porosity value (45.2%, Fig. 4.3) due to early-cemented facies that caused the obliteration of porosity compared to other sedimentary units.

Djebel Bou Dahar basin log		
Sedimentary unit	Initial ϕ (%)	ρ (g/cm^3)
Aalenian	66.4	2.690
Toarcian	69.8	2.732
Drowning	0	0
Sequence VI	67.8	2.686
Sequence V	67.5	2.687
Sequence IV	66.9	2.689
Sequence III	66.0	2.691
Sequence I and II	61.1	2.720

Djebel Bou Dahar platform log		
Sedimentary unit	Initial ϕ (%)	ρ (g/cm^3)
Aalenian	66.4	2.690
Toarcian	69.8	2.732
Drowning	0	0
Sequence VI*	45.2	2.696
Sequence V*	63.7	2.692
Erosion	0	0
Sequence I and II*	60.5	2.721

Tazoult - Amezraï logs		
Sedimentary unit	Initial ϕ (%)	ρ (g/cm^3)
Bin el Ouidane 1	66.2	2.692
Aguerd-n'Tazoult	66.6	2.684
Tafraout	64.9	2.676
Amezraï	65.5	2.701
Jbel Choucht / Aganane	67.3	2.694

Imilchil diapiric province logs		
Sedimentary unit	Initial ϕ (%)	ρ (g/cm^3)
Anemzi/Guettioua	56.9	2.692
Imilchil	65.8	2.674
Bin el Ouidane 3	66.7	2.689
Agoudime II	68.5	2.840
Agoudime I	67.7	2.678

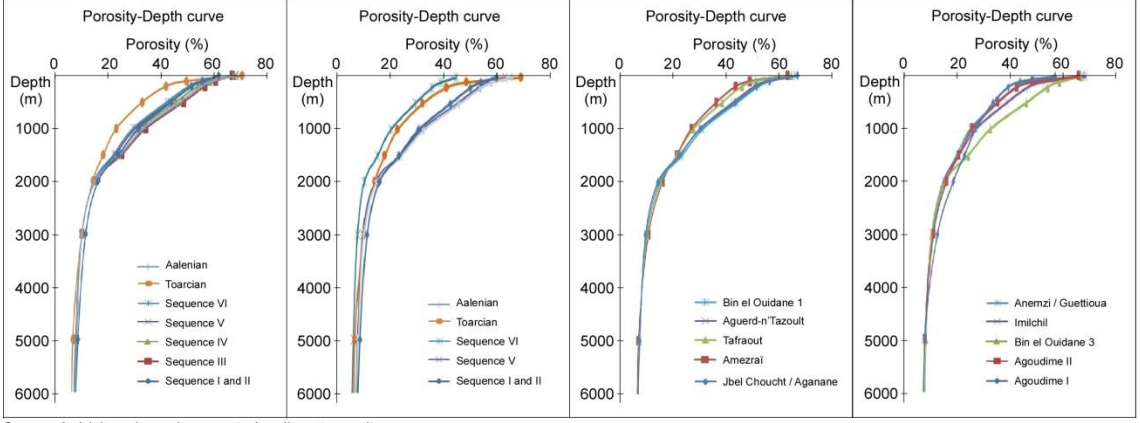

Star symbol (*) marks early cemented sedimentary units.

Fig. 4.3. Compilation of initial porosity and density values of all the units used to carry out the 1D subsidence analysis of the Djebel Bou Dahar, Tazoult–Amezraï area and Imilchil diapiric province. Graphs show the Porosity-Depth curves for each unit in Djebel Bou Dahar (Basin and Platform) the Tazoult–Amezraï area and Imilchil diapiric province.

The available thickness maps from the Imilchil diapiric province presented in the previous chapter allowed 3D model of the evolution of the area from 183 to 163 Ma to be built using Temis Flow software. This software calculates the total subsidence of each cell composing the modelled area using sediment decompaction and water depth. The porosity/depth curves defined by default by Temis Flow were modified using the data from Genex (Fig. 4.3) in order to be able to compare total subsidence rates from 1D model and total subsidence rates from the maps. Software limitations do not permit to calculate tectonic

4.2.2. THERMAL MODELLING

The presence of diapir structures produces thermal anomalies due to the high thermal conductivity of the salt (Petersen and Lerche, 1995; Petersen and Lerche, 1996; Magri et al., 2008). Thus, to avoid the potential impact of Tazoult diapir in the thermal field, the thermal modelling was only carried out in the centre of the Amezraï minibasin using GENEX® software. However, the availability of vitrinite samples in the Tazoult diapir stratigraphic log (Fig. 3.4) allowed presenting a first tentative thermal modelling based on Tazoult diapir log to be presented (Annexes, subsection 10.3).

Thermal modelling workflow was shown in Fig. 4.4.The input data for this modelling were: geological events such as deposition of the sedimentary units (including ages, thicknesses and lithological composition) and erosional events (including ages and amount of eroded deposits), petrophysical properties of the sedimentary units (in the present study the default properties established by the software were used), and thermal parameters. The output of this modelling was the thermal history of each sedimentary unit and of the entire sedimentary record. Consequently, it was obtained the evolution of temperature and evolution of the maturity of organic matter in the studied basin (Fig. 4.4).

The geological events from Pliensbachian to Bajocian in the Amezraï minibasin log were defined according to field outcrops and structural and sedimentological studies (see data in Fig. 3.3). In contrast, in the modelling process the palaeo heat flow values and potentially eroded deposits were undetermined. More than 18 models were performed, thus the specific thermal parameters and thickness of non-preserved deposits for each model are detailed in the results chapter to facilitate the reading (Section 6.2. Thermal modelling).

The thermal conditions and additional burial (associated to non-preserved sedimentary successions) needed to be calibrated. The calibration of these parameters was based on the comparison between vitrinite reflectance data from Amezraï minibasin log and the theoretical vitrinite reflectance curves calculated by the software (Fig. 4.4). In this case, GENEX® calculated two different vitrinite reflectance curves: Easy%Ro curve, based on models from Sweeney and Burnham (1990) and Sweeney et al. (1990), and IFPRo reflectance curve, that was constructed using a global database including data from North Sea, Pannonian Basin, Nova Scotia, Eastern Paris basin, among others. The thermal models evaluation was based on 14 samples coming from the Amezraï minibasin log, with a reflectance mean value of 1.53%, with absolute values

that progressively decreased towards the top of the succession (i.e. to 1.21%), showing a good fit with their relative stratigraphic position (Fig. 3.4).

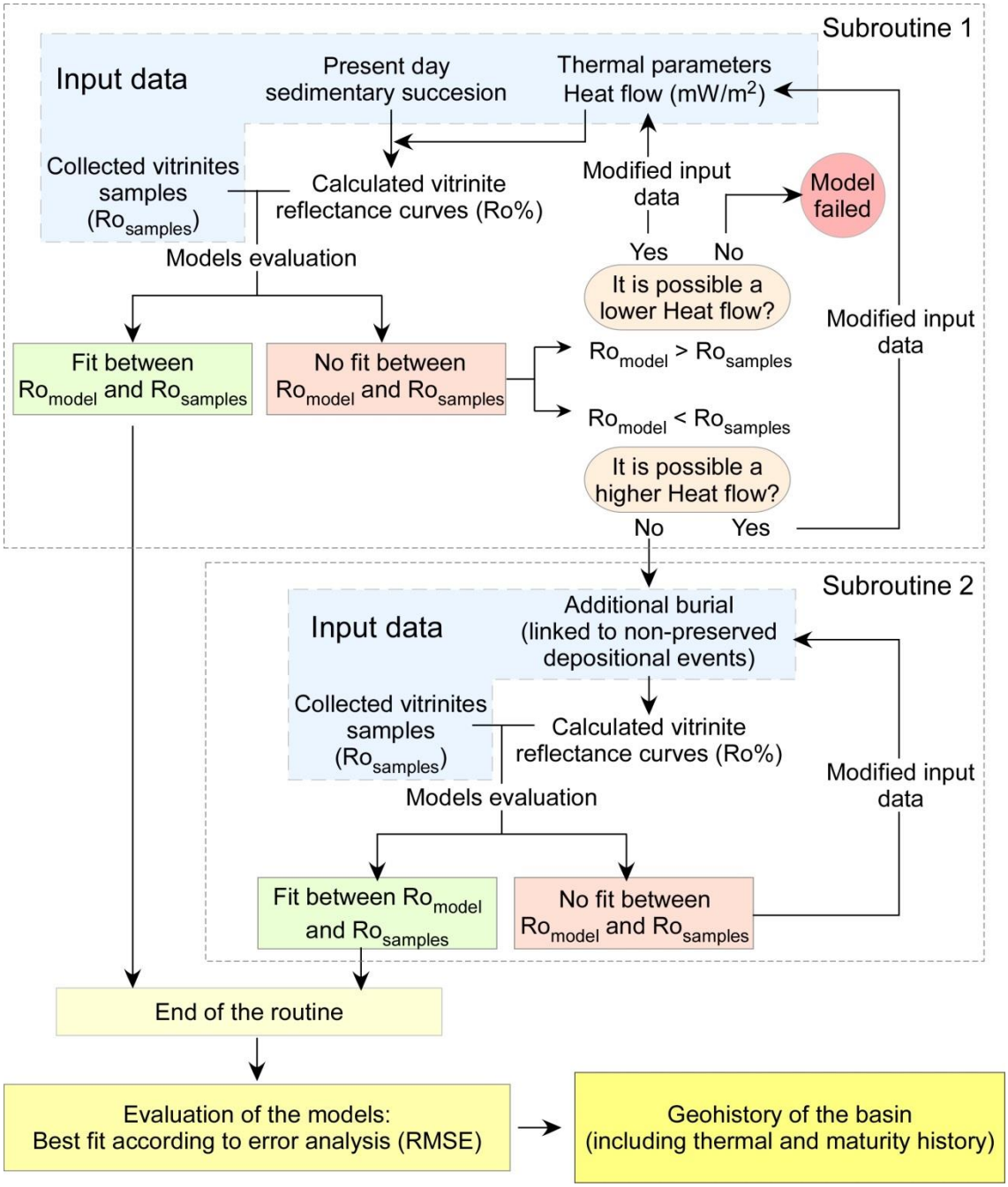

Fig. 4.4 .Workflow showing the routine used in the thermal modelling process including required loops when there is no fitting between the calculated vitrinite reflectance curves from the model (Ro_{model}) and the vitrinite reflectance distribution of the samples collected in the studied area ($Ro_{samples}$).

CHAPTER 5

Analogue modelling from extension to inversion of a rift diapiric basin

5. ANALOGUE MODELLING FROM EXTENSION TO INVERSION OF A RIFT DIAPIRIC BASIN

As it was detailed in Chapter 4 (Methods), three sets of analogue models (A, B and C; Fig. 4.2) were used to analyse the evolution of a diapiric basin during three different tectonic stages (extension, tectonic quiescence and compression). Additionally, diverse sedimentation patterns were applied during the extension and post–extension stages in order to examine how sedimentation influences in the final diapir geometry. These models were used to reach a better understanding of extensional salt-basin dynamics for the later interpretation of subsidence curves obtained from the Central High Atlas. Although the major depositional direction in the Central High Atlas was longitudinal, model with transverse deposition was also carried out to analyse the influence of both sedimentation patterns in diapir evolution.

5.1. MODEL A1; SYN-RIFT PHASE WITH NO SEDIMENTATION

Model A1 represented the evolution of a basin during extension (total extension of 2 cm corresponding to about 4% of extension) without the influence of syn-rift sedimentation (Fig. 5.1). The hangingwall of the graben subsided homogeneously during extension with a rate around 1 cm/h. After a total extension of 1 cm newly formed small grabens cut the pre-extension layer. These grabens were subparallel to the basement faults at depth and were located in their footwalls, close to the tip line of the basement fault (border graben) or in the footwall interior (lateral graben) (Fig. 5.1). These grabens were still extending at the end of the extensional phase (2 cm of total extension).

The cross-sections after extension showed roughly symmetric grabens affecting the pre-extension unit above the silicone layer (Fig. 5.1). Along the centre of the model, small border grabens showed rotation towards the main graben basin because of the forced folding of pre-extension beds above the basement faults. Both border and lateral grabens exhibited nucleation of small reactive triangular diapirs in their basal parts similar to the results of already-documented analogue model (e.g., Vendeville and Jackson, 1992; Nalpas and Brun, 1993; Rowan et al., 1999; Dooley et al., 2005; Hudec and Jackson, 2007). Along the footwall corners of the conjugate normal faults there was a necking effect producing a narrowing of the silicone layer (only 0.47 cm wide) or its final welding (Fig. 5.1). The thickness of the silicone used in this model (1 cm thick in the footwall and 2 cm thick in the hangingwall block) was not

thick enough to avoid the feeder closure (necking effect) caused by the subsidence of the hangingwall block and the related forced folding during extension. This necking effect was observable in other previous published analogue models, such as those of Nalpas and Brun (1993), Jackson and Vendeville (1994), Vendeville et al. (1995) in their Fig. 5, Dooley et al. (2003) in their Fig. 8 and 10 or Dooley et al. (2005).

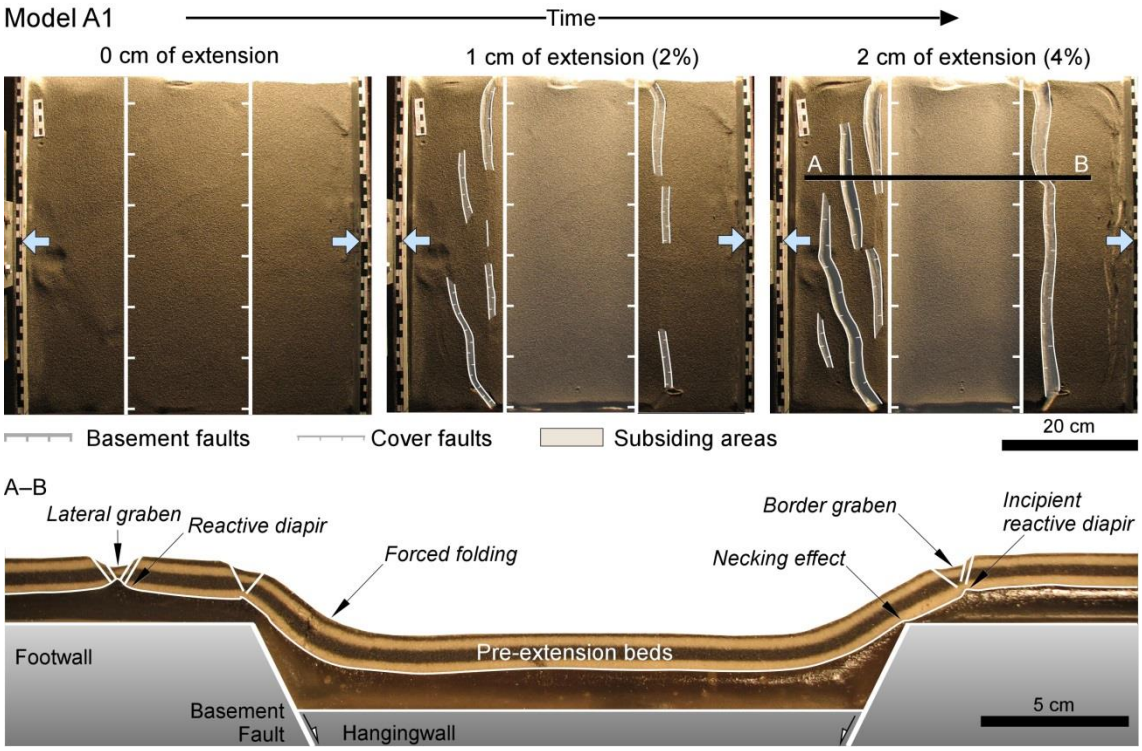

Fig. 5.1. Overhead views of Model A1 (total extension = 2 cm) showing the distribution of several newly formed grabens in the pre-extension beds. The model section shows the geometry of cover grabens bounded by two opposing normal faults rooted in incipient reactive diapirs

In Model A1 (Fig. 5.1), the combination of both extension and forced-folding mechanisms created new grabens developed close to and along the tip lines of the basement faults beneath the ductile and mobile detachment unit (silicone layer). This spatial distribution suggested a linkage or partial coupling between sub- and supra- silicone structures during extension. This models showed how extension is a mechanism that can readily trigger reactive and active diapirs in salt-related rift basins, as it was already demonstrate by the use of analogue models and case studies since the early 1990s (Vendeville and Jackson, 1992; Koyi et al., 1993; Nalpas and Brun, 1993; Jackson and Vendeville, 1994; Vendeville et al., 1995; Schultz-Ela and Jackson, 1996; Pascoe et al., 1999; Withjack and Callaway, 2000; Dooley et al., 2003; Kane et al., 2010; Duffy et al., 2013; Lewis et al., 2013).

5.2. MODELS B1, B2, B3 AND B4; SYN- AND POST–RIFT PHASES WITH VARIABLE SEDIMENTATION

Four models (B1, B2, B3, and B4 in Fig. 4.2) were developed using the same extension rate as that of Model A1 (1 cm/h for 2 h, a total extension of 2 cm) and a duration of the post–extension phase of 3 h. The thickness of the silicone layer in these models was higher than in Model A1 (2 cm in the footwall and 3 cm in the hangingwall) to minimize the necking effect in the early part of the modelling, which would hamper the evolution of diapiric structures. In models B1, B2 and B3, homogeneous syn-extension sedimentation was applied in the main subsiding area, corresponding to the graben basin between the two conjugate basement faults, with a sedimentation rate equivalent to the accommodation rate (subsidence of central block + silicone withdrawal). During the post–extension phase, different sedimentation patterns were applied for each model: homogeneous sedimentation for Model B1 (Fig. 5.2); longitudinal prograding sedimentation (parallel to the graben axis) in Model B2 (Fig. 5.3); and transverse prograding sedimentation (orthogonal to basin axis) in Model B3 (Fig. 5.4). Contrarily, the Model B4 has been carried out with longitudinal syn-extension and post–extension prograding sedimentation (Fig. 5.5).

Model B1, characterised by homogeneous sedimentation during both extension and post–extension phases, showed the development of elongated newly formed grabens very close to the tip lines of the main basement faults during the extension phase (Fig. 5.2). Taking the results from Model A1 as a reference, these elongated grabens marked the locations of reactive diapirs beneath the pre-extension sand layers. During the post–extension phase the homogeneous sedimentation in the central graben and associated silicone migration allowed a transition to occur from long and continuous reactive diapirs to more mature diapiric structures with different geometries.

Diapirs in the left side of the model showed geometries similar to those of salt rollers (roller-like diapirs in Fig. 5.2). Salt rollers are immature structures developed in extensional settings, and were defined as ridge-like diapirs, being asymmetrical in cross-section with a long gently dipping flank and a short, steep scarp flank delineated by a normal fault (Bally, 1981; Jackson and Talbot, 1986; Brun and Mauduit, 2009; Quirk and Pilcher, 2012). The diapir on the right-hand side of the model showed changes in its geometry from a roller-like diapir in section 25 (B-B’ in Fig. 5.2) to a well-developed passive diapir with steep walls, a smooth basinwards vergence, and incipient extrusion section 38 (A-A’) (Fig. 5.2). The silicone layer at the end of the experiment was thicker than 2.2 cm in both footwall blocks, whereas exceeded 1.7 cm in

thickness in the hangingwall along its central part. The necking effect narrowed the feeder to 0.20-0.65 cm in width. The area balances of the silicone layer calculated in sections 38 and 25 record similar reductions in silicone thickness (80% remaining) compared with its original thickness. This result indicates that silicone withdrawal occurred parallel to the direction of extension with little or no migration along the strike of the extension.

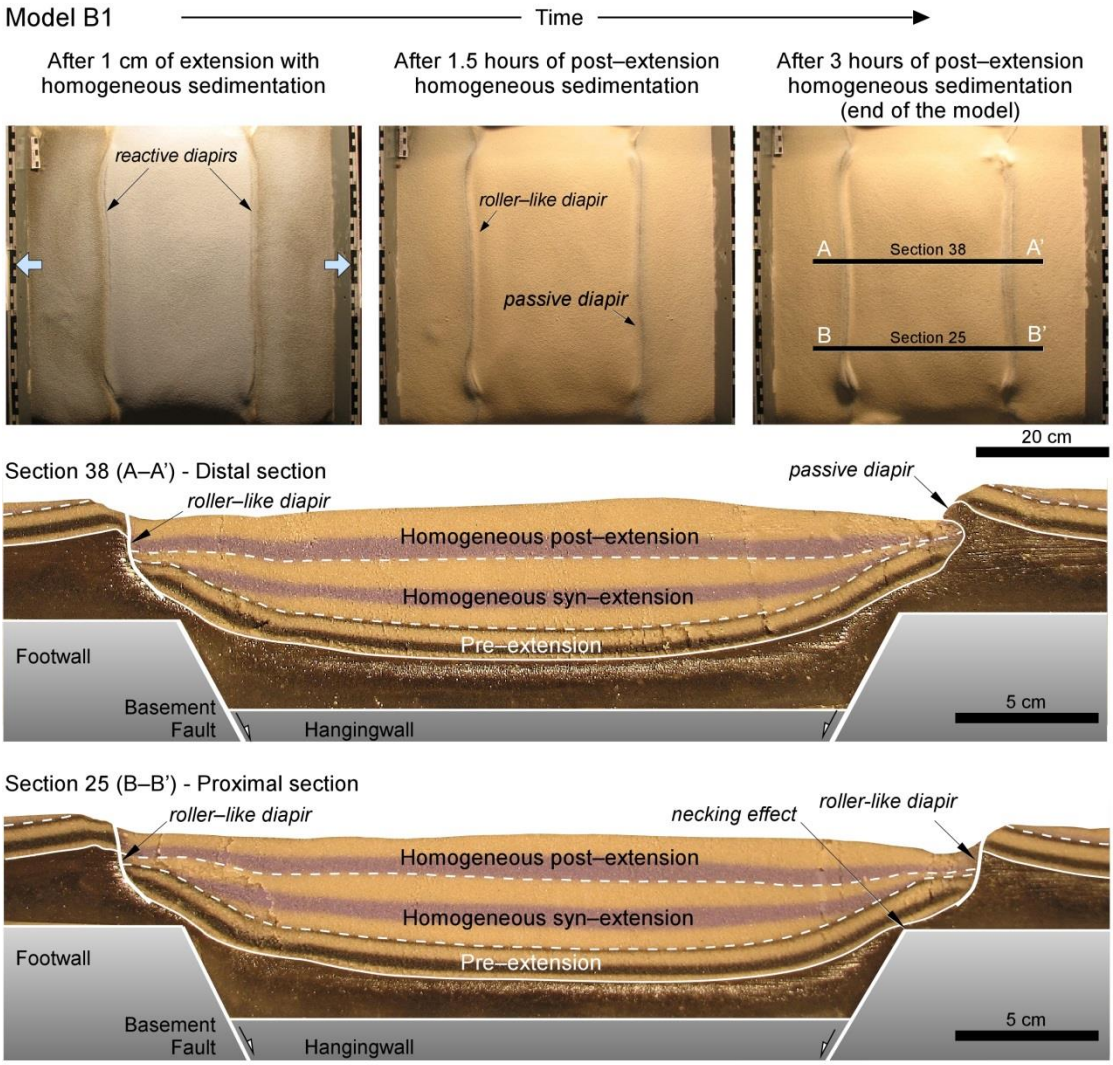

Fig. 5.2. Overhead views and sections showing the geometries resulting from Model B1. This model is characterised by an extensional phase (total extension = 2 cm) and a post–extensional phase (3 h) with homogeneous sedimentation during both phases. The thick white line marks the diapir wall acting as a normal fault.

In Model B1, the migration of ductile material towards the footwall domains, and especially towards the diapirs, caused the tilting and folding of the pre-extension sand layers resulting in flap structures flanking the diapiric structures (Schultz-Ela et al., 1993; Rowan et al., 2003; Schultz-Ela, 2003; Saura et al., 2016) (Fig. 5.2). The outward flanks of diapirs, refer to flap

structures located in the footwall of both basement faults, were low dipping, ranging from 9° to 16°. In contrast, in the hangingwall of the graben system, the inward flanks were steeper, with a mean inclination of 26° close to the basement faults, partly due to forced folding. In addition, the left-side inward flank shows a 0.5-cm short uppermost segment dipping up to 38° in both sections 25 and 38 (Fig. 5.2)

Model B2, which was characterised by extension homogeneous sedimentation followed by a longitudinal progradation of post–extension deposition, displayed elongated newly formed grabens close to the main basement faults associated with reactive diapirs, similar to that seen in Model B1 (Fig. 5.3). During the post–extension phase, the reactive diapirs evolved to passive diapirs along strike in areas of the graben characterized by high sedimentaration rates (section 25 B-B' in Fig. 5.3). The diapirs located in the proximal part of Model B2 were inward leaning, with very steep walls and incipient silicone extrusions on top of the model topography; resulting from migration of the silicone towards the diapir. Towards the distal part of the model, the silicone extrusion and diapir width increased, being less than 0.9 cm wide in the proximal part of the model and more than 1.2 cm wide in the distal part (Fig. 5.3). The difference in the diapir width and silicone extrusion formation can be correlated to the thickness variation of sedimentary pile. The mean value of the syn-extension sedimentary succession along strike was around 2.6 cm, but the post–extension sedimentary succession varied in thickness, being 3.5 times thinner in the distal domain than in the proximal domain (thicknesses of 0.45 cm and 1.5 cm, respectively). In this model, the diapir outward flanks displayed a dip range between 12° and 18° whereas the inward flanks were between 26° and 35°, which were similar dip ranges to those observed in Model B1. In section 25 (B-B' in Fig. 5.3), the short uppermost segment of the left-side inward flank, of 0.23 cm length (corresponding to few hundred meters in nature), was highly folded reaching a dip up to 84º (Fig. 5.3).

At the end of the experiment of Model B2, the silicone layer thicknesses seemed to be similar in proximal and distal domains (sections 25 B-B' and 39 A-A' in Fig. 5.3, respectively). However, there was more silicone preserved in the distal domain compared with the proximal domain (67% and 60%, respectively), indicating a migration of the silicone from proximal and overload to distal regions of the model. This migration of silicone was probably enhanced by the longitudinal progradation of the post–extension sedimentary wedge. The necking effects of the pre-extension deposits against the tip line of the basement normal faults were strong in the proximal areas (0.2 cm of width compared with 0.6 cm in the distal domain; Fig. 5.3), even

reaching the feeder welding stage. This configuration permitted the extrusion of silicone along the distal segments of the silicone walls, generating short overturned flanks showing a vergence towards the graben basin.

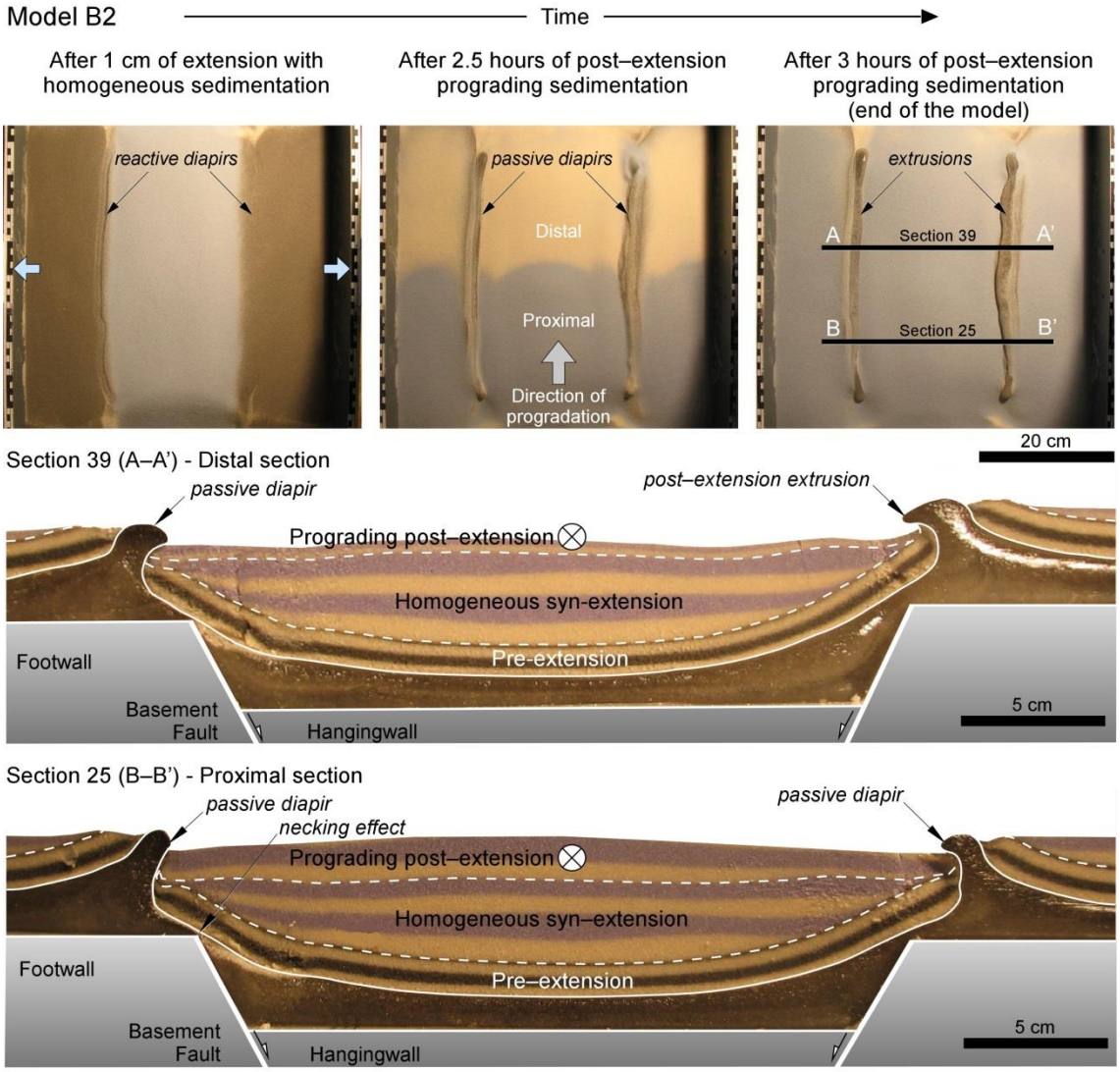

Fig. 5.3. Overhead views and sections showing the geometries resulting from Model B2. This model includes an extensional phase (total extension = 2 cm) with homogeneous sedimentation and a post–extensional phase (3 h) with longitudinal prograding sedimentation. The diapir geometries differ from the proximal (Section 25) to the distal domains (Section 39).

Model B3, which was characterised by extension homogeneous sedimentation followed by a transverse progradation of post–extension deposition, showed a symmetric development of elongated newly formed grabens during the extension phase bounding the central basement graben (Fig. 5.4). This configuration was comparable to those obtained in models B1 and B2. In contrast, Model B3 showed an asymmetric geometry across its strike during the post–

extension phase. It should be noted that in this model configuration the proximal domain was on the right-hand side whereas the distal domainwas on the left-hand side, in agreement with the direction of sedimentary progradation (Fig. 5.4). Passive diapir walls along the proximal domain were well developed and were characterised by very steep flanks in both sections 37 (B-B') and 33 (A-A') at the end of the experiment (Fig. 5.4). Conversely, the diapiric structures developed along the distal domain were incipient roller-like diapirs with a predominant right-dipping normal fault laterally evolving to silicone walls that were less developed with post–extension deposits that are three times thicker.

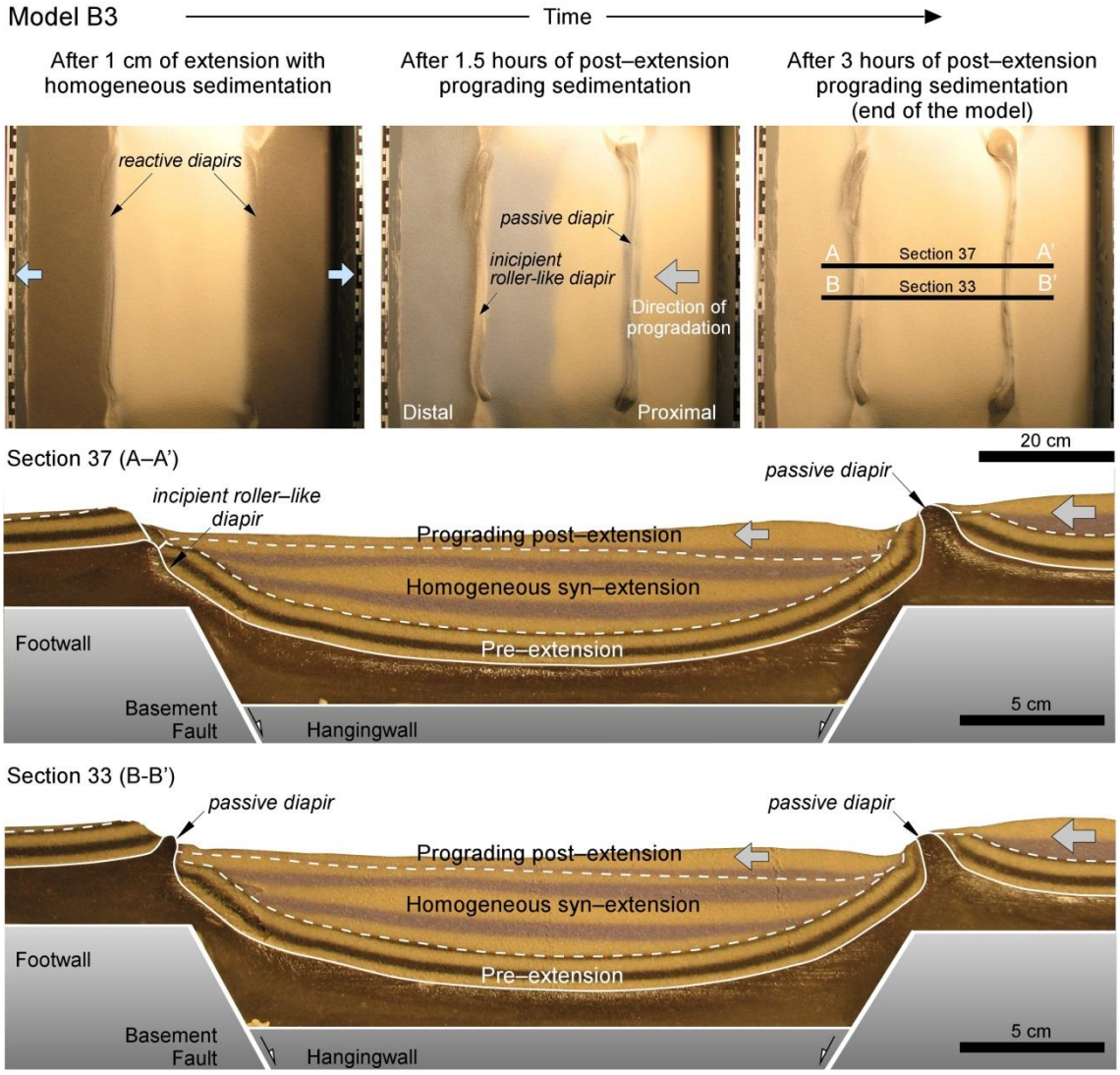

Fig. 5.4. Overhead views and sections showing the geometries resulting from Model B3. This model includes an extensional phase (total extension = 2 cm) with homogeneous sedimentation and a post–extensional phase (3 h) with transverse prograding sedimentation. The diapir geometries of the proximal domains (right-hand sides of the diagrams) differ from those of the distal domains (left-hand sides).

The final geometry of the silicone layer in Model B3 was asymmetric across the model with thinner and less preserved silicone in the proximal domain (1.22 cm thick compared with 1.76 cm in the distal domain). In this model, the necking effects were limited and the silicone feeder in each footwall corner constituted a 0.6-cm-wide zone and was thus open for silicone migration. The steepest flanks of the model correspond to the inward flanks of the proximal domain silicone walls. The dips of the inward flanks of the distal silicone walls ranged from 20° to 45° whereas the dips of the inward flanks of the proximal silicone walls ranged from 60° to overturned (inward flank of the passive diapir in the proximal domain; section 33 B–B' in Fig. 5.4). This flank overturning, which reached 1 cm in length, was clearly a diapiric contribution as the only tectonic mechanism operating in Model B3 is extension.

Model B4, which was characterised by extension and post–extension longitudinal sedimentary progradation, showed a final configuration that differed substantially from models B1, B2, and B3. After 1 cm of extension, the elongated grabens characterised by reactive diapirs at depth change their trend ahead of the significant prograding sedimentary lobe (Fig. Fig. 5.5A). At the same time, a normal collapse fault dipping towards the distal part of the model develops as a result of silicone migration in the same direction. The sedimentation pattern applied in Model B4 caused a marked variation in sediment thickness in the central graben, from 5.3 cm in the proximal part of the model to 1.3 cm in the distal part (Fig. 5.5B). The proximal domain of the model was characterised by extrusive diapirs that are well developed and subvertical or slightly vergent towards the graben. These diapirs were less than 1 cm wide and opened around 1 h after the end of extension. In this proximal part of the model, the silicone layer was 1.5 cm thick in the footwall domains and reached a minimum of 0.6 cm in the graben domain. The necking effect was extreme, and, as a consequence, the silicone feeders of both diapirs were welded (section 23 B–B' in Fig. 5.5A). The geometry of the silicone walls after the welding of the feeders differed slightly from that of previous models, with the inward flanks being slightly folded owing to local subsidence of the upper part within the silicone wall pedestal. The distal regions of the main basement graben were characterised by a much less evolved diapiric system, with stagnant reactive diapirs developing during the extensional phase. The silicone layer was characterised by a thickness of around 1.5 cm in the footwall domains and 3 cm in the hangingwall domain, with a very subtle necking effect on top of the footwall corner.

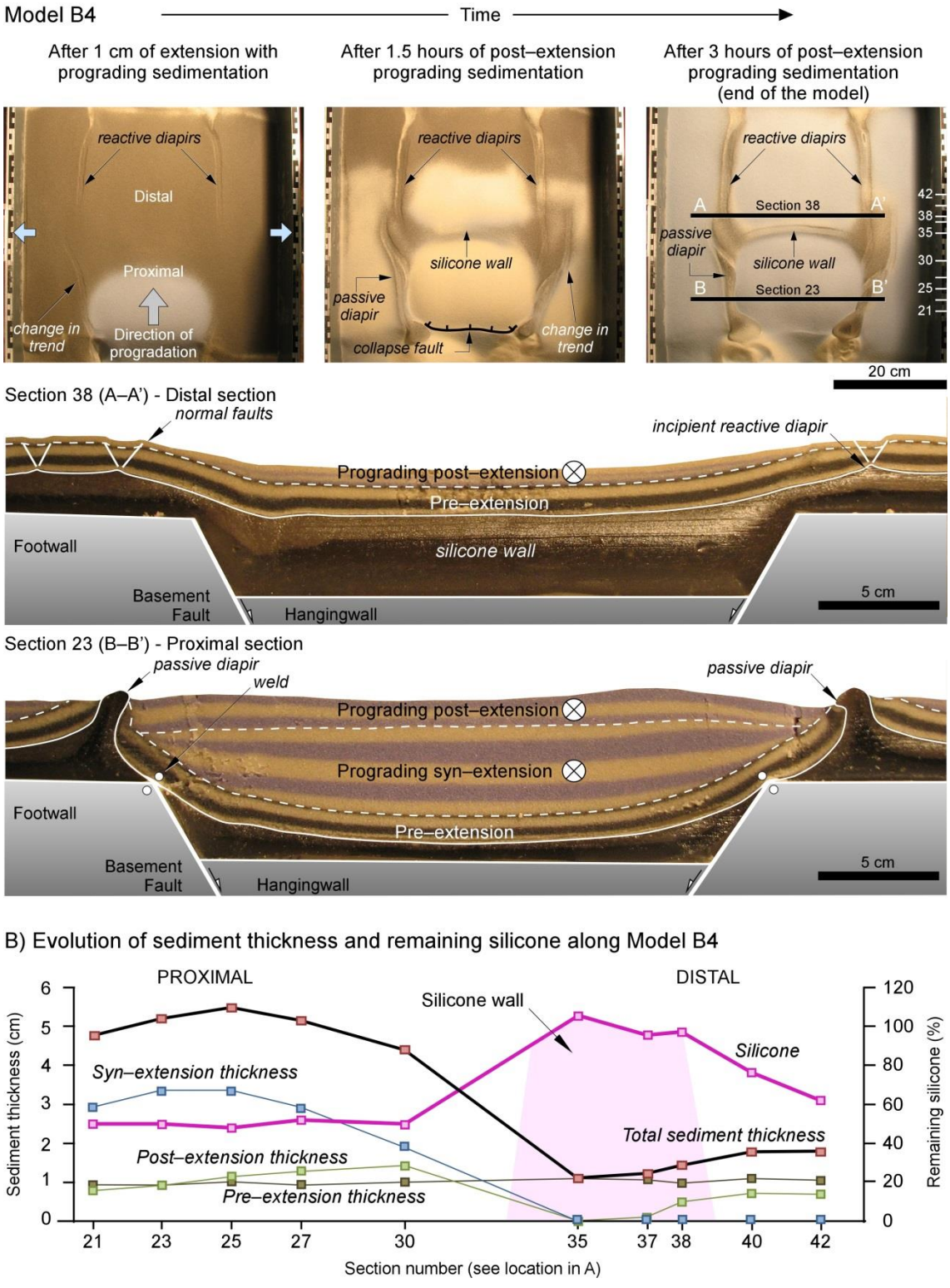

Fig. 5.5. A) Overhead views and sections showing the geometries resulting from Model B4. This model includes an extensional phase (total extension = 2 cm) and post–extensional phase (3 h) with longitudinal prograding sedimentation during both phases. B) Plot showing sediment thickness along the model as revealed by sections obtained from the model.

The most outstanding result from Model B4, however, was the growth of an arcuate silicone dome evolving towards a silicone wall growing perpendicular to the main direction of bordering silicone walls that separated the proximal and distal domains (Fig. 5.5). This silicone wall (section 38 in Fig. 5.5A) was perpendicular to the progradation direction, mimicking the shape of the sedimentary prograding system. A comparison of the area balance of the silicone layer before and after the deposition of the prograding sequence shows a greater reduction in the proximal domain (about 47% remaining) than in the distal domain (nearly 70% remaining). These differences recorded the axial flow of the silicone layer from proximal to distal domains as estimated in the plot of the remaining silicone area (Fig. 5.5B). The plot showed the inflation of the silicone layer predominantly from sections 35 to 38, forming the silicone wall in front of the thick sedimentary successions deposited in the proximal domain of the model. This orthogonal silicone structure, which was limited by the along-strike silicone walls, produced a compartmentalization of the silicone domain separating growing minibasins as well as controlling their size and the direction of their major axes. It was possible to infer from these results that a continuous progradation along the axis of the minibasin infilling the graben could produce either several of these orthogonal silicone walls (given sufficient available silicone) or a migrating silicone inflation (implying the depletion of the previous one through time and the formation of complex patterns of minibasin sedimentary infill).

The presented models B1, B2, B3 and B4 showed how sedimentation enhances the mobilization of the silicone and triggers passive diapirism after the reactive diapirism stage. The transition from reactive to passive diapirism by means of an active stage was not clearly identified. However, the occurrence of an active stage cannot be ruled out if the pre-extension sand layers are thinned enough to reach the threshold for forceful piercement (Vendeville and Jackson, 1992). During the passive diapirism, the ductile material emplaced below the grabens developed in the pre-extension layers during the reactive stage evolved into two clear diapir walls along the entire system.

Comparing models B1, B2, B3, and B4, the only difference in the extension phase was observed in Model B4, where the sedimentation coeval with extension progrades longitudinally to the rift system. Results after the extensional phase were observed only in overhead views. Whereas models B1, B2, and B3 show well-developed rectilinear reactive diapirs along the footwall blocks (extensional overhead views in Fig. 5.2, Fig. 5.3 and Fig. 5.4), Model B4 shows discontinuous and non-rectilinear reactive diapirs that were diverted by the silicone inflation ahead of the sedimentary prograding lobe at depth (extensional overhead

view in Fig. 5.5). The observed discontinuity was interpreted as the result of the interaction between the regional extension and the local stress field associated with silicone inflation caused by the thick and localised sedimentation of the prograding lobular wedge (Gaullier and Vendeville, 2005; Sellier et al., 2013).

The development of diapirs during the post–extensional phase differs between models B1 to B4 as the sedimentary patterns were distinct. Nevertheless, in overhead view, models B1 to B3 shared passive diapirs along the footwall blocks defining rectilinear silicone ridges. In contrast, Model B4 shows the growth of a perpendicular silicone wall developed ahead of the prograding sedimentary wedge accompanied by normal faulting across the proximal region of the sedimentary lobe caused by the withdrawal of silicone at depth (post–extensional overhead view in Fig. 5.5). The growth of this silicone wall was probably associated with the early progradation of the sedimentary wedge that caused the migration of silicone from the proximal towards the distal domains of the model due to differential loading (McClay et al., 2003; Hudec et al., 2009; Warsitzka et al., 2013).

The marked asymmetry of the sedimentary patterns of models B1 to B4 implicated the distinctive evolution of silicone diapirs from the proximal to distal domains of the model. Model B1, characterised by homogeneous post–extensional deposition, showed a homogeneous development of the silicone diapirs. The proximal domains of models B2, B3, and B4 display well-developed steep and inward-leaning passive diapirs owing to the equilibrium between sedimentation rate and diapir growth rate (Vendeville et al., 1993; Talbot, 1995; Giles and Lawton, 2002). The distal domains of models B2, B3, and B4 displayed very distinctive diapir evolutions. Model B2, with longitudinal post–extensional prograding sedimentation, showed significant silicone extrusion along the passive diapirs (section 39 in Fig. 5.3). These allochthonous bodies expanded on top of the hangingwall deposits because the post–extension sedimentation did not keep pace with diapir growth (Vendeville and Jackson, 1992; Vendeville et al., 1993; Talbot, 1995; Koyi, 1998). Model B3, with transverse post–extensional prograding sedimentation from right to left, showed in the distal domain poorly developed diapiric geometries evolving from incipient roller-like diapirs to passive diapirs (smaller than along the proximal domain) (sections 33 and 37 in Fig. 5.4). Model B4, with longitudinal syn- and post–extensional prograding sedimentation, displayed incipient reactive diapirs (section 38 in Fig. 5.5). The axial migration of silicone from the proximal into the distal domain together with the insufficient amount of sand deposited during the late post–extension phase limited the forced folding of pre-kinematic layers and did not generate

enough thinning of the pre-extension layers to allow the progression from incipient reactive diapiric structures to more evolved phases of diapirism. The results from analogue modelling presented in this work also showed that sedimentation patterns are closely related not only to the evolution of diapiric structures and their geometries but also to the evolution of the diapiric basin configuration.

5.3. MODELS C1 AND C2; SYN- AND POST–RIFT PHASES WITH HOMOGENEOUS SEDIMENTATION AND SUBSEQUENT COMPRESSION (6% AND 10% SHORTENING)

Models C1 and C2 portrayed compressional structures developed during basin inversion using simple extension and post–extension homogeneous sedimentation (Fig. 5.6). Both models were based on Model B1 and differ from each other with respect to the amounts of post–diapiric and pre-compression sedimentation (1.5 and 3 cm, respectively) and with respect to the applied shortening (3 and 5 cm corresponding to 6% and 10%, respectively). The applied 6% of shortening did not fully invert the central graben in Model C1, whereas 10% of shortening produced a total positive inversion (pop-up structure) of the central graben domain in Model C2 (2.5 and 4 cm of vertical uplift, respectively; Fig. 5.6). The upward movement of the hangingwall during compression reopened previously welded areas in the footwall corners (necking effect) and facilitated a renewed silicone flow towards the diapiric structures and footwall domains.

Model C1 was characterised by inversion of the central graben and gentle fold of the entire pre-, syn-, and post–extension sedimentary successions within the graben basin (minibasin) and by the rejuvenation of subvertical diapiric ridges along both footwall blocks (section 37 A-A’ in Fig. 5.6). The hangingwall pre-extension layers showed similar or slightly steeper flanks (dips of 30º to 45º) compared with the purely extensional models. However, the outward flanks of diapir silicone walls along the footwall blocks were somewhat steeper (up to 25º on the left-side and 35º on the right-side, respectively) than similar geometries in extensional models (between 15º and 25º). Rejuvenation subvertical diapirs, characterised by very steep or overturned flanks composed of thin pre-compression beds, caused the local redeposition of the pre-compression sand (taking into account the lack of syn-compressional deposition in the model). The vergence of silicone extrusion was away from the inverted central graben because of its higher elevation in contrast to the extensional models, in which topographic low was located in the subsiding central graben basin.

Model C2, after 5 cm of shortening and a thicker pre-compression sedimentary unit compared with C1, was characterised by positive inversion of the central graben and by the dome-shape folding of the entire sedimentary succession above the pop-up basement structure (section 34 A-A' in Fig. 5.6). The thicker pre-compression layers in Model C2 were deformed close to and above the rejuvenated diapirs. A large monocline was observed in the pre-compression units in the left-hand side of the model whereas the more evolved diapir in the right-hand side of the model produced a subvertical fold in the pre-compression layers (thrusted box-fold geometry). Roof-collapse normal faults occurred along the crest of the subvertical anticline as well as erosion and redeposition of sand along its flanks. However, the most noteworthy result was the full welding of both border silicone walls, resulting in detached silicone stocks, as well as the formation of a basal weld of the minibasin against the uplifted basement of the central graben. The welding of these structures gave rise to a quite different geometry for the resultant inverted model, achieved by increasing the shortening only from 6% to 10%. Regarding the thrust geometry along the diapir walls, the right side seemed to thrust above younger rocks of the central minibasin, it was the product of welding along the border diapir, thereby preserving the relative positions of the two flanks in Model C2 compared with C1 (Fig. 5.6). Compared with C1, the pre-extension layers in C2 showed a steeper inclination that occurred mostly after or close to the welding episode along the border silicone walls. The welding of the border diapirs and their subsequent buttressing resulted in an increase in the dips of the outward flanks (Fig. 5.6), which may be steeper than 50° where the flanks were subparallel to the welded diapir walls. The inward flanks of silicone diapir walls, limiting the central graben minibasin, showed dips of 26°–30° but can be very steep (75°) to overturned in their uppermost short segments close to the diapir wall (0.3 cm in the left-side flank of the minibasin and 0.5 cm in its right-side flank; Fig. 5.6).

Fig. 5.6. (Next page) Overhead views and sections showing models C1 and C2. These models are constituted by an extensional phase (total extension = 2 cm), a post–extensional phase with homogeneous sedimentation, and a final compression phase with a total amount of shortening of 3 cm (6%) in Model C1 and 5 cm (10%) in Model C2.

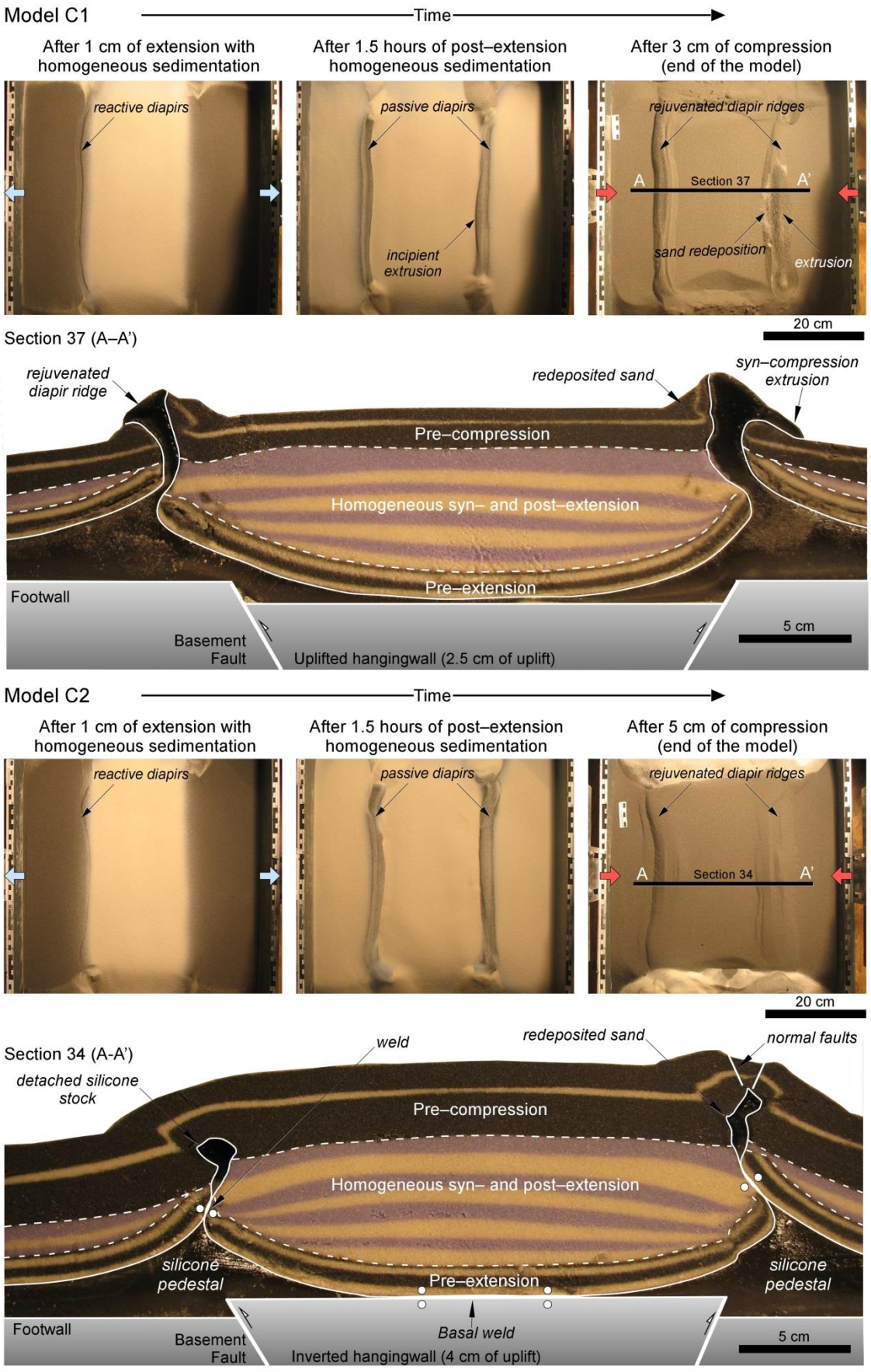
Model C1
Time
After 1 cm of extension with homogeneous sedimentation
After 1.5 hours of post–extension homogeneous sedimentation
After 3 cm of compression (end of the model)
reactive diapirs
passive diapirs
incipient extrusion
rejuvenated diapir ridges
A
Section 37
A'
sand redeposition
extrusion
20 cm
Section 37 (A–A')
rejuvenated diapir ridge
redeposited sand
syn–compression extrusion
Pre–compression
Homogeneous syn– and post–extension
Pre–extension
Footwall
Basement Fault
Uplifted hangingwall (2.5 cm of uplift)
5 cm
Model C2
Time
After 1 cm of extension with homogeneous sedimentation
After 1.5 hours of post–extension homogeneous sedimentation
After 5 cm of compression (end of the model)
reactive diapirs
passive diapirs
rejuvenated diapir ridges
A
Section 34
A'
20 cm
Section 34 (A-A')
weld
redeposited sand
normal faults
detached silicone stock
Pre–compression
Homogeneous syn– and post–extension
silicone pedestal
Pre–extension
silicone pedestal
Basal weld
Footwall
Basement Fault
Inverted hangingwall (4 cm of uplift)
5 cm

The presented compressional models showed that pre-compression salt structures have a major impact on the final configuration of an inverted salt basin, with the majority of compression deformation taking place in locations with a thin overburden, such as over the top of diapirs, as was extensively documented (Vially et al., 1994; Letouzey et al., 1995; Nalpas et al., 1995; Dooley et al., 2005; Rowan and Vendeville, 2006; Callot et al., 2007; Dooley et al., 2009; Burliga et al., 2012; Callot et al., 2012).

The comparison of extensional models B1 to B4 with compressional models C1 and C2 (characterised by 6% and 10% of shortening, respectively) allowed the silicone-related extension to be differentiated from the silicone-related compression effects on the geometry of silicone ridges. This was especially clear when comparing Model B1 and models C1 and C2, which were using homogeneous pre- syn- and post–extension sedimentation (Fig. 5.7).

All purely extensional models displayed diapiric flanks (flaps) with dips ranging from 8° to 17° in both footwall domains (outward flanks). Dips of the hangingwall flanks (inward flanks) are higher, reaching 18°–40° in the left-hand sides of the models and 25°–49° in their right-hand sides. Model B1 fitted in these ranges, with 9°–16° in the footwalls and 26° for both sides of the hangingwall (Fig. 5.7). Some of the plotted models showed short uppermost flank segments adjacent to diapirs with dips above 70°, and a few such flanks showed overturning. Models C1 and C2 showed a steepening of extensional diapir flanks but related only to the footwall domains, whereas hangingwall flanks showed similar dips to those of the extensional models, between 18º and 49º. Model C1, with 6% shortening, showed footwall flank dips of 30° and 36° for the left and right sides, respectively, whereas Model C2 displayed footwall flank dips of 45° and 50°. A comparison of these dips with those obtained in Model B1 indicated that the dips in the footwall flanks were steeper by about 20° and 35° with shortenings of 6% (C1) and 10% (C2), respectively. According to the compression models all footwall flanks dipping more than 17° needed the contribution of compression to develop.

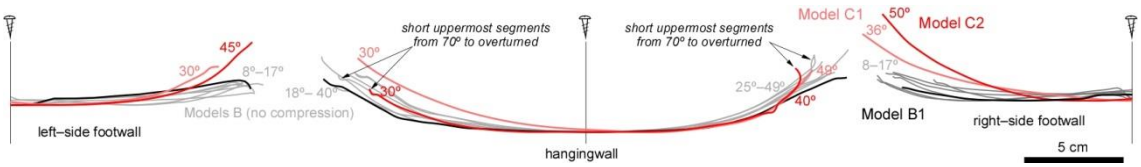

Fig. 5.7. Traces of pre-extension layers in purely extensional models and in models including 6% and 10% of compression. Compression causes the strongest steepening of pre-extension layers in the footwall domains

In the Tazoult and Jbel Azourki diapirs, the positions of basement faults in the cross-sections were inferred based on thickness variation between the two flanks of diapiric salt walls (ridges). However, their positions at depth lack precision, and commonly, the tiplines of the basement faults were located directly underneath the diapir salt walls at the surface (Martín-Martín et al., 2016). However, according to the presented results and those of previously published models (e.g., Dooley et al., 2005), diapiric structures were developed in the footwalls of the basement normal faults away from their tiplines. Thus, it was proposed a modification of the previous published cross-section in which the Tazoult and Jbel Azourki diapirs were located in the footwall domains of the basement normal faults that bound the Amezraï minibasin (Fig. 5.8).

The final geometry of diapirs after the shortening overprinting was another outcome from modelling that can be applied to better discriminate between extensional and compressional geometries as observed for models C1 and C2 (Fig. 5.8). The presented results showed that passive diapirs created during extension were tightened during subsequent compression, with reductions in diapir width ranging from 32% to 72% in Model C1 with 6% of shortening. These pre-existing diapirs were completely welded in Model C2 with 10% of shortening. In addition, the tightening and welding of diapirs may create a thrust weld, moving the footwall overburden above the thicker hangingwall post–silicone sedimentary pile. These results were consistent with field observations in the Tazoult and Jbel Azourki diapirs, which, under a regional shortening of 10.4% (Martín-Martín et al., 2016), were fully welded.

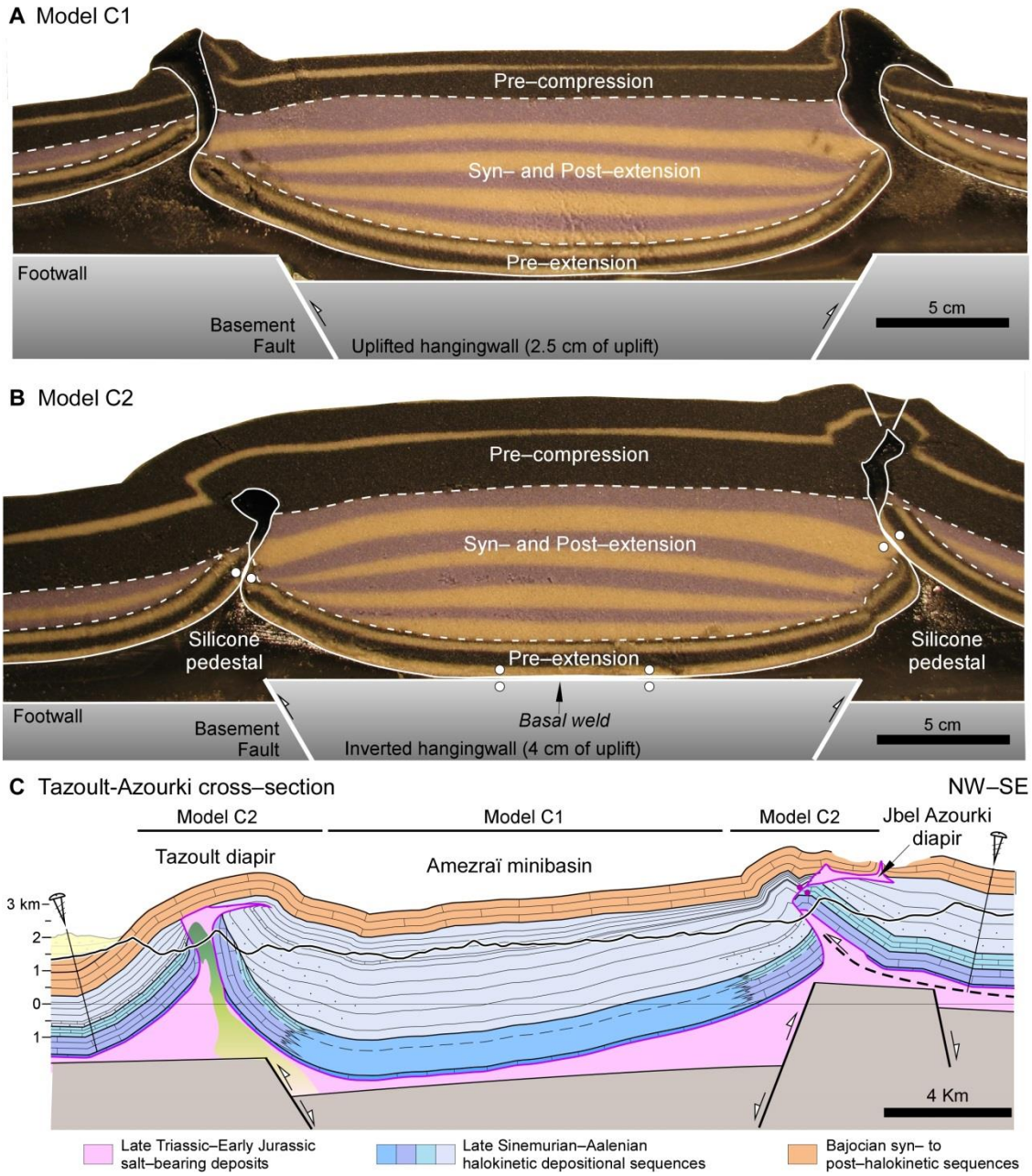

Fig. 5.8. A and B) Sections from models C1 and C2, respectively, showing the main sand units according to the timing of deposition (pre-extension syn- and post–extension, and pre-compression). C) A new proposed cross-section from the Tazoult-Jbel Azourki transect (modified from Martín-Martín, et al., 2016) with diapirs relocated on the footwalls of basement normal faults and black bars on top referring to geometries comparable to the corresponding analogue models. The lateral facies change from the oldest halokinetic depositional sequences represents the transition from shallow-marine (light blue) to deep-marine (dark blue) deposits as recently reported in the Central High Atlas diapiric structures by Joussiaume (2016), Malaval (2016), Martín-Martín et al. (2016), Teixell et al. (2017), and Vergés et al. (2017).

CHAPTER 6

Subsidence analysis and thermal modelling: Geohistory of the Central High Atlas (Morocco)

6. SUBSIDENCE ANALYSIS AND THERMAL MODELLING: GEOHISTORY OF THE CENTRAL HIGH ATLAS (MOROCCO)

6.1. SUBSIDENCE ANALYSIS

6.1.1. DJEBEL BOU DAHAR

As introduced earlier, the well-preserved carbonate platform-top to basin profiles of the Djebel Bou Dahar platform (Fig. 2.6) reveal stratal geometries that undergone relatively little deformation and allowed reconstruction of primary carbonate platform-basin relief (platform slope height from basin floor areas) throughout its evolution (Kenter and Campbell, 1991; Verwer et al., 2009a; Verwer et al., 2009b; Merino-Tomé et al., 2012; Della Porta et al., 2014). Subsidence analysis was performed in two locations: platform top and basin using data presented in Fig. 3.1.

The platform top subsidence curve (Fig. 6.1a) showed two short episodes of subsidence (Early Sinemurian and Late Pliensbachian, respectively), separated by a period of mild uplift during the time in which normal faults were active (Late Sinemurian-Early Pliensbachian). This was followed by a period of quiescence around the end of the Toarcian-Bajocian (i.e. Middle Jurassic). The first subsidence event occurred during Early Sinemurian (deposition of sequences I and II) with a tectonic subsidence rate of 0.03 mm yr^{-1} and total subsidence rate around 0.05 mm yr^{-1}. The second step of subsidence occurred at rates up to 0.04 mm yr^{-1} during the Late Pliensbachian (deposition of sequences V and VI). The total subsidence rates were also low but slightly higher than the tectonic subsidence rates, reaching values up to 0.05 mm yr^{-1} (Fig. 6.1a).

The subsidence curve of the basin area showed a unique subsiding event spanning between the Sinemurian and Pliensbachian periods (~17 Myr), followed by a stage of almost no subsidence during the Toarcian and Aalenian periods (~12 Myr) (Fig. 6.1b). The Sinemurian-Pliensbachian period showed tectonic subsidence rates of 0.03 mm yr^{-1} and the total subsidence was around 0.05 mm yr^{-1}, increasing slightly up to 0.06-0.08 mm yr^{-1} for both tectonic and total subsidence from the Early-Late Sinemurian boundary onwards (Sequence III base), coinciding with the onset of the southwards tectonic rotation of the Djebel Bou Dahar block and renewed extensional fault activity. The close parallel evolution of both tectonic and

total subsidence curves indicated that most of this subsidence was tectonic, as proved by the syndepositional activity of the normal faults bounding the basin (Merino-Tomé et al., 2012) (Fig. 6.1).

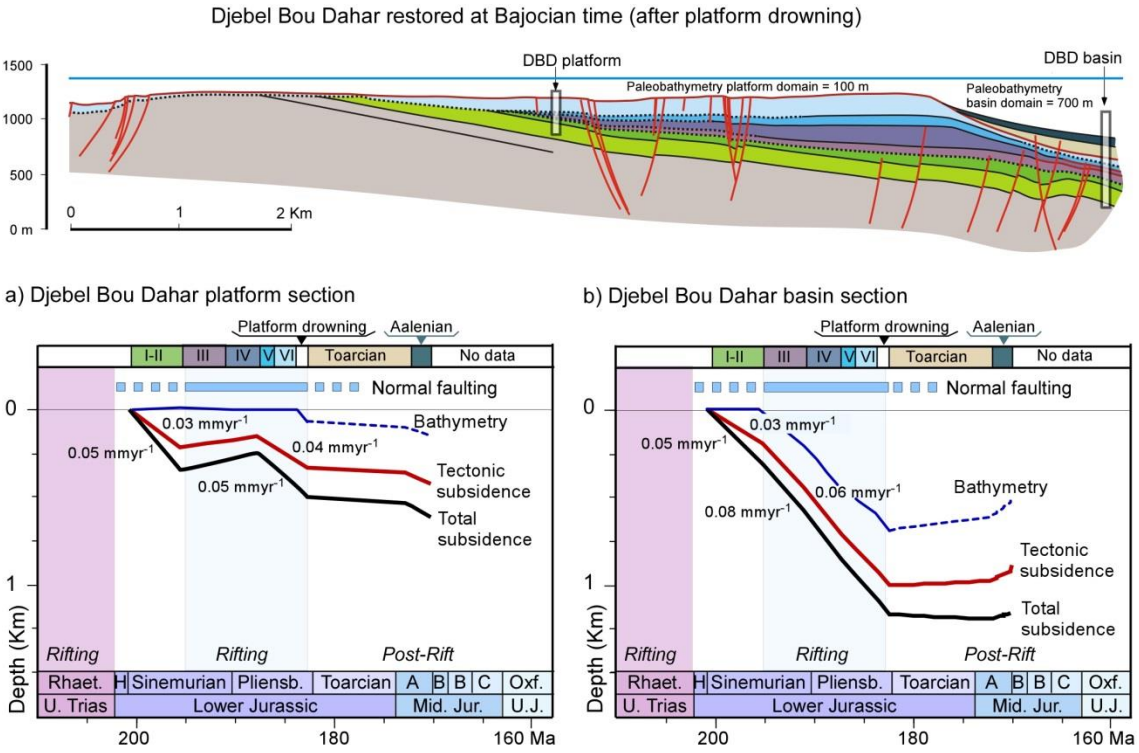

Fig. 6.1. Plots of total and tectonic subsidence curves from Djebel Bou Dahar platform and basin sections (see location in Fig. 2.5). Triassic rifting has not been modelled due to data being unavailable. Stratigraphic units according to logs in Fig. 3.1 projected on top of plots together with age of recorded normal fault activity (Merino-Tomé et al., 2012). The timing of normal faulting is considered in this study as the age range of the Lower Jurassic rifting. Time scale according to Gradstein et al. (2012).

In the platform domain, the subsidence model included the thickness of sequences I and II (Lower Sinemurian), equivalent to those measured in the basin (Fig. 3.1). During the sedimentation of these two units during early Sinemurian times, the first step of subsidence occurred at rates of 0.05 mm yr^{-1}, which showed a uniform distribution across the entire Djebel Bou Dahar platform. A major erosion surface was identified between sequences II and V (Late Sinemurian-Early Pliensbachian), related to the uplift of the footwall of the Djebel Bou Dahar fault block and southward tilt due to the activity of the N-dipping bounding normal fault (Merino-Tomé et al., 2012). As a result of this local erosion, the subsidence curve corresponding to the platform top showed a limited uplift from Late Sinemurian to Early Pliensbachian. This uplift was coeval to the increase in subsidence rates in the basin area. During Toarcian and Aalenian, a ceasing of the subsidence was recorded in the entire area.

The comparison between Djebel Bou Dahar subsidence curves with those presented by Lachkar et al. (2009) and Quiquerez et al. (2013) in the Rich region, about 100 km to the west of the study area (RT label in Fig. 1.1), helped to better constrain the Early Jurassic rift phase along the Fault Domain on the southern border of the Central High Atlas basin. This allowed base line subsidence rates and the timing of rift and post–rift subsidence phases to be established in the absence of diapiric processes. Lachkar et al. (2009) presented three different tectonic subsidence curves from the Rich transect where carbonate platforms developed on top of an extensional system. These subsidence curves correspond to three faulted blocks showing differential subsidence evolution from the margin to the inner part of the basin (Fig. 6.2).

The subsidence curve of the Djebel Bou Dahar platform top was comparable to the Boutazart curve. This latter curve corresponded to the shallower part of the rift basin in the Rich transect. Both, the Djebel Bou Dahar and Boutazart subsidence curves, showed a similar evolution corresponding to platform settings (Fig. 6.2). During the Late Sinemurian and Pliensbachian periods, the Boutazart section records a tectonic quiescence period with tectonic subsidence rates lower than 0.008 mm yr^{-1}, whereas in the Djebel Bou Dahar platform, the top curve shows a period of mild uplift followed by a renewed subsidence stage (0.04 mm yr^{-1}).

Subsidence curves obtained using data from more basinal settings in the Rich transect (Foum Zabel and Guerss curves in Fig. 6.2) also showed trends that are different to the Djebel Bou Dahar basin curve. The Foum Zabel section showed a period of low tectonic subsidence (0.01-0.03 mm yr^{-1}) during the Early Sinemurian, followed by a very high subsiding episode (average rate of 0.50 mm yr^{-1}) from late Sinemurian to the end of Pliensbachian times. The Guerss section (central part of the basin) showed a maximum tectonic subsidence during the Early Sinemurian, with tectonic subsidence rates ranging from 0.17 to 0.77 mm yr^{-1} (Lachkar et al., 2009). Both sections differed from the continuous subsiding curve (0.06 mm yr^{-1}) of the Djebel Bou Dahar basin section, in terms of rates and timing of maximum subsidence. Part of the substantial larger tectonic subsidence rates for the deep marine basins in the Rich transect, compared to the well-constrained Djebel Bou Dahar transect was the consequence of applying significantly larger palaeobathymetric estimations in the former locality (Dupré et al., 2007; Lachkar et al., 2009; Xie and Heller, 2009). The differences between both localities were interpreted as a result of a diachronous activity within a single rifting event occurred from Sinemurian to Pliensbachian times.

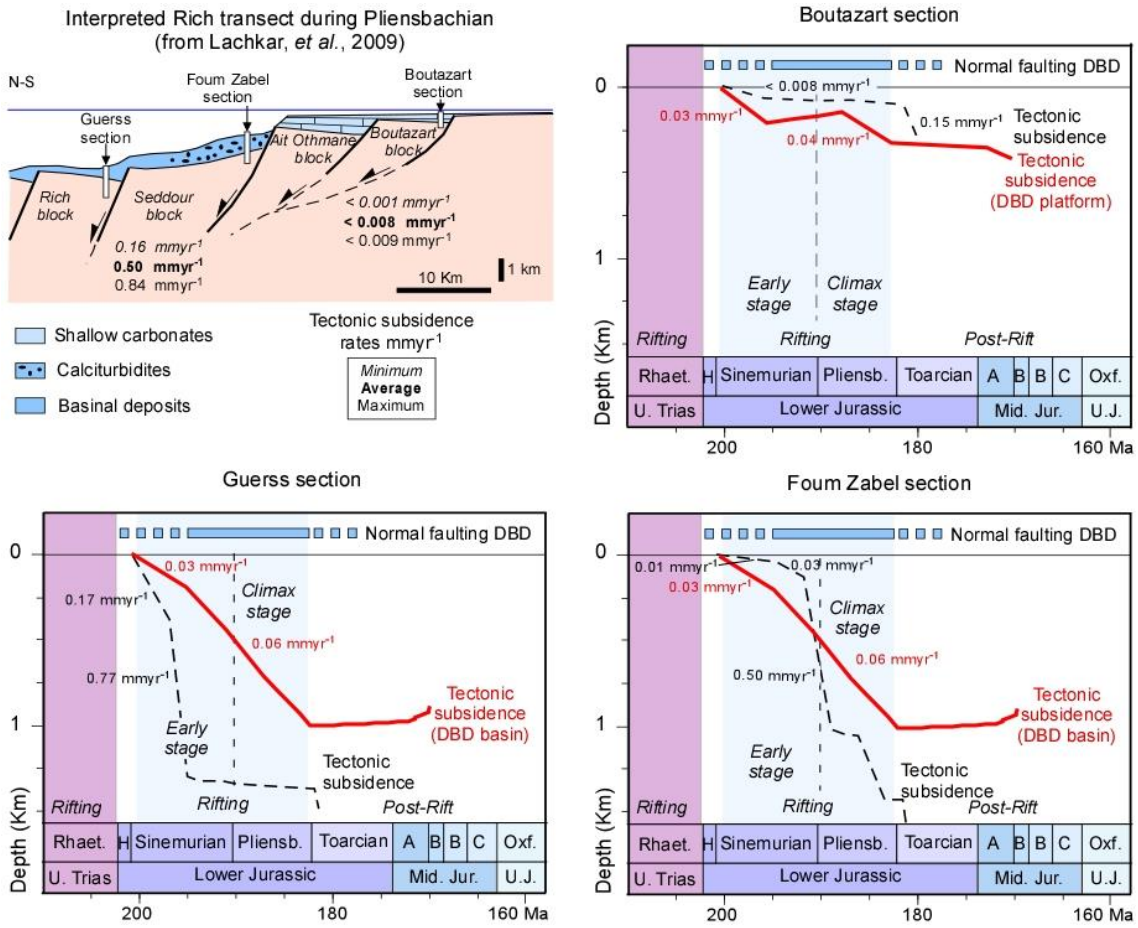

Fig. 6.2. Interpretation of the Rich transect including four different faulted blocks and the location of the three sections used to perform the subsidence analysis in the area (modified from Lachkar et al., 2009); plots show the average tectonic subsidence curve, including subsidence rates, from Boutazart, Foum Zabel and Guerss sections, respectively, and the obtained tectonic subsidence curves from the Djebel Bou Dahar area. Lower Jurassic rifting stages proposed by Lachkar et al. (2009) (early and climax stages) are plotted together with the timing of normal fault activity in Djebel Bou Dahar(Merino-Tomé et al., 2012).

6.1.2. TAZOULT – AMEZRAÏ AREA

The previous section examined the timing and rates of subsidence from the flanks of the High Atlas basin during the Early Jurassic rift phase. This section aimed to establish the subsidence of the southern flank of the Tazoult ridge and the centre of the adjacent Amezraï basin that were located in the unstable domain and thus were impacted by diapiric processes. The presented subsidence curves corresponded to the Tazoult diapir and the Amezraï minibasin section, according to the presented data in Chapter 3 (Fig. 3.3).

The Tazoult ridge and the Amezraï basin subsidence curves both showed a similar trend, but they were different in terms of the rates and amounts of total subsidence (Fig. 6.3). Both sections showed a significant subsidence event from the Sinemurian-Pliensbachian boundary at ~190 Ma to the end of the Aalenian at ~170 Ma, with two rapid periods of subsidence separated by a period of lower subsidence rates during Late Pliensbachian and Toarcian times (Fig. 6.3).

The first tectonic subsidence event that can be constrained in the Tazoult diapir flank occurred in the Early Pliensbachian (deposition of Jbel Choucht and Aganane formations) at rates of 0.15 mm yr^{-1}. From Late Pliensbachian to Toarcian, the subsidence rate decreased to 0.01 mm yr^{-1}, reaching a period of quiescence, lasting for about 4 Myr in the Toarcian-Aalenian transition. This quiet period encompassed the deposition of Tafraout and lowermost Aguerd-n'Tazoult formations in the central part of the basin. The final period of rapid tectonic subsidence occurred from the Aalenian to Bajocian periods, attained rates of 0.27 mm yr^{-1}, and was synchronous with deposition of the upper Aguerd-n'Tazoult and Bin el Ouidane 1 formations (Fig. 3.3 and Fig. 6.3). The total subsidence rates of the same periods are 0.22, 0.09 and 0.74 mm yr^{-1} respectively.

In the Amezraï minibasin, the first constrained Early Pliensbachian tectonic subsidence event occurred at rates of 0.17 mm yr^{-1} (Fig. 6.3). These rates were similar to those reported for the Tazoult diapir (Fig. 6.3). The following two periods, show comparable trend with the Tazoult section, but with higher tectonic subsidence rates of 0.06 mm yr^{-1} and 0.32 mm yr^{-1}, respectively during the late Pliensbachian-Toarcian and Aalenian. Total subsidence rates display the same trend, changing from 0.38 to 0.19 and finally to 0.98 mm yr^{-1}.

The Amezraï basin curve showed very rapid overall subsidence rates up to 0.98 mm yr^{-1} during Early to lowermost Middle Jurassic times, even when using low values of palaeobathymetry. Given the well-documented diapiric structures in this area, the timing of the rift phase obtained from subsidence curves in the Fault domain (Fig. 6.2) and the analysis of analogue models presented in the previous section, the Pliensbachian fast subsidence event was interpreted to be related to a combination of both normal faulting and diapiric salt withdrawal from the basin centre. Major differences between Tazoult and Amezraï subsidence curves occurred during Late Pliensbachian times, when the rapid deposition of the mixed carbonate-clastic Amezraï Formation occurred in the basin centre. It was the deposition of this unit that appears to have triggered the development of allochthonous salt sheets in both Tazoult and Jbel Azourki salt walls (Joussiaume et al., 2014; Saura et al., 2014; Malaval, 2016;

Martín-Martín et al., 2016). Thus, the continuous high subsidence recorded in the Amezraï basin subsidence from Latest Pliensbachian onwards would be mainly caused by salt withdrawal. Finally, in the Tazoult–Amezraï area, the facies and bathymetry estimation were considered constant throughout the entire area. Assuming deeper facies in the central part of the Amezraï basin and consequently deeper water depth values, the subsidence in the Amezraï basin would be higher than the present reported as well as the difference between the Tazoult flank and the basin centre would be enhanced.

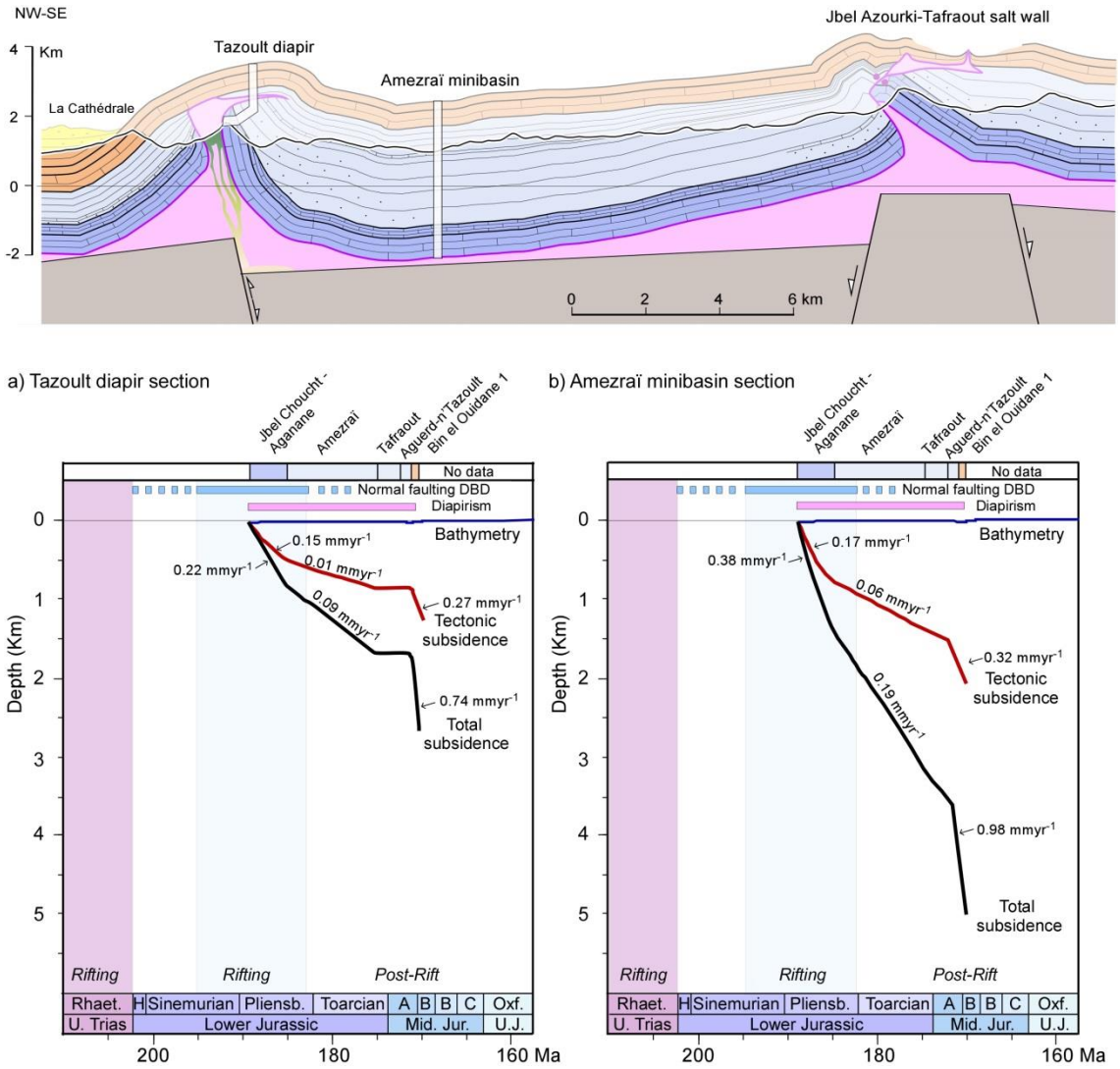

Fig. 6.3. Plots of total and tectonic subsidence curves from Tazoult diapir (a) and Amezraï minibasin (b) sections (see location in Fig. 3.3). Triassic and very early Lower Jurassic subsidence evolution is not modelled due to the lack of data. Stratigraphic units according to logs in Fig. 3.3 projected on top of plots. Time scale according to Gradstein et al. (2012).

6.1.3. IMILCHIL DIAPIRIC PROVINCE

The presented tectonic and total subsidence curves from the Imilchil diapiric province corresponded to two different stratigraphic logs (west and east) from the three adjoining minibasins described in the studied area: Ikassene, Lake Plateau and Ikkou (see location in Fig. 2.9 and Fig. 2.10). In the Imilchil diapiric province, ages of the outcropping sedimentary units ranged from Toarcian to Callovian, younger than the end of the rifting phase established in the Fault domain. Thus, although a longer rifting phase cannot be ruled out, the subsidence curves and maps from the Imilchil diapiric province would be roughly representative of the post–rift stage.

The subsidence curves obtained from the west and east Ikassene minibasin (Fig. 6.4a and b) showed a similar tectonic and total subsidence rate, 0.08-0.10 and 0.20-0.22 mm yr^{-1} respectively, during Toarcian times (183 to 172.5 Ma, deposition of the Agoudime I Fm.). These rates were constant in the western part of the basin up to the end of the Aalenian (top of Agoudime II Fm). Contrarily, in the eastern part of the basin (Fig. 6.4b) the tectonic and total subsidence rates increased from 0.08 to 0.10 and 0.22 to 0.34 mm yr^{-1} respectively. For Bajocian times, subsidence rates were only calculated in the west Ikassene minibasin, where Bin el Ouidane 3 Fm. is preserved. According to the models, during the deposition of this formation the tectonic and total subsidence rates decreased up to 0.03 and 0.09 mm yr^{-1} respectively.

In the Lake Plateau minibasin, the subsidence curves from west and east sectors showed similar trends up to the end of Bajocian. Toarcian to Aalenian period (183 to 170.2 Ma), corresponding to the deposition of deep marine deposits of the Agoudime I and II Fm., was characterized by tectonic subsidence rates of 0.08 mm yr^{-1} (in the west) and 0.06 mm yr^{-1} (in the east), whereas the total subsidence was 0.18 and 0.15 mm yr^{-1} in the west and east respectively (Fig. 6.4a and b). During the Bajocian (170.2 to 168.5 Ma), the subsidence was faster than in the previous times but rates in the west and east Lake Plateau minibasin were similar, about 0.12 and 0.10 mm yr^{-1} (tectonic subsidence rates) and 0.30 and 0.25 mm yr^{-1} (total subsidence rates).

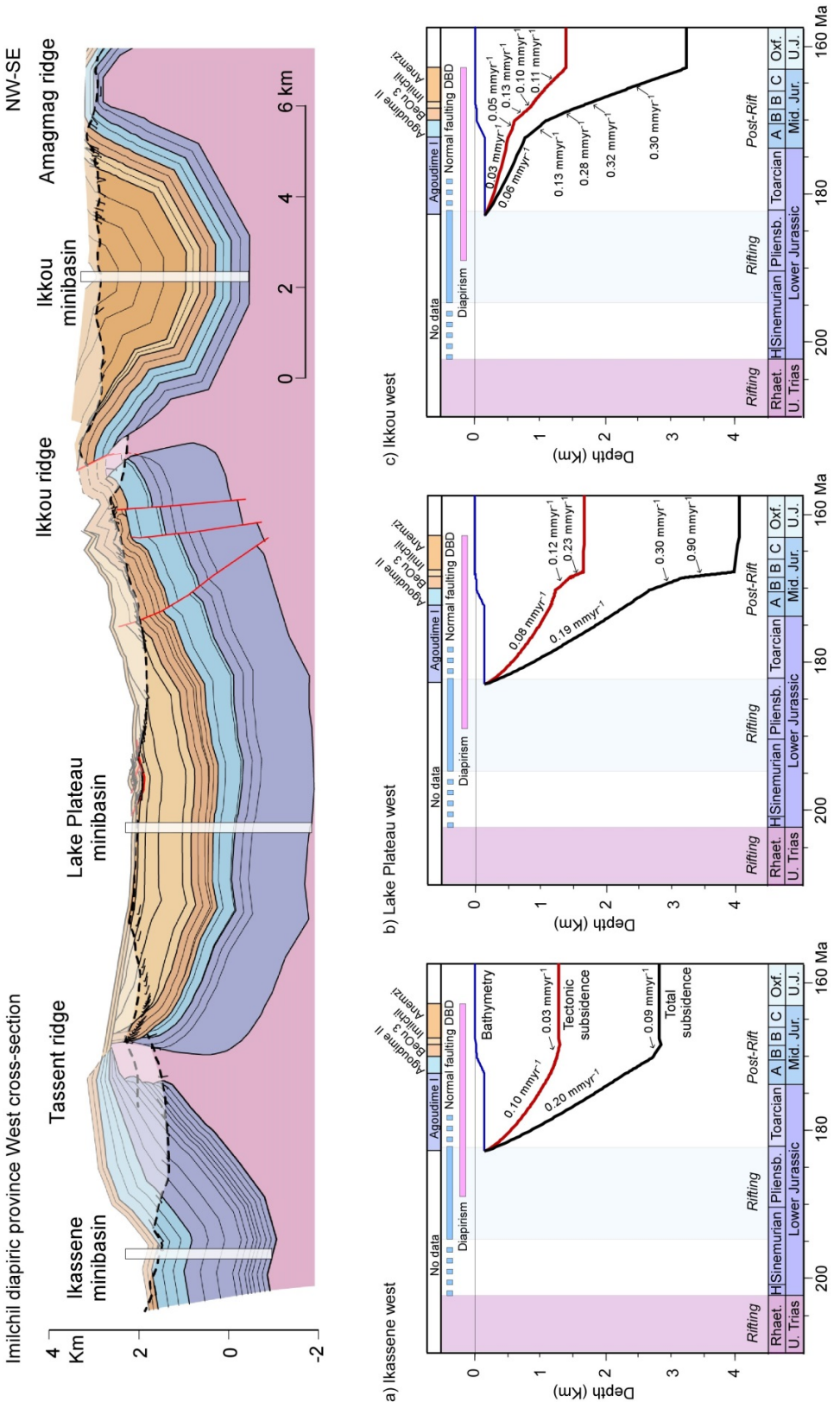

Fig. 6.4. (Continued in following page) West cross-section of Imilchil diapiric province showing the location of the logs used for subsidence analysis of Ikassene west (a), Lake Plateau west (b) and Ikkou west (c). Next page East cross-section of Imilchil diapiric province showing the location of the logs used for subsidence analysis of Ikassene east (d), Lake Plateau east (e) and Ikkou east (f). Time scale according to Gradstein et al. (2012).

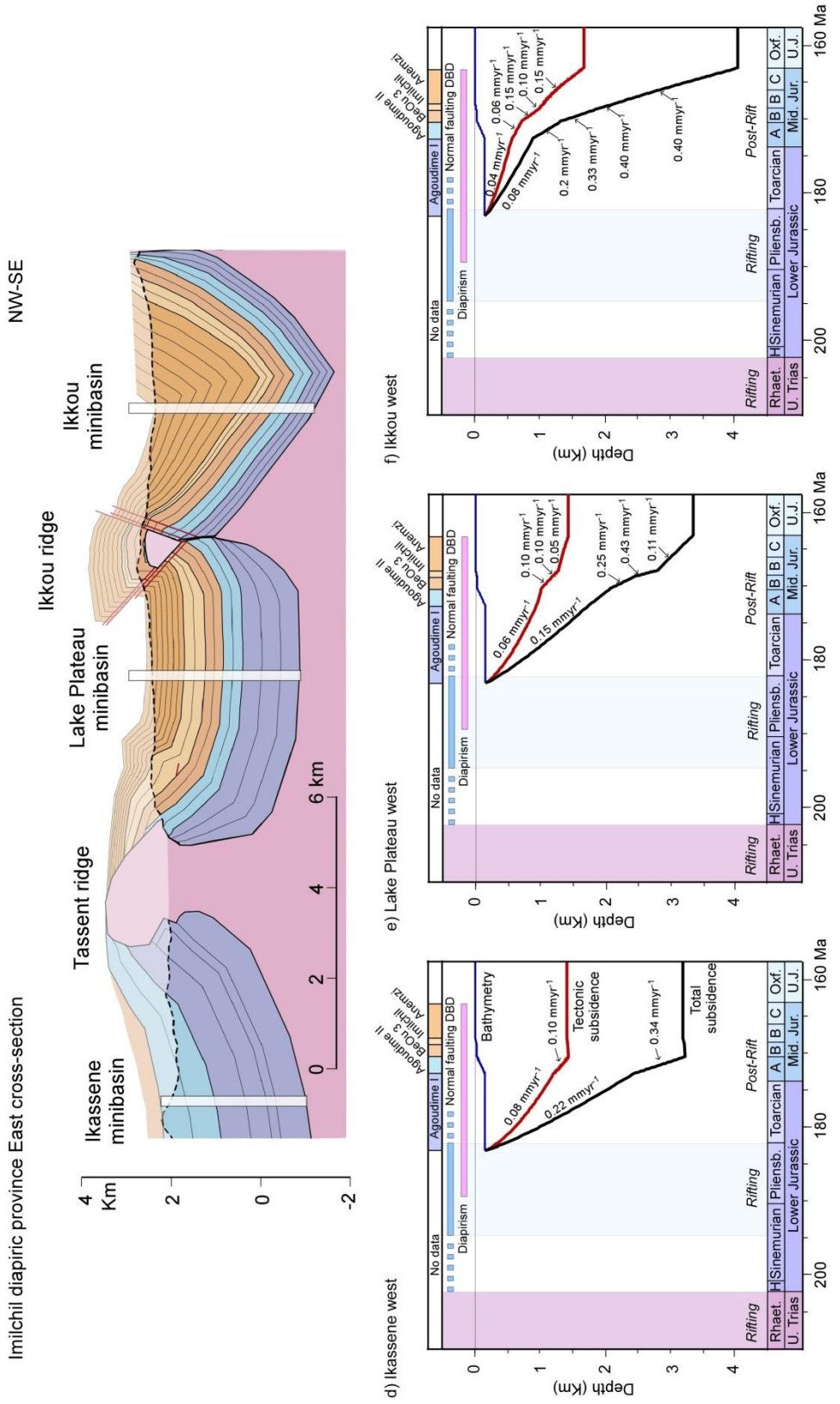

Fig. 6.4. Continued

During the Bathonian there was a different subsidence evolution regarding western and eastern part of the minibasin. In the west part of the Lake Plateau, an increase of subsidence rates was record with tectonic subsidence rate (0.23 mm yr^{-1}) two times higher than in the Bajocian whereas the total subsidence (0.90 mm yr^{-1}) was three times faster. Contrarily, in the east part of the minibasin the tectonic subsidence remained at rate of 0.10 mm yr^{-1} and the total subsidence was around 0.43 mm yr^{-1}. Finally, during the Late Bathonian – Callovian times, deposition of the continental Anemzi/Guettioua Fm., the west part of the Lake Plateau showed an abrupt ceasing of subsidence (forced by the model due to the thin Anemzi/Guettioua Fm. preserved in this part of the minibasin). Contrarily, the subsidence in the eastern part remained but with lower rates than in the previous times; 0.05 mm yr^{-1} of tectonic subsidence and 0.11 mm yr^{-1} of total subsidence (Fig. 6.4d).

In the Ikkou minibasin (Fig. 6.4e and f), the west and east subsidence curves showed a similar trend, but they were different in terms of the rates and amounts of total subsidence. Both plots showed a roughly increasing trend of the subsidence velocity but two clear stages were differentiated. The first stage was from Toarcian to Aalenian (183 to 170.2 Ma); when the tectonic subsidence rates were lower than 0.06 mm yr^{-1}. In the second stage, from Bajocian to Callovian (170.2 to 163 Ma), the tectonic subsidence was two times faster than the first stage, with rate higher than 0.10 mm yr^{-1}. In terms of total subsidence, the calculated rates in the western part of the Ikkou minibasin were lower than in the east. In the Ikkou west curve, the total subsidence rates changed progressively from 0.06 mm yr^{-1} during the Toarcian up to 0.3 mm yr^{-1} during the Late Bathonian-Callovian, whereas in the east Ikkou curve the rates varied from 0.08 mm yr^{-1} to 0.4 mm yr^{-1}.

Comparing the different curves obtained from the subsidence analysis, there were differences between the three minibasins but also within the same minibasin (Fig. 6.5). The maximum tectonic and total subsidence rates in the Ikassene minibasin were reached during the Aalenian (during the deposition of the Agoudime II Fm.). Contrarily, in the Lake Plateau the faster subsidence occurred during the deposition of the Imilchil Fm., during the Early Bathonian. However, this subsidence was not homogeneous and the western part of the basin subsided two times faster than the eastern part (Fig. 6.5). In the Ikkou minibasin, the maximum tectonic rate was reached during the Bajocian (Bin el Ouidane 3 Fm.), but with a very similar values than the reached during the late Bathonian-Callovian period (Anemzi/Guettioua Fm.). Contrarily, the faster total subsidence occurred from the Early

Bathonian to Callovian times (Imilchil and Anemzi/Guettioua Fm.), with highest rates recorded in the eastern part (Fig. 6.5).

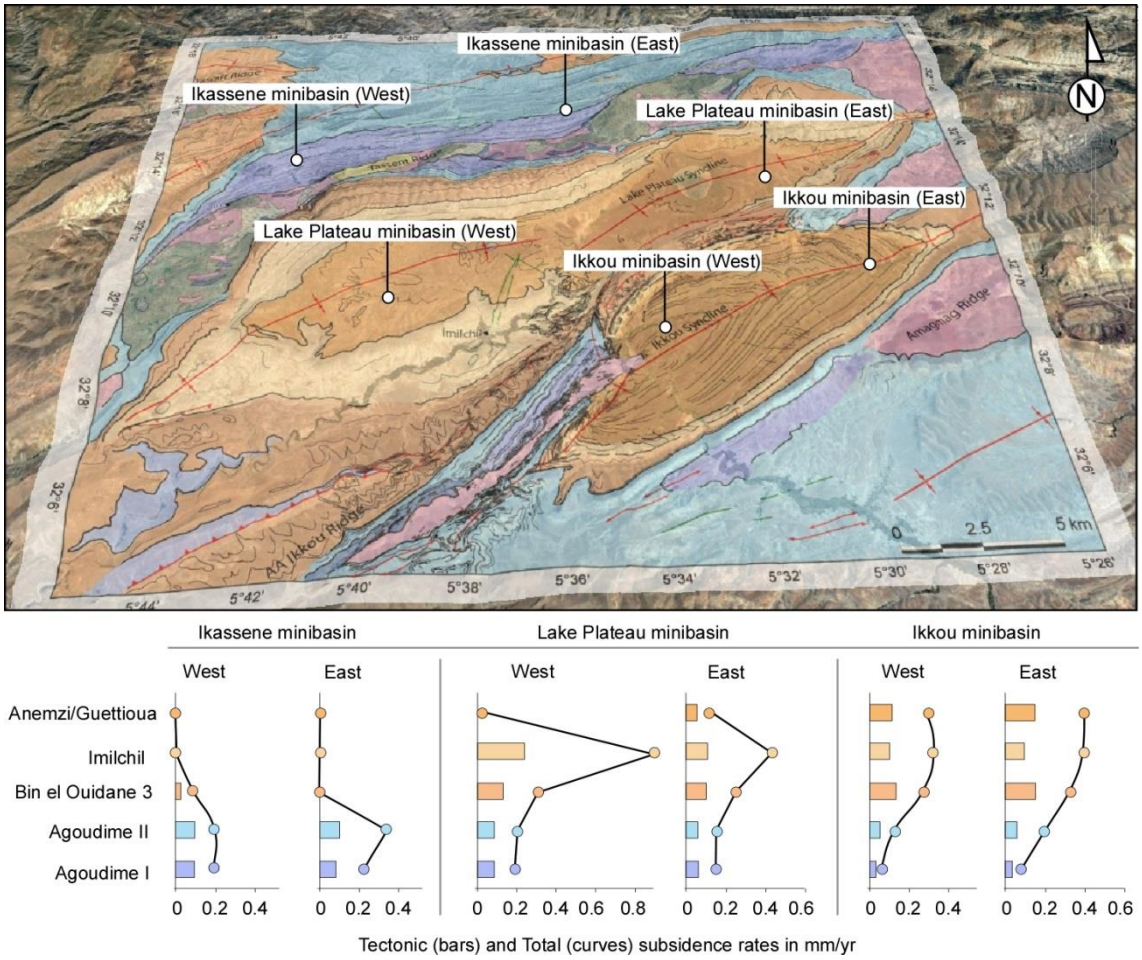

Fig. 6.5. Geological map of the Imilchil diapiric province (GDL, 2011) on Google Earth image showing the location of the stratigraphic logs used for the subsidence analysis. Plots show the tectonic and total subsidence rates (in mm yr^{-1}) obtained for each sedimentary unit. Tectonic subsidence rate are represented using coloured bars and total subsidence rates are represented using coloured dots. Colours are the same than the used in the geological map.

Maps corresponding to Toarcian and Early Aalenian times (183.0—172.5 Ma, Agoudime I Fm. deposition) show that the most subsidising minibasin was the Ikassene minibasin that reached maximum subsidence up to 1600 m with rates up to 0.18 mm yr^{-1} (Fig. 6.6), similar rates than the obtained from the Ikassene West and East 1D subsidence curves (0.20-0.22 mm yr^{-1}). The western sector of the Lake Plateau minibasin also subsided similarly (mean rate of 0.14 mm yr^{-1}) whereas the eastern sector records lower subsidence velocities (not higher than 0.1 mm yr^{-1}). The values of the eastern sector were slightly lower than the obtained in the 1D model of the Lake Plateau east curve (0.15 mm yr^{-1}). In the Ikkou minibasin the subsidence is

limited in both west and east sectors, with total subsidence not higher 700 m and total subsidence below 0.08 mm yr^{-1}.

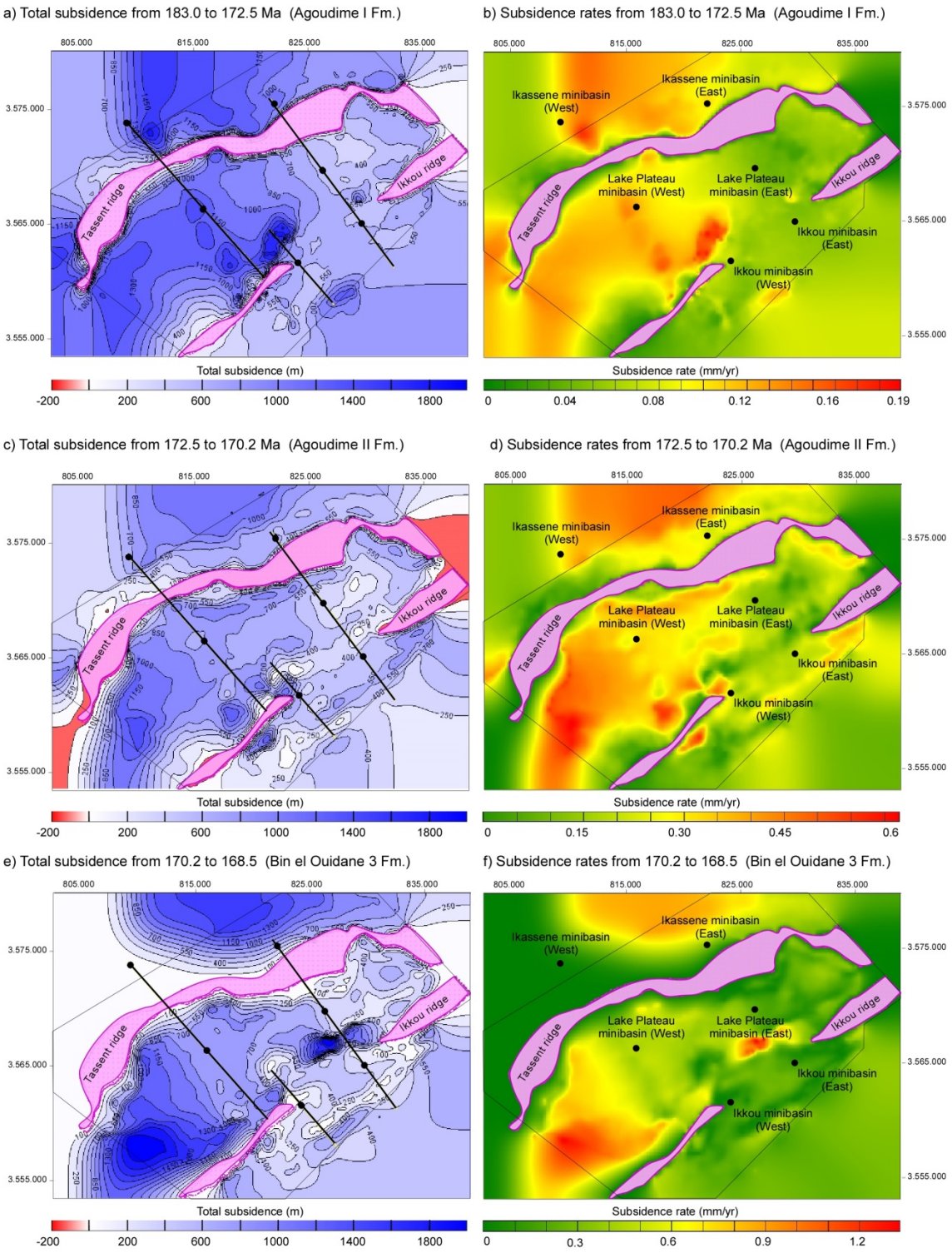

Fig. 6.6. Figure continued in following page (including figure caption)

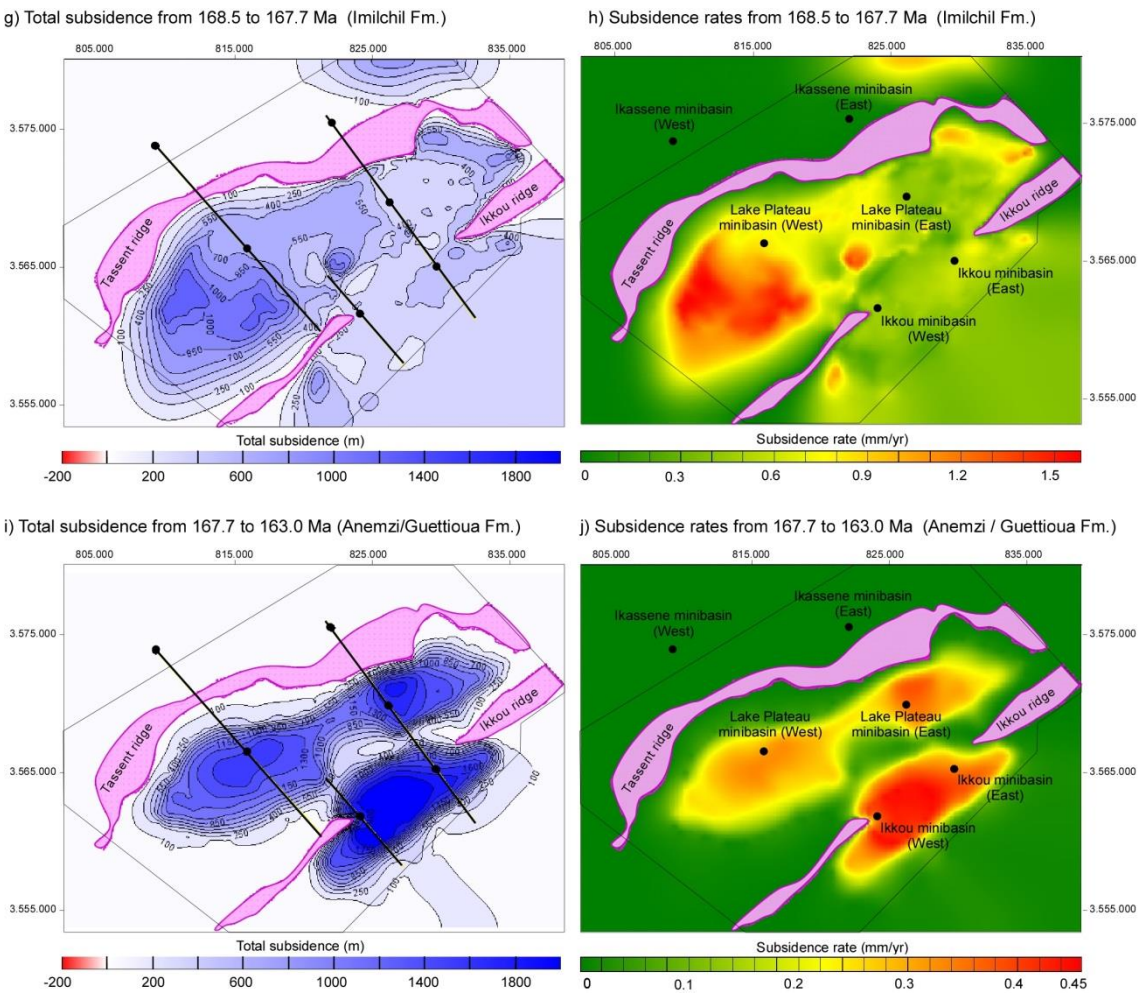

Fig. 6.6. a) to j) (Continued in following page) Total subsidence maps (left side images) and total subsidence rate maps (right-side images) for each sedimentary unit in the Imilchil diapiric province, colour scales are different for each map. The pink areas correspond to the present day diapiric ridges, the black dots show the location of the stratigraphic logs used to build the 1D subsidence curves (Fig. 6.4) and thin black boxes mark the area covered by the thickness values presented in Fig. 3.6. Total subsidence maps incorporate contour lines of 150m and the location of the structural cross–sections presented in Fig. 2.9.

From Bajocian times (170.2 to 168.5 Ma; deposition of Bin el Ouidane Fm.), the sedimentary record in the Ikassene minibasin was limited and there was no younger deposits outcropping. Thus, total subsidence and total subsidence rates for this time and for younger ages were not considered in the Ikassene minibasin. Concerning the Lake Plateau minibasin, the subsidence was faster than in the previous times with total subsidence ranging from 0.2 to 0.6 mm yr^{-1}, with faster subsidence recorded in the western part of the minibasin. The increasing trend compared to the previous stage was also observed in the 1D subsidence curves. In the Ikkou minibasin, the subsidence rate during this step was around 0.15—0.3 mm yr^{-1}, showing a constant subsidence from the deposition of the previous sedimentary unit. From 168.5 to 167.7 Ma, deposition of Imilchil Fm. during Bathonian, the subsidence rates were the highest

obtained in the Lake Plateau minibasin. The maximum subsidence velocity was recorded in the western part of the minibasin (up to 1.5 mm yr^{-1}), reaching values three times higher than the eastern sector (values around 0.5 mm yr-1). The Ikkou minibasin still subsided at slightly higher rates than the previous stage (around 0.45 mm yr^{-1}).

The most outstanding change was observed between the Bajocian (168.5-167.7 Ma) and the Callovian (167.7-163.0 Ma) maps (Fig. 6.6d and f). A shift of the maximum subsidence velocity was recorded in the Lake Plateau minibasin. At this stage, the faster subsidence was recorded in the eastern part with rates around 0.35 mm yr^{-1}, whereas the western part displayed an abrupt deceleration of the subsidence decreasing from the previous 1.5 mm yr^{-1} to 0.3 mm yr^{-1}. Contrarily, the Ikkou minibasin recorded the highest subsidence rates at this stage with velocities up to 0.45 mm yr^{-1}.

Comparing the different maps obtained from the subsidence analysis, the results record the same trend obtained from the 1D subsidence curves. The maximum total subsidence rate in the Ikassene minibasin was reached during the Aalenian (during the deposition of the Agoudime II Fm.). Contrarily, in the Lake Plateau the faster subsidence occurred during the deposition of the Imilchil Fm., during the Early Bathonian (168.5-167.7 Ma). However, this was not homogeneous and in the western part of the basin total subsidence rates were up to three times higher than the rates obtained in the east. In the Ikkou minibasin, the faster total subsidence occurred from the Early Bathonian to Callovian times (Imilchil and Anemzi/Guettioua Fm.).

The aforementioned subsidence occurred during the post–rift stage of the Jurassic rift basin mainly record the deposition and subsidence evolution during diapir phases coetaneous to thermal subsidence and without the influence of extension. Together with subsidence rates higher than rates reported in the faulted domain, a migration of the subsidence peaks through time was recorded from one minibasin to another and within the same minibasin (Fig. 6.5 and Fig. 6.6). This migration can be associated to complex salt withdrawal patterns linked to a differential loading on top of the evaporite-bearing deposits, source of the diapirs in the studied area, as it has been observed in the results of analogue modelling. The shift of the subsiding depocentres observed in the Imilchil diapiric province is similar to those reported in other diapiric provinces as in the Gulf of Mexico, where Barton et al. (1933) detected a migration of subsidence anomalies basinward in agreement with prograding sedimentation. From the same studied area, and similarly than in the Imilchil diapiric province, Diegel et al. (1995) show three calculated subsidence curves with diachronous subsidence anomalies

interpreted to be related to diachronous salt withdrawal pattern. In the Central North Sea, also differential subsidence due to prograding systems were described by Stewart and Clark (1999). In the Utsira High (northern North Sea) Jackson et al. (2010) point to a clear interaction between sedimentation and salt withdrawal as a predominant mechanism for the heterogeneous subsidence and complex basin architecture during the evolution of Jurassic minibasins in the area. Together with the sediment loading, in all these basins the shifting of depocenters and the related subsidence anomalies were also ruled by the grounding of the minibasins when the underlying salt is completely withdrawn (Worral and Snelson, 1989; Jackson and Talbot, 1994; Stewart and Clark, 1999).

6.1.4. COMPOSITE SUBSIDENCE CURVE FROM THE UNSTABLE DOMAIN

The lack of a continuous Early to Middle Jurassic succession in the unstable domain, prevented from calculating a continuous subsidence history for a single locality. Therefore, in order to obtain a first approach of the complete subsidence history in the unstable domain, a composite subsidence curve was constructed using the subsidence curves from Djebel Bou Dahar basin, Amezraï minibasin and Ikkou east minibasin curves (Fig. 6.7).

In the composite curve, the onset of extension was characterised by low subsidence rate followed by an abrupt change in the subsidence trend caused by the coeval rift climax extension and the onset of diapiric activity (Fig. 6.7). Quantification of fault activity and salt withdrawal during the Lower Jurassic subsidence phase, however, was not straightforward due to the lack of outcrops for estimating the thickness variation of the ductile evaporite-bearing unit. Nevertheless, the high tectonic and total subsidence rates in the Amezraï basin (up to 0.32 and 0.98 mm yr^{-1}, respectively) and in the Ikkou minibasin east, the Lake Plateau west and other minibasins from the Imilchil area (up to 0.23 and 0.9 mm yr^{-1}, respectively), compared to purely extensional tectonics recorded in the Djebel Bou Dahar or other areas of the basin margin, strongly suggest a salt tectonics control, as was reported in other salt basins worldwide (Wilson et al., 1989; Hodgson et al., 1992; Dupré et al., 2007; Hudec et al., 2009). In this scenario, the active interaction between sedimentation and salt movement, as it was proved in the presented analogue models (Chapter 5), would lead to cyclic acceleration of local sedimentation rates, salt withdrawal and creation of accommodation, resulting in the observed increase in the subsidence rate. Similar results were obtained in the Lusitanian basin (Portugal) where, based on seismic interpretation and well data, Wilson (1988) detected a

clear difference between salt-related and extensional subsidence pattern. This author compared the Bombarral sub-basin, flanked by diapiric structures, and the Arruda and Turcifal sub-basins, developed as half-graben structures. The salt-related Bombarral sub-basin subsides largely due to salt withdrawal whereas the subsidence in non-salt-related basins is more restricted.

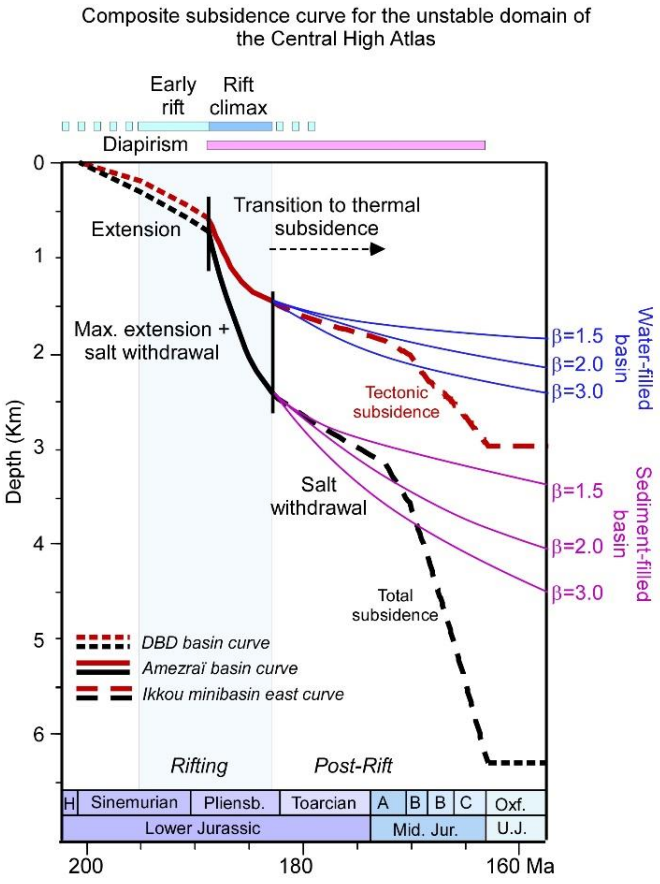

Fig. 6.7. Composite subsidence curve for the unstable domain of the Central High Atlas. Blue and pink curves correspond to calculated thermal subsidence curves associated to a variety of stretching factors (β) for a specific crust and lithosphere thicknesses (31.2 and 125 km respectively). The curves are redrawn from Allen and Allen (2005), modified from McKenzie (1978) and Sclater et al. (1980).

In the composite subsidence curve of the Central High Atlas unstable domain, a decrease in the subsidence rate marked the transition from rifting phase to post–rift phase (Fig. 6.7). The post–rift phase of an extensional basin is characterized by the thermal subsidence, which is the isostatic response of the cooling of the lithosphere after a crustal extension episode that caused an asthenospheric upwelling beneath the extended area (Angevine et al., 1989). The simple stretching model developed by McKenzie (1978), allow theoretical subsidence curves during the thermal subsidence to be calculated for a variety of stretching factors (β in Fig. 6.7). Although it was a roughly comparison, the obtained composite subsidence curve from the unstable domain of the Central High Atlas included an anomalous episode of accelerated

subsidence with respect to the expected thermal model curves based on McKenzie's model. This anomalous subsidence event would be linked to the additional subsidence created due to salt withdrawal from beneath the Ikkou minibasin east. Other minibasins from the Imilchil diapiric province also showed increasing subsidence phases in the different 1D subsidence models (Fig. 6.4 and Fig. 6.5) and modelled subsidence maps (Fig. 6.6) during the post–rift stage, differing from the expected thermal subsidence patterns. In the Gulf of Mexico, Diegel et al. (1995) also compared calculated subsidence curves obtained from Southern Louisiana onshore with theoretical thermal subsidence curve from McKenzie's model. As in the case of the Central High Atlas unstable domain (Fig. 6.7), these authors detected an anomalous subsidence event during the thermal subsidence phase, consisting of a sharp change on the tectonic subsidence curve with accelerated subsidence rates in the Miocene. This anomalous subsidence phase was interpreted as salt-related subsidence due to salt withdrawal. Similar results although without a quantified amount of subsidence anomaly was proposed in the North Sea by Hodgson et al. (1992), who report an anomalous enhance of the expected Cretaceous thermal subsidence due to halokinesis in the region of salt-related basins.

6.2. THERMAL MODELLING

To ascertain the post–Middle Jurassic geological history of the study region was not straightforward due to the general scarcity of sedimentary record in the Central High Atlas, where there are two contrasting proposed scenarios for the post–Middle Jurassic evolution.

Firstly, scattered synclines from the external parts of the Atlas (Ouaouizaght, Iouaridène and Aghzif-Nadour synclines in Fig. 6.8a) showed concordant thin and probably condensed Upper Jurassic-Lower Cretaceous red beds successions with thickness up to 1800 m (Ellouz et al., 2003; Haddoumi et al., 2010). Apatite fission track dating along the Imilchil transect (Fig. 6.8b) indicates more than 1.5 km of sedimentary burial after the emplacement of the Middle-Late Jurassic volcanic intrusions, which seems to corroborate this alternative (Barbero et al., 2007). However, the Anoual and Aït Attab synclines showed a sedimentary succession punctuated with unconformities or periods of potential non-deposition (sedimentary hiatus), which were diachronous through synclines (Haddoumi et al., 1998; Haddoumi et al., 2008). Oxfordian—Kimmeridgian and Valanginian—Barremian in the Anoual syncline, and Bajocian—Barremian in the Aït Attab.

In contrast, a second interpretation involving vertical motions of the West Moroccan Arch and extending eastward within the Central High Atlas during Upper Jurassic and Lower Cretaceous times was postulated by Frizon de Lamotte et al. (2009). This large-scale thermal doming was recorded in Paleozoic samples focus of thermochronological studies (Fig. 6.8b) from the surrounding Moroccan Meseta and the Anti-Atlas (Ghorbal et al., 2008; Missenard et al., 2008; Balestrieri et al., 2009; Saddiqi et al., 2009; Ruiz et al., 2011; Domènech, 2015). Local sedimentary hiatus, like the ones described in some syncline bordering the Central High Atlas, were used by these authors to reinforce Late Jurassic-Early Cretaceous widespread uplift interpretation

In this section, the undetermined parameters of geohistory in the studied area (palaeo heat flow and additional sedimentation) were constricted using the vitrinite reflectance data for the two aforementioned proposed post–Middle Jurassic scenarios applied to the Amezraï minibasin stratigraphic log (Fig. 6.8c); 1) Thermal models with continuous sedimentation during Upper Jurassic and Lower Cretaceous times and 2) Thermal models considering Late Jurassic-Early Cretaceous exhumation in the Central High Atlas. These scenarios provided two end-members for the post–Middle Jurassic unconstrained evolution of the Tazoult–Amezraï

area. All models include alpine inversion of the Central High Atlas divided in two steps, from 80 to 35 Ma (35% uplift and erosion) and from 35 to 0 Ma (65% of uplift and erosion), based on published works about Central High Atlas inversion (Fraissinet et al., 1988; Görler et al., 1988; Teixell et al., 2005; Tesón and Teixell, 2008; Tesón et al., 2010).

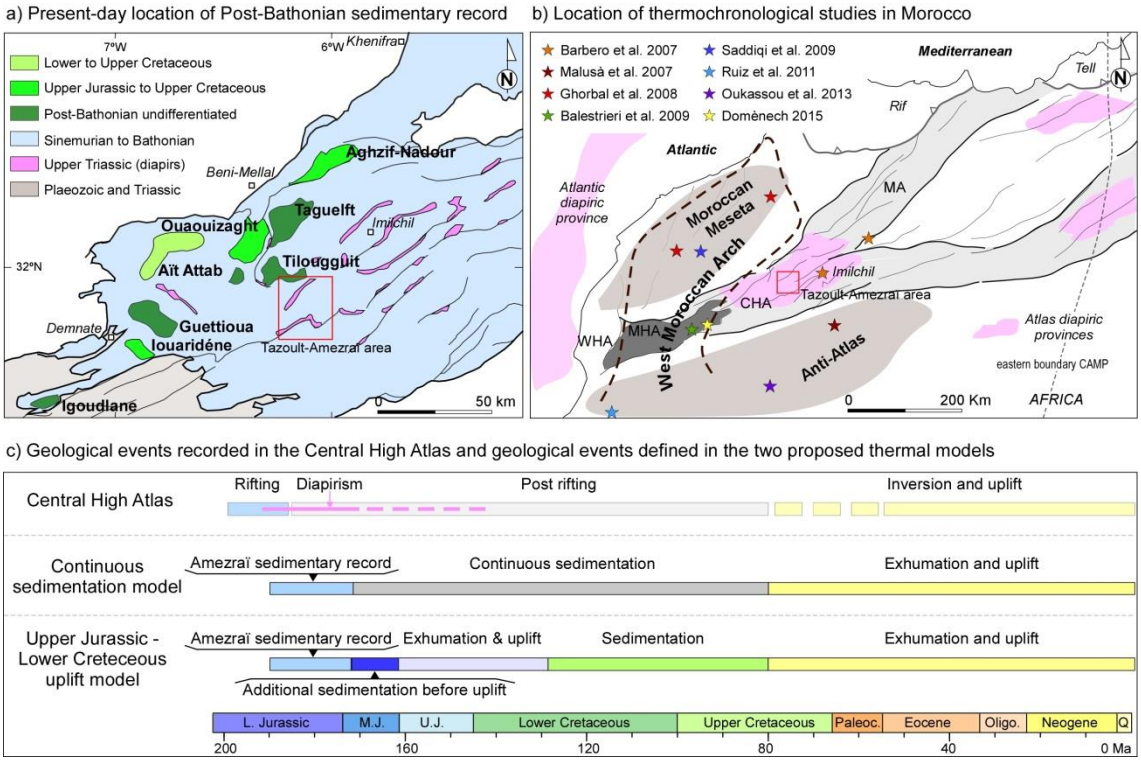

Fig. 6.8. a) Simplified geological map showing the location of synclines filled by post–Bathonian deposits (Modified from Haddoumi et al., 2010). b) Sketch map (Modified from Saura et al. 2014) showing the Moroccan Atlas system. Star symbols indicate the location of published thermochronological studies. Thick discontinuous line shows the boundary of the West Moroccan Arch from Frizon de Lamotte et al. (2009). c) Diagram showing geological events from the Central High Atlas regional and the detailed geological events defined for each proposed thermal model.

6.2.1. THERMAL MODELS CONSIDERING LATE JURASSIC AND EARLY CRETACEOUS CONTINUOUS SEDIMENTATION

As it was shown in the Method chapter, Fig. 4.4, the subroutine 1 of the thermal model was based on the present day sedimentary succession data and the thermal parameters (heat flow values), which are assumed and need to be evaluated.

The thermal history of the studied area was divided in two events; a high heat flow event and a low heat flow event each of them with a specific heat flow value. Additionally, three different durations of the high heat flow event were considered. A first scenario where the high heat flow event was short and restricted to the duration of the rifting phase (189 to 182.7

Ma; according to the normal faulting age established in Djebel Bou Dahar platform), a second scenario where the event was long and spans up to 140 Ma and a third scenario with a maximized duration of the event up to 110 Ma. In the two last scenarios, the high heat flow event was not only considering the rifting, but also the post–rift period. They are based on geological record of continuous magmatic intrusions up to the Early Cretaceous (140 Ma) and the emplacement of volcanic and subvolcanic rocks within the Central High Atlas crustal levels about 110 Ma (Frizon de Lamotte et al., 2008; Charrière et al., 2011; Michard et al., 2011), thus, potentially high heat flow needed to be considered up to these ages.

The low heat flow event was set at 60 mW/m^2 in agreement with thermal models and present-day heat flow regional data in the Central High Atlas (Rimi et al., 2005; Zeyen et al., 2005). However, heat flow during rifting was more complex to define and only was possible to put certain limits to try to constrain the observed data. For these reason three heat flow values were selected to be applied during the high heat flow event: 1) heat flow of 70 mW/m^2 according to thermal models of Sachse et al. (2012) in the Middle Atlas; 2) 105 mW/m^2) according to the higher value compiled in rifted basins (Allen and Allen, 2005), as well as to the mean value of heat flow calculated in the eastern arm of the East African Rift System, dominated by volcanic activity (Morgan, 1983) and 3) 120 mW/m^2 based on the highest value in basins with deep lithosphere involvement (Allen and Allen, 2005).

Thus, to sum up, the starting point of the modelling process were three thermal histories (short, long and maximized duration of the high heat flow event) characterized by three heat flow values for the high heat flow event (70, 105 and 120 mW/m^2) and one heat flow value for the low heat flow event (60 mW/m^2), resulting 9 different models to be evaluated using the Subroutine 1 of the modelling method (Fig. 4.4).

In models with a short high heat flow event, the calculated vitrinite reflectance curves from different heat flow values showed similar trend for vitrinite reflectance lower than 0.5%, but they diverge together with the increasing of the vitrinite reflectance (Fig. 6.9a). For the three applied heat flows (70, 105 and 120 mW/m^2) a reflectance of 0.5% was obtained between 600 and 700 m, with a minor difference of the required depth to reach the same degree of maturation (i.e. 100 m). Contrarily, a reflectance of 2.5% was obtained at depth of 3 km with a high heat flow of 120 mW/m^2 whereas more than 4 km were required applying 70 mW/m^2 (Fig. 6.9a). The highest difference between calculated reflectance curves was observed between heat flow of 70 and 105 mW/m^2 and between 70 and 120 mW/m^2. The difference between models of 105 and 120 mW/m^2 was lower (see bar plot in Fig. 6.9a).

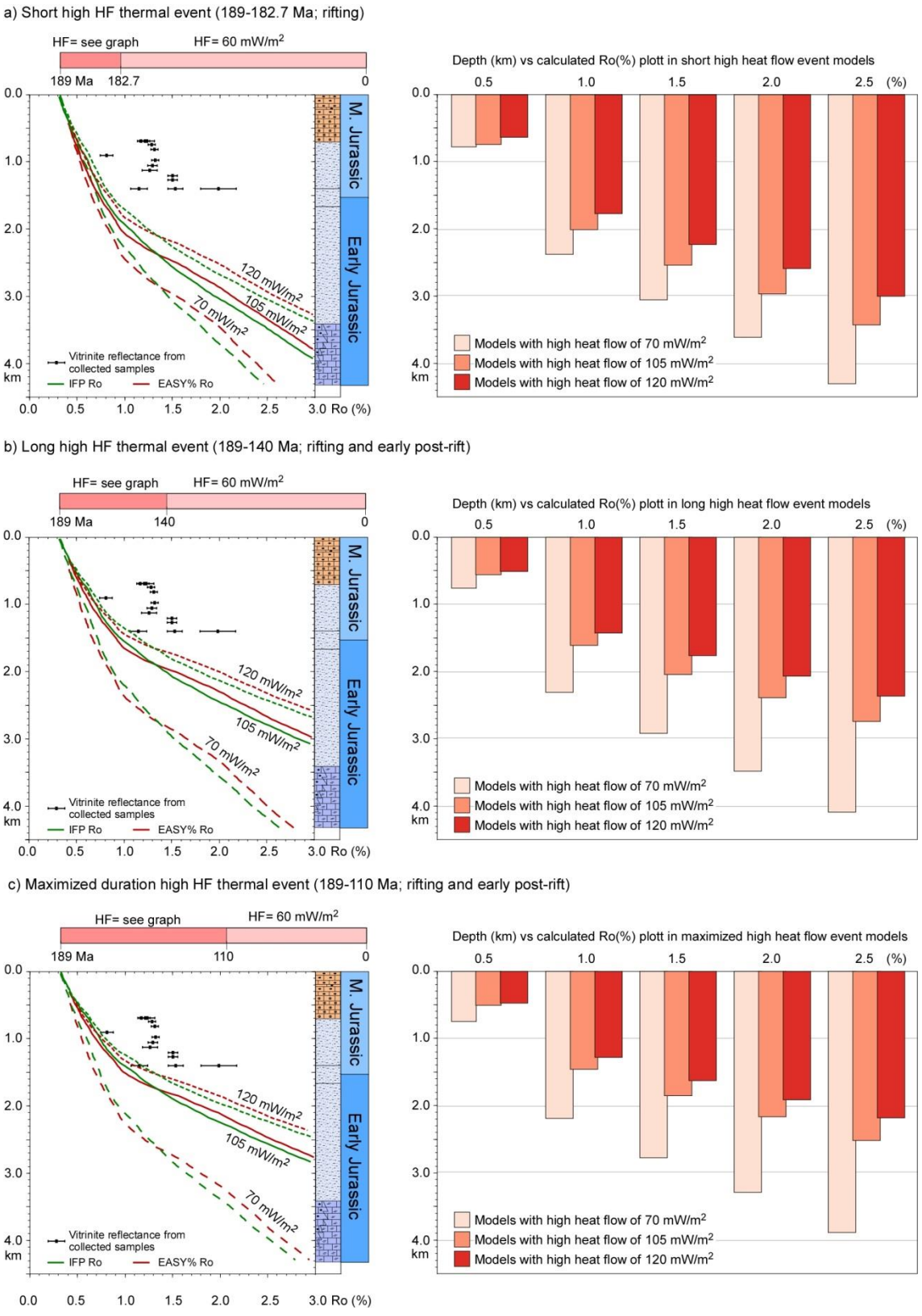

Fig. 6.9. Thermal model plots based on the present-day Amezraï minibasin stratigraphic section showing vitrinite reflectance from samples (black dots) and the calculated vitrinite reflectance curves (IFPRo and Easy%Ro) for high heat flow values of 70 mW/m^2, 105 mW/m^2 and 120 mW/m^2, and a period of low thermal conditions of 60 mW/m^2. a) b) and c) corresponds to models resulting from short, long and maximized period of high heat flow respectively.

The aforementioned trends are also obtained in models with long and maximized duration of the high heat flow event, but the divergence of the calculated reflectance curves from models with different high heat flow values was more dramatic than the previously exposed. In models with long high heat flow event (Fig. 5.5b), a reflectance of 2.5% is reach at 4.1 km depth applying a heat flow of 70mW/m^2, whereas using heat flow of 105 and 120 mW/m^2 this degree of maturation is reached at depths of 2.7 and 2.4 km respectively; a depth difference of 1.4-1.7 km between models. The difference of depth required to reach a 2.5% of vitrinite reflectance between different applied heat flows is equal in the maximized model, i.e 1.7 km (Fig. 6.9c).

None of the calculated vitrinite curves fitted with the distribution of the vitrinite reflectance from samples collected in the Amezraï minibasin stratigraphic log. In all the presented models, whatever was the duration of the high heat flow event and the amount of high heat flow applied, the calculated curves of reflectance were located in lower values than the reflectance measured in collected samples (Fig. 6.9). The best fit between calculated curves and the reflectance of the collected vitrinite samples was only reached applying very high amount of heat flow during the high heat flow event (Fig. 6.10). In the model where the high heat flow event is short, the amount of heat flow required is around 225 mW/m^2, whereas in models with long and maximized duration of the high heat flow event the required heat flow are 180 and 170 mW/m^2 respectively.

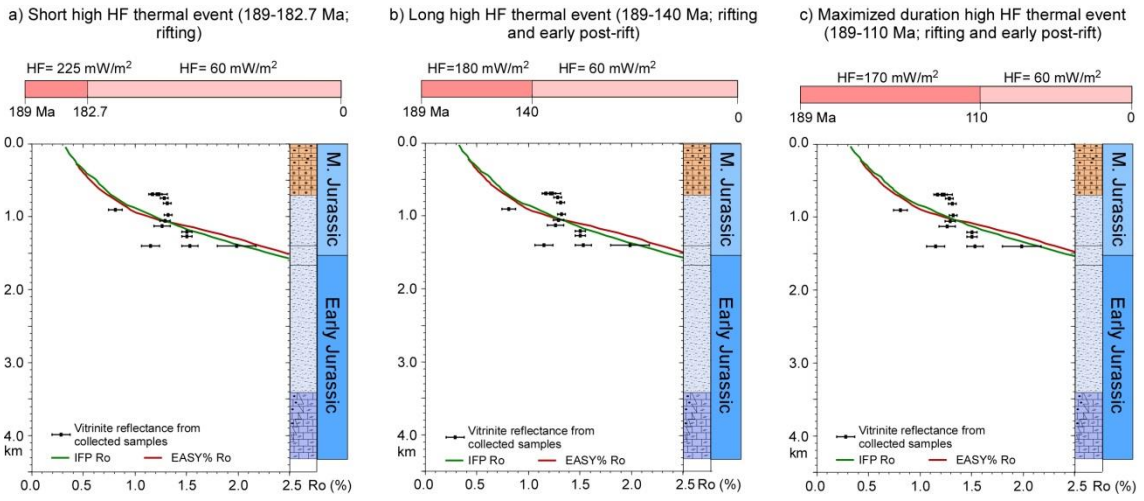

Fig. 6.10. Thermal model plots based on the present-day Amezraï minibasin stratigraphic section showing the best fit obtained between vitrinite reflectance from samples (black dots) and the calculated vitrinite reflectance profiles (IFPRo and Easy%Ro). This fit is reached using a) 225mW/m^2 heat flow in a short high heat flow event, b) 180mW/m^2 heat flow in a long high heat flow event, and c) 170mW/m^2 heat flow in a maximized duration of the high heat flow event. All models include a low heat flow event with thermal conditions of 60 mW/m^2.

Given the anomalous results obtained using the subroutine 1 of the thermal model, which only take into account the present day sedimentary record and the heat flow applied (Fig. 6.10), it was necessary to follow the subroutine 2 (Fig. 4.4) where additional burial was considered as a mechanism for increase the maturity of organic matter. Thus, these models were composed by 3 different geological events: deposition of the Amezraï minibasin section units from 189 to 170 Ma (based Amezraï minibasin section data presented in Fig. 3.3); 2) deposition of uppermost Middle Jurassic to Late Cretaceous sediments from 129.4 to 80 Ma (evaluated in the models) and 3) Alpine inversion of the Central High Atlas in two steps from 80 to 35 Ma (35% of uplift/exhumation) and from 35 to 0 Ma (65% of uplift/exhumation).

The resulting models showed a wide variability of required burial depending on the duration of the high heat flow event and the amount of heat flow applied (Fig. 6.11). In models with a short high heat flow event, the required burial to obtain a good fit between the calculated vitrinite reflectance curves and the reflectance from samples ranged from 2400 to 1700 m (Fig. 6.11a, d and g). In models with long and maximized duration of the high heat flow event this range is two times higher than in the short event models, and the required burial ranges from 2200 to 800 meters in the long event models (Fig. 6.11b, e and h) and from 2000 to 550 m in the models with maximized period of high heat flow event (Fig. 6.11c, f and i).

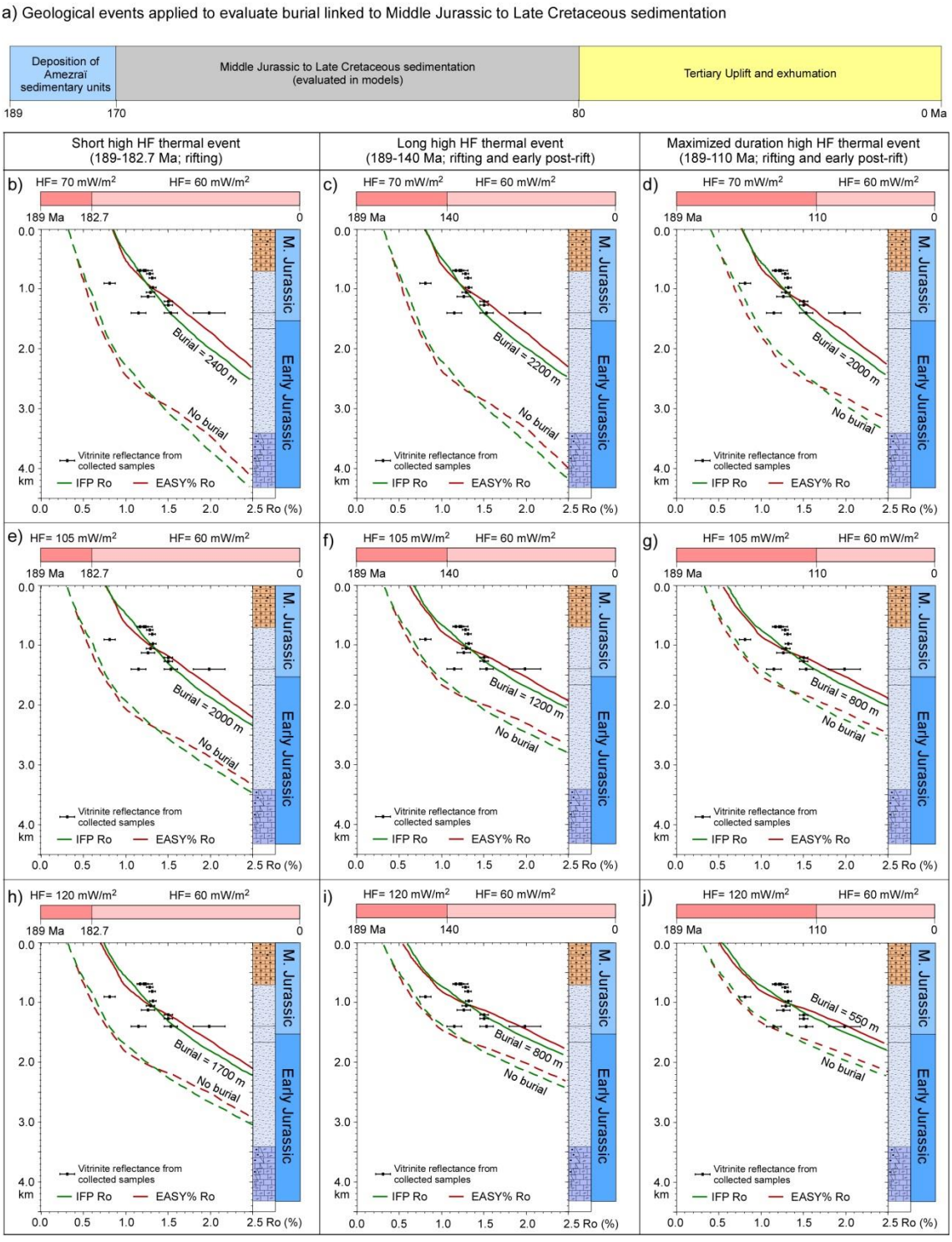

Fig. 6.11. a) Stages of burial and exhumation applied in the presented thermal models. Thermal model plots based on the present-day Amezraï minibasin stratigraphic section showing: calculated vitrinite reflectance profiles (IFPRo and Easy%Ro) resulting from a short (from 189 to 182.7 Ma), long (from 189 to 140 Ma) and maximized period of high heat flow occurrence (from 189 to 110 Ma) with heat flow of 70 mW/m^2 (b, c and d), 105 mW/m^2 (e, f and j) and 120 mW/m^2 (h, i and j). Dashed curves correspond to models with no additional burial and solid lines correspond to models with additional burial. The burial required to fit curves with analysed samples is detailed in each plot, and have been applied with a homogeneous sedimentation from 169 Ma to 80 Ma. All models include a period of low thermal conditions of 60 mW/m^2.

6.2.2. THERMAL MODELS CONSIDERING LATE JURASSIC-EARLY CRETACEOUS EXHUMATION IN THE CENTRAL HIGH ATLAS BASIN

Numerous pointers suggested Late Jurassic-Early Cretaceous uplift in NW Morocco, mostly along the Western Moroccan Arch (parallel to the Jurassic Atlantic Moroccan margin) and Anti-Atlas domain (parallel to the southern border of the Jurassic Atlas rift basin), based on thermochronological studies (Fig. 6.12). The inferred spread of such uplift inside the Jurassic Atlas rift basin was associated with a massive post–rift magmatic event (Frizon De Lamotte et al., 2015). The ending of this thermally-related uplift could range from 140 to 110 Ma (Frizon de Lamotte et al., 2008). Nonetheless, no direct indications were available in the central part of the Central High Atlas, where younger preserved sediments are Callovian in age (~163.5 Ma).

There were three different histories according to different thermal models from the Moroccan Atlas (Fig. 6.12) based on Apatite and Zircon fission tracks and U-Th/He diffusion in Paleozoic samples from the Moroccan Meseta and the West Moroccan Arch: i) thermal history that included two cooling path, the oldest during the Late Jurassic and Early Cretaceous and the youngest during the Cenozoic (Fig. 6.12). Both cooling episodes have been associated to the exhumation of the samples (Ghorbal et al., 2008; Saddiqi et al., 2009; Domènech et al., 2016); ii) thermal history characterised by a long cooling episode from Permian up to Early Cretaceous and a second cooling event linked to an exhumation of the samples of around 1.5 km during the Cenozoic times (Balestrieri et al., 2009; Ruiz et al., 2011; Oukassou et al., 2013); iii) thermal history characterised by tectonic quiescence only disrupted in the Cenozoic time by an abrupt cooling event (Malusà et al., 2007). This was also pointed Barbero et al. (2007) who reported in the central part of the Central High Atlas one first cooling event recorded in the Jurassic syenites of Imilchil linked to the post–magmatic thermal cooling of the intrusion and a the second cooling event linked to the Cenozoic exhumation which would be around 1.5 km. Although there was a wide variety of proposed exhumation histories in the atlas system, all the aforementioned thermochronological studies models coincided with a mean Cenozoic exhumation amount of 1500 m.

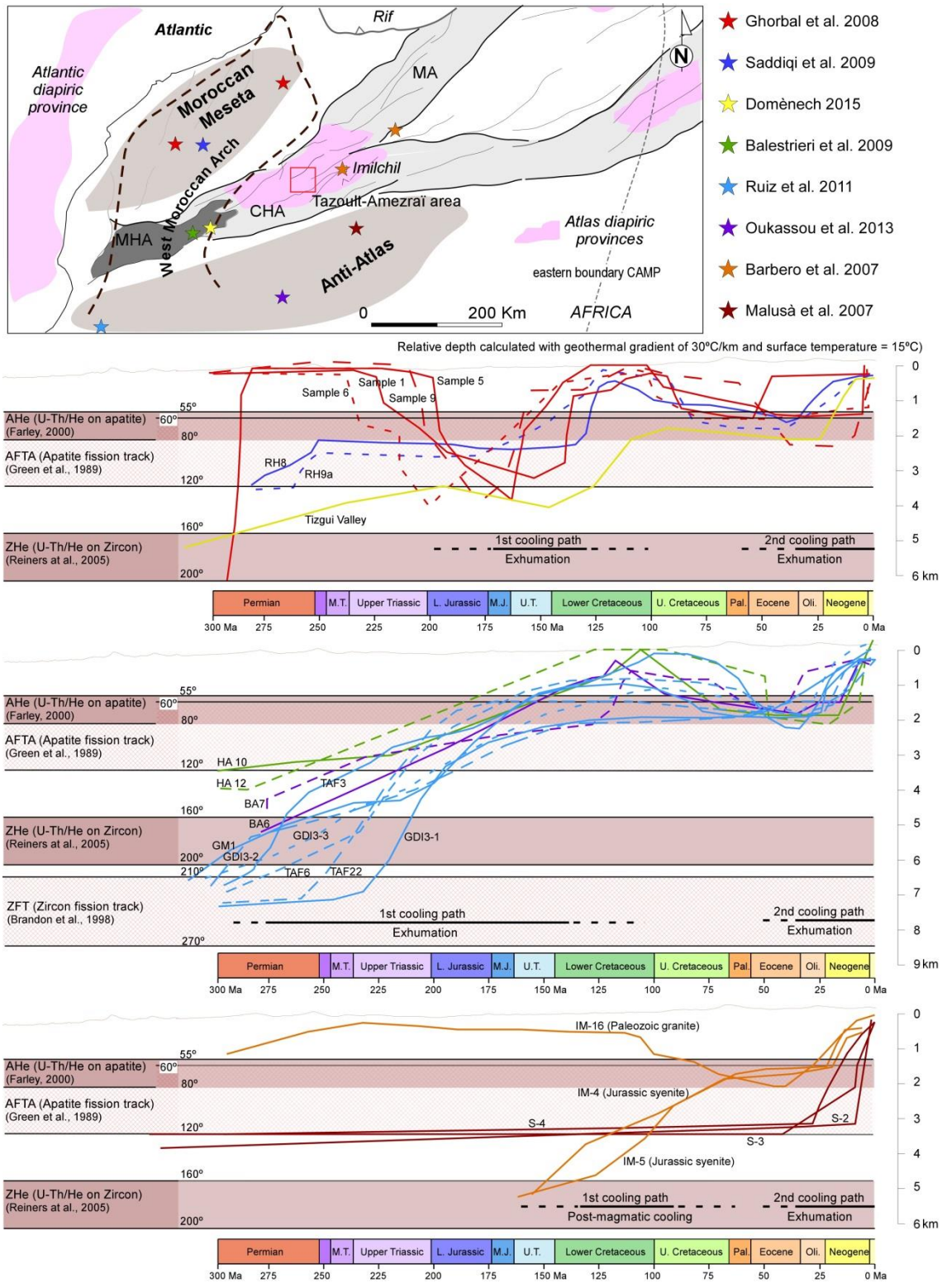

Fig. 6.12. Map of the Moroccan Atlas showing the location of samples (star symbol) used for the thermochronological models. The plots show published curves from thermochronological models coloured according to the associated sample in the map. The thermal bands of He retention zone and fission track annealing zone (from apatite and zircons) comes from Green et al. (1989), Brandon et al. (1998), Farley (2000) and Reiners et al. (2005).

The models presented in this section were designed to study the possibility that the Tazoult–Amezraï area was affected by the Upper Jurassic-Lower-Cretaceous exhumation event. These models were composed by five different geological events (Fig. 6.13a): 1) deposition of the Amezraï minibasin section units from 189 to 170 Ma (based Amezraï minibasin section data presented in Fig. 3.3); 2) Middle Jurassic additional deposition of certain amount of sediments from 170 to 163.5 Ma (evaluated in the models); 3) Late Jurassic – Early Cretaceous erosion of the Middle Jurassic additional deposits from 163.5 to 129.4 Ma (first dated Cretaceous deposition preserved in most external Atlas basin domains); 4) deposition of 1500 m of Cretaceous sediments (129.4 to 80 Ma); 5) Alpine inversion of the Central High Atlas in two steps from 80 to 35 Ma (35% of uplift/exhumation) and from 35 to 0 Ma (65% of uplift/exhumation). The amount of Cretaceous deposition (1500 m) was fixed according to the aforementioned thermochronological studies (Fig. 6.12). The thermal framework imposed to these models was the same than the presented in the models with continuous sedimentation; three lengths of high heat flow event (short, long and maximized), three heat flow values for the high heat flow event (70, 105 and 120 mW/m^2) and one heat flow value for the low heat flow event (60 mW/m^2).

Models with a high heat flow event of 70 mW/m^2 showed a good fit between calculated vitrinite reflectance curves and samples with a Middle Jurassic additional burial of 4 km and equivalent Late Jurassic–Early Cretaceous exhumation, independently of the duration of the high heat flow event (Fig. 6.13b, c and d). Models with high heat flow event of 105 mW/m^2 exposed a good fit between calculated curves and samples in models with short and long duration of the high heat flow event by applying Middle Jurassic burial of 2.25 and 1.7 km respectively, and equivalent Late Jurassic—Early Cretaceous exhumation (Fig. 6.13e and f). In a maximized high heat flow event of 105mW/m^2 (up to 110 Ma), the curves were located in higher values than the samples even with no additional sedimentation during the Middle Jurassic. Models with high heat flow of 120mW/m^2 a good fit between the calculated curves and the vitrinite reflectance from analysed samples was only reached using a short high heat flow event with 1.5 km of additional Middle Jurassic sedimentation, eroded during the Upper Jurassic-Lower Cretaceous exhumation event (Fig. 6.13h). In models with a long and maximized duration of the high heat flow event, with no Middle Jurassic additional burial applied, the calculated vitrinite reflectance curves were displaced towards higher values of reflectance than the analysed samples. Models with no Late Jurassic–Early Cretaceous exhumation and calculated curves displaced towards higher reflectance values than samples would require a reduction of the 1500 m of Late Cretaceous burial and Alpine exhumation.

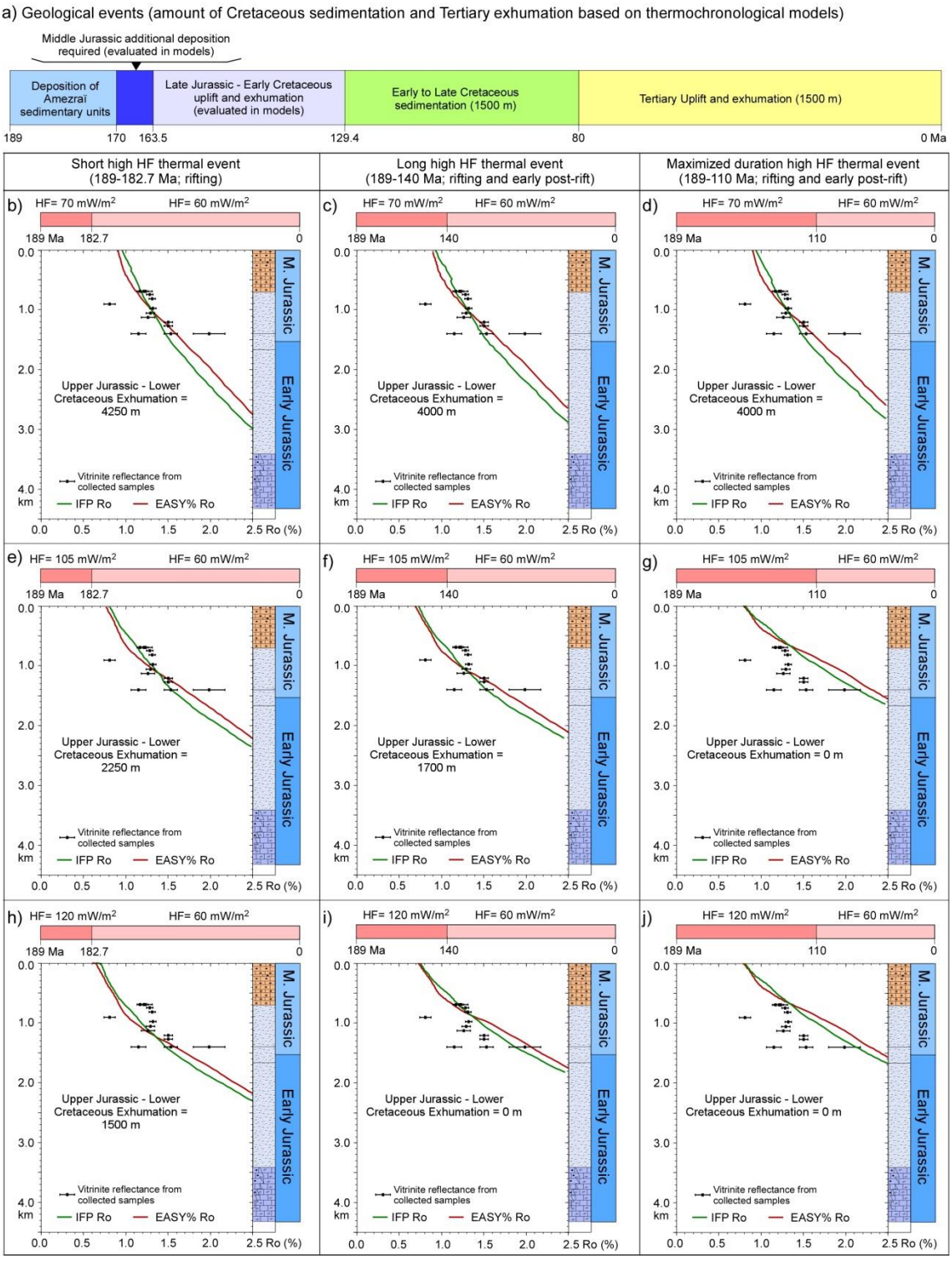

Fig. 6.13. a) Stages of burial and exhumation applied in the presented thermal models. The amount of exhumation and sedimentation after 129.4 Ma based on thermochronological models. Thermal model plots based on the present-day Amezraï stratigraphic section showing: calculated vitrinite reflectance profiles (IFPRo and Easy%Ro) resulting from short (b), long (c) and maximized (d) high heat flow event of 70mW/m^2. Plots e), f) and g) correspond to models with short, long and maximized period of high heat flow of 105 mW/m^2. h), i) and j) correspond to models with short, long and maximized duration of high heat flow of 120 mW/m^2. The additional burial and Upper Jurassic-Lower Cretaceous exhumation required to fit curves with analysed samples is detailed in each plot. All models include a period of low thermal conditions of 60 mW/m^2.

6.2.3. EVALUATION OF THERMAL MODELS

A wide range of thermal models were presented in this chapter, most of them with a similar fitting between calculated vitrinite reflectance curves and reflectance from data. However, it was possible to notice that some models have a better fit than others with a first qualitative estimation comparing the trend of the calculated curves and the distribution of vitrinite reflectance from samples (Fig. 6.11 and Fig. 6.13). So, in order to obtain a quantified evaluation of the thermal models "Root mean square error" (RMSE) was used to analyse and to select the best models to build a complete geohistory of the Amezraï minibasin.

The RMSE between observed data (samples) and calculated data (models) was determined according to the equation

$$RMSE = \frac{[\sum_{i=1}^{N}(X_{(i)obs} - X_{(i)calc})^2]^{\frac{1}{2}}}{N}$$

where X_{obs} was the observed data, X_{calc} was the calculated data and N corresponds to the number of points used for the analysis. The RMSE can be applied to analyse the error for each of the variables of the models; in this case depth and vitrinite reflectance (Ro%). Observed and calculated vitrinite reflectance values from the same reference depths were applied to the equation to evaluate the RMSE of vitrinite reflectance (Fig. 6.14). As lower is the obtained RMSE value (closer to 0) the better is the fit between the observed and the calculated values, and thus the better is the model.

It was not possible to apply straight this method using the vitrinite reflectance data coming from analysed samples because this data was not continuous along the entire stratigraphic log and it is restricted to a small range of depths (between 700 and 1400 m). So, the first step was to create an ideal trend for sample distribution without outliers (anomalous values of the vitrinite samples according to their stratigraphic position) (Fig. 6.14a). Using the equation from the ideal trend, it was possible to calculate the vitrinite reflectance values (Ro) for selected reference depths, Ro_{obs} in the RMSE equation. These Ro_{obs} will be compared with the vitrinite reflectance values extracted from models for the same reference depths, Ro_{calc} (Fig. 6.14b).

In terms of amount of heat flow, models with continuous sedimentation and heat flow values of 70 mW/m^2 showed the lowest RMSE values compared to other heat flow amounts (Fig. 6.14c). This also occurred in models with Upper Jurassic-Lower Cretaceous exhumation event (Fig. 6.14d). Thus, models with heat flow of 70 mW/m^2 were considered as the best

models. Contrarily, models with heat flow values of 120 mW/m^2 showed the highest values of RMSE. This was almost four times higher than RMSE from models with heat flow of 70 mW/m^2 and thus the models with this heat flow value were rejected. Models with heat flow of 105 mW/m^2 showed a medium error. Although the models with this 105 mW/m^2 could be considered not good enough, this heat flow was not rejected in order to use it as a maximum potential heat flow to occur in the studied area. In terms of length of high heat flow event, the continuous sedimentation models with a maximized duration of high heat flow event showed the higher values of RMSE, and thus the worst fit between the vitrinite reflectance values from collected samples and the calculated vitrinite reflectance curves (Fig. 6.14c). The RMSE of models with maximized high heat flow event were even higher in Upper Jurassic-Lower Cretaceous exhumation models (Fig. 6.14d). Thus, the maximized high heat flow event was not considered in the complete geohistory of the studied area. Models with short and long high heat flow events with a heat flow of 70 mW/m^2 showed similar RMSE values and thus it was not possible to reject one of both models.

To sum up, considering the aforementioned error analysis, from the 9 thermal histories evaluated, the best thermal models obtained in the Amezraï minibasin log were those with 70 and 105 mW/m^2 and short and long duration of the high heat flow event. This implied four different thermal and burial geohistories with two clear end-members; i) low thermal history (high heat flow of 70 mW/m^2 from 189 to 182.7 Ma followed by 60mW/m^2) which implied a maximum additional burial in the studied area about 2400 m and ii) high thermal history (high heat flow of 105 mW/m^2 from 189 to 140 Ma followed by 60mW/m^2) which implies a minimum additional burial of 1200 m.

a) Data from collected samples in the Amezraï minibasin log

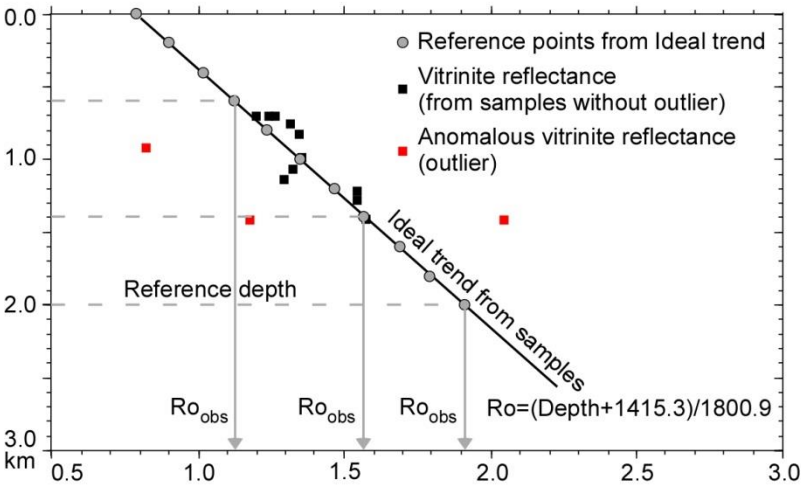

Reference depth	Ro_{obs} (from ideal trend)
0 m	0.78
200 m	0.89
400 m	1.00
600 m	1.12
800 m	1.23
1000 m	1.34
1200 m	1.45
1400 m	1.56
1600 m	1.67
1800 m	1.78
2000 m	1.89

b) Continuous sedimentation model (long high heat flow event; HF= 105 mW/m^2)

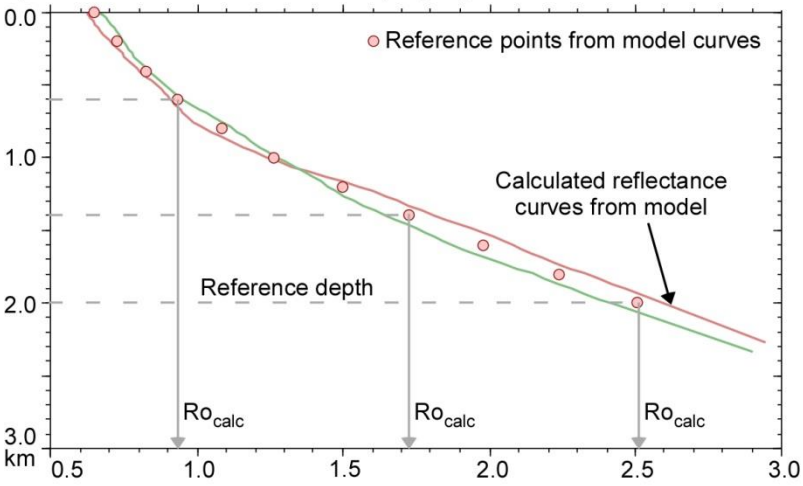

Reference depth	Ro_{calc} (from curves)
0 m	0.65
200 m	0.72
400 m	0.82
600 m	0.92
800 m	1.09
1000 m	1.25
1200 m	1.50
1400 m	1.72
1600 m	1.98
1800 m	2.25
2000 m	2.50

c) RMSE from continuous sedimentation models

Model set	Short high heat flow			Long high heat flow			Maximized high heat flow		
Heat flow (mW/m^2)	70	105	120	70	105	120	70	105	120
RMSE	0.0289	0.0432	0.1042	0.0293	0.0839	0.1146	0.0346	0.0988	0.1375

d) RMSE from Upper Jurassic-Lower Cretaceous exhumation models

Model set	Short high heat flow			Long high heat flow			Maximized high heat flow		
Heat flow (mW/m^2)	70	105	120	70	105	120	70	105	120
RMSE	0.0161	0.0391	0.0539	0.0157	0.0539	0.1218	0.0167	0.1822	0.1733

Fig. 6.14. a) Plot showing the ideal trend from vitrinite reflectance data of the analysed samples without considering outliers and resulting reflectance values from the reference depths. b) Example of extracting vitrinite reflectance values for the reference depths from the calculated reflectance of thermal models. The table show the obtained reflectance values in the model with continuous sedimentation, long duration of high heat flow event and heat flow amount of 105 mW/m^2. c) and d) Values of RMSE calculated for continuous sedimentation models and for Upper Jurassic-Lower Cretaceous exhumation models respectively.

6.2.4. GEOHISTORY MODEL OF THE TAZOULT–AMEZRAÏ AREA

From all the thermal models evaluated above, the two end members were selected to be coupled to the results of the subsidence analysis of the Amezraï minibasin log in order to build a complete geohistory for this part of the Central High Atlas.

In the continuous sedimentation model with a low thermal history (high heat flow of 70 mW/m^2 from 189 to 182.7 Ma followed by $60mW/m^2$) and additional burial of 2400m, the base of the sedimentary succession of the Amezraï basin reached temperatures of 250ºC close to the end of the continuous burial (≈ 85 Ma), when the maximum maturity of all the sedimentary units was reached (Fig. 6.15a). The Lower Jurassic deposits (Jbel Choucht-Aganane and Amezraï formations) entered into the oil and gas window during Middle Jurassic times, and progressively became over mature during Late Jurassic and Early Cretaceous. In contrast, the maturity of Tafraout Fm. (Middle Jurassic deposits) was continuous from oil window (Late Jurassic) to gas window (Late Cretaceous). The same trend was observed in the Aguerd-n'Tazoult Fm. and the Bin el Ouidane 1 Fm., which reached the peak oil threshold and the oil window respectively at Late Cretaceous, preceding the basin inversion and exhumation starting in the latest Cretaceous.

Model of continuous sedimentation with high thermal history (high heat flow of 105 mW/m^2 from 189 to 140 Ma followed by $60mW/m^2$) and additional burial of 1200 m showed that the peak of organic matter maturity was reached for all the sedimentary units during the Early Cretaceous, and it kept the same degree of maturity up to the onset of the Alpine inversion (Fig. 6.15b). The Lower Jurassic deposits (Jbel Choucht-Aganane and Amezraï formations) entered into the gas window during Middle Jurassic times, and then became over mature during Upper Jurassic and Lower Cretaceous times. In contrast, the Middle Jurassic sediments (Tafraout, Aguerd-n'Tazoult and Bin el Ouidane 1 formations) came into the oil window (vitrinite reflectance between 0.7 and 1.3%) early after their deposition and remained between the oil and gas windows up to the end of the continuous subsidence period (Upper Jurassic to Lower Cretaceous), preceding the Cenozoic basin inversion and exhumation.

Model with Late Jurassic–Early Cretaceous exhumation and low thermal history (high heat flow of 70 mW/m^2 from 189 to 182.7 Ma followed by $60mW/m^2$) showed a dramatic burial of the Amezraï minibasin due to the additional required 4.25 km-thick Middle Jurassic succession. Due to this early overburden, the Amezraï minibasin sedimentary succession reached the maximum temperature ($200<Tª<250$) and the maturity before Late Jurassic times. The same

results were obtained from the Model with Late Jurassic–Early Cretaceous exhumation and high thermal history (high heat flow of 105 mW/m^2 from 189 to 140 Ma followed by $60mW/m^2$). The required Middle Jurassic additional burial of around 1700 m caused that the Amezraï sedimentary succession reached the maximum temperature (250<Tª<300) and the maximum maturity before the Late Jurassic –Early Cretaceous exhumation.

According to these models, the Lower Jurassic deposits (Jbel Choucht-Aganane and Amezraï formations) became over mature at the Middle-Upper Jurassic boundary, overpassing the oil and gas windows thresholds in a very short time. In contrast, the Middle Jurassic sediments (Tafraout, Aguerd-n'Tazoult and Bin el Ouidane 1 formations) came into the range of oil and gas window (between 0.7 and 2.0%) and remained within this range during the entire evolution of basin (Fig. 6.16).

a) Model with short high heat flow event of 70 mW/m^2 and maximum burial (2400 m) with continuous sedimentation

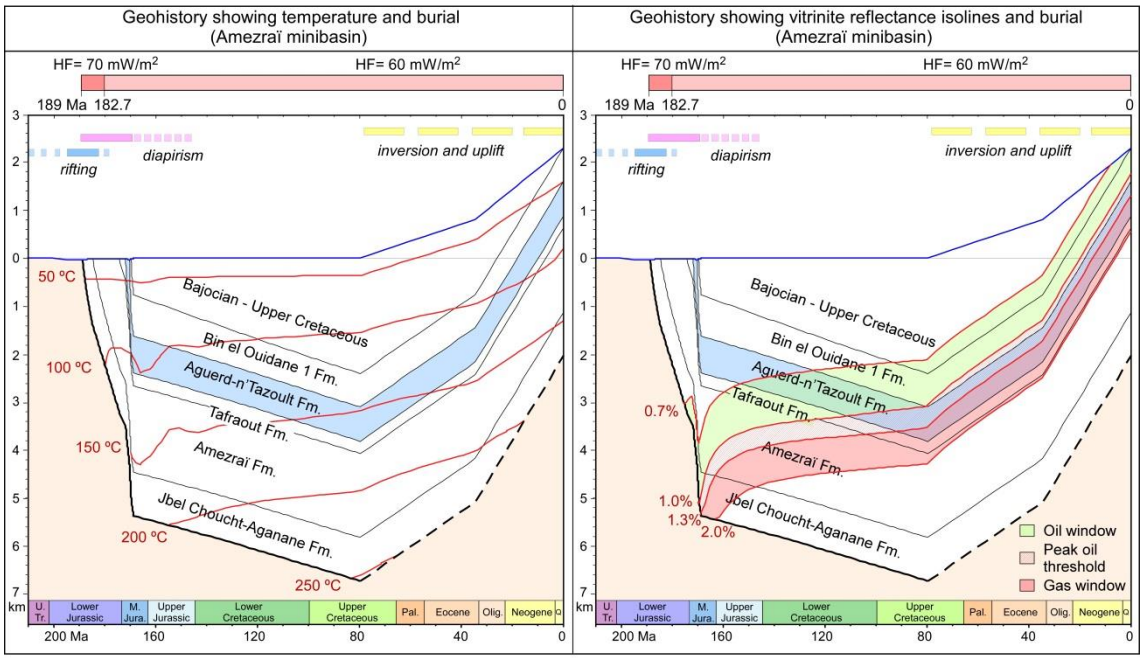

b) Model with long high heat flow event of 105 mW/m^2 and minimum burial (1200 m) with continuous sedimentation

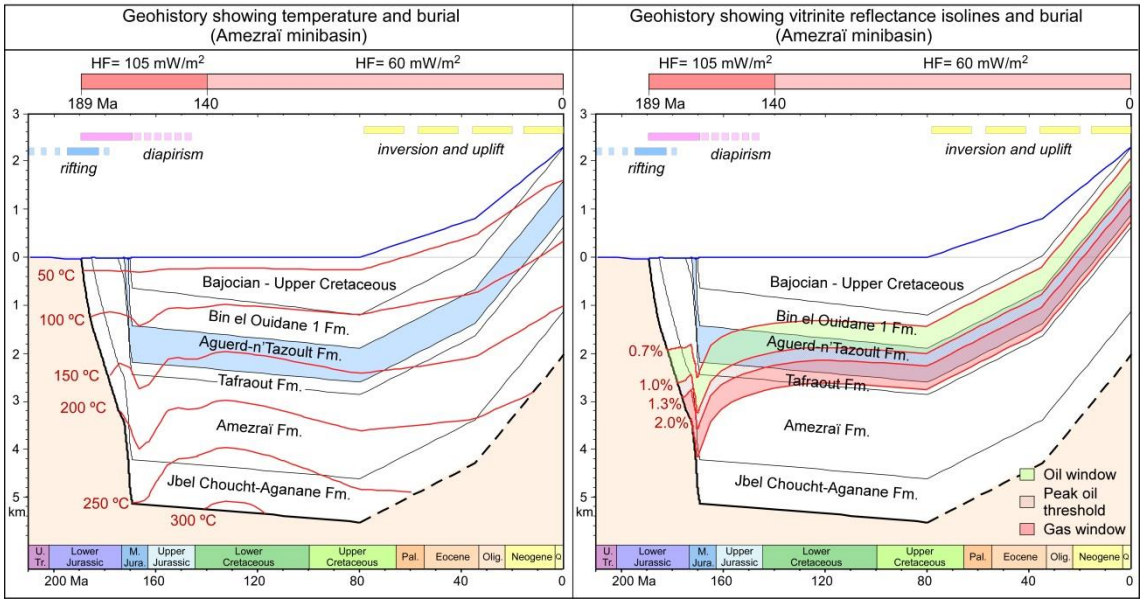

Fig. 6.15. a) Geohistory plots for the Amezraï minibasin using thermal model with short duration of high heat flow of 70 mW/m^2 and burial of 2400 m by continuous sedimentation and b) Geohistory plots for the Amezraï minibasin using thermal model with long duration of high heat flow of 105 mW/m^2 and burial of 1200 m by continuous sedimentation. Plots show the temperature evolution (left) and the vitrinite reflectance isolines distribution (right) in the basin. Blue band highlights the stratigraphic unit containing the vitrinite reflectance dataset (Aguerd-n'Tazoult Fm.). Time scale according to Gradstein et al. (2012).

a) Model with short high heat flow event of 70 mW/m^2 and maximum Late Jurassic-Early Cretaceous exhumation (4250 m)

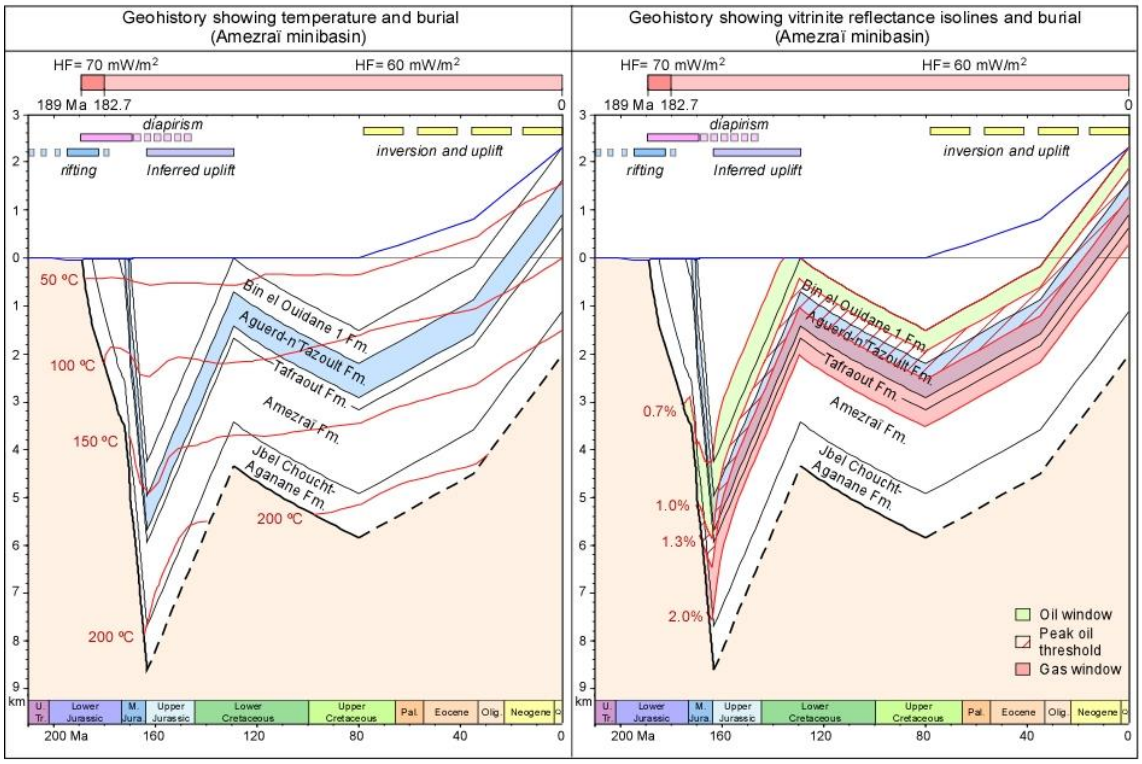

b) Model with short high heat flow event of 105 mW/m^2 and maximum Late Jurassic-Early Cretaceous exhumation (1700 m)

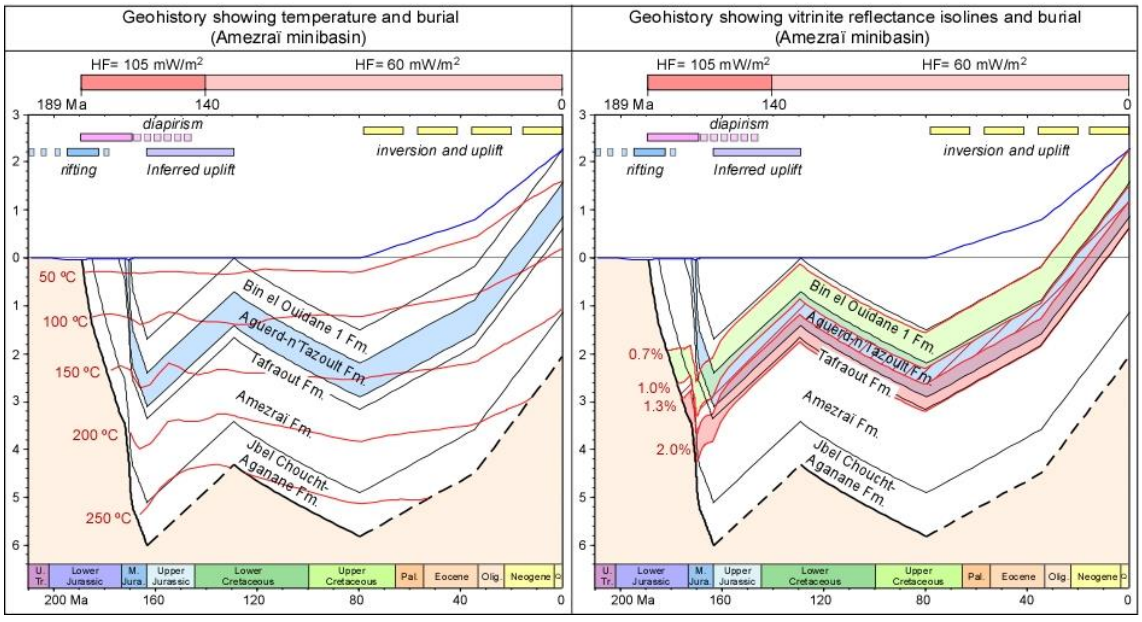

Fig. 6.16. a) Geohistory plots for the Amezraï minibasin using thermal model with short duration of high heat flow of 70 mW/m^2 and b) Geohistory plots for the Amezraï minibasin using thermal model with long duration of high heat flow of 105 mW/m^2. Both models include the additional burial and uplift/exhumation episodes detailed in the section 5.2.3. Plots show the temperature evolution (left) and the vitrinite reflectance isolines distribution (right) in the basin. Blue band highlights the stratigraphic unit containing the vitrinite reflectance dataset (Aguerd-n'Tazoult Fm.). Time scale according to Gradstein et al. (2012).

CHAPTER 7

DISCUSSION

7. DISCUSSION

7.1. ANALOGUE MODELLING RESULTS APPLIED TO THE CENTRAL HIGH ATLAS SALT-RELATED STRUCTURES

In the Central High Atlas, Triassic or Jurassic normal faults are only outcropping in the westernmost part of the range or in the basin margins (Jacobshagen, 1992), whereas in the inner part of the basin these normal faults are located beneath a thick Jurassic to Cretaceous sedimentary cover. This configuration hampered the identification and precise location of these structures at depth, which could only be inferred based on structural models and cross-section restoration (Laville, 1988; Poisson et al., 1998; Teixell et al., 2003). In the Tazoult diapir, the presence of a basement fault beneath or very closed to the diapiric structure was inferred based on thickness variation between both flanks of the structure and the monocline delineated by Bajocian carbonates in close association with the inversion of the normal fault (Martín-Martín et al., 2016). These authors proposed a basement configuration where diapirs were located directly above the tip line of basement normal faults. However, analogue modelling results as well as other previously published models (i.e. Dooley et al., 2005) suggested that both diapirs (Tazoult and Azourki) are probably located on the footwall itself rather than directly above the tip line of basement faults (Fig. 7.1). The rearrangement of the basement faults location implied higher necking effect in the vicinities of the basement normal faults than the proposed by Martín-Martín et al. (2016) and similar to the one observed in the presented models.

In the Tazoult diapir, the onset of diapirism and the formation of a reactive diapir, phase equivalent to the Model A1 (Fig. 7.1A'), was interpreted to take place after early Sinemurian times (Martín-Martín et al., 2016), during the syn-extensional regime occurred during late Sinemurian – Pliensbachian in the Central High Atlas (Ellouz et al., 2003; Lachkar et al., 2009; Moragas et al., 2016). In this setting, the extension linked to the Lower Jurassic rifting faulted and fragmented the Hettangian–early Sinemurian carbonates enhancing the rise of diapirs in reactive manner in their earlier stage. Thus, based on the analogue models, here was presented a first approach of the geometry of the Tazoult diapir during this early stage (Fig. 7.1A). The geometry of the Tazoult diapir during Late Pliensbachian was characterized by vertical walls related to a change in the dynamic of the diapir that becomes passive (Fig. 7.1B). This geometry was similar to those obtained in models with sedimentation rate equal to the

diapir growth velocity Fig. 7.1B'), where equilibrium between diapir growth and sedimentation rate contributes into the stability of the diapir walls (Vendeville et al., 1993; Talbot, 1995). However, small differences between both rates were pointed by Martín-Martín et al. (2016) based on observed wedge geometries of the Pliensbachian deposits. The equilibrium between diapir growth and sedimentation rate spanned up to Toarcian times, when an increase in the ratio of diapir growth and sedimentation rate was recorded (Fig. 7.1C and D).

During the passive stage of the Tazoult evolution occurred during Toarcian and Aalenian, the diapir expanded laterally forming an allochthonous salt sheet towards the hanging wall of a basement graben. This type of geometry suggested that sedimentation rate during post–extension phase did not keep the pace with diapir growth, as it was recorded in the distal part of the prograding Model B2 (Fig. 7.1D'). The Tazoult ridge dynamics changed during this period with an increase in the rate of salt upwelling in relation to the sedimentation rate in the vicinity of the diapir. Martín-Martín et al. (2016) associated the allochthonous salt sheet formation to a coetaneous high sedimentation rate in the central part of the Amezraï basin. However, the presented results showed that the silicone extrusion could also be formed during a post–extension stage with very low sedimentation rate across the entire model (Fig. 7.1E'). Thus, although a differential sedimentation rate from the centre of the Amezraï basin and the Tazoult flanks coeval to the formation of allochthonous bodies is expected as in other diapiric basins, model results pointed that the entire thickness of the sedimentary pile needs to be considered in the mobilization of the ductile substrate that feeds allochthonous sheets.

The Jbel Azourki-Tafraout diapir limited the south margin of the Amezraï minibasin (Fig. 7.1E) and included a south leaning allochthonous salt sheet as it was described in the northern margin for the Tazoult diapir. This spatial distribution did not fit with our models, where the two resulting allochthonous sheets were leaning towards the central part of the system. Thus, based on modelling results and the section from the studied area, the flowing direction of the Jbel Azourki-Tafraout extrusion was interpreted to be caused by a subsiding graben located south of the diapir (already proposed by Martín-Martín et al., 2016), regional southward tilting of the basement structure located south of the diapir, a lower sedimentation rate in the south than in the northern side of the Jbel Azourki-Tafraout, or a combination of these factors.

Although the presented models helped to improve the interpretation of the Tazoult diapir evolution, some interesting differences were highlighted. In the presented models, the pre-extension sand layers were upward folded constituting flap structures. This geometry cannot be corroborated in the Tazoult salt wall where Early Jurassic pre-rift units only crop out as

allochthonous blocks within the diapir. In the same way, the presented models did not reproduce the southern megaflap of the Tazoult diapir (Saura et al., 2014; Martín-Martín et al., 2016; Vergés et al., 2017). Megaflap structures are kilometre scale panels of deep minibasin strata, rotated with a vertical attitude after diapir breakthrough (Ferrer et al., 2016; Rowan et al., 2016); however, in the presented models the deepest beds, pre-extension sand layers, only reach sub-vertical to overturned attitude in their uppermost part, close to the diapir structures (Fig. 7.1). The length of the sub-vertical to overturned segment was less than 1 cm, equivalent to less than 800 m in the reality; thus, the presented models would require longer and/or higher salt withdrawal rate from minibasin towards the diapirs to obtain megaflap geometry similar to the one from Tazoult salt wall.

Fig. 7.1. (next page) Step by step evolution of the Tazoult diapir from the onset of diapirism to the fossilization of the diapiric structures (A to D) coupled with images of equivalent stages obtained from analogue modelling (A'-D'). E and E', respectively, restored cross-section of the Tazoult diapir-Azourki diapir transect (modified from Martín-Martín et al., 2016) and image of equivalent stage obtained from analogue modelling. The amount of sedimentation in the hangingwall of the present models is comparable to the minimum thickness in the Amezraï minibasin obtained from the conservative regional cross-section proposed by the authors.

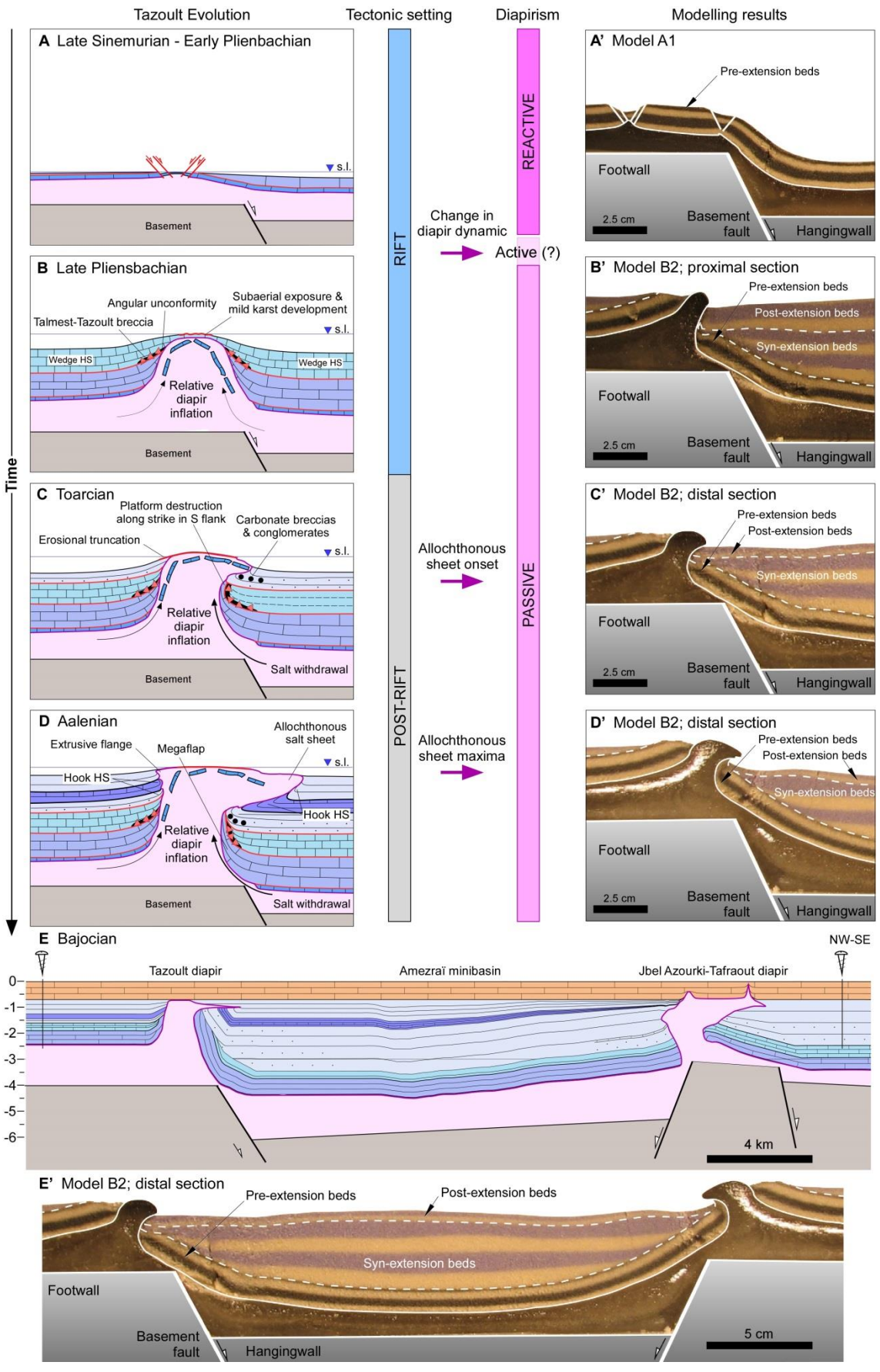
Tazoult Evolution
Tectonic setting
Diapirism
Modelling results
A Late Sinemurian - Early Plienbachian
s.l.
Basement
B Late Pliensbachian
Angular unconformity
Subaerial exposure & mild karst development
Talmest-Tazoult breccia
Wedge HS
Wedge HS
Relative diapir inflation
C Toarcian
Platform destruction along strike in S flank
Carbonate breccias & conglomerates
Erosional truncation
Salt withdrawal
D Aalenian
Extrusive flange
Megaflap
Allochthonous salt sheet
Hook HS
Hook HS
Time
RIFT
POST-RIFT
REACTIVE
PASSIVE
Change in diapir dynamic
Active (?)
Allochthonous sheet onset
Allochthonous sheet maxima
A' Model A1
Pre-extension beds
Footwall
2.5 cm
Basement fault
Hangingwall
B' Model B2; proximal section
Pre-extension beds
Post-extension beds
Syn-extension beds
C' Model B2; distal section
D' Model B2; distal section
E Bajocian
NW-SE
Tazoult diapir
Amezraï minibasin
Jbel Azourki-Tafraout diapir
0
-1
-2
-3
-4
-5
-6
4 km
E' Model B2; distal section
5 cm

7.2. RIFT TO POST–RIFT SUBSIDENCE EVOLUTION IN THE CENTRAL HIGH ATLAS

7.2.1. EARLY AND MIDDLE JURASSIC SUBSIDENCE EVOLUTION

The Central High Atlas underwent Triassic rifting (phase 1) and Lower Jurassic rifting (phase 2) as showed in Fig. 2.1. The lack or non-observation of Triassic rift deposits in the study areas and the Middle Atlas did not permit to model this first rift phase (Fig. 7.2). Thus, this Triassic rift phase 1 was only indicated in the Aït Chedri Tizgui locality in the Atlantic Moroccan Atlas (Fig. 7.2). This locality subsided ~3.4 km during the Triassic, as also evidenced in its continuation in the Agadir Basin (Zühlke et al., 2004) and in the offshore seismic lines (Hafid et al., 2008; Tari and Jabour, 2013). The Aït Chedri Tizgui in the Atlantic Atlas shows a rather continuous sedimentation from the Jurassic to present day, consistent with a passive margin setting (ACT in Fig. 7.2). This subsidence pattern was also record in the subsidence curve from Essaouira basin published by Ellouz et al. (2003) (Fig. 7.2) The Triassic rift phase 1 was also recorded in well-developed half graben structures with thick siliciclastic sedimentary successions in several localities of the Western High Atlas (e.g., Baudon et al., 2009; Redfern et al., 2010; Domènech, 2015; Domènech et al., 2015).

Conversely, the subsidence curves for the Lower Jurassic rift phase (phase 2) can be calculated all around the Central High Atlas and the Middle Atlas (Fig. 7.2). During rift phase 2, the Lower Jurassic basin geometry was complex, comprising a number of NE-SW oriented tectonic highs separating deeper basins (Fig. 2.5 and Fig. 7.2). Subsidence histories were complex, depending on this palaeogeography and thus published subsidence analyses may show local rather than rift basin scale results (e.g., Poisson et al., 1998; Bracène et al., 2003; Ellouz et al., 2003; Patriat et al., 2003; Lachkar et al., 2009). Therefore, the comparison of subsidence curves from the studied areas with other curves from the Central High Atlas can help to better understand the tectonic framework of the rift basin in which the Djebel Bou Dahar, the Tazoult–Amezraï and the Imilchil diapiric province were placed.

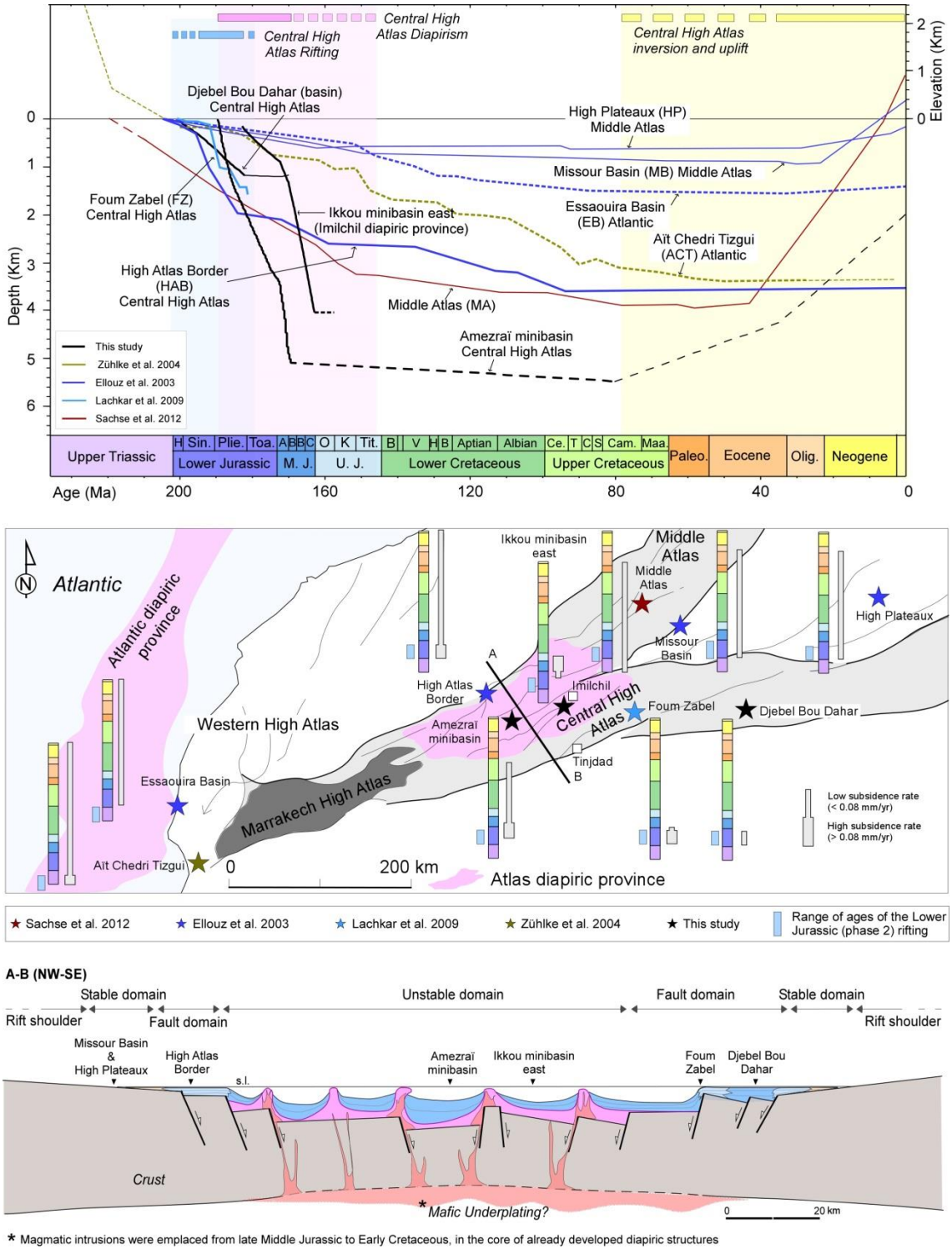

Fig. 7.2. Comparison of total subsidence curves from the studied areas with subsidence curves from other localities in the Moroccan Atlas(Time scale according to Gradstein et al., 2012). The map shows the subsidence rate through time for each plotted location. The presented cross–section corresponds to an interpretation of the Central High Atlas rift basin architecture at Pliensbachian time. It includes the relative position within the basin of some of the locations with subsidence analyses presented in the plot.

The High Plateaux and Missour Basin subsidence curves, which were derived from the margins of the Central High Atlas rift basin (Fig. 7.2), were relatively smooth and showed low tectonic subsidence rates (< 0.02 mm yr^{-1}) during the Jurassic and through the Cretaceous and Palaeogene periods, exemplifying the stable domain of the rift basin (Fig. 7.2). In contrast, subsidence curves from the Fault domain of the rift basin tend to show a short period of rapid subsidence during the Lower Jurassic (Sinemurian-Pliensbachian), followed by slower subsidence rates that may continue until the uppermost Middle Jurassic in the High Atlas locality comprising the Foum Zabel from Lachkar et al. (2009), the High Atlas Border from Ellouz et al. (2003) and the Djebel Bou Dahar basin curve from the present study. These subsidence curves from the Fault domain indicated a rifting episode from Sinemurian to Pliensbachian times with a diachronous fault activity, as pointed out by the subsidence variations through time detailed in Section 6.1.1 (Subsidence analysis of Djebel Bou Dahar). This Sinemurian to Pliensbachian time range, shorter than the rifting phase reported in the Middle Atlas by Zizi (1996), was in agreement with observed tectonostratigraphic relationships reported by Poisson et al. (1998) from Tinjdad area (see location in Fig. 7.2) where Toarcian marls fossilised pre-Toarcian normal faults. Generally, the tectonic subsidence rates recorded in the Fault domain are lower in the shallower areas of Djebel Bou Dahar and Rich transect (< 0.1 mm yr^{-1}), whereas the tectonic subsidence rates reached high values in the basinal domain (up to 0.5 mm yr^{-1}), as it is shown in Foum Zabel and Djebel Bou Dahar basin curves in Fig. 7.2. During Sinemurian-Pliensbachian times, high subsidence rates (up to 0.2 mm yr^{-1}) were also recorded in the High Atlas border curve described by Ellouz et al. (2003), which corresponded to the northern border of the Central High Atlas basin (Fig. 7.2).

The obtained subsidence curves from the Fault domain and the unstable domain show clearly differences in terms subsidence rates and period of the fastest subsidence (Fig. 7.2). This was clearly recorded in the Amezraï minibasin and Ikkou minibasin subsidence curves which are the most distinctive in the Central High Atlas basin (Fig. 7.2). Total subsidence curve from Amezraï minibasin show subsidence rates up to 0.98 $mmyr^{-1}$, which were rates one order of magnitude higher than in the Djebel Bou Dahar area. The Ikkou minibasin subsidence rates reached values up to 0.40 $mmyr^{-1}$, although total subsidence rates up to 0.9 $mmyr^{-1}$ were also obtained in the Imilchil diapiric province. The fastest subsidence episodes occurred diachronously from the different localities within the unstable domain; it was during Toarcian-Aalenian in the Amezraï minibasin and during Bathonian-Callovian in the Ikkou minibasin. At smaller scale, as within the Imilchil diapiric province, migration of subsiding depocenters was also recorded in the three adjacent studied minibasins (Ikassene, Lake Plateau and Ikkou). Both

Amezraï and Ikkou subsidence curves showed rapid subsidence episodes after the assumed end of the rifting phase, overprinting the transition between rift and post–rift phases. Thus, the unstable domain located in the diapiric rift axis displayed: i) subsidence rates one order of magnitude higher than rates from basin periphery, ii) spatial and temporal migration of subsidence peaks from regarding different minibasins and iii) anomalous high subsidence amounts during post–rift phase compared to the expected thermal subsidence rates. Taking into account all the plotted subsidence curves as well as the learnings from analogue models, the aforementioned characteristics pointed to a combination of normal fault extension and salt withdrawal from beneath the minibasin during the rifting, being the salt-related subsidence predominant during the post–rift and masking the estimated subsidence pattern of a rift to post–rift transition in the unstable domain.

The presented comparison of new subsidence curves with previous published subsidence studies carried out in the Central High Atlas was a good approach of the subsidence patterns heterogeneities in the different tectonic domains defined within the Central High Atlas Jurassic rift basin, mainly in the unstable domain where the diapirism is a prevalent mechanism during both rift and post–rift phases.

7.2.2. POST–MIDDLE JURASSIC EVOLUTION

The post–Middle Jurassic evolution of the Central High Atlas rift basin remains less well constrained, due to the scattered nature of its younger sedimentary record, which generally crops out within isolated outliers and also along the marginal areas of the present Atlas Mountains. The thermal and burial models for the Tazoult–Amezraï basin transect, allow some key elements of the post–Middle Jurassic evolution of this area to be inferred. In this thesis, the presented thermal modelling evaluated using vitrinite reflectance data was based on two potential geohistory models for the Central High Atlas rift basin (Tazoult—Amezraï area). A first model characterised by a roughly continuous but small sedimentary record from Late Jurassic to Late Cretaceous and an alternative model characterized by Late Jurassic-Early Cretaceous and Cenozoic uplift events.

For each geohistory, the thermal history has been divided in two events; a high heat flow event and a low heat flow event with different durations: short high heat flow event (189 to 182.7 Ma), long high heat flow event (189 to 140 Ma) and maximized high heat flow event

(189 to 110 Ma). Considering the error analysis presented section 5.2.3 (Evaluation of thermal models), from the nine proposed thermal histories, two end-members were selected. First, the so-called low thermal history with high heat flow of 70 mW/m^2 from 189 to 182.7 Ma followed by 60mW/m^2, where the high thermal heat flow was limited duration of the rifting phase. Contrarily, the so-called high thermal history was characterized by a high heat flow of 105 mW/m^2 from 189 to 140 Ma followed by 60mW/m^2, where the high heat flow spanned the Early Jurassic rift and the early post–rift and fit with the ages stablished for the emplacement of Middle to Upper Jurassic intrusions within the diapir cores all along the Central High Atlas (Laville and Harmand, 1982; Frizon de Lamotte et al., 2008; Charrière et al., 2011; Saura et al., 2014; Martín-Martín et al., 2016).

The two thermal histories were applied to evaluate the two proposed post–Middle Jurassic histories of the Central High Atlas: i) post–Middle Jurassic evolution with long-term and low-rate subsidence episode associated to sedimentation during Late Jurassic–Early Cretaceous up to the inversion during the Alpine orogeny and ii) post–Middle Jurassic evolution including two exhumation events, in the Late Jurassic–Early Cretaceous and during the Alpine orogeny, proposed by Frizon de Lamotte et al. (2009) according to observations in the West Moroccan Arch.

The model with Late Jurassic–Early Cretaceous sedimentation showed that the Amezraï minibasin required post–Middle Jurassic overburden that ranged between 1200 and 2400 m in thickness, corresponding to the high and low thermal history, respectively. This 1200 to 2400 m-thick overburden was eroded during the Alpine orogeny. Other localities around the Central High Atlas showed burial histories that were directly comparable to the results presented here.

Ellouz et al. (2003) reported c. 1800 m of post–Bajocian deposits in the northern border of the Central High Atlas. Apatite fission track data (Barbero et al., 2007) also indicate a significant overburden of more than 1500 m in the Imilchil transect to the east of the study area, as well as a continuous exhumation starting in the latest Cretaceous. Haddoumi et al. (2002) and Haddoumi et al. (2010) also described several hundred metres of Upper Jurassic to early Upper Cretaceous aged “couches rouges” (i.e. red beds) cropping out in the Ouaouizaght syncline (located in the northern border of the rift basin). Using illite “crystallinity” analysis, Brechbühler et al. (1988) determined a 6 km thick sedimentary pile of post–Toarcian sediments in the Errachidia-Midelt transect, located 162 km eastward of the Tazoult–Amezraï area. Thus, post–Middle Jurassic burial seems generalised in the Central High Atlas sedimentary basin.

The alternative scenario proposing the western segment of the Tethyan Atlas as uplifted after Middle Jurassic times (e.g., Beauchamp et al., 1999; Frizon de Lamotte et al., 2008) has also been tested by means of thermal modelling. However, this exhumation model was constructed assuming two consecutive poorly constrained subsidence-uplift events from the Late Jurassic to present day.

The model with two exhumation events showed that the Amezraï minibasin required an additional overburden between 1.7 and 4.25 km in thickness, corresponding to high and low thermal histories, respectively. The calculated overburden was completely eroded during the Late Jurassic–Early Cretaceous exhumation and followed by around 1.5 km-thick deposits eroded during the Alpine orogeny.

The uplift models provide a suitable fit between vitrinite reflectance curves and samples. However, the complexity of the geological processes (involving km-scale vertical movements) as well as the lack of match with the geological observations in the Central High Atlas strongly suggests that the widening of the uplift and exhumation along the West Moroccan Arch was not reaching the study area. Nevertheless, this uplift and exhumation event recorded more than 100 km westward from the studied area could have influenced in the limited and condensed amount of deposits that are required in models with Upper Jurassic – Early Cretaceous sedimentation.

7.3. ALONG STRIKE SUBSIDENCE VARIATIONS OF THE ATLAS FROM MOROCCO TO TUNISIA

The Atlas system can be divided into two major domains: the Atlantic and the Tethyan provinces having different subsidence histories (Le Roy et al., 1998; Le Roy and Piqué, 2001; Frizon de Lamotte et al., 2008; Frizon de Lamotte et al., 2011) (Fig. 7.3). The Atlantic domain, corresponding to the Western Atlas and offshore Morocco, was characterised by a major Triassic rifting stage inferred to have evolved into a drift stage from the Early Jurassic to the Late Cretaceous(Hafid, 2000; Zühlke et al., 2004; Hafid et al., 2008) (Aït Chedi Tizgui; ACT in Fig. 7.3). In the Central Atlas (Tethyan domain), a distinct second rift phase occurred during Lower Jurassic times (Fig. 7.2).

The analysis of the variations of the subsidence history along the axis of the Atlas rift system in the Tethyan domain was not intended to be conclusive and only aimed to give some thoughts about these variations from Morocco to Tunisia, based on available subsidence

studies when integrated with the results obtained from the present research. It is important to realise during this evaluation that subsidence curves are strongly influenced depending on used data, methodology and on their tectonic locations. Despite these potential limitations, three different subsidence analyses were contrasted along the strike of the Atlas basin: the total and tectonic subsidence curves for the Amezraï basin in the west (Central High Atlas in Morocco; CHA), the total subsidence curve from the Bled Chetihat basin in the Saharan Atlas in Algeria (SA in Fig. 7.3), and the tectonic subsidence curve of the Gabés Basin in the Tunisian Atlas (GB in Fig. 7.3).

The subsidence history of the Bled Chetihat basin in the Saharan Atlas comprised the complete Jurassic, Cretaceous and Palaeogene successions (Bracène et al., 2003). The total subsidence curve showed a regional period of fast subsidence, in different steps, from Early Jurassic to Middle Cretaceous, followed by a period of slow subsidence in order to reach the upper part of the Oligocene. During Late Oligocene this time, the top of the Upper Triassic unit reached its maximum depth at > 6 km below sea level, just before the onset of exhumation (Fig. 7.3). The Triassic top was located at depths of 4.2 km, at present elevated during the Atlas tectonic inversion (Bracène et al., 2003; their Fig. 13). Interpreted seismic lines in the western Saharan Atlas show the deepest synclines that are still located at depths of ~6 km (Bracène et al., 2003; their Fig. 16).

Subsidence analysis showed low subsidence rates of 0.05 mm yr^{-1} in Early and Middle Jurassic times, followed by a period of larger subsidence (up to 0.20 mm yr^{-1}) during Late Jurassic and Early Cretaceous times. This second period of fast subsidence was synchronous to diapiric growth and salt withdrawal from basins, which probably increased subsidence rates (Fig. 7.3). Afterwards, the subsidence curve showed a slow period of subsidence up to the late Oligocene prior to widespread uplift during the Neogene and the main inversion in the late Lutetian (discussed but not shown in the SA subsidence curve of Bracène et al., 2003) (Fig. 7.3).

The subsidence histories of Chotts, Gabès and Hammamet basins in southern Tunisia have been analysed by Patriat et al. (2003) (see their Fig. 11). These authors divide the subsidence history into three main events, evolving from rifting to compression, as displayed in the tectonic subsidence curve for the Gabés Basin (GB in Fig. 7.3). The Lower Jurassic to Aptian-Albian boundary main rifting period was characterised by a long and constant subsidence with low rates of about 0.02 mm yr^{-1}. Furthermore, the Aptian to Late Cretaceous transition period was characterised by variable subsidence among different basins that was attributed to the important role of active halokinesis, working since Aptian times (Perthuisot, 1981; Snoke et al.,

1988) or even older (Boukadi and Bedir, 1996). Starting in the Paleocene, inversion tectonics affected specific structures in southern Tunisia, as clearly imaged in seismic lines showing a major Oligocene post–folding unconformity. Patriat et al. (2003) concluded that salt diapirism rejuvenation and reactivation were also common during this phase of shortening, spanning from the Eocene to present day (Fig. 7.3).

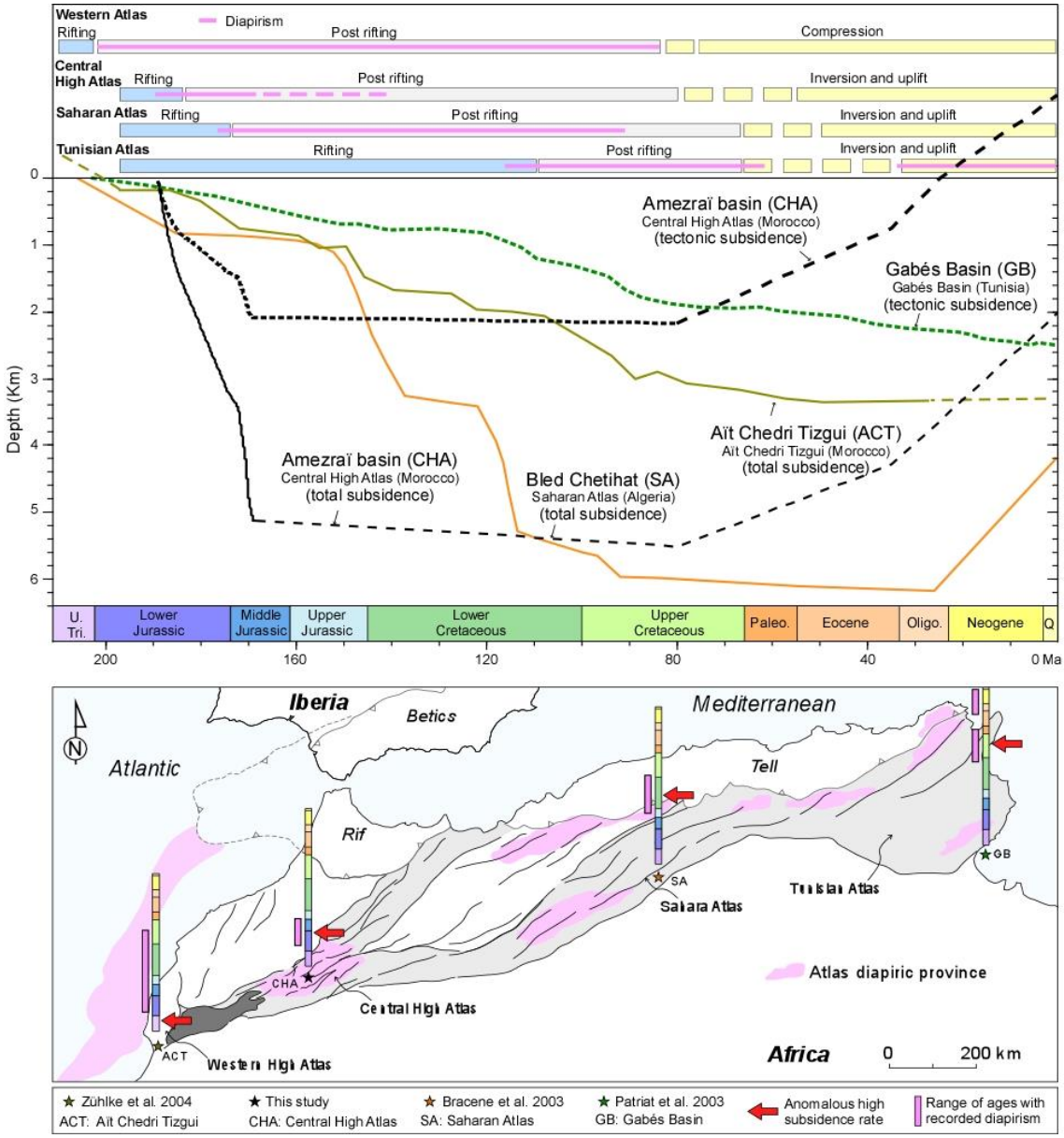

Fig. 7.3. Subsidence curves and tectonic stages from West High Atlas (Zühlke et al., 2004), Central High Atlas (this study), Algeria (Bracène et al., 2003) and Tunisia (Patriat et al., 2003). Diapirism (pink bar) is associated with different stages. Amezraï minibasin total subsidence is compared with Bled Chetihat and Aït Chedri Tizgui curves, and the Amezraï tectonic curve is compared with the Gabés basin tectonic curve. The map shows the ages of the main peak of subsidence in each locality and the age of diapirism.

The comparison among selected subsidence curves from the Tethys domain showed diachronous highest rates of subsidence as well as maximum burial, becoming younger towards the east (Fig. 7.3). In the Central High Atlas (Amezraï basin), the highest rates of tectonic and total subsidence occurred during the Early and Middle Jurassic. The maximum burial, according to the presented geohistory model, was achieved during the Late Cretaceous with maximum thicknesses of almost 5.5 km. In the Saharan Atlas in Algeria (Bled Chetihat basin), the fastest and maximum subsidence (> 4 km) occurred during the Early Cretaceous whereas rifting ended during the Middle Jurassic. The maximum burial recorded in the Bled Chetihat basin was attained during the late Oligocene with maximum thicknesses of almost 6.2 km. In the Tunisian Atlas (Gabés Basin), showing a maximum subsidence of 3.5 km, the tectonic subsidence displayed a long-lasting and smooth curve up to present day. The highest rates of tectonic subsidence roughly coinciding with the Early-Late Cretaceous boundary, seems related to the Sirt rifting in Libya that also affected the eastern margin of Tunisia (Frizon de Lamotte et al., 2009 and references therein).

The diachronism between extension and diapirism compared to the subsidence curves may strongly indicate that peaks of fastest subsidence in Morocco and Algeria must be related to salt withdrawal from beneath the studied locations during diapirism stages. Although in Tunisia the rifting phase was longer and high subsidence rate peaks were partially coeval to the extension, diapirism cannot be ruled out as additional subsidence mechanism as would be suggested by the large amount of diapiric structures described for the area.

CHAPTER 8

CONCLUSIONS

8. CONCLUSIONS

The Central High Atlas in Morocco, recently interpreted by our working group as an extensive diapiric province, was studied in this thesis to analyse and understand the dynamics of the diapiric basin during the Early Jurassic rift and subsequent post–rift phases using a multidisciplinary methodology that integrated fieldwork, analogue models and subsidence and thermal numerical modelling. Two regions were examined to assess the effects of salt tectonics in the evolution of the basin; the Djebel Bou Dahar platform-basin system represented the Fault domain of the rift basin where diapiric activity was not described and the Tazoult–Amezraï area and Imilchil diapiric province corresponding to the unstable domain of the basin characterised by the presence of diapiric salt ridges and minibasins.

Analogue models were used to analyse the evolution of the diapiric structures developed during Early and Middle Jurassic in the Central High Atlas. The results from five different extensional models with different depositional patterns for rift and post–rift showed the close interaction between extension, diapirism and sedimentation in the evolution of diapiric basins. Once the diapirism began triggered by regional extension (total extension of 4%), syn- and post–extension sedimentary pattern (homogeneous, longitudinal prograding and transverse prograding) had a major influence on the evolution of diapirism and on the final configuration of the diapiric basin. Diapir geometry varied in proximal and distal domains of the models, relative to the sedimentary source, due to the differences between diapir growth velocity and sedimentation rate.

Rectilinear reactive diapirs along the footwalls of basement faults developed during syn-extension homogeneous sedimentation (models B1, B2 and B3), whereas during longitudinal prograding sedimentation coeval with extension non-rectilinear reactive diapirs grew discontinuously because of the silicone inflation ahead of the proximal differential sedimentary load (Model B4). Along-strike continuous passive diapirs grew to different extent depending on the applied post–extension sedimentary pattern. Homogeneous passive diapiric grew with homogeneous deposition (Model B1), whereas well-developed passive diapirs with silicone extrusion increasing from proximal to distal domains were developed with longitudinal prograding sedimentation (Model B2). In transverse prograding sedimentation well- to poorly developed passive and roller-like diapirs developed from proximal to distal domains respectively (Model B3). Non-continuous diapirs inherited from the extension phase also

evolved differently during the post–extension longitudinal progradation, varying from well-developed passive diapirs in proximal domains to incipient reactive diapirs in distal domains (Model B4). All models showed that as thicker is the sedimentary pile higher is the narrowing of the silicone layers on the footwall corners (necking effect). These models depicted how extension and salt withdrawal, influenced by sedimentary patterns, were two interacting mechanisms that caused subsidence during extension, whereas salt migration was the controlling subsidence process during post–extension phases.

The results from models provided clues for the evolution of diapiric structures that, sometimes, were not easy to interpret in the field. In addition, the already published evolution of the Tazoult diapir was evaluated according to the models and the geometry during the reactive phase of the Tazoult diapir was proposed.

The results of the models including compression phase with 6% (Model C1) and 10% (Model C2) of shortening showed that the compression of a salt-related basin resulted in: i) the steepening of the outward flanks of pre-compression silicone diapir walls with dips increasing from 8°–17° prior to compression to 30°–50° after compression; ii) the reopening of the diapir feeding pathway, reducing the necking effect; iii) the tightening of the silicone diapir walls by 32% to 72% with 6% shortening and the full welding of these walls, associated with the development of silicone stocks, when shortening reached 10%. Observations from the models were compared with the published interpretation of the Tazoult–Amezraï area, where Tazoult and Jbel Azourki diapirs are bounding the Amezraï minibasin. Similar compression-related geometries to those obtained in the models were described in the Central High Atlas where, after a calculated shortening of 10.4%, both diapiric structures became welded.

The influence on subsidence patterns of the interaction between both extensional and salt tectonics observed in the analogue models was also studied using calculated total and tectonic subsidence curves computed using GENEX® 4.0.3 software and total subsidence maps built using Temis flow (both software provided BEICIP-FRANLAB).

Subsidence curves in the non-diapiric and marginal Djebel Bou Dahar platform and adjacent basin showed similar long-term and low-rate tectonic and total subsidence of around 0.06 and 0.08 mm yr^{-1} during Sinemurian and Pliensbachian times. The roughly parallel evolution of both total and tectonic subsidence curves indicated the tectonic influence in total subsidence of the platform-basin system, as corroborated by the syndepositional activity of outcropping normal faults. Comparison between Djebel Bou Dahar curves with curves from other localities

of the Fault domain strongly suggested Sinemurian to Pliensbachian ages for the rifting phase of the Central High Atlas.

The subsidence curves from the unstable/diapiric domain, located in the rift axis, were the most distinctive ones compared with subsidence curves from other domains of the Central High Atlas Jurassic rift basin. From the unstable domain, subsidence curves in the Tazoult salt wall and Amezraï minibasin revealed up to one order of magnitude higher subsidence rates than in the Djebel Bou Dahar marginal carbonate platform. The SE flank of the Tazoult salt wall subsided tectonically at rates between 0.01 and 0.27 $mmyr^{-1}$ and with total subsidence rates between 0.09 to 0.74 $mmyr^{-1}$. From Pliensbachian to Early Aalenian, subsidence rates up to two-fold their equivalent in the Tazoult salt wall characterised the sinking evolution of the Amezraï minibasin involving tectonic subsidence rates between 0.06 and 0.32 $mmyr^{-1}$ and total subsidence rates between 0.19 and 0.98 $mmyr^{-1}$.

Also in the unstable domain, subsidence curves and maps from the Imilchil diapiric province showed similar subsidence rates than the obtained in the Amezraï minibasin. The analysis of the Ikassene, Lake Plateau and Ikkou minibasins revealed migration of the subsiding depocentres. The maximum tectonic and total subsidence rates in the Ikassene minibasin were reached during the Aalenian (0.10 and 0.34 $mmyr^{-1}$, respectively), whereas in the Lake Plateau minibasin the faster subsidence occurred during the Early Bathonian, with tectonic and total subsidence rates two times higher in the west (0.23 and 0.90 $mmyr^{-1}$) than in the eastern part of the minibasin (0.10 and 0.43 $mmyr^{-1}$). Contrarily, in the Ikkou minibasin the maximum tectonic and total subsidence rates occurred in the eastern part, reaching their maximum values during the Bajocian (0.15 and 0.40 $mmyr^{-1}$) and spanning up to the Callovian.

A composite subsidence curve was built using Djebel Bou Dahar basin, Amezraï minibasin and Ikkou east minibasin curves, representing the entire Early and Middle Jurassic subsidence evolution of the unstable domain. Comparison of this curve with theoretical thermal subsidence curves from Mackenzie's model for different stretching factors showed how composite subsidence curve exceeded the expected subsidence trend associated with thermal subsidence during post–rift phases. The subsidence mechanisms in the unstable domain were a combination of normal fault extension and salt withdrawal from beneath the minibasin during rifting (Sinemurian-Pliensbachian), being the salt-related subsidence predominant during the post–rift and masking the estimated subsidence pattern of a rift to post–rift transition.

For the first time, 27 new vitrinite reflectance data were used to build the thermal evolution and associated geohistory of the Central High Atlas. Vitrinite reflectance data from the Amezraï minibasin, which ranged from 0.81 to 1.98% and displayed a good fit with their relative Lower Jurassic stratigraphic positions, were used to evaluate the geohistory of the minibasin without the influence of thermal anomalies linked to salt diapirs and magmatic intrusions.

From a total amount of 9, two thermal histories were selected as the end–members of the thermal history of the Amezraï minibasin: i) Low thermal history characterised by a rifting with a heat flow of 70 mW/m^2 (from 189 to 182.7 Ma) followed by a period with heat flow of 60 mW/m^2 and ii) High thermal history characterised by rifting and early post–rift with a heat flow of 105 mW/m^2 (from 189 to 140 Ma) followed by a period of 60mW/m^2. Both thermal histories required additional burial to obtain a good fit between vitrinite reflectance data from samples and calculated reflectance curves from thermal models. The two thermal histories were applied to evaluate the two proposed post–Middle Jurassic histories of the Central High Atlas: i) post–Middle Jurassic evolution with long-term and low-rate subsidence episode associated to sedimentation during Late Jurassic–Early Cretaceous up to the inversion during the Alpine orogeny and ii) post–Middle Jurassic evolution including two exhumation events, in the Late Jurassic–Early Cretaceous and during the Alpine orogeny, proposed by Frizon de Lamotte et al. (2009) according to observations in the West Moroccan Arch.

The model with Late Jurassic–Early Cretaceous sedimentation showed that the Amezraï minibasin required post–Middle Jurassic overburden that ranged between 1200 and 2400 m in thickness, corresponding to the high and low thermal history, respectively. This 1200 to 2400 m-thick overburden was eroded during the Alpine orogeny. The model with two exhumation events showed that the Amezraï minibasin required an additional overburden between 1.7 and 4.25 km in thickness, corresponding to high and low thermal histories, respectively. The calculated overburden was completely eroded during the Late Jurassic–Early Cretaceous exhumation and followed by around 1.5 km-thick deposits eroded during the Alpine orogeny. The exhumation model involving km-scale vertical movements depicted complex geological processes that did not match with the geological observations in the Central High Atlas; strongly suggesting that the uplift and exhumation along the West Moroccan Arch (WMA) did not reach the Central High Atlas. Nevertheless, the WMA uplift and exhumation event recorded more than 100 km westward from the studied area had a limited influence.

The comparison of subsidence curves from this study with Saharan Atlas and Tunisian Atlas showed that peak of subsidence in these salt-related domains became younger to the east.

REFERENCES

9. REFERENCES

Alves, T.M., Manuppella, G., Gawthorpe, R.L., Hunt, D.W., Monteiro, J.H., 2003. The depositional evolution of diapir- and fault-bounded rift basins: Examples from the Lusitanian Basin of West Iberia. Sedimentary Geology 162, 273-303.

Allemand, P., Brun, J.P., Davy, P., Van den Driessche, J., 1989. Symétrie et asymétrie des rift et mécanismes d'amincissement de la lithosphère. Bulletin de la Société Géologique de France 3, 445-451.

Allen, P.A., Allen, J.R., 2005. Basins Analysis. Principles & Applications, 2nd ed. Blackwell Scientific Publications, Oxford, pp. 451.

Amilibia, A., McClay, K.R., Sàbat, F., Muñoz, J.A., Roca, E., 2005. Analogue modelling of inverted oblique rift systems. Geologica Acta 3, 251-271.

Angevine, C.L., Heller, P.L., Paola, C., 1989. Quantitative Sedimentary Basin Modeling, pp. 139.

Arboleya, M.L., Teixell, A., Charroud, M., Julivert, M., 2004. A structural transect through the High and Middle Atlas of Morocco. Journal of African Earth Sciences 39, 319-327.

Athy, L.F., 1930. Density, porosity, and compaction of sedimentary rocks. AAPG Bull. 14, 1-24.

Ayarza, P., Alvarez-Lobato, F., Teixell, A., Arboleya, M.L., Tesón, E., Julivert, M., Charroud, M., 2005. Crustal structure under the central High Atlas Mountains (Morocco) from geological and gravity data. Tectonophysics 400, 67-84.

Babault, J., Teixell, A., Struth, L., Van Den Driessche, J., Arboleya, M.L., Tesón, E., 2013. Shortening, structural relief and drainage evolution in inverted rifts: insights from the Atlas Mountains, the Eastern Cordillera of Colombia and the Pyrenees. Geological Society, London, Special Publications 377, 141-158.

Balé, P., 1986. Tectonique cadomienne en Bretagne nord. Interaction décrochement chevauchement: champs de déformation et modélisations expérimentales. Ph.D thesis, Univerité de Renne 1.

Balestrieri, M.L., Moratti, G., Bigazzi, G., Algouti, A., 2009. Neogene exhumation of the Marrakech High Atlas (Morocco) recorded by apatite fission-track analysis. Terra Nova 21, 75-82.

Ballard, J.F., Brun, J.P., Van den Driessche, J., Allemand, P., 1987. Propagation des chevauchements audessus des zones de décololement: Modèles expérimentaux. Comptes Rendus de l'Academie des Sciences de Paris-Série IIA 305, 1249-1253.

Bally, A.W., 1981. Thoughts on the tectonics of folded belts. Geological Society of London (Special Publication) 9, 13-32.

Baqués, V., Moragas, M., Travé, A., Vergés, J., Martín-Martín, J.D., Saura, E., Messager, G., Hunt, D., 2015. Diagenetic evolution of platform carbonates linked to the diapir growth (Central High Atlas, Morocco), 15th Bathurst Conference of Carbonate Sedimentologists, University of Edinburgh (Edinburgh, UK).

Barbero, L., Teixell, A., Arboleya, M.-L., Rio, P.d., Reiners, P.W., Bougadir, B., 2007. Jurassic-to-present thermal history of the central High Atlas (Morocco) assessed by low-temperature thermochronology. Terra Nova 19, 58-64.

Barton, D.C., Ritz, C.H., Hickey, M., 1933. Gulf coast geosyncline. AAPG Bulletin 17, 1446-1458.

Baudon, C., Fabuel-Perez, I., Redfern, J., 2009. Structural style and evolution of a late Triassic rift basin in the Central High Atlas, Morocco: Controls on sediment deposition. Geological Journal 44, 677-691.

Beauchamp, W., Allmendinger, R.W., Barazangi, M., Demnati, A., El Alji, M., Dahmani, M., 1999. Inversion tectonics and the evolution of the High Atlas Mountains, Morocco, based on a geological-geophysical transect. Tectonics 18, 163-184.

Bond, G.C., Kominz, M.A., 1984. Construction of tectonic subsidence curves for the early Paleozoic miogeocline, southern Canadian Rocky Mountains: Implications for subsidence mechanisms, age of breakup, and crustal thinning. Geological Society of America Bulletin 95, 155-173.

Bouchouata, A., 1994. La ride de Talmest-Tazoult (Haut Atlas Central Maroc), lithostratigraphie, biostratigraphie et relations tectonique-sédimentation au cours du Jurassique. Strata, série 2 (memoires) 25, 219.

Bouchouata, A., Canerot, J., Souhel, A., Almeras, Y., 1995. Jurassic sequence stratigraphy and geodynamic evolution in the Talmest-Tazoult area, Central High Atlas, Morocco. Comptes Rendus de l'Académie des Sciences 320, 749-756.

Boukadi, N., Bedir, M., 1996. Halokinesis in Tunisia: Tectonic context and chronology of events. Comptes Rendus de l'Academie de Sciences - Serie IIa: Sciences de la Terre et des Planetes 322, 587-594.

Bracène, R., 2002. Geodynamique du nord de l'Algerie: Impact sur l'exploration pétrolière. Université de Cergy-Pontoise, Paris, p. 197.

Bracène, R., Patriat, M., Ellouz, N., Gaulier, J.-M., 2003. Subsidence history in basins of northern Algeria. Sedimentary Geology 156, 213-239.

Brandon, M.T., Roden-Tice, M.K., Garver, J.I., 1998. Late Cenozoic exhumation of the Cascadia accretionary wedge in the Olympic Mountains, northwest Washington State. Geological Society of America Bulletin 110, 985-1009.

Brechbühler, Y.A., Bernasconi, R., Schaer, J.P., 1988. Jurassic sediments of the Central High Atlas of Morocco: Deposition, burial and erosian history, in: Jacobshagen, V. (Ed.), The Atlas System of Morocco. Springer Berlin Heidelberg, pp. 201-217.

Brede, R., Hauptmann, M., Herbig, H.G., 1992. Plate tectonics and intracratonic mountain ranges in Morocco - The mesozoic-cenozoic development of the Central High Atlas and the Middle Atlas. Geologische Rundschau 81, 127-141.

Brun, J.P., Mauduit, T.P.O., 2009. Salt rollers: Structure and kinematics from analogue modelling. Marine and Petroleum Geology 26, 249-258.

Burliga, S., Koyi, H.A., Chemia, Z., 2012. Analogue and numerical modelling of salt supply to a diapiric structure rising above an active basement fault. Geological Society, London, Special Publications 363, 395-408.

Callot, J.P., Jahani, S., Letouzey, J., 2007. The role of pre-existing diapirs in fold and thrust belt development, in: Lacombe, O.L., J.; Roure, F.; Vergés, J. (Ed.), Thrust Belts and Foreland Basins From Fold Kinematics to Hydrocarbon Systems., pp. 309-326.

Callot, J.P., Trocmé, V., Letouzey, J., Albouy, E., Jahani, S., Sherkati, S., 2012. Pre-existing salt structures and the folding of the Zagros Mountains. Geological Society, London, Special Publications 363, 545-561.

Cohen, H.A., McClay, K., 1996. Sedimentation and shale tectonics of the northwestern Niger Delta front. Marine and Petroleum Geology 13, 313-328.

Contreras, J., Zühlke, R., Bowman, S., Bechstädt, T., 2010. Seismic stratigraphy and subsidence analysis of the southern Brazilian margin (Campos, Santos and Pelotas basins). Marine and Petroleum Geology 27, 1952-1980.

Courel, L., Aït Salem, H., Benaouiss, N., Et-Touhami, M., Fekirine, B., Oujidi, M., Soussi, M., Tourani, A., 2003. Mid-Triassic to Early Liassic clastic/evaporitic deposits over the Maghreb Platform. Palaeogeography, Palaeoclimatology, Palaeoecology 196, 157-176.

Charrière, A., Ibouh, H., Haddoumi, H., 2011. Central High Atlas from Beni Mellal to Imilchil. Notes et Memoires du Service Géologique du Maroc 559, 109-164.

Davy, P., Cobbold, P.R., 1991. Experiments on shortening of a 4-layer model of the continental lithosphere. Tectonophysics 188, 1-25.

Della Porta, G., Merino-Tomé, O., Kenter, J.A.M., Verwer, K., 2014. Lower Jurassic Microbial and Skeletal Carbonate Factories and Platform Geometry (Djebel Bou Dahar, High Atlas, Morocco) Deposits, Architecture, and Controls of Carbonate Margin, Slope and Basinal Settings. SEPM Society for Sedimentary Geology, pp. 237-263.

Diegel, F.A., Karlo, J.F., Schuster, D.C., Shoup, R.C., Tauvers, P.R., 1995. Cenozoic structural evolution and tectono-stratigraphic framework of the Northern Gulf Coast Continental Margin, in: Jackson, M.P.A., Roberts, D.G., Snelson, S. (Eds.), Salt tectonics: a global perspective, AAPG Memoir 65, pp. 109-151.

Doglioni, C., Dagostino, N., Mariotti, G., 1998. Normal faulting vs regional subsidence and sedimentation rate. Marine and Petroleum Geology 15, 737-750.

Domènech, M., 2015. Rift opening and inversion in the Marrackech High Atlas: integrated structural and thermochronologic study, Unitat Geotectònica. Universitat Autònoma de Barcelona, Bellaterra, Spain, p. 157.

Domènech, M., Teixell, A., Babault, J., Arboleya, M.-L., 2015. The inverted Triassic rift of the Marrakech High Atlas: A reappraisal of basin geometries and faulting histories. Tectonophysics 663, 177-191.

Domènech, M., Teixell, A., Stockli, D.F., 2016. Magnitude of rift-related burial and orogenic contraction in the Marrakech High Atlas revealed by zircon (U-Th)/He thermochronology and thermal modelling. Tectonics 35, 2609-2635.

Dooley, T., Hudec, M.R., Carruthers, D., Jackson, M.P.A., Luo, G., 2017. The effects of base-salt relief on salt flow and suprasalt deformation patterns - Part 1: Flow across simple steps in the base of salt. Interpretation 5, 1-23.

Dooley, T., McClay, K.R., Hempton, M., Smit, D., 2005. Salt tectonics above complex basement extensional fault systems: Results from analogue modelling, in: Doré, A.G., Vining, B.A. (Eds.), Petroleum Geology: North-West Europe and Global Perspectives. Geological Society London, pp. 1631-1648.

Dooley, T., McClay, K.R., Pascoe, R., 2003. 3D analogue models of variable displacement extensional faults: applications to the Revfallet Fault system, offshore mid-Norway. Geological Society, London, Special Publications 212, 151-167.

Dooley, T.P., Jackson, M.P.A., Hudec, M.R., 2009. Inflation and deflation of deeply buried salt stocks during lateral shortening. Journal of Structural Geology 31, 582-600.

Du Dresnay, R., 1976. Carte Géologique du Marroc Huat Atlas D'Anoual-Bou Anane (Haut Atlas Oriental), Notes et Memoires du Service Géologique du Maroc (246).

Duffy, O.B., Gawthorpe, R.L., Docherty, M., Brocklehurst, S.H., 2013. Mobile evaporite controls on the structural style and evolution of rift basins: Danish Central Graben, North Sea. Basin Research 25, 310-330.

Dupré, S., Bertotti, G., Cloetingh, S., 2007. Tectonic history along the South Gabon Basin: Anomalous early post–rift subsidence. Marine and Petroleum Geology 24, 151-172.

Ellouz, N., Patriat, M., Gaulier, J.-M., Bouatmani, R., Sabounji, S., 2003. From rifting to Alpine inversion: Mesozoic and Cenozoic subsidence history of some Moroccan basins. Sedimentary Geology 156, 185-212.

Ettaki, M., Ibouh, H., Chellaï, E.H., Milhi, A., 2007. Liassic diapiric structures from the Central High Atlas, Morocco; Ikerzi ride example. Africa Geoscience Review 14, 79-93.

Fadile, A., 2003. Carte Géologique du Marroc, feuille Imilchil, Notes et Memoires du Service Géologique du Maroc (397).

Farley, K.A., 2000. Helium diffusion from apatite: General behavior as illustrated by Durango fluorapatite. Journal of Geophysical Research B: Solid Earth 105, 2903-2914.

Fatah, S.E.M., Bensaïd, M., Dahmani, M., 1990. Carte Géologique du Marroc, feuille Tounfite, Notes et Memoires du Service Géologique du Maroc (357).

Faugère, E., Brun, J.P., 1984. Modélisation expérimentale de la distension continentale. Compte-Rendus de l'Académie des Sciences de Paris 299, 365-370.

Ferrer, O., Carrera, N., Roca, E., Muñoz, J.A., Rowan, M.G., Giles, K.A., 2016. Experimental approach to megaflap development during passive salt diapirism: Controlling factors and kinematics (abs.), AAPG/Society of Exploration Geophysicists International Conference and Exhibition, Barcelona, Spain, p. 285.

Fraissinet, C., El Zouine, M., Morel, J.-L., Poisson, A., Andrieux, J., Faure-Muret, A., 1988. Structural evolution of the southern and northern Central High Atlas in paleogene and Mio-Pliocene times, in: Jacobshagen, V. (Ed.), The Atlas System of Morocco. Springer Berlin Heidelberg, pp. 273-291.

Frizon de Lamotte, D., Bezar, B.S., Bracène, R., Mercier, E., 2000. The two main steps of the Atlas building and geodynamics of the western Mediterranean. Tectonics 19, 740-761.

Frizon De Lamotte, D., Fourdan, B., Leleu, S., Leparmentier, F., De Clarens, P., 2015. Style of rifting and the stages of Pangea breakup. Tectonics 34, 1009-1029.

Frizon de Lamotte, D., Leturmy, P., Missenard, Y., Khomsi, S., Ruiz, G., Saddiqi, O., Guillocheau, F., Michard, A., 2009. Mesozoic and Cenozoic vertical movements in the Atlas system (Algeria, Morocco, Tunisia): An overview. Tectonophysics 475, 9-28.

Frizon de Lamotte, D., Raulin, C., Mouchot, N., Wrobel-Daveau, J.-C., Blanpied, C., Ringenbach, J.-C., 2011. The southernmost margin of the Tethys realm during the Mesozoic and Cenozoic: Initial geometry and timing of the inversion processes. Tectonics 30, 1-22.

Frizon de Lamotte, D., Zizi, M., Missenard, Y., Hafid, M., Azzouzi, M., Maury, R.C., Charrière, A., Taki, Z., Benammi, M., Michard, A., 2008. The Atlas System, Continental Evolution: The Geology of Morocco, pp. 133-202.

Fullea, J., Fernàndez, M., Afonso, J.C., Vergés, J., Zeyen, H., 2010. The structure and evolution of the lithosphere-asthenosphere boundary beneath the Atlantic-Mediterranean Transition Region. Lithos 120, 74-95.

Gaullier, V., Vendeville, B.C., 2005. Salt tectonics driven by sediment progradation: Part II - Radial spreading of sedimentary lobes prograding above salt. AAPG Bulletin 89, 1081-1089.

GDL, 2011. Integrated Structural and Geodynamic Research Studies: High Atlas Diapiric Ridges and Platform Margins. Group of Dynamics of the Lithosphere Institute of Earth Sciences "Jaume Almera", CSIC, Barcelona (GDL-Statoil internal report), pp. 402.

GDL, 2012. Integrated Structural and Geodynamic Research Studies: Tectonic structure of the early-middle Jurassic High Atlas Basin: Relationships between salt diapirism, blind normal faults and volcanism and carbonate platform margins. Group of Dynamics of the Lithosphere Institute of Earth Sciences "Jaume Almera", CSIC, Barcelona (GDL-Statoil internal report), pp. 340.

Ge, H., Jackson, M.P.A., Vendeville, B.C., 1997. Kinematics and dynamics of salt tectonics driven by progradation. AAPG Bulletin 81, 398-423.

Ghorbal, B., Bertotti, G., Foeken, J., Andriessen, P., 2008. Unexpected Jurassic to Neogene vertical movements in ‘stable’ parts of NW Africa revealed by low temperature geochronology. Terra Nova 20, 355-363.

Giles, K.A., Lawton, T.F., 2002. Halokinetic sequence stratigraphy adjacent to the El Papalote diapir, Northeastern Mexico. AAPG Bulletin 86, 823-840.

Gomez, F., Beauchamp, W., Barazangi, M., 2000. Role of the Atlas Mountains (northwest Africa) within the African-Eurasian plate-boundary zone. Geology 28, 775-778.

Görler, K., Helmdach, F.-F., Gaemers, P., Heißig, K., Hinsch, W., Mädler, K., Schwarzhans, W., Zucht, M., 1988. The uplift of the central High Atlas as deduced from neogene continental sediments of the Ouarzazate province, Morocco, in: Jacobshagen, V. (Ed.), The Atlas System of Morocco. Springer Berlin Heidelberg, pp. 359-404.

Gouiza, M., Bertotti, G., Hafid, M., Cloetingh, S., 2010. Kinematic and thermal evolution of the Moroccan rifted continental margin: Doukkala-High Atlas transect. Tectonics 29, 1-22.

Gradstein, F.M., Ogg, J.G., Schmitz, M.D., Ogg, G.M., 2012. The Geologic Time Scale 2012. Elsevier, Boston.

Graham, R., Jackson, M., Pilcher, R., Kilsdonk, B., 2012. Allochthonous salt in the sub-Alpine fold–thrust belt of Haute Provence, France. Geological Society, London, Special Publications 363, 595-615.

Green, P.F., Duddy, I.R., Laslett, G.M., Hegarty, K.A., Gleadow, A.J.W., Lovering, J.F., 1989. Thermal annealing of fission tracks in apatite 4. Quantitative modelling techniques and extension to geological timescales. Chemical Geology: Isotope Geoscience Section 79, 155-182.

Grélaud, C., Razin, P., Joussiaume, R., Malaval, M., Vergés, J., Saura, E., Martín-Martín, J.D., Moragas, M., Hunt, D., Messager, G., 2014. Diapiric control on Jurassic carbonate systems of the High Atlas Basin, Morocco, AAPG Annual Meeting, Houston, Texas.

Guerra, M.C.M., Underhill, J.R., 2012. Role of halokinesis in controlling structural styles and sediment dispersal in the Santos Basin, offshore Brazil. Geological Society, London, Special Publications 363, 175-206.

Guiraud, R., 1998. Mesozoic rifting and basin inversion along the northern African Tethyan margin: an overview. Geological Society, London, Special Publications 132, 217-229.

Gupta, S., Cowie, P.A., Dawars, N.H., underhill, J.R., 1998. A mechanism to explain rift-basin subsidence and stratigraphic patterns through fault-array evolution. Geology 26, 595-598.

Haddoumi, H., Charrière, A., Feist, M., Andreu, B., 2002. New ages (Upper Hauterivian-Lower Barremian) of the continental 'Red Beds' of the Moroccan central High Atlas; consequences on the ages of the magmatism and of the Mesozoic tectonics of the Atlasic Belt. Nouvelles datations (Hauterivien supérieur-Barrémien inférieur) dans les «Couches rouges» continentales du Haut Atlas central marocain ; conséquences sur l'âge du magmatisme et des structurations mésozoïques de la chaîne Atlasique 1, 259-266.

Haddoumi, H., Charrière, A., Mojon, P.O., 2010. Stratigraphy and sedimentology of the Jurassic-Cretaceous continental " Redbeds" of the central High Atlas (Morocco): Paleogeographical and geodynamical implications. Geobios 43, 433-451.

Hafid, M., 2000. Triassic-early Liassic extensional systems and their Tertiary inversion, Essaouira Basin (Morocco). Marine and Petroleum Geology 17, 409-429.

Hafid, M., Tari, G., Bouhadioui, D., Moussaid, I., Echarfaoui, H., Salem, A., Nahim, M., Dakki, M., 2008. Atlantic Basins, Continental Evolution: The Geology of Morocco, pp. 303-329.

Hafid, M., Zizi, M., Bally, A.W., Ait Salem, A., 2006. Structural styles of the western onshore and offshore termination of the High Atlas, Morocco. Comptes Rendus - Geoscience 338, 50-64.

Hailwood, E.A., Mitchell, J.G., 1971. Palaeomagnetic and Radiometric Dating Results from Jurassic Intrusions in South Morocco. Geophysical Journal International 24, 351-364.

Herkat, M., 1982. Lithostratigraphie et sédimentologie des formations carbonatées du jurassique supérieur des monts des Oulad Nail et de la terminaison orientale du Djebel Amour (Atlas saharien). Université de Pau et des Pays de l'Adour, Pau (France), p. 304.

Hodgson, N.A., Farnsworth, J., Fraser, A.J., 1992. Salt-related tectonics, sedimentation and hydrocarbon plays in the Central Graben, North Sea, UKCS. Geological Society of London (Special Publication) 67, 31-63.

Hudec, M.R., Jackson, M.P.A., 2007. Terra infirma: Understanding salt tectonics. Earth-Science Reviews 82, 1-28.

Hudec, M.R., Jackson, M.P.A., Schultz-Ela, D.D., 2009. The paradox of minibasin subsidence into salt: Clues to the evolution of crustal basins. Geological Sociaty American Bulletin 121, 201-221.

Ibouh, H., Michard, A., Charrière, A., Benkaddour, A., Rhoujjati, A., 2014. Tectonic-karstic origin of the alleged "impact crater" of Lake Isli (Imilchil district, High Atlas, Morocco). Comptes Rendus - Geoscience 346, 82-89.

Jackson, C.A.L., Kane, K.E., Larsen, E., 2010. Structural evolution of minibasins on the Utsira High, northern North Sea; implications for Jurassic sediment dispersal and reservoir distribution. Petroleum Geoscience 16, 105-120.

Jackson, C.A.L., Lewis, M.M., 2015. Structural style and evolution of a salt-influenced rift basin margin; the impact of variations in salt composition and the role of polyphase extension. Basin Research 28, 81-102.

Jackson, M.P.A., Talbot, C.J., 1986. External shapes, strain rates, and dynamics of salt structures. Geological Society of America Bulletin 97, 305-323.

Jackson, M.P.A., Talbot, C.J., 1994. Advances in salt tectonics in: Hancock, P.L. (Ed.), Continental deformation. Pergamon Press, New York, pp. 159-179.

Jackson, M.P.A., Vendeville, B.C., 1994. Regional extension as a geologic trigger for diapirism. Geological Society of America Bulletin 106, 57-73.

Jackson, M.P.A., Vendeville, B.C., Shultz-Ela, D.D., 1994. Structural dynamics of salt systems. Annual Review of Earth and Planetary Sciences 22, 93-117.

Jacobshagen, V., 1992. Major fracture zones of Morocco: The South Atlas and the Transalboran fault systems. Geologische Rundschau 81, 185-197.

Jarvis, G.T., 1984. An extensional model of graben subsidence the first stage of basin evolution. Sedim. Geol. 40, 13-31.

Jenny, J., Le Marrec, A., Monbaron, M., 1981. Middle Jurassic red beds of central High Atlas (Morocco): lithostratigraphic correlations, dating data and tectono- sedimentary framework. Bulletin, Societe Geologique de France 23, 627-639.

Jossen, J.A., Couvreur, G., 1990. Carte Géologique du Marroc, feuille Zawyat Ahançal, Notes et Memoires du Service Géologique du Maroc (355).

Joussiaume, R., 2016. "Les relations entre diapirisme et sédimentation: Exemple du Jurassique moyen de la région d'Imilchil, Haut-Atlas central, Maroc". (The relationships between diapirism and sedimentation: An example from the Middle Jurassic of the Imilchil area, Central High-Atlas, Morocco.). Université Bordeaux-Montaigne Pessac, France.

Joussiaume, R., Malaval, M., Razin, P., Grélaud, C., Messager, G., Martín-Martín, J.D., Saura, E., Moragas, M., Vergés, J., Hunt, D., 2014. Characterization of syn-diapiric Jurassic sedimentation in the Taghia and Tazoult areas, Central High Atlas, Morocco, 19th International Sedimentological Congress. International Association of Sedimentologist, Geneva, Switzerland, p. 335.

Kane, K.E., Jackson, C.A.L., Larsen, E., 2010. Normal fault growth and fault-related folding in a salt-influenced rift basin: South Viking Graben, offshore Norway. Journal of Structural Geology 32, 490-506.

Kenter, J.A.M., Campbell, A.E., 1991. Sedimentation on a Lower Jurassic carbonate platform flank: geometry, sediment fabric and related depositional structures (Djebel Bou Dahar, High Atlas, Morocco). Sedimentary Geology 72, 1-34.

Koyi, H., 1996. Salt flow by aggrading and prograding overburdens. Geological Society, London, Special Publications 100, 243-258.

Koyi, H., 1998. The shaping of salt diapirs. Journal of Structural Geology 20, 321-338.

Koyi, H., Jenyon, M.K., Petersen, K., 1993. The effect of basement faulting on diapirism. Journal of Petroleum Geology 16, 285-312.

Krantz, R.W., 1991. Measurements of friction coefficients and cohesion for faulting and fault reactivation in laboratory models using sand and sand mixtures. Tectonophysics 188, 203-207.

Lachkar, N., Guiraud, M., El Harfi, A., Dommergues, J.L., Dera, G., Durlet, C., 2009. Early Jurassic normal faulting in a carbonate extensional basin: Characterization of tectonically driven platform drowning (High Atlas rift, Morocco). Journal of the Geological Society 166, 413-430.

Laville, E., 1988. A multiple releasing and restraining stepover model for the Jurassic strike-slip basin of the Central High Atlas (Morocco), in: Mainspeizer, W. (Ed.), Triassic-Jurassic Rifting: Continental breakup and the origin of the Atlantic Ocean and Passive Margins. Elsevier Science, New York, pp. 409-523.

Laville, E., 2002. Role of the Atlas Mountains (northwert Africa) whithin the African-Eurasian plate-boundary zone: Comment and Reply. Geology 30, 95-96.

Laville, E., Harmand, C., 1982. Magmatic and tectonic evolution of Mesozoic intracontinental basin High-Atlas Mountains, Morocco: a model of synsedimentary anorogenic intrusions linked to strike slip faults. Bulletin de la Société Géologique de France 24, 213-227.

Laville, E., Lesage, J.-L., Seguret, M., 1977. Geometrie, cinematique (dynamique) de la tectonique atlasique sur le versant sud du Haut Atlas marocain; apercu sur les tectoniques hercyniennes et tardi-hercyniennes. Bulletin de la Societe Geologique de France Series 7 Vol. XIX, 527-539.

Laville, E., Piqué, A., 1992. Jurassic penetrative deformation and Cenozoic uplift in the Central High Atlas (Morocco): A tectonic model. structural and orogenic inversions. Geologische Rundschau 81, 157-170.

Laville, E., Pique, A., Amrhar, M., Charroud, M., 2004. A restatement of the Mesozoic Atlasic Rifting (Morocco). Journal of African Earth Sciences 38, 145-153.

Le Roy, P., Guillocheau, F., Piqué, A., Morabet, A.M., 1998. Subsidence of the Atlantic Moroccan margin during the Mesozoic. Canadian Journal of Earth Sciences 35, 476-493.

Le Roy, P., Piqué, A., 2001. Triassic-Liassic western Moroccan synrift basins in relation to the Central Atlantic opening. Marine Geology 172, 359-381.

Letouzey, J., Colletta, B., Vially, R., Chermette, J.C., 1995. Evolution of Salt-Related Structures in Compressional Settings, in: Jackson, M.P.A., Roberts, D.G., Snelson, S. (Eds.), AAPG Memoir 65 on Salt Tectonics: a global perspective, pp. 41-60.

Lewis, M.M., Jackson, C.A.L., Gawthorpe, R.L., 2013. Salt-influenced normal fault growth and forced folding: The Stavanger Fault System, North Sea. Journal of Structural Geology 54, 156-173.

Magri, F., Littke, R., Rodon, S., Bayer, U., Urai, J.L., 2008. Temperature fields, petroleum maturation and fluid flow in the vicinity of salt domes, in: Littke, R., Bayer, U., Gajewski, D., Nelskamp, S. (Eds.), Dynamic of complex intracontinental basin: The Central European Basin System. Springer, pp. 323 - 344.

Malaval, M., 2016. "Enregistrement sédimentaire de l'activité diapirique associée à la ride du Jbel Azourki, Haut Atlas central, Maroc: Impact sur la géométrie des dépôts et la distribution des faciès des systèmes carbonatés et mixtes du Jurassique inférieur". (Synsedimentary record of diapiric activity related to the Jbel Azourki ridge, Central High Atlas, Morocco: Impact on

depositional geometries and facies distribution of the Lower Jurassic carbonate and mixed systems.). Université Bordeaux-Montaigne Pessac, France.

Malaval, M., Joussiaume, R., Razin, P., Grélaud, C., Messager, G., Martín-Martín, J.D., Saura, E., Moragas, M., Vergés, J., Hunt, D., 2014. Characterization of syn-diapiric Jurassic sedimentation in the Imilchil area, Central High Atlas, Morocco, 19th International Sedimentological Congress. International Association of Sedimentologist, Geneva, Switzerland, p. 461.

Malavieille, J., 1984. Modélisation expérimentale des chevauchements imbriqués: application aux chaînes de montagnes. Bulletin de la Société Géologique de France XXVI, 129-138.

Malusà, M.G., Polino, R., Feroni, A.C., Ellero, A., Ottria, G., Baidder, L., Musumeci, G., 2007. Post–Variscan tectonics in eastern anti-atlas (Morocco). Terra Nova 19, 481-489.

Mannie, A.S., Jackson, C.A.L., Hampson, G.J., 2014. Structural controls on the stratigraphic architecture of net-transgressive shallow-marine strata in a salt-influenced rift basin: Middle-to-Upper Jurassic Egersund Basin, Norwegian North Sea. Basin Research 26, 675-700.

Martín-Martín, J.D., Vergés, J., Saura, E., Moragas, M., Messager, G., Baqués, V., Razin, P., Grélaud, C., Malaval, M., Joussiaume, R., Casciello, E., Cruz-Orosa, I., Hunt, D.W., 2016. Diapiric growth within an Early Jurassic rift basin: the Tazoult salt wall (Central High Atlas, Morocco). Tectonics 35, 1-31.

Masrouhi, A., Bellier, O., Koyi, H., 2014. Geometry and structural evolution of Lorbeus diapir, northwestern Tunisia: polyphase diapirism of the North African inverted passive margin. International Journal of Earth Sciences 103, 881-900.

Mattauer, M., Tapponier, P., Proust, F., 1977. Sur les mécanismes de formation des chaines intracontinentales: L'exemple des chaines atlasiques du Maroc. Bull. Soc. Géol. France 77 (7), 521-526.

McClay, K., Dooley, T., Lewis, G., 1998. Analog modeling of progradational delta systems. Geology 26, 771-774.

McClay, K., Dooley, T., Zamora, G., 2003. Analogue models of delta systems above ductile substrates, in: Van Rensbergen, P., Hillis, R.R., Maltman, A.J., Morley, C.K. (Eds.), Subsurface sediment mobilization. Geological Society of London (Special Publication), pp. 411-428.

McClay, K., Muñoz, J.A., García-Senz, J., 2004. Extensional salt tectonics in a contractional orogen: A newly identified tectonic event in the Spanish Pyrenees. Geology 32, 737–740.

McKenzie, D.P., 1978. Some remarks on the development of sedimentary basins. Earth and Planetary Science Letters 40, 25-32.

Merino-Tomé, O., Porta, G.D., Kenter, J.A.M., Verwer, K., Harris, P.M., Adams, E.W., Playton, T., Corrochano, D., 2012. Sequence development in an isolated carbonate platform (Lower Jurassic, Djebel Bou Dahar, High Atlas, Morocco): Influence of tectonics, eustacy and carbonate production. Sedimentology 59, 118-155.

Michard, A., Ibouh, H., Charrière, A., 2011. Syncline-topped anticlinal ridges from the High Atlas: A Moroccan conundrum, and inspiring structures from the Syrian Arc, Israel. Terra Nova 23, 314-323.

Milhi, A., Ettaki, M., Chellai, E.H., Hadri, M., 2002. The lithostratigraphic formations of moroccan jurassic central High-Atlas: Interelationships and paleogeographic reconstitution. Revue de Paleobiologie 21, 241-256.

Missenard, Y., Saddiqi, O., Barbarand, J., Leturmy, P., Ruiz, G., Haimer, F.-Z.E., Lamotte, D.F.d., 2008. Cenozoic denudation in the Marrakech High Atlas, Morocco: insight from apatite fission-track thermochronology. Terra Nova 20, 221-228.

Missenard, Y., Zeyen, H., Frizon de Lamotte, D., Leturmy, P., Petit, C., Sébrier, M., Saddiqi, O., 2006. Crustal versus asthenospheric origin of relief of the Atlas Mountains of Morocco. Journal of Geophysical Research 111, 1-13.

Mohriak, W.U., Leroy, S., 2012. Architecture of rifted continental margins and break-up evolution: insights from the South Atlantic, North Atlantic and Red Sea–Gulf of Aden conjugate margins, in: Mohriak, W., Danforth, A., Post, P.J., Brown, D., Tari, G., Nemčok, M., Sinha, N. (Eds.), Conjugate Divergent Margins. Geological Society, London, Special Publications, pp. 1-39.

Moragas, M., Vergés, J., Saura, E., Martín-Martín, J.-D., Messager, G., Merino-Tomé, Ó., Suárez-Ruiz, I., Razin, P., Grélaud, C., Malaval, M., Joussiaume, R., Hunt, D.W., 2016. Jurassic rifting to post–rift subsidence analysis in the Central High Atlas and its relation to salt diapirism. Basin Research, 1-27.

Morgan, P., 1983. Constraints on rift thermal processes from heat flow and uplift. Tectonophysics 94, 277-298.

Moseley, F., Cuttell, J.C., Lange, E.W., Stevens, D., Warbrick, J.R., 1981. Alpine tectonics and diapiric structures in the Pre-Betic zone of southeast Spain. Journal of Structural Geology 3, 237-251.

Nalpas, T., Brun, J.P., 1993. Salt flow and diapirism related to extension at crustal scale. Tectonophysics 228, 349-362.

Nalpas, T., Le Douaran, S., Brun, J.-P., Unternehr, P., Richert, J.-P., 1995. Inversion of the Broad Fourteens Basin (offshore Netherlands), a small-scale model investigation. Sedimentary Geology 95, 237-250.

Neumaier, M., Back, S., Littke, R., Kukla, P.A., Schnabel, M., Reichert, C., 2015. Late Cretaceous to Cenozoic geodynamic evolution of the Atlantic margin offshore Essaouira (Morocco). Basin Research 28, 712-730.

Nouiouat, S., 1994. Etude sédimentologique des récifs du Jurassique supérieur (passage Oxfordien - Kimméridgien) de l'Atlas saharien centro-oriental (Djebel Amour-Ouled- Naïl). Organisation de l'écosystème récifa l'eustatisme, mise en place. Université des Sciences et de la tecnologie Houari Boumediene, Algiers (Algeria).

Oujidi, M., Courel, L., Benaouiss, N., El Mostaine, M., El Youssi, M., Et Touhami, M., Ouarhache, D., Sabaoui, A., Tourani, A., 2000. Triassic series of Morocco: stratigraphy, palaeogeography and structuring of the southwestern Peri-Tethyan platform. An overview, in: Crasquin-Soleau, S., Barrier, E. (Eds.), Peri-Tethys Memoir 5: New data on Peri-Tethyan sedimentary basins. Mémoires du Muséum National d´Histoire Naturelle, Paris, pp. 23-38.

Oukassou, M., Saddiqi, O., Barbarand, J., Sebti, S., Baidder, L., Michard, A., 2013. Post–Variscan exhumation of the Central Anti-Atlas (Morocco) constrained by zircon and apatite fission-track thermochronology. Terra Nova 25, 151-159.

Pascoe, R., Hooper, R., Storhaug, K., Harper, H., 1999. Evolution of extensional styles at the southern termination of the Nordland Ridge, Mid-Norway: A response to variations in coupling above Triassic salt, Petroleum Geology Conference Proceedings, pp. 83-90.

Patriat, M., Ellouz, N., Dey, Z., Gaulier, J.M., Kilani Haten Ben, H., 2003. The Hammamet, Gabès and Chotts basins (Tunisia): A review of the subsidence history. Sedimentary Geology 156, 241-262.

Pereira, R., Alves, T.M., 2011. Margin segmentation prior to continental break-up: A seismic-stratigraphic record of multiphased rifting in the North Atlantic (Southwest Iberia). Tectonophysics 505, 17-34.

Perthuisot, V., 1981. Diapirism in Northern Tunisia. Journal of Structural Geology 3, 231-235.

Perthuisot, V., Rouvier, H., 1992. The diapirs from central and eastern Maghreb: diverse apparatus resulting from a complex structural and petrogenetic development. Bulletin - Societe Geologique de France 163, 751-760.

Petersen, K., Lerche, I., 1995. Quantification of thermal anomalies in sediments around salt structures. Geothermics 24, 253-268.

Petersen, K., Lerche, I., 1996. Temperature dependence of thermal anomalies near evolving salt structures: importance for reducing exploration risk. Geological Society, London, Special Publications 100, 275-290.

Pierre, A., Durlet, C., Razin, P., Chellai, E.H., 2010. Spatial and temporal distribution of ooids along a Jurassic carbonate ramp: Amellago outcrop transect, High-Atlas, Morocco, in: Van Buchem, F.S.P., Gerdes, K.D., Esteban, M. (Eds.), Mesozoic and Cenozoic Carbonate Systems of the Mediterranean and the Middle East: Stratigraphic and Siagenetic Reference Models. Geological Society of London, Special Publications, pp. 65-88.

Piqué, A., Charroud, M., Laville, E., Aït Brahim, L., Amrhar, M., 2000. The Thethys southern margin in Morocco: Mesozoic and Cenozoic evolution of the Atlas domain, in: Crasquin, S., Barrier, E. (Eds.), Peri-Tethys Memoir 5: New data on peri-Tethyan sedimentary basins. Mémoires du Muséum National d´Histoire Naturelle, Paris, pp. 93-106.

Piqué, A., Tricart, P., Guiraud, R., Laville, E., Bouaziz, S., Amrhar, M., Ait Ouali, R., 2002. The Mesozoic-Cenozoic Atlas belt (North Africa): an overview. Geodinamica Acta 15, 185-208.

Poisson, A., Hadri, M., Milhi, A., Julien, M., Andrieux, J., 1998. The Central High-Atlas (Morocco). Litho- and chrono-stratigraphic correlations during Jurassic times between Tinjdad and Tounfite. Origin of Subsidence, in: Crasquin, S., Barrier, E. (Eds.), Peri-Tethys Memoir 4: Epicratonic Basins of Peri-Tethyan Platforms. Mémoires du Muséum National d´Histoire Naturelle, Paris, pp. 237-256.

Quiquerez, A., Sarih, S., Allemand, P., Garcia, J.P., 2013. Fault rate controls on carbonate gravity-flow deposits of the Liassic of Central High Atlas (Morocco). Marine and Petroleum Geology 43, 349-369.

Quirk, D.G., Pilcher, R.S., 2012. Flip-flop salt tectonics. Geological Society, London, Special Publications 363, 245-264.

Redfern, J., Shannon, P.M., Williams, B.P.J., Tyrrell, S., Leleu, S., Fabuel Perez, I., Baudon, C., Štolfová, K., Hodgetts, D., van Lanen, X., Speksnijder, A., Haughton, P.D.W., Daly, J.S., 2010. An integrated study of Permo-Triassic basins along the North Atlantic passive margin: implication for future exploration. Geological Society, London, Petroleum Geology Conference series 7, 921-936.

Reiners, P.W., Ehlers, T.A., Zeitler, P.K., 2005. Past, present, and future of thermochronology, Reviews in Mineralogy and Geochemistry, pp. 1-18.

Richardson, N.J., Underhill, J.R., Lewis, G., 2005. The role of evaporite mobility in modifying subsidence patterns during normal fault growth and linkage, Halten Terrace, Mid-Norway. Basin Research 17, 203-223.

Rimi, A., Fernández, M., Manar, A., Matsushima, J., Okubo, Y., Morel, J.-L., Winckel, A., Zeyen, H., 2005. Geothermal anomalies and analysis of the gravity, fracturing and magnetic features in Morocco, Proceedings World Geothermal Congress, Antalya, Turkey.

Ríos, J.M., 1948. Diapirismo. Boletin Geológico y Minero de España LX.

Rodgers, J., 1987. Chains of basement uplifts within cratons marginal to orogenic belts. Am. J. Sci. 287, 661-692.

Rowan, M.G., Giles, K.A., Hearon, T.E., Fiduk, J.C., 2016. Megaflaps adjacent to salt diapirs. AAPG Bulletin 100, 1723-1747.

Rowan, M.G., Jackson, M.P.A., Trudgill, B.D., 1999. Salt-related fault families and fault welds in the northern Gulf of Mexico. AAPG Bulletin 83, 1454-1484.

Rowan, M.G., Lawton, T.F., Giles, K.A., Ratliff, R.A., 2003. Near-salt deformation in La Popa basin, Mexico, and the northern Gulf of Mexico: A general model for passive diapirism. AAPG Bulletin 87, 733–756.

Rowan, M.G., Vendeville, B.C., 2006. Foldbelts with early salt withdrawal and diapirism: Physical model and examples from the northern Gulf of Mexico and the Flinders Ranges, Australia. Marine and Petroleum Geology 23, 871-891.

Rowan, M.G., Vendeville, B.C., 2007. Shortening of salt diapirs and minibasin in both passive margin and convegent-margin settings, MAPG First International Conference & Exhibition, Marrakech, Morocco.

Ruiz, G.M.H., Sebti, S., Negro, F., Saddiqi, O., Frizon De Lamotte, D., Stockli, D., Foeken, J., Stuart, F., Barbarand, J., Schaer, J.P., 2011. From central Atlantic continental rift to Neogene uplift - western Anti-Atlas (Morocco). Terra Nova 23, 35-41.

Sachse, V.F., Leythaeuser, D., Grobe, A., Rachidi, M., Littke, R., 2012. Organic geochemistry and petrology of a lower Jurassic (Pliensbachian) petroleum source rock from Aït Moussa, Middle Atlas, Morocco. Journal of Petroleum Geology 35, 5-23.

Saddiqi, O., El Haimer, F.Z., Michard, A., Barbarand, J., Ruiz, G.M.H., Mansour, E.M., Leturmy, P., Frizon de Lamotte, D., 2009. Apatite fission-track analyses on basement granites from south-western Meseta, Morocco: Paleogeographic implications and interpretation of AFT age discrepancies. Tectonophysics 475, 29-37.

Saura, E., Ardèvol, L., Teixell, A., Vergés, J., 2016. Rising and falling diapirs, shifting depocenters, and flap overturning in the Cretaceous Sopeira and Sant Gervàs subbasins (Ribagorça Basin, southern Pyrenees). Tectonics 35, 638-662.

Saura, E., Vergés, J., Martín-Martín, J.D., Messager, G., Moragas, M., Razin, P., Grélaud, C., Joussiaume, R., Malaval, M., Homke, S., 2014. Syn-to post–rift diapirism and minibasins of the Central High Atlas (Morocco): the changing face of a mountain belt. Journal of the Geological Society 171, 97-105.

Sclater, J.G., Christie, R.A.F., 1980. Continental stretching: An explanation of the post–mid-Cretaceous subsidence of the central North Sea Basin. Journal of Geophysical Research 85, 711 - 739.

Sclater, J.G., Jaupart, C., Galson, D., 1980. The heat flow through oceanic and continental crust and the heat loss of the Earth. Reviews of Geophysics 18, 269-311.

Schaer, J.P., Persoz, F., 1976. Aspects structuraux et petrographiques du Haut-Atlas calcaire de Midelt (Maroc). Bulletin de la Societe Geologique de France Series 7 Vol. XVIII, 1239-1250.

Schultz-Ela, D.D., 2003. Origin of drag folds bordering salt diapirs. AAPG Bulletin 87, 757-780.

Schultz-Ela, D.D., Jackson, M.P.A., 1996. Relation of subsalt structures to suprasalt structures during extension. AAPG Bulletin 80, 1896-1924.

Schultz-Ela, D.D., Jackson, M.P.A., Vendeville, B.C., 1993. Mechanics of active salt diapirism. Tectonophysics 228, 275-312.

Sellier, N.C., Vendeville, B.C., Loncke, L., 2013. Post–Messinian evolution of the Florence Rise area (Western Cyprus Arc) Part II: Experimental modeling. Tectonophysics 591, 143-151.

Septfontaine, M., 1988. Biozonation (by means of imperforate foraminifera) of the Liasic carbonate inner platform of the High Atlas (Morocco) - "Biozonation (A l'Aide des foraminiferes imperforés) de la plate-forme interne carbonatée Liasique de Haut Atlas (Moroc)". Revue de Micropaleontologie 27, 209-229.

Snoke, A.W., Schamel, S., Karasek, R.M., 1988. Structural evolution of Djebel Debadib anticline: a clue to the regional tectonic style of the Tunisian Atlas. Tectonics 7, 497-516.

Souhel, A., Canerot, J., El Bchari, F., Chafiki, D., Gharib, A., El Hariri, K., Bouchouata, A., 2000. The Liassic carbonate platform on the western part of the Central High Atlas (Morocco): stratigraphic and palaeogeographic patterns, in: Crasquin, S., Barrier, E. (Eds.), Peri-Tethys Memoir 5: New data on peri-Tethyan sedimentary basins. Mémoires du Muséum National d´Histoire Naturelle, Paris, pp. 39-56.

Stapel, G., Cloetingh, S., Pronk, B., 1996. Quantitative subsidence analysis of the Mesozoic evolution of the Lusitanian basin (western Iberian margin). Tectonophysics 266, 493-507.

Steckler, M.S., Watts, A.B., 1978. Subsidence of the Atlantic-type continental margin off New York. Earth and Planetary Science Letters 41, 1-13.

Stewart, S.A., Clark, J.A., 1999. Impact of salt on the structure of the Central North Sea hydrocarbon fairways, Petroleum Geology Conference Proceedings, pp. 179-200.

Studer, M., Du Dresnay, R., 1980. Deformations synsedimentaires en compression pendant le Lias superieur et le Dogger, au Tizi n'Irhil (Haut Atlas central de Midelt, Maroc). Bulletin de la Societe Geologique de France Series 7 Vol. XXII, 391-397.

Sweeney, J.J., Burnham, A.K., 1990. Evaluation of a simple model of vitrinite reflectance based on chemical kinetics. American Association of Petroleum Geologists Bulletin 74, 1559-1570.

Sweeney, J.J., Talukdar, S., Burnham, A., Vallejos, C., 1990. Pyrolysis kinetics applied to prediction of oil generation in the Maracaibo Basin, Venezuela. Organic Geochemistry 16, 189-196.

Talbot, C.J., 1995. Molding of salt diapirs by stiff overburden, in: Jackson, M.P.A., Roberts, D.G., Snelson, S. (Eds.), Salt tectonics: a global perspective, AAPG Memoir 65, pp. 61-75.

Tari, G., Jabour, H., 2013. Salt tectonics along the Atlantic margin of Morocco. Geological Society, London, Special Publications 369, 337-353.

Tari, G., Molnar, J., Ashton, P., 2003. Examples of salt tectonics from West Africa: A comparative approach, pp. 85-104.

Teixell, A., Arboleya, M.L., Julivert, M., Charroud, M., 2003. Tectonic shortening and topography in the Central High Atlas (Morocco). Tectonics 22, 1-14.

Teixell, A., Ayarza, P., Zeyen, H., Fernandez, M., Arboleya, M.-L., 2005. Effects of mantle upwelling in a compressional setting: the Atlas Mountains of Morocco. Terra Nova 17, 456-461.

Teixell, A., Barnolas, A., Rosales, I., Arboleya, M.-L., 2017. Structural and facies architecture of a diapir-related carbonate minibasin (lower and middle Jurassic, High Atlas, Morocco). Marine and Petroleum Geology 81, 334-360.

Tesón, E., Pueyo, E.L., Teixell, A., Barnolas, A., Agustí, J., Furió, M., 2010. Magnetostratigraphy of the ouarzazate basin: Implications for the timing of deformation and mountain building in the High Atlas Mountains of Morocco. Geodinamica Acta 23, 151-165.

Tesón, E., Teixell, A., 2008. Sequence of thrusting and syntectonic sedimentation in the eastern Sub-Atlas thrust belt (Dadès and Mgoun valleys, Morocco). International Journal of Earth Sciences 97, 103-113.

Turner, P., Sherif, H., 2007. A giant Late Triassic-Early Jurassic evaporitic basin on the Saharan Platform, North Africa, in: Schreiber, B.C., Lugli, S., Babel, M. (Eds.), Evaporites through space and time. Geological Society Special Publication, pp. 87-105.

Vendeville, B.C., 2005. Salt tectonics driven by sediment progradation: Part I - Mechanics and kinematics. AAPG Bulletin 89, 1071-1079.

Vendeville, B.C., Ge, H., Jackson, M.P.A., 1995. Scale models of salt tectonics during basement-involved extension. Petroleum Geoscience 1, 179-183.

Vendeville, B.C., Jackson, M.P.A., 1992. The rise of diapirs during thin-skinned extension. Marine and Petroleum Geology 9, 331-354.

Vendeville, B.C., Jackson, M.P.A., Weijermars, R., 1993. Rates of salt flow in passive diapirs and their source layers, Rates of Geologic Processes, GCSSEPM Fundation 14th Annual Research Conference, pp. 269-276.

Vergés, J., Moragas, M., Martín-Martín, J.D., Saura, E., Razin, P., Grélaud, C., Malaval, M., Joussiaume, R., Messager, G., Sharp, I., Hunt, D.W., 2017. Salt tectonics in the Atlas mountains of Morocco, in: Soto, J.I., Tari, G., Flinch, J. (Eds.), Permo-Triassic Salt Provinces of Europe, North Africa and the Atlantic Margins: Tectonics and hydrocarbon potential Elsevier.

Verwer, K., Oscar, M.T., Kenter, J.A.M., Porta, G.D., 2009a. Evolution of a high-relief carbonate platform slope using 3D digital outcrop models: Lower jurassic djebel bou dahar, high atlas, Morocco. Journal of Sedimentary Research 79, 416-439.

Verwer, K., Porta, G.D., Merino-Tomé, O., Kenter, J.A.M., 2009b. Controls and predictability of carbonate facies architecture in a Lower Jurassic three-dimensional barrier-shoal complex (Djebel Bou Dahar, High Atlas, Morocco). Sedimentology 56, 1801-1831.

Vially, R., Letouzey, J., Bénard, F., Haddadi, N., Desforges, G., Askri, H., Boudjema, A., 1994. Basin inversion along the North African Margin; The Saharan Atlas (Algeria), in: Roure, F., Pétrole, I.F.d. (Eds.), Peri-Tethyan platforms, Arles, France, pp. 79-118.

Warme, J.E., 1988. Jurassic carbonate facies of the Central and Eastern High Atlas rift, Morocco, in: Jacobshagen, V.H. (Ed.), The Atlas System of Morocco. Springer Berlin Heidelberg, pp. 169-199.

Warsitzka, M., Kley, J., Jähne-Klingberg, F., Kukowski, N., 2017. Dynamics of prolonged salt movement in the Glückstadt Graben (NW Germany) driven by tectonic and sedimentary processes. International Journal of Earth Sciences 106, 131-155.

Warsitzka, M., Kley, J., Kukowski, N., 2013. Salt diapirism driven by differential loading — Some insights from analogue modelling. Tectonophysics 591, 83-97.

Watts, A.B., Steckler, M.S., 1981. Subsidence and tectonics of Atlantic-type continental margins. Oceanologica Acta 1, 143-153.

Weijermars, R., Jackson, M.P.A., Vendeville, B., 1993. Rheological and tectonic modeling of salt provinces Tectonophysics 217, 143-174.

Wilmsen, M., Neuweiler, F., 2008. Biosedimentology of the Early Jurassic post–extinction carbonate depositional system, central High Atlas rift basin, Morocco. Sedimentology 55, 773-807.

Wilson, R.C.L., 1988. Mesozoic of the Lusitanian Basin, Portugal. Revista de la Sociedad Geológica de España 1, 393-407.

Wilson, R.C.L., Hiscott, R.N., Willis, M.G., Gradstein, F.M., 1989. The Lusitanian Basin of West-Central Portugal: Mesozoic and Tertiary Tectonic, Stratigraphic, and Subsidence History, in: Tankard, A.J., Balkwill, H.R. (Eds.), Extensional Tectonics and Stratigraphy of the North Atlantic Margins, AAPG Memoir 46, Chapter 22, pp. 341-361.

Withjack, M.O., Callaway, S., 2000. Active normal faulting beneath a salt layer: An experimental study of deformation patterns in the cover sequence. AAPG Bulletin 84, 627-651.

Worral, D.M., Snelson, S., 1989. Evolution of the northern Gulf of Mexico with emphasis on Cenozoic growth faulting and the role of salt, in: Bally, A.W., Palmer, A.R. (Eds.), The Geology of America. The Geological Society of America, pp. 97-138.

Wu, J.E., McClay, K.R., 2011. Two-dimensional analog modeling of fold and thrust belts: Dynamic interactions with syncontractional sedimentation and erosion. AAPG Memoir, 301-333.

Xie, X., Heller, P.L., 2009. Plate tectonics and basin subsidence history. Geological Society of America Bulletin 121, 55-64.

Zeyen, H., Ayarza, P., Fernàndez, M., Rimi, A., 2005. Lithospheric structure under the western African-European plate boundary: A transect across the Atlas Mountains and the Gulf of Cadiz. Tectonics 24, 1-16.

Ziegler, P.A., Cloetingh, S., van Wees, J.-D., 1995. Dynamics of intra-plate compressional deformation: the Alpine foreland and other examples. Tectonophysics 252, 7-59.

Zizi, M., 1996. Triassic-Jurassic extensional systems and their Neogene reactivation in Northern Morocco (the Rides pre-Rifaines and Guercif Basin). Rice University, Houston.

Zouaghi, T., Bédir, M., Ayed-Khaled, A., Lazzez, M., Soua, M., Amri, A., Inoubli, M.H., 2013. Autochthonous versus allochthonous Upper Triassic evaporites in the Sbiba graben, central Tunisia. Journal of Structural Geology 52, 163-182.

Zühlke, R., Bouaouda, M.S., Ouajhain, B., Bechstädt, T., Leinfelder, R., 2004. Quantitative Meso-/Cenozoic development of the eastern Central Atlantic continental shelf, western High Atlas, Morocco. Marine and Petroleum Geology 21, 225-276.

ANNEXES

10. ANNEXES

10.1. STATISTICAL ANALYSIS OF FREQUENCIES DISTRIBUTION: FILTERING IMILCHIL DIAPIRIC PROVINCE THICKNESS MAPS

3D surfaces of the bases of the outcropping sedimentary units in the Imilchil diapiric province were available to be used in the present research (Fig. 10.1). Using Move software (Midland Valley), GDL provide a large amount of thickness data measured orthogonal to the surfaces (Fig. 10.1). However, anomalous thickness values have been detected from thickness maps. These anomalies are mainly located in the vicinities of the diapiric structures, where the overturned layers from the 3D model caused the overestimation of thicknesses.

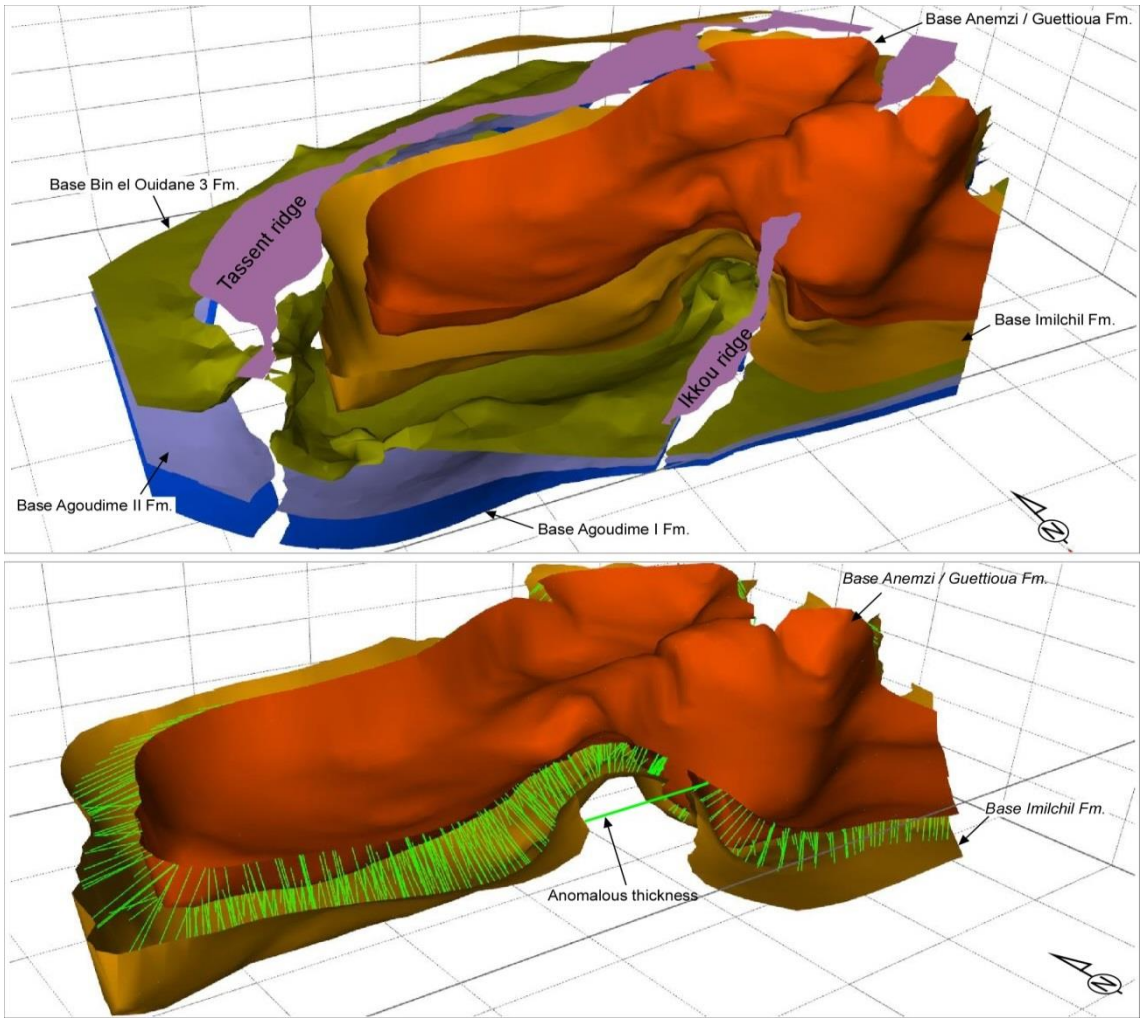

Fig. 10.1. a) Screenshot showing the 3D surfaces corresponding to the 5 sedimentary units described in the Imilchil diapiric province. b) Detail of Imilchil and Anemzi/ Guettioua Fm. bases used to calculate thickness values (green lines).

To build thickness maps for each sedimentary unit outcropping in the Imilchil Diapiric Province, statistical analysis of frequencies distribution has been applied in order to filter the extreme values considered as thickness anomalies. This statistical method analyse the frequency of the occurrence of values (in this case thickness of the analysed sedimentary units) within a particular interval.

Between 1500 and 6900 discrete thickness values are obtained from 3D models corresponding to the five studied sedimentary units (Agoudime I, Agoudime II, Bin el Ouidane 3, Imilchil and Anemzi/Guettioua formations). To carry out the frequency distribution analysis of those values, several parameters are required for each sedimentary unit (Fig. 10.2):

N: Total amount of thickness measures

Hn: Highest thickness value

Ln: Lowest thickness value

Rm: Range of measures = *Hn* – *Ln*

C: Number of intervals = 1+3.33 log(*N*)

h: Width of the intervals = *Rm*/*C*

Xi-1: Lowest value of the interval range. For the first interval, *Xi-1* is the lowest thickness value (*Ln*)

Xi: Highest value of the interval range. *Xi*= *Xi-1* + *h*

Ni: Number of values within the interval

Rf: Relative frequency = *Ni*/*N*

The relative frequency value is the criterion used to select the anomalous thickness values. Therefore, thickness values included in intervals with a relative frequency equal or below 2% are considered outliers within the total data and not included in the interpolation of thickness maps. For example, Agoudime I Fm. is composed by a total amount of 6808 thickness values extracted from 3D model, with the lowest value (Ln) equal to 83.81m and the highest (Hn) equal to 13475.77m. From those, values higher than 1997.81m of thickness are considered anomalous because they are within an interval with a relative frequency equal or lower than 2%. The same threshold is applied to the other sedimentary units, and thus, outliers in Agoudime II Fm. are those higher than 1446.16 m, for Bin el Ouidane 3 Fm. are higher than 2568.28 m, for Imilchil FM. are higher than 1659.32 and for Anemzi / Guettioua Fm. outliers are higher than 2719.1 m.

Agoudime I Fm.

Parameters			Interval	Xi-1	Xi	Ni	Rf
			1	83.81	1040.81	6077	89%
			2	1040.81	1997.81	638	9%
			3	1997.81	2954.81	65	1%
			4	2954.81	3911.81	6	0%
			5	3911.81	4868.81	4	0%
N=	6808		6	4868.81	5825.81	4	0%
Hn=	13475.77		7	5825.81	6782.81	3	0%
Ln=	83.81		8	6782.81	7739.81	0	0%
Rm=	13391.96		9	7739.81	8696.81	3	0%
C=	13.7639551	≈ 14	10	8696.81	9653.81	1	0%
h=	956.568571		11	9653.81	10610.8	2	0%
Xi-1=	83.81		12	10610.8	11567.8	1	0%
			13	11567.8	12524.8	0	0%
			14	12524.8	13481.8	4	0%
					N=	6808	

Agoudime II Fm.

Parameters			Interval	Xi-1	Xi	Ni	Rf
			1	1.16	290.16	760	11%
			2	290.16	579.16	2116	31%
			3	579.16	868.16	2333	35%
			4	868.16	1157.16	1123	17%
			5	1157.16	1446.16	240	4%
N=	6742		6	1446.16	1735.16	57	1%
Hn=	4036.75		7	1735.16	2024.16	42	1%
Ln=	1.16		8	2024.16	2313.16	33	0%
Rm=	4035.59		9	2313.16	2602.16	15	0%
C=	13.7498665	≈ 14	10	2602.16	2891.16	10	0%
h=	288.256429		11	2891.16	3180.16	5	0%
Xi-1=	1.16		12	3180.16	3469.16	5	0%
			13	3469.16	3758.16	2	0%
			14	3758.16	4047.16	1	0%
					N=	6742	

Bin el Ouidane 3 Fm.

Parameters			Interval	Xi-1	Xi	Ni	Rf
			1	0.28	856.28	3557	72%
			2	856.28	1712.28	1191	24%
			3	1712.28	2568.28	197	4%
			4	2568.28	3424.28	7	0%
			5	3424.28	4280.28	2	0%
N=	4959		6	4280.28	5136.28	0	0%
Hn=	11983.64		7	5136.28	5992.28	0	0%
Ln=	0.28		8	5992.28	6848.28	0	0%
Rm=	11983.36		9	6848.28	7704.28	1	0%
C=	13.3056624	≈ 14	10	7704.28	8560.28	0	0%
h=	855.954286		11	8560.28	9416.28	0	0%
Xi-1=	0.28		12	9416.28	10272.3	2	0%
			13	10272.3	11128.3	1	0%
			14	11128.3	11984.3	1	0%
					N=	4959	

Imilchil Fm.

Parameters			Interval	Xi-1	Xi	Ni	Rf
			1	4.32	335.32	866	23%
			2	335.32	666.32	1375	36%
			3	666.32	997.32	902	24%
			4	997.32	1328.32	342	9%
			5	1328.32	1659.32	273	7%
N=	3778		6	1659.32	1990.32	6	0%
Hn=	4306.76		7	1990.32	2321.32	4	0%
Ln=	4.32		8	2321.32	2652.32	5	0%
Rm=	4302.44		9	2652.32	2983.32	2	0%
C=	12.9122823	≈ 13	10	2983.32	3314.32	2	0%
h=	330.956923		11	3314.32	3645.32	0	0%
Xi-1=	4.32		12	3645.32	3976.32	0	0%
			13	3976.32	4307.32	1	0%
					N=	3778	

Anemzi/Guettioua Fm.

Parameters			Interval	Xi-1	Xi	Ni	Rf
			1	1.1	303.1	181	12%
			2	303.1	605.1	198	13%
			3	605.1	907.1	142	9%
			4	907.1	1209.1	112	7%
			5	1209.1	1511.1	167	11%
N=	1564		6	1511.1	1813.1	301	19%
Hn=	3622.72		7	1813.1	2115.1	251	16%
Ln=	1.1		8	2115.1	2417.1	98	6%
Rm=	3621.62		9	2417.1	2719.1	44	3%
C=	11.6368084	≈ 12	10	2719.1	3021.1	36	2%
h=	301.801667		11	3021.1	3323.1	24	2%
Xi-1=	1.1		12	3323.1	3625.1	10	1%
					N=	1564	

Fig. 10.2. Quantified parameters used for the frequency distribution analysis for each sedimentary unit in the Imilchil diapiric province. Red boxes highlight the threshold value for filtering each thickness map.

10.2. ANALOGUE MODELS A0: TESTING THE THICKNESSES OF THE LAYERS

The first extensional analogue model was designed with a silicone layer of 1.5 cm in the hangingwall and 1 cm in the footwalls covered by a 0.5 cm thick pre–extension layer. Using a constant velocity of 0.5 cm/h applied to each mobile wall by a screw jack, the total deformation velocity in the model was 1 cm/h with a total extension of 2 cm (equal to the Model A1). At the end of the extension, without the influence of sedimentation, cross-section only revealed small-scale disturbances of the silicone layer beneath the extensional grabens affecting the pre-extension sand layers, but no well-defined reactive diapirs as in the Model A1 were obtained. Thus, thicknesses of the silicone layer in the hangingwall and pre-extension sand layer were increased in the Model A1 as it was detailed in Chapter 4 “Methods”.

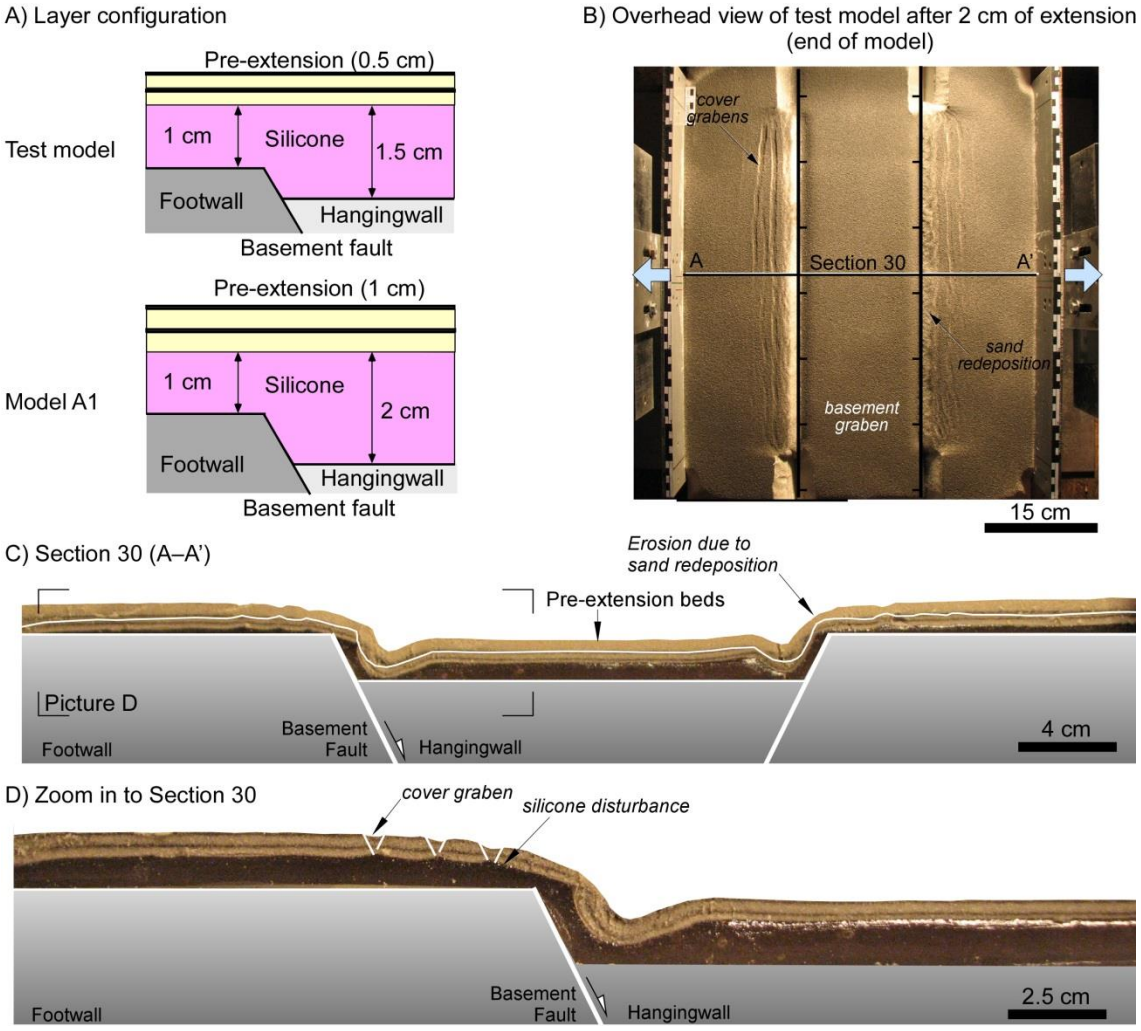

Fig. 10.3. A) Layering configuration of testing model and Model A1; B) Overhead view of Test model (total extension=2 cm) showing the distribution of several newly formed grabens in the pre-extension beds; C) and D) Cross-sections showing the silicone disturbance beneath the cover grabens bounded by two opposing normal faults.

10.3. THERMAL MODELLING OF THE TAZOULT DIAPIR LOG

As it has been detailed in Subchapter 6.2 Thermal modelling, the presence of diapiric structures causes anomalies in the thermal field of a basin due to the high thermal conductivity of salt (Petersen and Lerche, 1995; Petersen and Lerche, 1996). For that, in the presented thesis only the Amezraï stratigraphic log, located far from the potential thermal influence of the Tazoult and Azourki diapirs, have been used in the analysis of the thermal models. However, the availability of vitrinite samples in the Tazoult diapir stratigraphic log allows presenting a first approach of the potential variations of thermal history far and close to Tazoult diapir (Fig. 3.4).

In order to compare both Tazoult diapir and Amezraï minibasin thermal histories, the thermal parameters (heat flow) and burial amounts obtained in models of Late Jurassic–Early Cretaceous sedimentation from the Amezraï minibasin analysis (Fig. 6.11) were applied to the Tazoult diapir log. Thus, in Figure X the nine models are: a) Short high heat flow event (70 mW/m^2) with additional burial of 2400 m; b) Long high heat flow event (70 mW/m^2) with additional burial of 2200 m; c) Maximized high heat flow event (70 mW/m^2) with additional burial of 2000 m; d) Short high heat flow event (105 mW/m^2) with additional burial of 2000 m; e) Long high heat flow event (105 mW/m^2) with additional burial of 1200 m; f) Maximized high heat flow event (105 mW/m^2) with additional burial of 800 m; g) Short high heat flow event (120 mW/m^2) with additional burial of 1700 m; h) Long high heat flow event (120 mW/m^2) with additional burial of 800 m; and i) Maximized high heat flow event (120 mW/m^2) with additional burial of 550 m.

All models show calculated vitrinite reflectance curves with higher reflectance values than the analysed samples at same reference depth and, consequently, the presented thermal models evidence that the samples from Tazoult diapir log are less mature than Amezraï minibasin samples (Fig. 10.4). These could be associated to: i) a lower heat flow amount in the Tazoult diapir log than in the Amezraï minibasin log due to the thermal anomalies associated to the presence of Tazoult salt diapir; ii) a thinner amount of burial in the Tazoult diapir log than the one obtained in the models from the central part of the Amezraï minibasin; pointing to differential Post–middle Jurassic subsidence evolution in both localities or iii) a combination of both factors. Due to the limited available data and information for ages younger than Middle Jurassic it is not possible to precise further which factor controls the maturity variations from both localities.

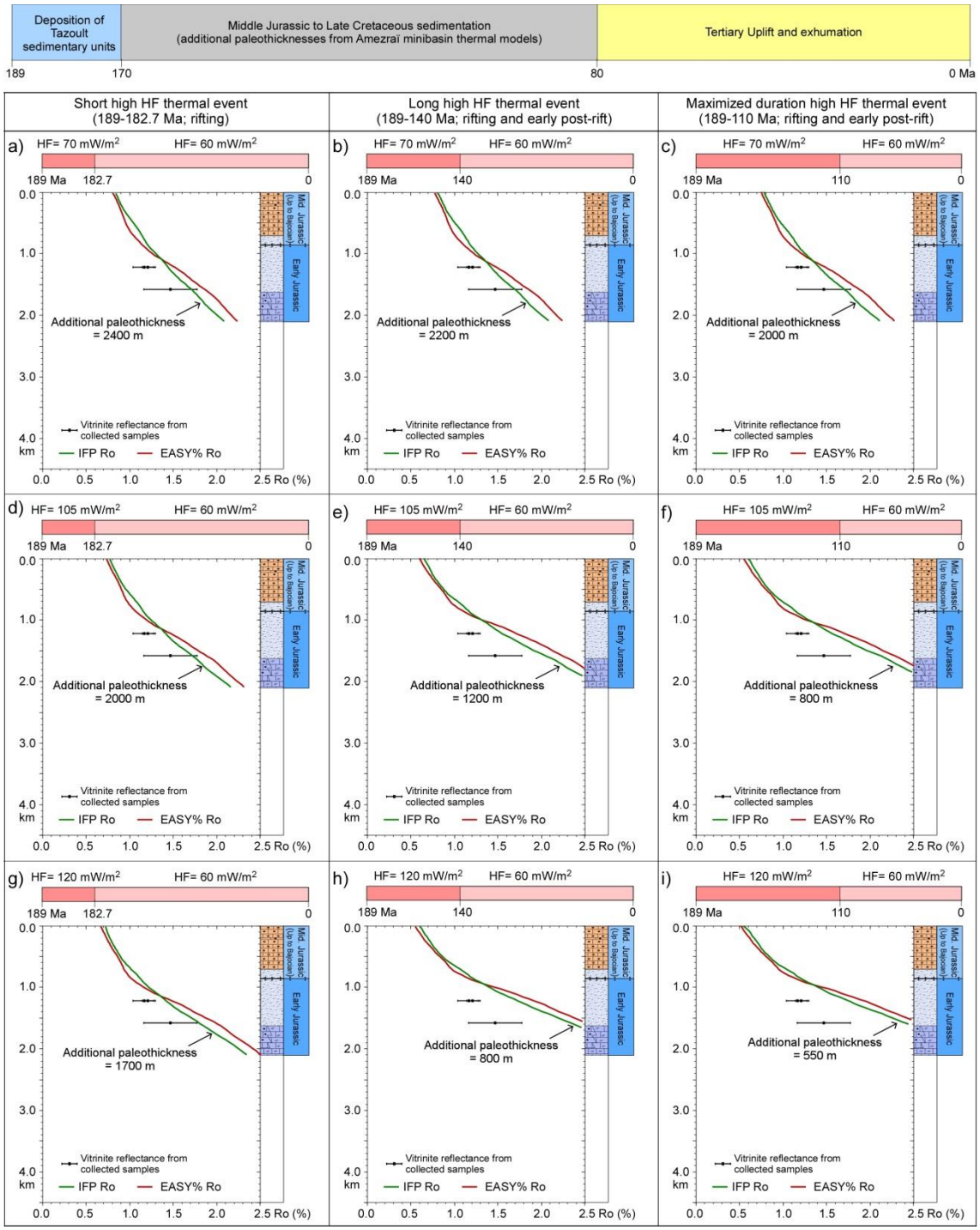

Fig. 10.4. Thermal model plots based on the present-day Tazoult diapir stratigraphic section showing: calculated vitrinite reflectance profiles (IFPRo and Easy%Ro) resulting from a short (from 189 to 182.7 Ma), long (from 189 to 140 Ma) and maximized period of high heat flow occurrence (from 189 to 110 Ma) with heat flow of 70 mW/m^2 (a, b and c), 105 mW/m^2 (d, e and f) and 120 mW/m^2 (g, h and i). Red and green lines correspond to the calculate vitrinite reflectance curve obtained using the same amount of burial than in the Amezraï stratigraphic log (see Section 6.2.1 for details) with a homogeneous sedimentation from 169 Ma to 80 Ma. All models include a period of low thermal conditions of 60 mW/m^2.